Mechanical locking distributions on the plate interface estimated from seafloor and onshore geodetic observation data

海底および陸上測地観測データから推定される
プレート境界面上の力学的固着分布

木村　洋
(KIMURA, Hiroshi)

A dissertation for the degree of Doctor of Science
Department of Earth and Environmental Sciences,
Graduate School of Environmental Studies, Nagoya University

（名古屋大学大学院環境学研究科地球環境科学専攻学位論文　博士（理学））

January 2021

Abstract

Interplate earthquakes occur in areas where an interseismic slip deficit or strain accumulates on the plate interface. Because the slip deficit rate is larger in the mechanical locking zone than that on the plate interface around it, it is essential to reveal the spatial distribution of interplate mechanical locking to accurately evaluate seismic (and accompanying tsunami) potential at subduction zones. Many previous studies estimated slip deficit rate distributions from geodetic observation data based on a pure kinematic framework in which fault dislocation and elastic response at the surface are considered without any mechanical constraints; using this approach, it is impossible to identify the mechanically locked zone from the estimated slip deficit rate distributions. To overcome this limitation, this study developed a new physical model that describes the relation between the mechanical locking on the plate interface and surface crustal deformation by considering the mechanical constraints on the plate interface. The proposed model was incorporated in an inversion approach adopting the replica Monte Carlo method, based on Bayesian estimation, to estimate mechanical locking distributions along the subduction zone based on geodetic observation data. This model was first applied to onshore and seafloor geodetic observation data in northeast Japan during the interseismic period to estimate mechanical locking distributions along the Japan and Kuril Trenches; next, it was applied to onshore and seafloor geodetic observation data in southwest Japan during the interseismic period to estimate mechanical locking distributions along the Nankai Trough. For northeast Japan, two mechanical locking segments were estimated on the plate interface where the 2011 Mw 9.0 Tohoku earthquake occurred. The results obtained by the model indicate that the coseismic slip area is significantly larger than the mechanical locking zone, and strong motion generation areas tended to be located at the edges of mechanical locking distributions. These findings imply that the model can be

used to predict coseismic slip areas, brittle rupture, accompanying slip areas, and potential strong motion generation areas of future earthquakes. For southwest Japan, four mechanically locked segments were estimated along the Nankai Trough. Clear complementation between the mechanical locking distribution and the slow earthquake occurrence zone, implying the capability of estimation of the frictional states on the plate interface, were identified. Furthermore, it was predicted that potential strong motion generation areas along the Nankai Trough may be larger than that along the Japan Trench. Applying the new model to subduction zones as well as splay or inland faults may enable the advanced evaluation of seismic hazard for interplate and intraplate earthquakes globally.

Acknowledgements

I first want to thank my supervisor, Dr. Keiichi Tadokoro, for his fundamental role in my research. He has provided me with significant guidance and assistance throughout the course of this study. He encouraged my research and provided many important opportunities, such as those to participate in seafloor geodetic observations in research vessels from Kumano to Okinawa and campaign GNSS observation in Zenisu Reef. Moreover, his knowledge in seismology, geodesy, and modeling was indispensable. I am grateful for his feedback and support when drafting manuscripts or presenting at conferences and seminars. This thesis could not have been completed without his support throughout my time at Nagoya University.

I would also like thank Dr. Takeo Ito for helping me develop my research strategy and providing crucial advice for modeling, computing, and observation techniques. I am grateful for his assistance in revising my first paper that was accepted to Journal of Geophysical Research (JGR): Solid Earth at midnight on the day before his GNSS observation in Mt. Ontake. I am also thankful for him allowing me to use workstations with the world's most powerful CPUs and GPUs, which led to significant increases in my calculation speeds. He heavily contributed to the creation of the programming code used for my master's thesis. My doctoral study would not be advanced without his aid.

Furthermore, I would like thank Dr. Koshun Yamaoka, who has provided me with significant support and advice for my research strategy in geodynamics seminars. His guidance was integral in developing the skills required to draft effective manuscripts and communicate my research. His advice always proved helpful, specifically for writing this thesis as well as my paper for JGR and papers presented at conferences.

I would also like to thank Dr. Ryohei Sasajima, who now researches at Kyoto University. The novel physical model developed in this study was first inspired by his

ideas. I am grateful for his advice and guidance throughout the course of my research. The programming code used in this study contains many subroutines that were originally developed by Dr. Sasajima. I would like to thank Mr. Kenji Matsuhiro, Dr. Natsuki Kinugasa, Dr. Kenji Yasuda, and the crews of research vessels for supporting the observations that were essential for this project. Additionally, I would like to thank Dr. Naoki Suda and Dr. Tomoeki Nakakuki at Hiroshima University, who taught me the foundations of geophysical research and computing techniques. My understanding of slow earthquakes was significantly supported by Dr. Suda. I would like to thank many researchers in Tohoku University, JAMSTEC, and Japan Coast Guard for providing the opportunity for discussion regarding the observation, modeling, coding, and implications of the results. I would also like to thank all teachers, researchers, and fellow students in the Earth and Planetary Dynamics department for their comments and advice. In particular, I am grateful to Mr. Shuhei Tsuji for our discussions, which have been very helpful for my research. His knowledge of computers also guided the selection of my workstation used for this study.

I also thank the Geophysical Survey Institute for making the GEONET available and Dr. Takao Tabei for providing the ZENISU site observational data. The model of plate interface by Iwasaki et al. (2015) is available at http://evrrss.eri.u-tokyo.ac.jp/database/PLATEmodel/PLMDL_2016/ with their references. The repeating earthquakes and slip distributions of past megathrust earthquakes in northeast Japan were published as referenced in the paper and were made available to us by Dr. Naoki Uchida at Tohoku University (https://www.aob.gp.tohoku.ac.jp/~uchida/page_3.html). The Generic Mapping Tools (Wessel et al., 2013) were used to prepare most figures. The computing code developed and used in this study is available from https://github.com/kimhiroshiedu/PassiveSlip.git. This study was supported by the Japan

Society for the Promotion of Science (JSPS) Grant-in-Aid for JSPS Fellows KAKENHI, Grant Number 20J13179.

Finally, I would like to thank my father, mother, and older brother, who supported me both financially and emotionally throughout my work at Nagoya University. They have always encouraged me to pursue my dream. This thesis would not have been completed without their support. They are the most important people to me, and I dedicate this thesis to them.

Contents

Abstract 1

Acknowledgements 3

Chapter 1 Introduction 21

Chapter 2 Physical modeling of mechanical locking and its application in northeast Japan 28

2.1. Introduction 28

2.2. Methods and data 29

2.2.1. Physical model relating mechanical locking to crustal deformations 30

2.2.2. Bayesian estimation 37

2.2.3. Crustal deformation data in northeast Japan 43

2.2.4. Configuration of block boundary and plate interface geometry 47

2.3. Estimated mechanical locking distributions 51

2.4. Discussion 58

2.4.1. Comparison with kinematic coupling distributions 58

2.4.2. Correspondence with interplate earthquakes 62

2.4.3. Comparison with strong motion generation areas 70

2.4.4. Effects of plate interface geometries 73

2.4.5. Effects of block division models 76

2.5. Chapter summary 79

Chapter 3 Interplate mechanical locking distributions along the Nankai Trough estimated by the proposed model 81

3.1. Introduction 81

3.2. Methods and data 84

3.2.1. Configuration of replica exchange Monte Carlo Sampling 84

3.2.2. Crustal deformation data in southwest Japan 84

3.2.3. Block boundaries 88

3.2.4. Interface geometries of block boundaries and subducting plates 92

3.3. Estimated mechanical locking distributions and slip deficit rates 95

3.4. Discussion 105

3.4.1. Comparison with kinematic coupling distributions 105

3.4.2. Implicated frictional states from slow earthquake distributions 111

3.4.3. Correspondence with interplate earthquakes 115

3.4.4. Spatial relationship between mechanical locking zone and strong motion generation area 120

3.4.5. Comparison with subducted topographic anomalies 125

3.5. Chapter summary 127

Chapter 4 Conclusions 129

Appendix A Rigid motion and internal block strain results: Northeast Japan 134

A.1. Estimated Euler vectors and calculated rigid motions 134

A.2. Estimated internal block strains 138

Appendix B Rigid motion and internal block strain results: Southwest Japan 142

B.1. Estimated Euler vectors and the ratio between rigid motion and displacement due to slip deficit 142

B.2. Estimated internal block strains 147

Appendix C Displacement rate data for REMC inversion 151

C.1. Northeast Japan 151

C.2. Southwest Japan 160

References 177

List of Figures

Figure 1.1. Concept of “locking” states on the plate interface in the previous (kinematic) and proposed models. (a) In the pure kinematic model, “locking” states indicate kinematic states, such as slip deficit rate or coupling coefficient. (b) In the new physical model, “locking” states directly represent the mechanical states, that is, mechanically locked (hatched area) or creeping (non-hatched area). 25

Figure 2.1. Schematic imaging of the mechanical locking zone on the plate interface. Each triangle indicate subfaults. Red subfaults are mechanically locked. The remaining white subfaults are creeping. Subfaults were determined to be mechanically locked based on the centroid depths of subfaults and up-dip (red circles) and down-dip (blue circles) limit depths, as follows: If the centroid of the subfault is between the up- and down-dip limit depths, the subfault is considered mechanically locked, else, the subfault considered creeping.....34

Figure 2.2. Map showing observational data used in this chapter. Gray vectors with white squares and blue vectors with white circles indicate displacement rate vectors at the onshore GNSS (GEONET) and seafloor GNSS/A sites, respectively. Yellow vectors show the Pacific Plate motion relative to the Eurasian plate calculated on the basis of the MORVEL plate motion model (DeMets et al., 2010). Red stars indicate the epicenters of the Mw 7.1 Miyagi and Mw 6.9 Fukushima earthquakes. Color scale of the map represents the elevation and bathymetry of SRTM30_PLUS (Becker et al., 2009). 46

Figure 2.3. Map showing the block boundaries around northeast Japan. Abbreviations of each block are as follows: PAC, Pacific Plate; AMU, Amurian plate; OKH, Okhotsk plate; IZO, Izu-Ogasawara block; TFA, Tohoku Forearc block; TBA, Tohoku Backarc block; and NGT, Niigata block. 48

Figure 2.4. Configuration of plate and block interfaces. (a) Three-dimensional map showing the

interface of the block and subducting plates, observed from the north-northeast. Triangles on the interface are subfaults. The color scale means the depths. Black lines show the coast lines. (b) Map showing subfaults on the subducting plate interface. Green lines indicate the iso-depth contours of subducting plate interface. zup and zdown are sampled along the pink lines.....50

Figure 2.5. Map showing estimated mechanical locking distributions on the plate interface along the Nankai Trough. Color scale indicates the locking probability of each subfault given by Equation 29. Orange dashed lines indicate the iso-depth contours of the subducting plate interface. Black dashed lines indicates the boundary of the plate interface. The lower surface of the overriding Nankai block interfaces with the upper surface of the subducting Philippine Sea Plate to the west and north of the line, whereas it interfaces with the upper surface of the subducting Izu Micro Plate to the east and south of the line.....54

Figure 2.6. Graphs showing PDFs of the up- and down-dip depths and the locking probability Pl along lines A, B, C, D, E, and F in Figure 3.6. For each subfigure, PDFs and the locking probability are plotted for whole sampling depths in the left panels, whereas they are plotted for model area depths (i.e., top and bottom depths coincide with the trench and 60 km depth, respectively) in the right panels. PDFs are normalized such that the sum of the value for each bin becomes 1. Horizontal red and blue solid lines indicate the mean values of the up- and down-dip depths calculated from all samples, respectively. Mean values are described on or under the lines. The 95 percentile confidence interval values are described in brackets to the right of the mean value. The scale of PDFs and locking probability is shown in the bottom and top axes for each panel, respectively.....55

Figure 2.7. Same as Figure 2.6, but along the gray lines SA, SB, SC, and SD in Figure 2.5. 57

Figure 2.8. Calculated slip deficit rate distributions along the Kuril and Japan Trenches. (a) To calculate the slip deficit rate distribution, subfaults whose locking probability is larger than

0.5 (Figure 2.5) were selected to be the mechanically locked zone. The selected subfaults are denoted in black. (b) Map showing the slip deficit rate distributions derived from the locking distributions shown in (a). Blue lines indicate the slip deficit rate contours with an interval of 10 mm/yr, starting from 10 mm/yr. 61

Figure 2.9. Map showing the spatial relationship between mechanical locking distributions, coseismic slips, and postseismic slips. White solid lines indicate the coseismic slip contours of the Mw 8.0 Tokachi earthquake in 2003 (Yamanaka & Kikuchi, 2003) and Mw 9.0 Tohoku earthquake in 2011 (Iinuma et al., 2012). White dashed lines indicate the postseismic slip contours of the Mw 8.0 Tokachi earthquake in 2003 (Miyazaki et al., 2004) and Mw 9.0 Tohoku earthquake in 2011 (Iinuma et al., 2016). Red stars indicate the epicenters of the two earthquakes. Gray solid lines indicate the coseismic slip contours of other interplate earthquakes occurring in northeast Japan (Murotani et al., 2003; Nagai et al., 2001; Yamanaka, 2005). 68

Figure 2.10. Coseismic slip simulation results of the 2011 Tohoku earthquake. (a) Map showing rupture distributions. The red areas were defined as the coseismic rupture (brittle rupture) areas, and only the coseismic slip in these areas was given. The slip magnitude provided in the simulation is 35 m in the Miyagi segment and 10 m in the Fukushima segment. Only the constant strain condition was considered on the possible slip area (blue area), and any other constraints or boundary conditions were not adopted for evaluating slip behavior in the blue area. (b) Map showing the total coseismic slip on the plate interface. Blue lines indicate slip contours with an interval of 5 m. (c) Map showing surface displacements as the response of the total slip on the plate interface at the onshore and seafloor sites used in this study. Red-enclosed white arrows indicate the calculated displacements. Black arrows indicate the observed coseismic displacements analyzed by the Advanced Rapid Imaging and Analysis team at JPL and Caltech (JPL & Caltech, 2011; ftp://sideshow.jpl.nasa.gov/pub/usrs/ARIA/)

for onshore sites and the Japan Coast Guard (Yokota et al., 2018) for seafloor sites. 69

Figure 2.11. Coseismic slip simulation results of the 2003 Tokachi earthquake. (a) Map showing rupture distributions. The red areas were defined as the coseismic rupture (brittle rupture) areas, and only the coseismic slip in these areas was given. The slip magnitude provided in the simulation is 5 m in the coseismic rupture area. As same as the case of the coseismic slip simulation of the 2011 Tohoku earthquake, only the constant strain condition was considered on the possible slip area (blue area), and any other constraints or boundary conditions were not adopted for the slip behavior on the blue area. (b) Map showing the total coseismic slip on the plate interface. Blue lines indicate slip contours with an interval of 1 m. (c) Map showing the surface displacements as the response of the total slip on the plate interface at the onshore and seafloor sites used in this study. Red-enclosed white arrows indicate the calculated displacements. Black arrows indicate the observed coseismic displacements (Larson & Miyazaki, 2008).....70

Figure 2.12. Map showing the spatial relationship between mechanical locking zones and SMGAs. Black meshes indicate the estimated mechanical locking zone shown in Figure 2.8(a). Pink and yellow closed lines indicate the SMGAs of the Mw 8.0 earthquake in 2003 estimated by Nozu & Irikura (2008) and Kamae & Kawabe (2004), respectively. Cyan and green closed lines indicate the SMGAs of the Mw 9.0 earthquake in 2011 estimated by Kurahashi & Irikura (2013) and Asano & Iwata (2012). Red stars indicate the epicenters of the two earthquakes.....72

Figure 2.13. Comparison of mechanical locking distributions between two plate geometry models. (a) Map showing iso-depth contours of “Model I” (green lines; Iwasaki et al., 2015) and “Model H” (orange lines; Hirose et al., 2008; Kita et al., 2010; Nakajima et al., 2009; Nakajima & Hasegawa, 2006). The contour interval is 20 km in depth. (b) Map showing the mechanical locking distributions expressed as the locking probability estimated using Model

I. (c) Same as (b) but using Model H. 75

Figure 2.14. Comparison of mechanical locking distributions and residual vectors for Models O and S. (a) Map showing the mechanical locking distributions estimated in Model O, which is the original block division model used in the main analyses and contains 7 blocks. Background color scale indicates the locking probability. Gray solid lines indicate block boundaries. (b) Same as (a) but for Model S, which is an additional block division model and contains 4 blocks. Gray dashed lines indicate the block boundaries existing in Model O but not in Model S. (c) Map showing residual vectors between observed and calculated displacement rates (observation minus calculation) for Model O. (d) Same as (c) but for Model S. 78

Figure 3.1. Interplate coupling estimated by Kimura et al. (2019). Squares and circles indicate the onshore GNSS and seafloor GNSS/A observation sites, respectively. (a) Map showing the coupling distributions, expressed as coupling coefficient (background color scale). Orange and green lines indicate the iso-depth contours. (b) Map showing the slip deficit rate distribution (background color scale). Black lines on the plate interface indicate the iso-depth contours. 82

Figure 3.2. Map showing displacement rate vectors used. Gray and purple vectors represent the displacement rate vectors of GEONET and ZENISU. Red, green, and blue vectors represent the displacement rate vectors of seafloor GNSS/A site obtained by Nagoya University, Nagoya and Tohoku Universities (shared site), and the Japan Coast Guard. Yellow vectors show the Philippine Sea (PHS) plate motion relative to the Amurian (AMU) plate calculated on the basis of the MORVEL plate motion model (DeMets et al., 2010). Color scale of the map represents the elevation and bathymetry of SRTM30_PLUS (Becker et al., 2009). 87

Figure 3.3. Map showing tectonic settings of southwest Japan. Black lines, red dots, and solid or dashed lines show active fault trace lines (Nakata & Imaizumi, 2002), epicenters of ordinary

earthquakes, and major tectonic structures (line or zone), respectively. The detected period and magnitude range of plotted earthquakes are 1994–2016 and Mw ≥2, respectively. MTL, Median Tectonic Line; ZR, Zenisu Ridge; ISTL, Itoigawa–Shizuoka Tectonic Line; NKTZ, North Chugoku Shear Zone (San-in shear zone); BSG, Beppu-Shimabara Graben. 90

Figure 3.4. Map showing the block boundaries (black bold lines). Abbreviations indicate block names: AMU, Amurian plate; OKH, Okhotsk plate; YAZ, Yangtze plate; ONN, Okinawa-North block; ONS, Okinawa-South block; KIN, Kinki block; CHB, Chubu block; STU, Setouchi block; NAN, Nankai block; IMP, Izu Micro Plate; IZO, Izu Ogasawara block; PHS, Philippine Sea Plate; PAC, Pacific Plate. Green dashed lines indicates the iso-depth contours of subducting plate interfaces (Iwasaki et al., 2015). The small map shown at right-bottom in the map represents the entire model region. The red-hatched region in the small map was focused on in this chapter.....91

Figure 3.5. Interface geometries of block boundaries and subducting plates. (a) The three-dimensional map showing the interfaces of blocks and subducting plates. This map shows the WSW orientation. Triangular meshes on the interface are subfaults. The geometry of the subducting plate interface was taken from Iwasaki et al. (2015). The color scale indicates the interface depths. Black solid and dashed lines represent coast lines and trough axes. (b) Map showing subfaults (gray triangles) on the plate interface along the Nankai Trough. Green lines indicate iso-depth contours of the upper surfaces of the subducting plate interfaces, with a depth interval of 10 km starting from 10 km in depth. Blue dashed line indicates the boundary of the plate interface. The lower surface of the overriding Nankai block is contacting with the upper surface of the subducting Philippine Sea Plate at the west and north of the line, whereas it is contacting with the upper surface of the subducting Izu Micro Plate at the east and south of the line. 94

Figure 3.6. Map showing estimated mechanical locking distributions on the plate interface along

the Nankai Trough. Background color scale indicates the locking probability of each subfault given by Equation 29. Green dashed lines indicate the iso-depth contours of the subducting plate interface. Names of mechanical locking segment are italicized.....99

Figure 3.7. Graphs showing PDFs of the up- and down-dip depths and Pl along the line A, B, C, D, E, and F shown with green solid lines in Figure 3.6. For each subfigure, PDFs and Pl are plotted for whole sampling depths in the left panels and for model area depths (i.e., top and bottom depths coincide with the trench and 60 km depth, respectively) in the right panels. PDFs are normalized such that the sum of the value for each bin becomes 1. Horizontal red and blue solid lines indicate the mean value of the up- and down-dip depths calculated from all the samples. Mean values are described on or under the lines. The 95 percentile confidence interval values are described in brackets to the right of the mean value. The scales of PDFs and Pl are shown in the bottom and top axes for each panel, respectively. 100

Figure 3.8. Slip deficit rate distributions along the Nankai Trough. (a) Map showing the selected subfaults (black subfault) whose locking probabilities is larger than 0.5 and that were assumed to be mechanically locked. (b) Map showing the slip deficit rate distributions calculated on the basis of the mechanical locking distributions and Equation 10. The two-dimensional PDFs of relative motion (slip deficit) rates at cross A and B are shown in Figure 3.10. 102

Figure 3.9. Uncertainties of Euler vectors of subducting plates relative to the Nankai Forearc block. (a) Map showing the two-dimensional PDF of the Euler vector of the subducting Philippine Sea Plate relative to Nankai Forearc block. The background color scale means the probability distribution of the Euler pole location. The gray star indicates the mean value, and the orange circle indicate the Euler pole estimated by Kimura et al. (2019). (b) Graph showing the probability distribution of the Euler pole angular velocity of the subducting Philippine Sea Plate relative to the Nankai Forearc block. The clockwise rotation

corresponds to positive angular velocity. The black vertical line indicates the mean value. The orange vertical line indicates the angular velocity estimated by Kimura et al. (2019). (c) Same as (a) but the Euler vector of the subducting Izu Micro Plate relative to the Nankai Forearc block. (d) Same as (b) but the Euler vector angular velocity of the subducting Izu Micro Plate relative to the Nankai Forearc block. 103

Figure 3.10. Uncertainties of relative motion rate in the western (point A in Figure 3.8b) and eastern (point B in Figure 3.8b) parts of the model region. (a), (c) Graphs showing the PDF of the northern and eastern plate convergence rates at the western part of the model region, respectively. (b) Graph showing the two-dimensional probability distribution of the northing and easting plate convergence rates at the western part of the model region. Background color indicates the normalized probability density. (d), (f) Same as (a) and (c) but for the eastern part of the model region, respectively. (e) Same as (b) but for the eastern part of the model region. 104

Figure 3.11. Comparison of mechanical locking distributions, kinematic coupling distributions, slip deficit rate distributions, and residuals. (a) Map showing the mechanical locking distributions along the Nankai Trough expressed as the locking probability. The hatched regions exhibit the locking probability larger than 0.5. (b) Map showing the kinematic coupling distributions estimated by Kimura et al. (2019). The color scale means the coupling coefficient at each subfault. (c) Map showing slip deficit rate distributions on the plate interface calculated on the basis of the mechanical locking zones, hatched regions in (a). Abbreviations indicate the block name (Figure 3.4). (d) Map showing the slip deficit rate distribution on the basis of the kinematic coupling distribution (Kimura et al., 2019). (e) Map showing the residuals, observed displacement rate minus calculated displacement rate obtained in this study. (f) Same as (e) but for Kimura et al. (2019).....108

Figure 3.12. Comparison of the slip deficit rate distributions and residuals. (a) Map showing the

slip deficit rate distributions at the offshore region between the Shikoku and Kii locking segments. Hatched zones represent the mechanical locking zones that are the same as those in Figure 3.11(a). (b) Same as (a) but the artificial mechanical locking zone was situated at the region exhibiting almost zero locking probability at the offshore region between the off Shikoku and off Kii locking segments. (c), (d) Residuals which were calculated on the basis of the slip deficit rate distributions shown in (a) and (b), respectively. 110

Figure 3.13. Comparison of mechanical locking distributions with slow earthquake distributions in southwest Japan. The background color indicates the locking probability. Deep tremor, deep VLFE, shallow tremor, and shallow VLFE were shown as white circles, gray circles, white stars, and gray stars, respectively. Deep SSE is shown with magenta rectangles. The following are references for each slow earthquake: Deep tremor, Obara et al. (2010); Deep VLFE, Ito et al. (2009); Deep SSE, Nishimura et al. (2013); Shallow tremor, Obana & Kodaira (2009) and Yamashita et al. (2015); Shallow VLFE, Takemura et al. (2019). Detection periods are from 2001 to 2017 for deep tremor, from 2003 to 2008 for deep VLFE, from 2004 to 2012 for deep SSE, from 2003 to 2013 for shallow tremor, from 2003 to 2018 for shallow VLFE. All data were available from Slow Earthquake Database, developed by Kano et al. (2018) 114

Figure 3.14. Comparison with coseismic slip area of 1944 and 1946 Nankai Trough earthquakes. Yellow stars indicate epicenters of the 1944 M 7.9 Tonankai and 1946 M 8.0 Nankai Earthquakes. These two epicenters refer to the Japan Meteorological Agency hypocenter catalogue. Coseismic slip distributions of the above two earthquakes are shown with contours. The coseismic slip distributions were estimated by seismic wave data (Murotani et al., 2015; Yamanaka, 2006) and the geodetic observation data (Sagiya & Thatcher, 1999). (a) Map showing the coseismic slip distributions and hypocenters as well as the mechanical locking distribution. The color scale indicates the locking probability. (b) Same as (a) but as

with the kinematic coupling distribution (Kimura et al., 2019). The color scale indicates the coupling coefficient.....119

Figure 3.15. Map showing strong motion generation areas of the 1944 M 7.9 Tonankai Earthquake (cyan closed line) and 1946 M 8.0 Nankai Earthquake (yellow closed line) estimated from seismic intensity records (Kanda et al., 2004). The background color scale indicates mechanical locking distributions expressed as locking probability. 123

Figure 3.16. Map showing mechanical locking distributions, epicenters, coseismic slip distributions, and SMGAs along the Nankai Trough and Japan and Kuril Trench. Background color represents locking probability. Colored stars, contour lines, and enclosed area indicate epicenters, coseismic slip distributions (Murotani et al., 2015; Yamanaka, 2006; Yamanaka & Kikuchi, 2003; Yokota et al., 2011), and SMGAs (Kamae & Kawabe, 2004; Kanda et al., 2004; Kurahashi & Irikura, 2013; Nozu & Irikura, 2008), respectively, of past megathrust earthquakes. Pink, light gray, green, and yellow coloring corresponds to the 2003 Tokachi (Mw 8.0), 2011 Tohoku (Mw 9.0), 1944 Tonankai (M 7.9), and 1946 Nankai (M 8.0) earthquakes, respectively. Dashed lines indicate iso-depth contours with 10 km depth intervals. Gray lines indicate block boundaries. 124

Figure 3.17. Map showing the surface tracing of major topographic anomalies on the subducted plate interface and mechanical locking distributions expressed as the locking probability along the Nankai Trough. The following are references for each topographic anomaly: Paleo Zenisu ridge, Park et al. (2004); High-density buried rock, Kaneda et al. (2006); Muroto seamount, Kodaira et al. (2002); Kyushu–Palau ridge Park et al. (2009).....126

Figure 4.1. Schematic imaging of mechanical locking and slip behaviors on the plate interface along the Japan and Kuril Trenches and along the Nankai Trough.....133

Figure A.1. Map showing calculated vectors and relative motion rates. Black and red arrows depict the rigid motion rate and elastic response from interplate slip deficits, respectively.

The reference for rigid motion is the Eurasian plate. The color scale shown along the block boundary line represents the relative block motion rate. 137

Figure A.2. Map showing principal strain rates calculated from estimated internal block strain rates. Green cross arrows indicate principal strain rates. The locations where strain crosses are plotted are reference points, which are the centroid of the observation site network within each block. Red lines are active fault tracings (Nakata & Imaizumi, 2002). The black and white circles indicate earthquake epicenters and mechanisms. Earthquakes that occurred offshore the Pacific Plate side were removed from the figure. Mechanism data were provided by the F-net broadband seismograph network maintained by the NIED (Okada et al., 2004). The data period, magnitude range, and lower depth limit are 1997–2010, 3–7.5, and 20 km, respectively. 141

Figure B.1. Map showing the calculated displacement rates. Black and red arrows depict the rigid motion rate and elastic response from interplate slip deficits. The reference for rigid motions is the Amurian plate. The color scale shown along the block boundary line represents relative block motion rate. 146

Figure B.2. Map showing the principal strain rates calculated from the estimated internal block strain rates (Table B.2). Green cross arrows are the principal internal block strain rates. The locations where the strain crosses are plotted is the reference point, which is the centroid of the observation site network within each block. Note that the actual centroid location of the observation network included in the Amurian plate is located at the point outside of the Amurian plate and near the centroid location of the Setouchi block. To avoid that one may confuse to recognize the strain rates of Setouchi block and Amurian plate, the principal strain rate cross of the Amurian plate were replotted inside of the Amurian plate. Red lines are active fault tracings (Nakata & Imaizumi, 2002). The black and white circles indicate the earthquake epicenters and mechanisms. Earthquakes that occurred offshore of the Pacific

Plate side are removed from the figure. The mechanism data were provided by the F-net broadband seismograph network maintained by the NIED (Okada et al., 2004). The data period, magnitude ranging, and lower depth limit are 2006–2009 3–6, and 20 km, respectively. 150

List of Tables

Table A.1. List of Euler vector estimates. All Euler vectors are relative to the Eurasian plate. Positive angular velocities indicate counterclockwise rotation. Pole location and angular velocity of the Pacific Plate area refer to the MORVEL plate model (DeMets et al., 2010). Covariances are Cartesian and have units of 10^{-8} rad^2/Myr^2.....136

Table A.2. List of internal block strain estimates. Normal strain rates area measured as extensional positive. Reference points of each block are centroids of the observation site network within each block. 140

Table B.1. List of Euler vector estimates. All Euler vectors are relative to Amurian plate. Positive angular velocities are counterclockwise rotation. Pole location and angular velocity of Pacific and Yangtze plates are fixed to the value presented by MORVEL plate model (DeMets et al., 2010), and they were not estimated in this study. Covariances are Cartesian and have units of 10^{-8} rad^2/Myr^2. 145

Table B.2. List of internal block strain estimates. The unit of strain rates is 10^{-9}/yr. Normal strain rates area measured as extensional positive. Reference points of each block area centroid of the observation site network within each block. 149

Table C.1. List of displacement rates at onshore and seafloor observation sites in northeast Japan used in the analysis outlined in Chapter 2. The reference frame is the Eurasian plate, taken from the MORVEL plate motion model (DeMets et al., 2010).....151

Table C.2. List of displacement rates at onshore and seafloor observation sites in southwest Japan used in the analysis of Chapter 3. The reference frame is Amurian plate of MORVEL plate motion model (DeMets et al., 2010). 160

Chapter 1
Introduction

The Earth's surface is covered by numerous rigid plates. Due to plate motion and interactions, strain accumulates on plates and plate boundaries. Earthquakes are a common phenomenon by which strain accumulated during interseismic periods is released. In particular, interplate earthquakes occur to release shear strain that has accumulated on plate interfaces during interseismic periods. As interplate earthquakes can cause strong ground shaking and large tsunamis, which lead to serious damages to human life and property, it is essential to assess seismic potential accurately for the mitigation and prevention of earthquake disasters.

Shear strain is accumulated during the interseismic period due to the mechanical locking plate boundary between the upper surface of the subducting plate and the lower surface of the overriding plate. At the mechanically locked zone, the relative motion rate on the plate interface is zero. Following the backslip model (Savage, 1983), in which the kinematic state on the plate interface is expressed as the superimposing of steady slip (plate convergence) and slip in the opposite sense to plate convergence ("backslip" or "slip deficit"), this condition is explained as the slip deficit rate being equal to the plate convergence rate at the mechanically locked zone. In contrast, at the area that is sufficiently far from the mechanical locking zone, the relative motion rate on the plate interface is equal to the plate convergence rate—that is, the slip deficit rate is zero. At the middle regions, the relative motion rate and slip deficit rate are larger than zero and smaller than the plate convergence rate owing to the spatial continuity of the plate interface.

Surface response due to slip deficits on plate interfaces can be perceived as crustal

deformations that occur during the interseismic period, according to the geodetic observations performed using the Global Navigation Satellite System (GNSS). Spatial distributions of the slip deficit rate on the plate interface have been estimated similarly in previous studies (e.g., Carvajal-Soto et al., 2020; Hanifa et al., 2014; Loveless & Meade, 2010; Métois et al., 2016; Villegas‐Lanza et al., 2016; Wallace, 2004). Furthermore, transient coseismic or postseismic slip distributions on the plate interface during earthquakes have been estimated using the seismogram data (e.g., Koper et al., 2012; Yagi & Fukahata, 2011; Yamanaka & Kikuchi, 2003) or surface displacement data observed by GNSS (e.g., Klein et al., 2017; Miyazaki et al., 2004; Simons et al., 2011). By comparing slip distributions between interseismic and coseismic (and/or postseismic) periods, good spatial correlation between large coseismic slips and interseismic high slip deficit rate distributions has been revealed (e.g., Hashimoto et al., 2012; Loveless & Meade, 2015; Moreno et al., 2010).

In Japan, there are many onshore GNSS sites that provide high-accuracy crustal deformation data. The Geospatial Information Authority of Japan (GSI) has operated a continuous onshore geodetic observation network (GEONET) covering the Japan archipelago since the 1990s (Nakagawa et al., 2009). Currently, approximately 1,300 GEONET sites are in operation. Using onshore crustal deformation data, interplate coupling distributions have been estimated along the subduction zone (Hashimoto et al., 2009, 2012; Liu et al., 2010; Loveless & Meade, 2010, 2015; Suwa et al., 2006). However, the resolution power in offshore regions, which comprise the majority of possible megathrust earthquake sources, is typically poor owing to the long distance from onshore GNSS observation sites. Suito (2017a) reported that the GEONET cannot detect events with magnitudes smaller than Mw 6.5 on the Pacific Plate and Mw 6.0 on the Philippine Sea Plate; these data were derived from a simple simulation in which the

displacement at GEONET sites due to fault slip on the plate interface was calculated on the basis of elastic half space. Thus, it is essential to observe seafloor offshore crustal movements to enhance the resolution power and detect interplate coupling distributions. Recently, seafloor geodetic observation networks adopting a GNSS/Acoustic combination technique have been developed along subduction zones (Kido et al., 2015; Tadokoro et al., 2012; Yokota et al., 2018). The total number of GNSS/A sites has reached approximately 60 around Japan. GNSS/A observations are mainly conducted at Nagoya University and Tohoku University and by the Japan Coast Guard. Using seafloor GNSS/A data, it is possible to capture offshore crustal displacement fields in and around Japan.

Most previous studies, including those cited above, have estimated spatial distributions of the interplate slip deficit or the interplate coupling coefficient, which is the ratio between the slip deficit rate and plate convergence rate; these studies were conducted using the pure kinematic model (Figure 1.1(a)) wherein the coupling states (coupling coefficients or slip deficit rates) are estimated independently for each subfault or by using smoothing operations that are not based on actual physics of the area (e.g., Hashimoto et al., 2012; Kimura et al., 2019; Liu et al., 2010; Loveless & Meade, 2010; Nishimura et al., 2018; Suwa et al., 2006). This method is very simple and can be used to estimate interplate coupling distributions that can explain observed crustal deformations without considering any mechanical constraints of the plate interface. However, due to its simplicity, it exhibits the following limitations. First, because the model does not consider physical continuity such as stress or slip continuity based on actual mechanics, estimated coupling distributions may exhibit radical changes at adjacent subfaults, implying the existence of an artificial stress. Second, because the coupling state estimates are expressed with kinematic values, such as slip deficit rate or coupling coefficient, the mechanical locking condition on the plate interface cannot be determined from the estimated coupling

distribution. The plate interface exhibiting high slip deficit rate is not always mechanically locked. Nevertheless, some previous studies assumed the region where the high slip deficit rate or coupling coefficient were estimated as “asperity” and assessed the seismic potential from the coupling or slip deficit rate distributions using the aforementioned model. The maximum coseismic slip magnitude on the “asperity” can be roughly predicted from the evaluation. However, it must be noted that the earthquake would be nucleated depending on the stress condition and frictional strength (i.e., mechanical states) on the plate interface. Thus, it is essential to estimate the spatial distributions of mechanical locking states on the plate interface. The mechanical state is considered to be equivalent to the frictional state, which can control the slip behaviors on the plate interface. Hence, revealing this can facilitate the prediction of coseismic slip areas, maximum coseismic slip magnitude, and slip behaviors (e.g., brittle rupture, accompanying sliding, slow slip, and short period seismic wave radiation) of future earthquakes.

To overcome these limitations, a new physical model was developed in this study that relates mechanical locking on the plate interface to surface crustal deformations (Figure 1.1(b)). The proposed model enables the direct estimation of mechanical locking distributions and the accompanying slip deficit rates from the observed crustal deformation data. In this model, only two mechanical conditions (known as “binary locking” in Herman & Govers, 2020) were allowed on the plate interface, namely “mechanically locked” and “creeping (unlocked).” In the mechanically locked zone, finite shear tractions work, and the slip deficit whose velocity is equal to the relative block motion (plate convergence) rate exists. Shear strain in the area increases over time. The creeping zone encompasses all plate interface areas outside of the mechanical locking zone. Although shear tractions do not work in the creeping zone, slip deficits whose

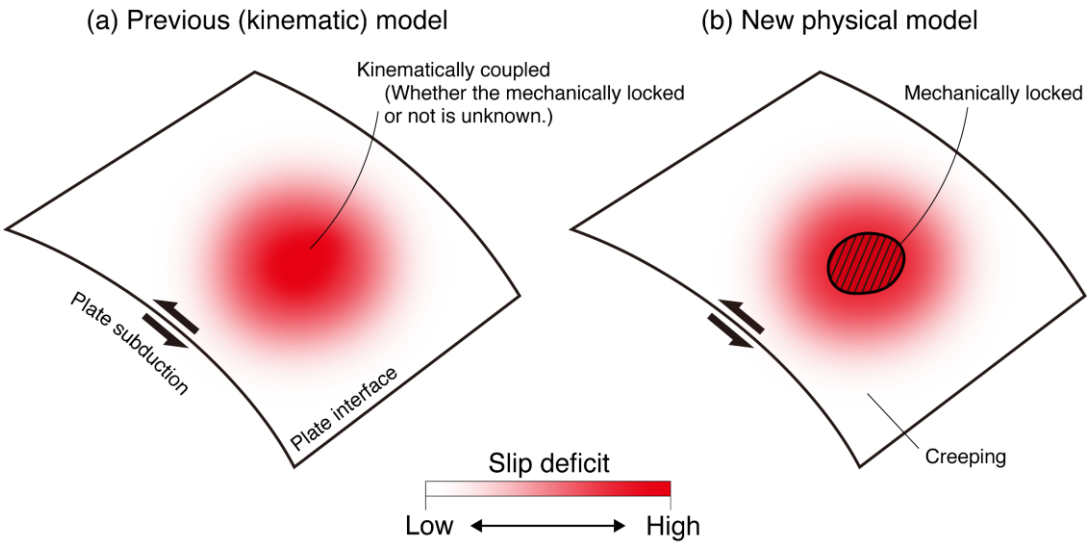

Figure 1.1. Concept of "locking" states on the plate interface in the previous (kinematic) and proposed models. (a) In the pure kinematic model, "locking" states indicate kinematic states, such as slip deficit rate or coupling coefficient. (b) In the new physical model, "locking" states directly represent the mechanical states, that is, mechanically locked (hatched area) or creeping (non-hatched area).

velocity is zero or less than the relative block motion rate are accompanied by mechanical locking to satisfy the constant strain states. The slip deficit rate in the creeping zone decays with the distance from the mechanical locking zone. While the absolute (background) strain value is not clear in the creeping zone, shear strain does not change over time to satisfy the constant strain state in the creeping zone. This concept is based on the suggestion that both the mechanical locking zones and the plate interface around them should accumulate slip deficits owing to the mechanical continuity of the plates (Wang & Dixon, 2004). It is worth noting that other mechanical effects, such as friction, viscosity, and their heterogeneities, are not explicitly modeled in this study. Similar concepts have been modeled in previous studies (e.g., Almeida et al., 2018; Bürgmann, 2005; Herman et al., 2018). And inversion methods to estimate the mechanical locking distributions from the geodetic observation data were proposed (Herman & Govers, 2020;

Johnson & Fukuda, 2010; Ortega, 2013).

Mechanical locking distributions have not been estimated along the subduction zone in Japan, where megathrust earthquakes have repeatedly occurred. Revealing the mechanical locking distributions along the Nankai Trough is an urgent task because the average recurrence interval of the megathrust earthquake in this area is 100–150 years (Ando, 1975; Garrett et al., 2016), and over 70 years have passed since the last megathrust earthquakes of 1944 (M 7.9) and 1946 (M 8.0). Thus, this study aims developed a new physical model based on the concept described above to estimate mechanical locking distributions along subduction zones in Japan using geodetic observation data. The remainder of this thesis is constructed as follows. In Chapter 2, a model is proposed that describes the relation between interplate mechanical locking and surface crustal deformation, including the block motion and block internal strain effects; subsequently, a novel inversion method is presented for estimating mechanical locking distributions using the Bayesian approach based on geodetic observation data. The proposed model was first applied to northeast Japan to estimate mechanical locking distributions along the Kuril and Japan Trenches. In this region, Mw 8.0 Tokachi Earthquake and Mw 9.0 Tohoku Earthquake occurred in 2003 and 2011, respectively. Interplate kinematic coupling distributions were estimated using onshore GNSS data prior to the 2003 Tokachi Earthquake. Coseismic slip distributions and strong motion generation areas of the two earthquakes were also estimated from the seismic waveform data. Thus, the estimated mechanical locking distribution using the new physical model was compared to these distributions. The estimated distributions were also compared to the kinematic coupling distributions that were estimated in previous studies. This section also presents the results of tests in which the configuration of the block divisions and the plate interface geometries were changed to verify the effects caused by these configurations. In Chapter

3, the proposed model was applied to estimate mechanical locking distributions along the Nankai Trough in southwest Japan. I compared the results with the kinematic coupling distributions estimated by Kimura et al. (2019) to reveal the spatial relationship between the mechanical locking and kinematic coupling estimated from geodetic observation data. Moreover, the results from the comparison of the estimated mechanical locking distributions with slow earthquakes detected during the interseismic period and strong motion generation areas of 1944 Tonankai and 1946 Nankai earthquakes are presented to evaluate the frictional states on the plate interface and determine possible factors causing the radiation of the short-period seismic waves from the strong motion generation area, respectively. In Chapter 4, I summarize the main results of this study and describe the implications of the results. I also present suggestions for applying the proposed model and the findings from this study in future research.

Chapter 2
Physical modeling of mechanical locking and its application in northeast Japan

2.1. Introduction

In this chapter, a newly developed physical model is reported that relates mechanical locking on the plate interface to surface crustal deformation. An inversion adopting the Bayesian approach with the proposed model was achieved for onshore and seafloor geodetic observation data in northeast Japan to estimate mechanical locking distributions along the Kuril and Japan Trenches.

In northeast Japan, the Pacific Plate subducts beneath the overriding plates along the Japan and Kuril Trench with a convergence rate of ~9 cm/yr (DeMets et al., 2010). The interplate earthquakes of around M 7 have repeatedly occurred at an interval of approximately 30 years along the Japan Trench (Yamanaka & Kikuchi, 2004). Large (> M 8) interplate earthquakes, such as the Mw 8.2 Tokachi Earthquake in 1968 and the Mw 9.0 Tohoku Earthquake in 2011 have occurred at longer intervals. Along the Kuril Trench, earthquakes with > M 8 have recurred at an average interval of 100 years (Satake, 2015). In addition, the occurrence of unusual tsunami earthquakes at an interval of ~500 years, sometimes called the "17 century type earthquake," was implicated from the geological records at coastal region (Satake et al., 2008). The rupture (coseismic slip) areas, sometimes called "asperities," of earthquakes have previously been estimated using seismic waveform data (Nagai et al., 2001; Yagi, 2004; Yamanaka & Kikuchi, 2004), tsunami data (Ioki & Tanioka, 2016; Tanioka et al., 1996), and geodetic data (Iinuma et al., 2012; Miyazaki & Larson, 2008; Simons et al., 2011). In northeast Japan, interplate coupling distributions prior to the 2003 Tokachi Earthquake (or 2011 Tohoku Earthquake)

have been estimated using onshore GNSS observation data based on the pure kinematic model (Hashimoto et al., 2009; Loveless & Meade, 2010; Suwa et al., 2006). Moreover, interplate coupling conditions have been discussed on the basis of seafloor GNSS/A observation data in the Tohoku region (Sato et al., 2013). The comparison of interplate coupling distributions in the interseismic period and coseismic slip distributions have been studied previously (Hashimoto et al., 2012; Itoh et al., 2019; Loveless & Meade, 2015). However, mechanical locking distributions have not been estimated in this region. Thus, the relationship among the mechanical locking, kinematic coupling, and coseismic (postseismic) slip distributions is not clear.

As northeast Japan is a rare region where dense geodetic observation data (including seafloor GNSS/A data as well as onshore GNSS data) prior to the megathrust earthquake are available, it is possible to verify the proposed model by comparing interseismic mechanical locking, kinematic coupling, and coseismic slip distributions. The proposed model was first applied to the northeast Japan region. Because the onshore GNSS (GEONET) observation data prior to the 2003 Tokachi Earthquake and seafloor GNSS/A observation data as well as onshore GNSS data prior to the 2011 Tohoku Earthquake are available, it is possible to estimate the mechanical locking distribution at the interseismic period and compare it with coseismic (postseismic) slip distributions, hypocenters, and strong motion generation areas. The performance of the proposed model was verified by this comparison.

2.2. Methods and data

In this chapter, I first describe the proposed model that relates the mechanical locking on the plate interface to surface crustal deformations. This model was applied to geodetic observation data in northeast Japan to estimate mechanical locking distributions along the

Kuril and Japan Trenches (reported in this chapter) and in southwest Japan to estimate mechanical locking distributions along the Nankai Trough (reported in Chapter 3). This study adopted a replica exchange Monte Carlo (REMC) method, which utilizes Bayesian estimation, to estimate mechanical locking distributions from the surface displacement rate dataset. I present the algorithm of the REMC method and the configuration of a priori distributions. Then, I briefly denote the data processing procedure for obtaining the surface displacement rate that was used for the Bayesian inversion. Finally, I described the block division configurations and plate interface geometry used in the analysis.

2.2.1. Physical model relating mechanical locking to crustal deformations

The surface displacement $\boldsymbol{v}_{\mathrm{cal}}$ is expressed as a sum of the rigid block motion (rotation) $\boldsymbol{v}_{\mathrm{rigid}}$, surface response of the slip deficit on the plate interface $\boldsymbol{v}_{\mathrm{sd\_plate}}$, surface response of the slip deficit on the inland block boundary $\boldsymbol{v}_{\mathrm{sd\_inland}}$, and internal strains $\boldsymbol{v}_{\mathrm{instrain}}$.

$$\boldsymbol{v}_{\mathrm{cal}} = \boldsymbol{v}_{\mathrm{rigid}} + \boldsymbol{v}_{\mathrm{sd\_plate}} + \boldsymbol{v}_{\mathrm{sd\_inland}} + \boldsymbol{v}_{\mathrm{instrain}} \quad (1)$$

This formulation is sometimes called the block motion (block fault) model (e.g., Carvajal-Soto et al., 2020; Kimura, Ito, et al., 2019; Loveless & Meade, 2010; Nishimura et al., 2018). The term $\boldsymbol{v}_{\mathrm{rigid}}$ can be described by using Euler vectors $\boldsymbol{\omega}$ as follows:

$$\boldsymbol{v}_{\mathrm{rigid}} = \boldsymbol{\omega}_{\mathrm{i}} \times \boldsymbol{r}_{\mathrm{k}}, \quad (2)$$

where $\boldsymbol{r}$ is the location vector, and subscripts i and k denote the block and site,

respectively. Surface displacement can be expressed by rigid motion $\boldsymbol{v}_{\mathrm{rigid}}$ because the plate tectonics theorem assumes the medium of the plate or block as the rigid body. However, actual plates or blocks deform elastically due to tectonics such as plate subduction or interactions owing to plate motion. Therefore, the proposed model considers these deformations from second to fourth terms in the right-hand side in Equation (1). The second term $\boldsymbol{v}_{\mathrm{sd\_plate}}$ is the core of this model because it includes the elastic response from the mechanical locking on the plate interface. This model allows for two locking states on the plate interface: mechanically locked (in which finite shear traction is working on the plate interface) and creeping (in which the zero-shear traction is working on the plate interface). The term $\boldsymbol{v}_{\mathrm{sd\_plate}}$ can be expressed as follows:

$$\boldsymbol{v}_{\mathrm{sd\_plate}} = \boldsymbol{G}_{\mathrm{l}}\dot{\boldsymbol{s}}_{\mathrm{l}} + \boldsymbol{G}_{\mathrm{c}}\dot{\boldsymbol{s}}_{c}, \tag{3}$$

where $\dot{\boldsymbol{s}}_{\mathrm{l}}$ and $\dot{\boldsymbol{s}}_{c}$ are the slip deficit rate on the mechanical locking subfaults and on the creeping subfaults, respectively, and $\boldsymbol{G}_{\mathrm{l}}$ and $\boldsymbol{G}_{\mathrm{c}}$ are the Green's functions describing the relationship between the slip deficit rates on the mechanically locked subfaults and creeping subfaults to surface displacement rates, respectively. In this study, the elastic half space medium was assumed, and the aforementioned Green's functions were calculated on the basis of triangular dislocation model (Meade, 2007). The terms $\dot{\boldsymbol{s}}_{\mathrm{l}}$ and $\dot{\boldsymbol{s}}_{\mathrm{c}}$ are related to the mechanical constraints, namely, constant strain states in the creeping region. Shear strains due to $\dot{\boldsymbol{s}}_{\mathrm{l}}$ and $\dot{\boldsymbol{s}}_{\mathrm{c}}$ are calculated as follows. First, shear strains on the creeping zone $\dot{\boldsymbol{\varepsilon}}_{\mathrm{l}}$ due to the slip deficit rates on imposed in the mechanical locking zone $\dot{\boldsymbol{s}}_{\mathrm{l}}$ are determined using the following equation:

$$\dot{\boldsymbol{\varepsilon}}_{\mathrm{l}} = \boldsymbol{G}_{I}^{\varepsilon}\dot{\boldsymbol{s}}_{\mathrm{l}}, \tag{4}$$

where $\boldsymbol{G}_{\mathrm{I}}^{\varepsilon}$ is a coefficient matrix that relates $\dot{\boldsymbol{s}}_{\mathrm{I}}$ to $\dot{\boldsymbol{\varepsilon}}_{\mathrm{I}}$. Next, similarly, shear strains on the creeping zone $\dot{\boldsymbol{\varepsilon}}_{\mathrm{c}}$ due to the slip deficit rates induced in the creeping zone $\dot{\boldsymbol{s}}_{\mathrm{c}}$ are calculated as follows:

$$\dot{\boldsymbol{\varepsilon}}_{\mathrm{c}} = \boldsymbol{G}_{\mathrm{c}}^{\varepsilon}\dot{\boldsymbol{s}}_{\mathrm{c}}, \tag{5}$$

where $\boldsymbol{G}_{\mathrm{c}}^{\varepsilon}$ is a coefficient matrix that relates $\dot{\boldsymbol{s}}_{\mathrm{c}}$ to $\dot{\boldsymbol{\varepsilon}}_{\mathrm{c}}$. The coefficient matrices $\boldsymbol{G}_{\mathrm{I}}^{\varepsilon}$ and $\boldsymbol{G}_{\mathrm{c}}^{\varepsilon}$ in this study were calculated on the basis of triangular dislocation model (Meade, 2007), as same as $\boldsymbol{G}_{\mathrm{I}}$ and $\boldsymbol{G}_{\mathrm{c}}$. The total strain rate on the creeping subfaults is the sum of $\dot{\boldsymbol{\varepsilon}}_{\mathrm{I}}$ and $\dot{\boldsymbol{\varepsilon}}_{\mathrm{c}}$. This model assumes the constant strain state on the creeping zone, that is, the shear strain does not temporarily change on the creeping zone. To satisfy this constrain, the sum of $\dot{\boldsymbol{\varepsilon}}_{\mathrm{I}}$ and $\dot{\boldsymbol{\varepsilon}}_{\mathrm{c}}$ becomes zero as follows:

$$\dot{\boldsymbol{\varepsilon}}_{\mathrm{I}} + \dot{\boldsymbol{\varepsilon}}_{\mathrm{c}} = \boldsymbol{0}. \tag{6}$$

This equation implies that shear strain on the creeping subfaults due to slip deficits on mechanically locked subfaults is released by shear strains owing to the induced slip deficit on creeping subfaults. Substituting Equation (4) and (5) into Equation (6), the relationship between imposed slip deficit on mechanically locked subfaults and induced slip deficit on the creeping subfaults can be derived as follows:

$$\dot{\boldsymbol{s}}_{\mathrm{c}} = -(\boldsymbol{G}_{\mathrm{c}}^{\varepsilon})^{-1}\boldsymbol{G}_{\mathrm{I}}^{\varepsilon}\dot{\boldsymbol{s}}_{\mathrm{I}}. \tag{7}$$

The slip deficit rate on mechanically locked subfaults is equivalent to the relative block

motion rate that is the difference between the two rigid block motion rates. Thus,

$$\dot{\boldsymbol{s}}_{\mathrm{l}} = (\boldsymbol{\omega}_{\mathrm{e}} - \boldsymbol{\omega}_{\mathrm{f}}) \times \boldsymbol{r}_{\mathrm{l}}, \tag{8}$$

where $\boldsymbol{r}_{\mathrm{l}}$ denote the location vector of mechanically locked subfaults, and $\boldsymbol{\omega}_{\mathrm{e}}$ and $\boldsymbol{\omega}_{\mathrm{f}}$ denote the Euler vectors of the block e and f, respectively. Note that actual relative block motion, which is described in Equation (8), should be calculated at the surface and not at the subfault location because the relative block motion rate at a block boundary should be the same between the surface and subsurface. However, the difference between the distance from Earth's center to the subfault center and that to the surface where the subfault center is projected is within 80 km at maximum. This minute difference in distance accounts for only ~1% of the difference between actual relative block motion and that calculated using Equation (8), which is almost same as the uncertainties of the crustal deformation data. Thus, it is reasonable to approximate the relative block motion rate using Equation (8). Considering Equation (8), Equation (7) can be modified as follows:

$$\dot{\boldsymbol{s}}_{\mathrm{c}} = -(\boldsymbol{G}_{\mathrm{c}}^{\varepsilon})^{-1}\boldsymbol{G}_{\mathrm{l}}^{\varepsilon}(\boldsymbol{\omega}_{\mathrm{e}} - \boldsymbol{\omega}_{\mathrm{f}}) \times \boldsymbol{r}_{\mathrm{l}} \tag{9}$$

Using Equation (8) and (9), Equation (3) can be revised as follows:

$$\boldsymbol{v}_{\mathrm{sd\_plate}} = [\boldsymbol{G}_{\mathrm{l}} - \boldsymbol{G}_{\mathrm{c}}(\boldsymbol{G}_{\mathrm{c}}^{\varepsilon})^{-1}\boldsymbol{G}_{\mathrm{l}}^{\varepsilon}](\boldsymbol{\omega}_{\mathrm{e}} - \boldsymbol{\omega}_{\mathrm{f}}) \times \boldsymbol{r}_{\mathrm{l}} \tag{10}$$

Using Equation (10), total slip deficits on the plate interface and the surface response from the slip deficits can be calculated if the mechanically locked location is

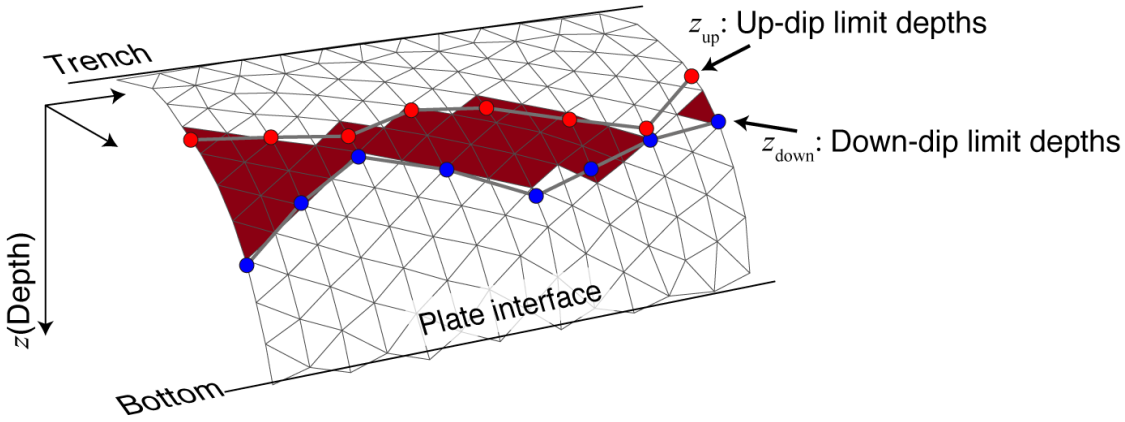

Figure 2.1. Schematic imaging of the mechanical locking zone on the plate interface. Each triangle indicate subfaults. Red subfaults are mechanically locked. The remaining white subfaults are creeping. Subfaults were determined to be mechanically locked based on the centroid depths of subfaults and up-dip (red circles) and down-dip (blue circles) limit depths, as follows: If the centroid of the subfault is between the up- and down-dip limit depths, the subfault is considered mechanically locked, else, the subfault considered creeping.

known. However, which subfaults are mechanically locked is unknown. Hence, parameterization of the mechanically locked zone is necessary to invert the surface crustal deformation and determine the mechanical locking distributions. This model assumes that the belt-like mechanical locking zone is prescribed by the up- and down-dip depth limitation (z_{up} and z_{down}, respectively), as shown as Figure 2.1. The subfaults whose center is located between z_{up} and z_{down} are assumed to be mechanically locked. The combination of z_{up} and z_{down} are the model parameters to be estimated. Previous studies parameterized the locking states for each subfault using binary values, 0 (creeping) and 1 (mechanical locking), and estimated the locking states for each subfault independently (Herman & Govers, 2020; Johnson & Fukuda, 2010). Nevertheless, it is considered that the parameterization to identify mechanically locked subfaults proposed in this study is better because following problems appear in the previous method: the

computational time become significantly longer as the number of subfault increases; complex mechanical locking distributions would be estimated if the subfault size is small. As the subducting plate interface is the focus of this study, the surface response from the slip deficits on the inland block boundaries was calculated on the basis of the kinematic framework, following previous studies (Carvajal-Soto et al., 2020; Kimura et al., 2019; Loveless & Meade, 2010; Nishimura et al., 2018). In the kinematic framework, the orientation and degree of the slip deficit rate is defined as the reverse orientation of the relative block motion and the rate produced by the relative block motion rate and coupling coefficient, respectively. Then, the slip deficit rate on the subfaults of the inland block boundaries $\dot{\boldsymbol{s}}_{\mathrm{b}}$ can be expressed as follows:

$$\dot{\boldsymbol{s}}_{\mathrm{b}} = C_{\mathrm{b}}(\boldsymbol{\omega}_{\mathrm{e}'} - \boldsymbol{\omega}_{\mathrm{f}'}) \times \mathbf{r}_{\mathrm{b}}, \tag{11}$$

where the $\boldsymbol{\omega}_{\mathrm{e}'}$ and $\boldsymbol{\omega}_{\mathrm{f}'}$ denote the Euler vectors of two adjacent blocks, $\mathbf{r}_{\mathrm{b}}$ denotes the location vector of the subfaults on the inland block boundaries, C_{b} denotes the coupling coefficient of the subfault on the inland block boundaries. Then, $\boldsymbol{v}_{\mathrm{sd\_inland}}$ is calculated as follows:

$$\boldsymbol{v}_{\mathrm{sd\_inland}} = \boldsymbol{G}_{\mathrm{b}} C_{\mathrm{b}}(\boldsymbol{\omega}_{\mathrm{e}'} - \boldsymbol{\omega}_{\mathrm{f}'}) \times \mathbf{r}_{\mathrm{b}}, \tag{12}$$

where C_{b} is the coupling coefficient of the subfault on the inland block boundaries, and $\boldsymbol{G}_{\mathrm{b}}$ is the Green's function that relates the slip deficit rates of the subfaults on the inland block boundaries to the surface displacement rates. The Green's function $\boldsymbol{G}_{\mathrm{b}}$ was calculated using the code reported by Meade (2007) as $\boldsymbol{G}_{\mathrm{l}}$ and $\boldsymbol{G}_{\mathrm{c}}$. Here, only the positive slip deficit is allowed, and forward slip expressed as the negative slip deficit is not

allowed. Hence, C_{b} can take any value between 0 and 1. To calculate $\boldsymbol{v}_{\mathrm{instrain}}$, the uniform internal strain was assumed for all blocks. That is,

$$\boldsymbol{v}_{\mathrm{instrain}} = \dot{\boldsymbol{E}}\boldsymbol{r}'_{\mathrm{k}}, \tag{13}$$

where $\dot{\boldsymbol{E}}$ and $\boldsymbol{r}'_{\mathrm{k}}$ denote the internal strain rate tensor and the site location whose origin is the center of the site network inside each block, respectively. Using Equations (2), (10), (12), and (13), Equation (1) can be expressed as follows:

$$\begin{aligned}\boldsymbol{v}_{\mathrm{cal}} = {} & \boldsymbol{\omega}_{\mathrm{i}} \times \boldsymbol{r}_{\mathrm{k}} \\ & + [\boldsymbol{G}_{\mathrm{l}} - \boldsymbol{G}_{\mathrm{c}}(\boldsymbol{G}_{\mathrm{c}}^{\varepsilon})^{-1}\boldsymbol{G}_{\mathrm{l}}^{\varepsilon}](\boldsymbol{\omega}_{\mathrm{e}} - \boldsymbol{\omega}_{\mathrm{f}}) \\ & + \boldsymbol{G}_{\mathrm{b}}C_{\mathrm{b}}(\boldsymbol{\omega}_{\mathrm{e}'} - \boldsymbol{\omega}_{\mathrm{f}'}) \times \boldsymbol{r}_{\mathrm{b}} \\ & + \dot{\boldsymbol{E}}\boldsymbol{r}'_{\mathrm{k}}\end{aligned} \tag{14}$$

Equation (14) can be rewritten as the observation equation form as follows:

$$\boldsymbol{d} = g(\boldsymbol{m}), \tag{15}$$

where $\boldsymbol{d}$ is the observation vector, $\boldsymbol{m}$ is the model parameter vectors, and $g(\,)$ is the nonlinear operator that relates $\boldsymbol{m}$ to $\boldsymbol{d}$. Because the model parameters $\boldsymbol{m}$, which contains the Euler vector $\boldsymbol{\omega}$, up- and down-dip limitation depths of the mechanical locking zone (z_{up} and z_{down}, respectively), coupling coefficient C_{b}, and the internal strain rate $\dot{\boldsymbol{E}}$ cannot be estimated uniquely, I adopted the Bayesian approach to obtain a probability density function (PDF) of $\boldsymbol{m}$, which is described in the next section.

2.2.2. Bayesian estimation

I estimated all model parameters simultaneously from an inversion. The observation equation is described as Equation (15). Because the model parameters cannot be solved uniquely, a Bayesian estimation was used to estimate the PDFs of all model parameters. The Bayesian estimation used in this study was based on Bayes' theorem, and the formulation is expressed as

$$p(\boldsymbol{m}|\boldsymbol{d}) = \frac{p(\boldsymbol{d}|\boldsymbol{m})p(\boldsymbol{m})}{p(\boldsymbol{d})}, \tag{16}$$

where $p(\boldsymbol{m})$ is a prior PDF of model parameters, $p(\boldsymbol{d})$ is the PDF of the observations (marginal PDF), $p(\boldsymbol{d}|\boldsymbol{m})$ is a conditional PDF of $\boldsymbol{d}$ given $\boldsymbol{m}$ and referred as the likelihood function, and $p(\boldsymbol{m}|\boldsymbol{d})$ is a conditional PDF of $\boldsymbol{m}$ given $\boldsymbol{d}$ that is referred as the posterior PDF. Because the observations are now fixed, $p(\boldsymbol{d})$ becomes a constant. Then, Equation (16) can be rewritten as follows:

$$p(\boldsymbol{m}|\boldsymbol{d}) \propto p(\boldsymbol{d}|\boldsymbol{m})p(\boldsymbol{m}). \tag{17}$$

I define the likelihood function $p(\boldsymbol{d}|\boldsymbol{m})$ using the L_1 norm as follows:

$$p(\boldsymbol{d}|\boldsymbol{m}) = \exp\left(-\sum_{\mathrm{i}=1}^{M}\left|\frac{d_{\mathrm{i}} - g(m)}{\sigma_{\mathrm{i}}}\right|\right), \tag{18}$$

$$\sigma_{\mathrm{i}} = \sqrt{\sigma_{\mathrm{obs_i}}^2 + \sigma_{\mathrm{model_i}}^2}, \tag{19}$$

where M denotes the number of observation data, that is, three times number of sites, and σ_{i} is the uncertainty of d_{i}. The L_1 norm is useful for measuring the goodness of model parameter realization with lower sensitivity for outliers (Menke, 2012). The uncertainties accompanying the data contains the observation error σ_{obs} and the model error σ_{model}. While the observation error can be identified from the data processing, any a priori information for the model error is not given. Thus, this value was assumed as 1 mm/yr in this study.

Prior PDFs of the model parameters are defined as follows. For z_{up} and z_{down}, the following three states were allowed: z_{up} and z_{down} can cross; z_{up} can range between the trench depth minus $2\times z_{\mathrm{W}}$ and bottom depths, where z_{W} is the trench and bottom depths difference; z_{down} can range between the trench depth and bottom depth plus $2\times z_{\mathrm{W}}$. These constraints are similar to those reported by Ortega (2013), but he did not allow the crossing of z_{up} and z_{down}. Formulating these constraints, prior PDFs z_{up} and z_{down} becomes

$$p(z_{\mathrm{up}}) = \begin{cases} 1, & (z_{\mathrm{trench}} - 2z_{\mathrm{W}} \le z_{\mathrm{up}} \le z_{\mathrm{bottom}}) \\ 0, & (otherwise) \end{cases}, \tag{20}$$

and

$$p(z_{\mathrm{down}}) = \begin{cases} 1, & (z_{\mathrm{trench}} \le z_{\mathrm{down}} \le z_{\mathrm{bottom}} + 2z_{\mathrm{W}}) \\ 0, & (otherwise) \end{cases}, \tag{21}$$

where z_{trench} and z_{bottom} indicate the model region trench and bottom depths, respectively. In the model region of northeast Japan, z_{trench} and z_{bottom} were adopted to be 0 km and 80 km in depth, respectively. Then, z_{W} becomes 80 km. Although one may assume that z_{up} and z_{down} should be sampled within the model region depths,

sampling outside the model region depths is permitted because the mixing rate becomes considerably lower, and the calculation cost increases significantly with a strict constraint that does not allow sampling outside of the model region depths. The coupling coefficient C_{b} is allowed to range from 0–1, and a prior PDF of it can be formulated as follows:

$$p(C_{\mathrm{b}}) = \begin{cases} 1, & (0 \leq C_{\mathrm{b}} \leq 1) \\ 0, & (otherwise) \end{cases}. \tag{22}$$

For the Euler vector and internal strain rate, constraints were not operated. Thus, uniform distributions are adopted according to prior PDFs:

$$p(\boldsymbol{\omega}) = 1, \tag{23}$$

and

$$p(\dot{E}) = 1. \tag{24}$$

The Bayesian inversion in this study cannot be solved analytically. Thus, I adopted the REMC method (Earl & Deem, 2005; Habeck et al., 2005; Swendsen & Wang, 1986), which is a Markov chain Monte Carlo (MCMC) method (Hastings, 1970; Metropolis et al., 1953) to obtain the posterior PDFs of all model parameters simultaneously. A Monte Carlo algorithm conducts repeated random sampling to obtain numerical results, and a Markov chain is a stochastic model in which the current state only depends on the previous state (Hastings, 1970; Metropolis et al., 1953). The MCMC method enables us to obtain the PDFs of all model parameters numerically even if the posterior PDF cannot be solved analytically. The standard MCMC method is useful particularly in the case that the posterior PDF of the model parameters has a unimodal distribution. However,

posterior PDFs commonly have multimodal distributions in practice. In this case, standard MCMC sampling is sometimes trapped in local lobes. Adopting the REMC method would overcome the trapping problem and is capable of sampling more effectively than the standard MCMC method. REMC conducts the tempering of the sampling chains at different densities during the sampling processes. Tempering relaxes the likelihood function that effectively flattens peaks, thereby facilitating Markov chain transitions. By simulating numerous parallel sampling and exchanging the chains, sampling efficiency is improved, and the multimodal PDF can be estimated far more easily when compared to the results obtained using general MCMC methods.

A primary element of REMC sampling is the standard MCMC algorithm. Here, I first summarize a major algorithm of the standard MCMC method, called the Metropolis–Hasting (M–H) algorithm (Hastings, 1970; Metropolis et al., 1953).

The M–H method consists of the following five steps:

Step 1: Set the initial value of all model parameters m_0 and calculate the likelihood $p(\boldsymbol{d}|\boldsymbol{m}_0)$.

Repeat Step 2 to Step 5 until the posterior PDF converges.

Step 2: Propose a candidate model parameter $\boldsymbol{m}^*$ from the proposal PDF with respect to the current (e.g., when the iteration number equals n) sample $\boldsymbol{m}_\mathrm{n}$. Here, although the form of the proposal PDF can control the convergence rate, it is known that posterior PDF does not depend on the proposal PDF. In this study, I select the normal distribution function, that is, $N(\boldsymbol{m}_\mathrm{n}, \boldsymbol{\gamma})$, as the proposal PDF. The standard deviation $\boldsymbol{\gamma}$ plays a roll of scale factor of the distance between $\boldsymbol{m}_\mathrm{n}$ and $\boldsymbol{m}^*$.

Step 3: Calculate the "acceptance probability" r using the posterior PDF with respect to the candidate $\boldsymbol{m}^*$ and the posterior PDF with respect to the current model $\boldsymbol{m}_\mathrm{n}$, as follows:

$$r = min\left(1, \frac{p(\boldsymbol{d}|\boldsymbol{m}^*)p(\boldsymbol{m}^*)}{p(\boldsymbol{d}|\boldsymbol{m}_{\mathrm{n}})p(\boldsymbol{m}_{\mathrm{n}})}\right), \tag{25}$$

where the function $min(A, B)$ responds the minimum value from A or B.

Step 4: Determine whether the candidate $\boldsymbol{m}^*$ is accepted or rejected on the basis of acceptance ratio defined as Equation (25). If $\boldsymbol{m}^*$ is accepted, the current $\boldsymbol{m}_{\mathrm{n}}$ moves to the candidate as $\boldsymbol{m}_{\mathrm{n+1}} = \boldsymbol{m}^*$; otherwise, the current $\boldsymbol{m}_{\mathrm{n}}$ remains as $\boldsymbol{m}_{\mathrm{n+1}} = \boldsymbol{m}_{\mathrm{n}}$.

Step 5: Draw the posterior PDF $p(\boldsymbol{m}_{\mathrm{n}}|\boldsymbol{d})$ from the sampling $\boldsymbol{m}_{\mathrm{n}}$.

Next, I summarized the REMC algorithm. Let us consider the sampling chains as follows:

$$p(m_{\mathrm{i}}|d, T_{\mathrm{i}}) \propto p(m_{\mathrm{i}}|d)^{1/T_i}, \tag{26}$$

where the subscript i indicates the "chain number," and T_{i} $(\mathrm{i} = 1,2, \ldots, N)$ represents the temperature of each chain. The total number of chains is N. T_{i} satisfies the rule $1 = T_1 < T_2 < T_2 < \ldots < T_{\mathrm{N}}$. As the chain number increases (i.e., as T_{i} increases), the target PDF becomes smoother. The REMC algorithm then proceeds according to the following steps:

Step 1: Set the initial value of all model parameters $m_{\mathrm{i}}^{(0)}$ and calculate the likelihood $p\left(d\middle|m_{\mathrm{i}}^{(0)}, T_i\right)$ for each chain.

Repeat Step 2 to Step 4 until the posterior PDF converges.

Step 2: Obtain the next sample $m_{\mathrm{i}}^{(\mathrm{n})}$ following Step 2 to Step 5 of the M–H algorithm.

Step 3: After every several steps, two chains of i-th and (i+1)-th ($1 \leq \mathrm{i} \leq N$) are randomly selected to calculate the "exchanging probability" q as follows:

$$q = min\left(1, \frac{p\left(m_{\mathrm{i}+1}^{(\mathrm{n})}\middle|d, T_{\mathrm{i}}\right)p\left(m_{\mathrm{i}}^{(\mathrm{n})}\middle|d, T_{\mathrm{i}+1}\right)}{p\left(m_{\mathrm{i}}^{(\mathrm{n})}\middle|d, T_{\mathrm{i}}\right)p\left(m_{\mathrm{i}+1}^{(\mathrm{n})}\middle|d, T_{\mathrm{i}+1}\right)}\right). \quad (27)$$

Step 4: Exchange current samples between the two chains, that is, $\boldsymbol{m}_{\mathrm{i}+1}^{(\mathrm{n})} \leftarrow \boldsymbol{m}_{\mathrm{i}}^{(\mathrm{n})}$ and $\boldsymbol{m}_{\mathrm{i}}^{(\mathrm{n})} \leftarrow \boldsymbol{m}_{\mathrm{i}+1}^{(\mathrm{n})}$, with the exchanging probability defined as Equation (27).

Step 5: Draw the posterior PDF $p\left(m_{\mathrm{i}}^{(\mathrm{n})}\middle|d\right)$ from the sampling m_{i}. The target PDF is $p(m_1|d)$.

For this calculation, the initial conditions of model parameters were set as follows: The initial $\boldsymbol{\omega}$ is estimated considering only the rigid block motion part of the block motion model; the initial z_{up} and z_{down} is a uniquely distributed random value ranging from 0 to 60 km that is consistent with the model region depth ranging; the initial C_{b} of each subfault is a uniquely distributed random value ranging from 0 to 1; and the initial $\dot{\boldsymbol{E}}$ is a uniquely distributed random value ranging from -10^{-10} to 10^{-10}/yr. The number of iterations and number of chains are 2.08×10^6 and 10, respectively. The temperature of REMC is configured to be a geometric sequence of $T_{\mathrm{i}} = 1.67^{\mathrm{i}-1}$ so that $T_{10} = 100$. In this study, 10% of the first iteration sampling was rejected as burn-in. This calculation was performed using MATLAB with a workstation consisting of 44 cores of CPU E5-2699 v4 (2.20 GHz), 5120 CUDA cores of GPU (1455 MHz), and 264 gigabytes memory.

Although all model parameters can be estimated as posterior PDFs simultaneously using the REMC method, I evaluated estimated mechanical locking distributions, which are discussed in the following chapters. The results of rigid motion and internal block

strain rates are summarized in Appendix A.

2.2.3. Crustal deformation data in northeast Japan

The surface displacement rates were used as data for REMC inversion to estimate interplate mechanical locking distributions. In Japan, the onshore GNSS observation network (GEONET) was developed by GSI in 1996, which now operates over 1300 stations. The F3 solutions, which are daily coordinate data from GEONET stations, are available via the GSI homepage (https://terras.gsi.go.jp/). Additionally, seafloor geodetic observation sites employing the GNSS/Acoustic combination technique have been installed along the subduction zone of the Pacific Ocean side from off Nemuro through off Okinawa since the 2000s. I use both onshore and seafloor crustal deformation data in northeast Japan. The data I used in the analysis of northeast Japan and the data processing methods for obtaining displacement rates at each site are outlined below.

The displacement rate and uncertainties of GEONET sites in northeast Japan were estimated using F3 daily coordinate data. The data period is from January 1996 to July 2003. In total, data from 447 GEONET sites were considered. First, I removed the offset included in the coordinate data due to maintenance working such as antenna replacements, based on the offset-correction list provided by GSI (https://mekira.gsi.go.jp/JAPANESE/corrf3o.dat). Then, model displacement was assumed to fit the coordinate data:

$$\begin{aligned} x_i^n(t) = {} & a_i^n t + b_i^n \\ & + c_i^n \cos\left(\frac{2\pi t}{365.25}\right) + d_i^n \sin\left(\frac{2\pi t}{365.25}\right) \\ & + e_i^n \cos\left(\frac{4\pi t}{365.25}\right) + f_i^n \sin\left(\frac{4\pi t}{365.25}\right), \end{aligned} \tag{28}$$

where x is the position of a site at time t, a is the mean value of the displacement rate per one year, b is the offset, c and d are amplitudes of annual changes, and e and f are amplitude of semiannual changes. The subscript i indicates a component (east, north, or vertical), and the superscript n indicates a site. The first term on the right-hand side is the trend of displacement, the third and fourth terms are annual changes, and the fifth and last terms are semiannual changes. All parameters described above were estimated simultaneously by the linear least squares, and the a_i^n was used as the average displacement rate per year in this study. Mean uncertainties of displacement rates in the east, north, and vertical components of GEONET sites are 0.1, 0.1, and 0.2 mm/yr, respectively. In general, displacement caused by coseismic and/or postseismic slip has been recorded at some GNSS sites, However, because no major earthquakes have occurred in the study period, I did not model coseismic and/or postseismic displacement in the above equation. Although a seismic swarm occurred offshore at the southeast Izu Peninsula following the Miyake island volcanic eruption and affected the surface velocity near the Izu Peninsula (Kaidzu et al., 2000), no corrections were made because this study focused on surface displacement in Tohoku and Hokkaido, which are north of the Izu region.

Additionally, I estimated the displacement rate and its uncertainties of seafloor GNSS/A sites. The coordinate data were downloaded from the data repository (https://www1.kaiho.mlit.go.jp/KOHO/dataservice/DATA/sgo/, Yokota et al., 2018). The data period is from January 2002 to February 2011. I estimated the displacement rate from the coordinate data by linear regression based on the model equation containing the first and second terms of the right-hand side of the Equation (28). Because the typical observational interval of the GNSS/A site is once or twice in a year, temporal resolution is insufficient to consider annual and/or semiannual displacements. Thus, I did not

consider annual and semiannual displacements in the linear regression for the GNSS/A data. Note that during the GNSS/A data period, two relatively large interplate earthquakes of $> M$ 7 occurred near the seafloor GNSS/A sites off Tohoku, namely: the 2005 Mw 7.1 Miyagi Earthquake and 2008 Mw 6.9 Fukushima Earthquake (Figure 2.2). Thus, data periods for each seafloor site were selected to avoid the effects of these earthquakes, following the method proposed by Sato et al. (2013) in which the interplate coupling offshore Tohoku prior to the 2011 Tohoku Earthquake was estimated using seafloor GNSS/A observation data. Mean uncertainties of displacement rates in the east and north components of the GNSS/A sites are 16 mm/yr and 14 mm/yr, respectively. Note that the vertical component of the GNSS/A could not be obtained due to lack of coordinate data.

The displacement rates at the GEONET and GNSS/A sites were translated from the International Reference Frame (ITRF) 2005 to Eurasian plate reference frame using the Euler vectors of the Mid-Ocean Ridge VELocity (MORVEL) plate model (DeMets et al., 2010; Figure 2.2; Table C.1).

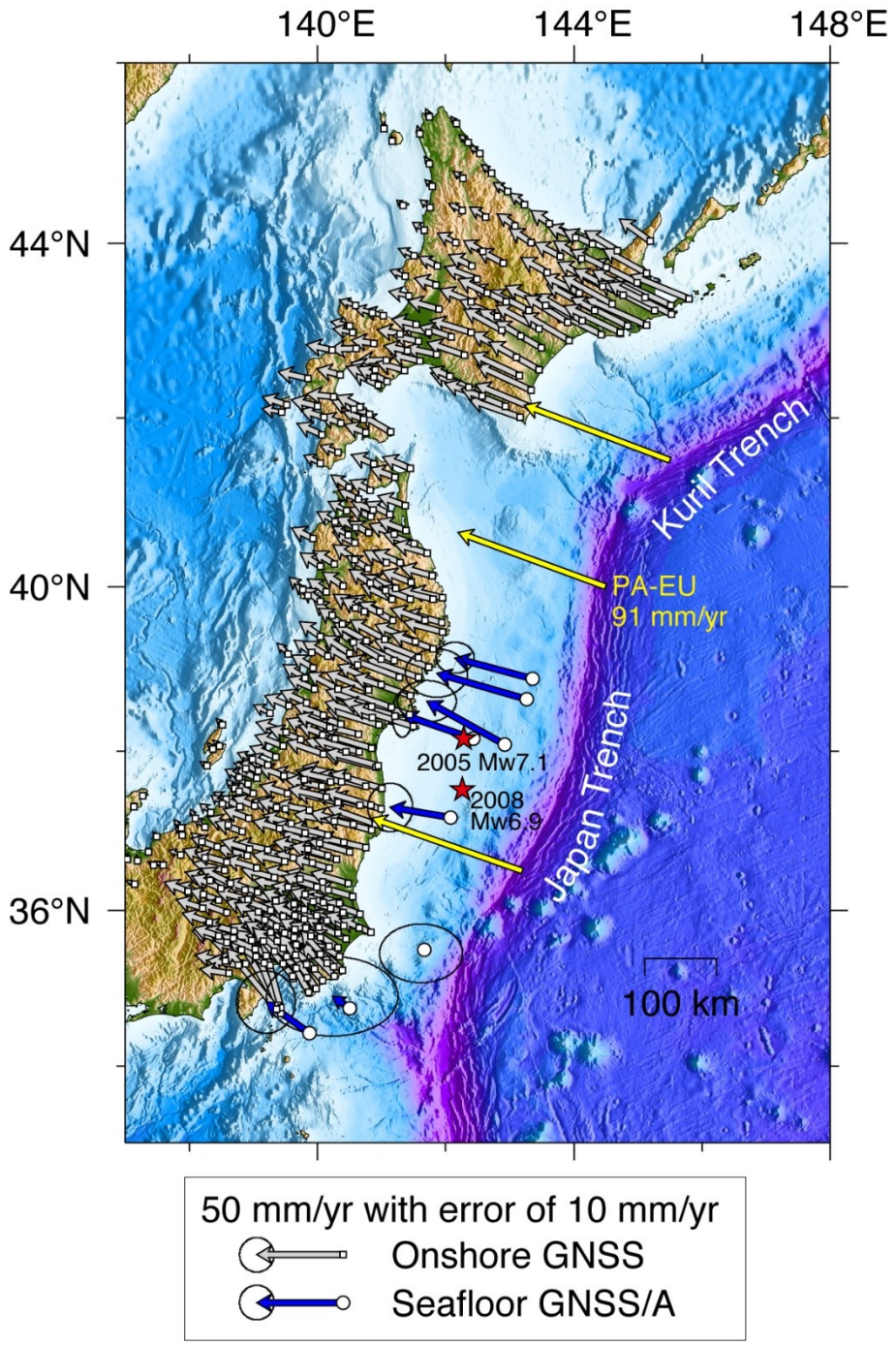

Figure 2.2. Map showing observational data used in this chapter. Gray vectors with white squares and blue vectors with white circles indicate displacement rate vectors at the onshore GNSS (GEONET) and seafloor GNSS/A sites, respectively. Yellow vectors show the Pacific Plate motion relative to the Eurasian plate calculated on the basis of the MORVEL plate motion model (DeMets et al., 2010). Red stars indicate the epicenters of the Mw 7.1 Miyagi and Mw 6.9 Fukushima earthquakes. Color scale of the map represents the elevation and bathymetry of SRTM30_PLUS (Becker et al., 2009).

2.2.4. Configuration of block boundary and plate interface geometry

According to the global plate model (Bird, 2003), northeast Japan is composed of four major plates: Pacific, Philippine Sea, Amurian, and Okhotsk (North America) Plates. The Pacific Plate subducts beneath the Okhotsk and Philippine Sea Plate along the Kuril, Japan, and Izu–Ogasawara Trenches. The theoretical plate motion rate of the Pacific Plate is approximately 9 cm/yr relative to the Eurasian Plate along the Japan Trench (DeMets et al., 2010). The Philippine Sea Plate subducts beneath the Okhotsk Plate along the Sagami Trough. These plates can be assumed rigid bodies, and their motion is the independent rotation prescribed by Euler vectors. In the regional-scale, the overriding plates can be divided into independent blocks based on geological, geodetic, and seismological features. In the eastern part of Okhotsk Plate, GNSS observation analysis has suggested that there is a long and wide shear concentrating zone extending with NE–SW orientation, called the Niigata–Kobe Tectonic Zone (NKTZ; Sagiya et al., 2000). In the central part of northeast Japan, the long and high Ou Backbone Range extends with approximate N–S orientation. This mountain range is a volcanic front where many active volcanoes are aligned, and many reverse faults exist along the mountain range, with relatively large intraplate earthquakes sometimes occurring along the fault zone (Nakata & Imaizumi, 2002). Furthermore, the strain concentrations along the mountain range are also suggested by the GNSS observations (Miura et al., 2002). This volcanic front extends to Hokkaido, and its direction shifts to NNE–SSW along the Kuril Trench. The forearc side of the volcanic front, called the Outer Kuril Arc, is considered to move westward relative to central Hokkaido (Kimura, 1986). This tectonic motion is often referred to as the Kuril forearc sliver. In northeastern Hokkaido, there are active faults with dominant N–S strikes. Recently, slow slip events have been detected along the fault zone by GNSS

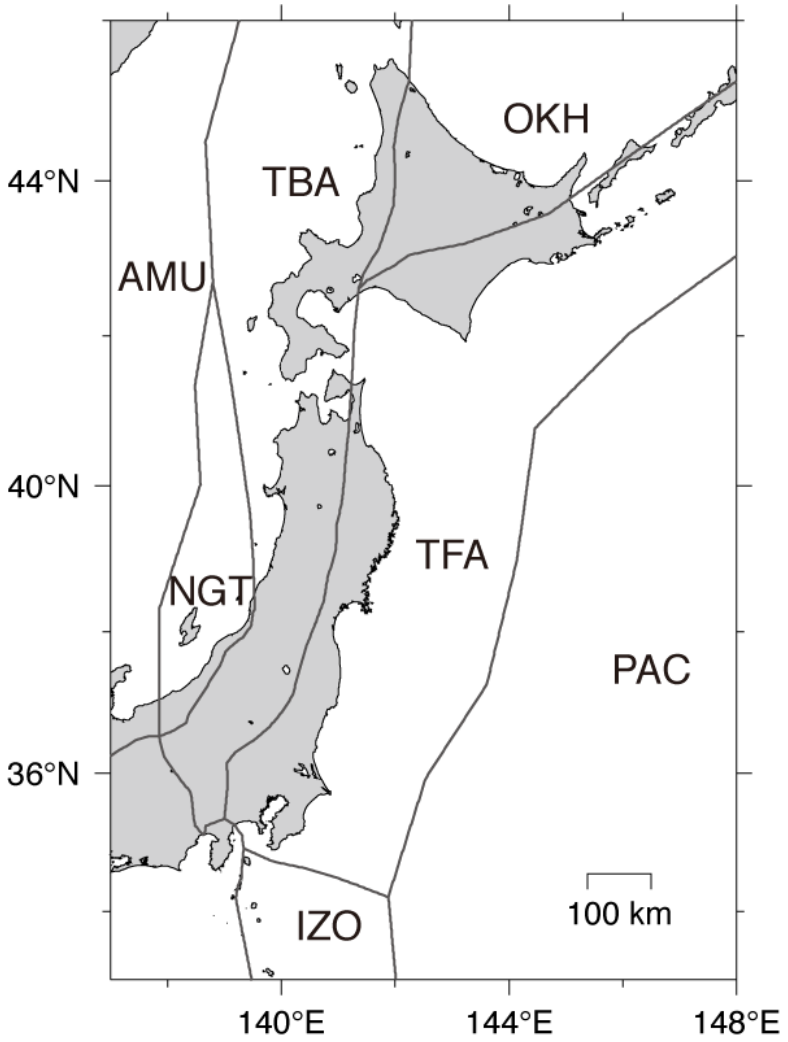

Figure 2.3. Map showing the block boundaries around northeast Japan. Abbreviations of each block are as follows: PAC, Pacific Plate; AMU, Amurian plate; OKH, Okhotsk plate; IZO, Izu-Ogasawara block; TFA, Tohoku Forearc block; TBA, Tohoku Backarc block; and NGT, Niigata block.

observations (Ohzono et al., 2015). In the eastern part of the Philippine Sea Plate, the backarc spreading along the Izu-Ogawawara islands, which is consistent with geological structures, has been suggested by GNSS observations and block modeling (Nishimura, 2011). I set the block boundaries in the overriding blocks on the basis of the tectonic backgrounds described above and divided northeast Japan into 7 rigid blocks for analysis.

I generated a set of subfaults on the subducting Pacific Plate interface along the Kuril

and Japan Trenches and the subducting Izu–Ogasawara block interface along the Sagami Trough based on the plate geometry model compiled by Iwasaki et al. (2015). Triangular meshes were adopted for the subfault because a triangles can express curved surfaces such as subducting plate interfaces more easily than rectangles. The length of the subfault on the plate interface is approximately 20 km. The depth ranges from trench depth to 80 km along the Kuril and Japan Trenches and from trough depth to 60 km along the Sagami Trough. Additionally, I generated triangular subfaults along the inland block boundaries. The dip angle and lower limit of the subfault are 90° and 20 km in depth, respectively.

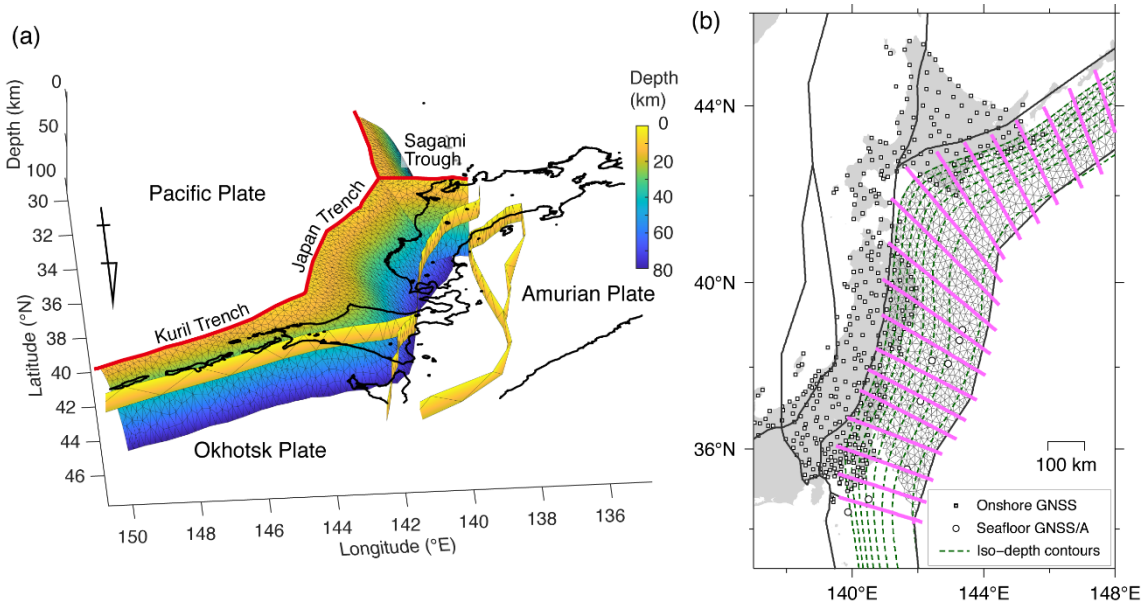

Figure 2.4. Configuration of plate and block interfaces. (a) Three-dimensional map showing the interface of the block and subducting plates, observed from the north-northeast. Triangles on the interface are subfaults. The color scale means the depths. Black lines show the coast lines. (b) Map showing subfaults on the subducting plate interface. Green lines indicate the iso-depth contours of subducting plate interface. $\boldsymbol{z_{up}}$ and $\boldsymbol{z_{down}}$ are sampled along the pink lines.

2.3. Estimated mechanical locking distributions

Figure 2.5 shows the estimated mechanical locking distributions along the Japan and Kuril trenches. The background color scale indicates the locking probability P_l at each subfault l, which is defined as follows:

$$P_l = \frac{N_{l_{Locking}}}{N_{l_{Total}}}, \tag{29}$$

where $N_{l_{Total}}$ denotes the number of total sampling, and $N_{l_{Locking}}$ denotes the number of sampling that the subfault l was judged to be mechanically locked. This probability was calculated from all samples of original chain (i.e., chain number = 1 in which T=1) except the samples within the burn-in period after the REMC iterations. Additionally, Figure 2.6 shows PDFs of the up- and down-dip depth limits and the locking probability P_l along lines A, B, C, D, E, and F from Figure 2.5. Two separated mechanical locking segments were estimated offshore Miyagi and Fukushima, and one locking zone extending with NE–SW orientation was estimated in eastern Hokkaido along the Kuril Trench.

In the mechanical locking segment extending off eastern Hokkaido, numerous subfaults with low P_l were broadly distributed around the locked subfaults with high P_l. The PDFs exhibit multimodal or flat-shaped peaks (Figure 2.6). The 95 percentile confidence intervals at cross sections A, B, and C were 51 (up-dip in A), 67 (down-dip in A), 40 (up-dip in B), 50 (down-dip in B), 35 (up-dip in C), and 25 km (down-dip in C). Although almost all samples were within the model region depth ranges, more than half of samples of the up-dip depths in lines A and C, almost all samples of the up-dip depths in line B, and some samples of the down-dip depths in line A were outside the model

region depths (i.e., sampled at the depths shallower than trenches or deeper than the bottom). The peaks of the PDF estimated outside of the model region depths indicate that the edge of the model region (trench or bottom) is completely mechanically locked. For example, the trench along line A can be assumed to be mechanically locked. In that case, an exact PDF peak depth does not have a physically important meaning because the mechanical locking states would not change even if the peak depths changed within the depth ranging outside model region depths.

Note that, although there are high P_l zones extending to east of Nemuro, I did not focus on the result in this area because this region is near the boundary of the study area, and poor data coverage hindered the ability to achieve high-resolution and accurate estimates for mechanical locking distributions.

Off northern Tohoku, almost all subfaults exhibit a P_l of ~0 (Figure 2.5). I plotted the PDFs and P_l along lines SA, SB, SC, and SD (Figure 2.7). Almost all samples of the up- and down-dip depths along these lines were observed to intersect. At line SC, the PDFs of both up- and down-dip depths were almost equal, and their 95 percentile confidence intervals were very large.

In the locking segments off Miyagi and Fukushima, there were only some subfaults showing a low P_l around the subfaults with a high P_l. Although there were some possible mechanical locking subfaults between certain segments situated off Miyagi and off Fukushima, the P_l was lower than 0.3. The PDFs of both the up- and down-dip limitation depths had a relatively sharp and unimodal peak along the lines D, E, and F (Figure 2.6d, e, and f). The 95 percentile confidence intervals at these lines were 5 (up-dip in D), 4 (down-dip in D), 9 (up-dip in E), 6 (down-dip in E), 9 (up-dip in F), and 16 km (down-dip in F). These confidence interval values are notably smaller than those in eastern Hokkaido, implying that the resolution of data off Miyagi and Fukushima is much

higher than that off eastern Hokkaido.

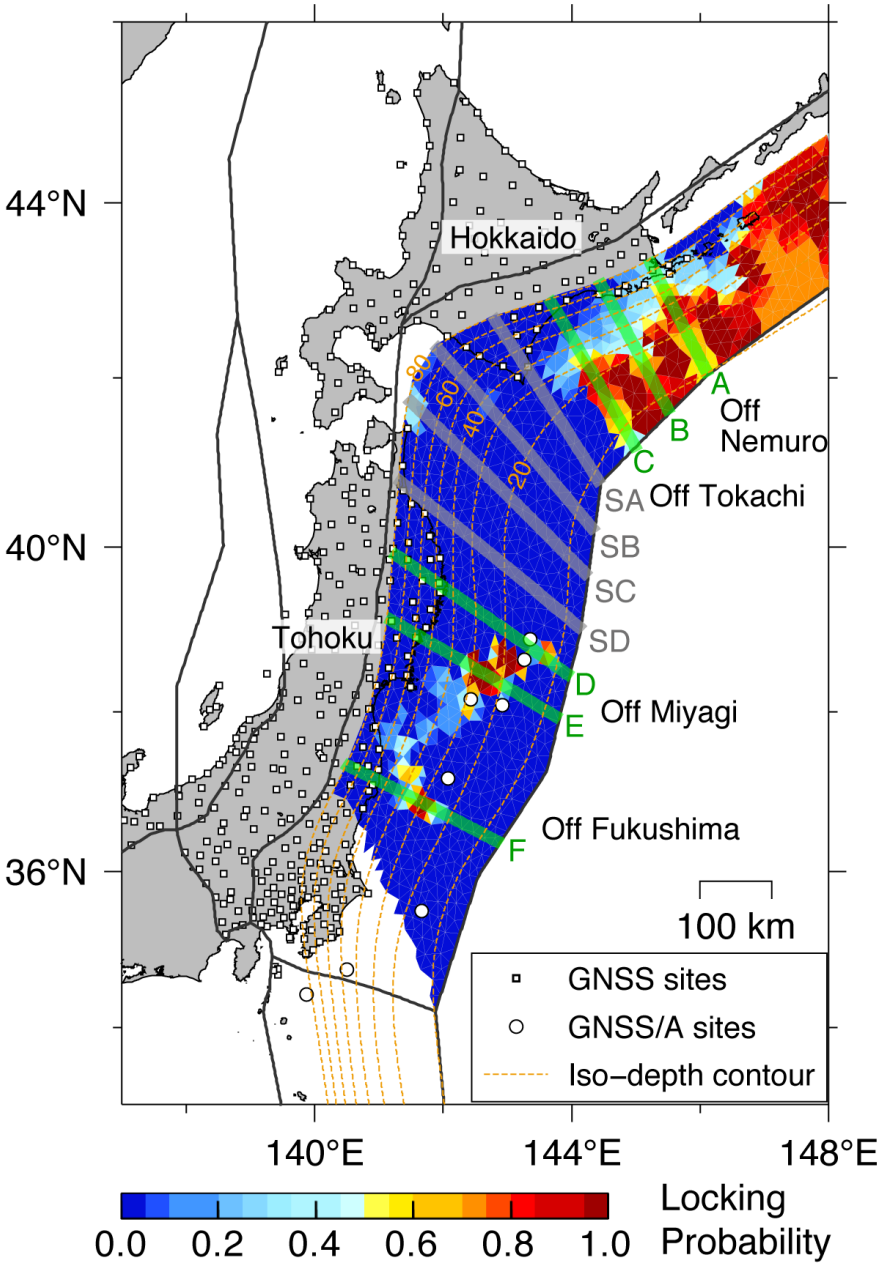

Figure 2.5. Map showing estimated mechanical locking distributions on the plate interface along the Nankai Trough. Color scale indicates the locking probability of each subfault given by Equation (29). Orange dashed lines indicate the iso-depth contours of the subducting plate interface. Black dashed lines indicates the boundary of the plate interface. The lower surface of the overriding Nankai block interfaces with the upper surface of the subducting Philippine Sea Plate to the west and north of the line, whereas it interfaces with the upper surface of the subducting Izu Micro Plate to the east and south of the line.

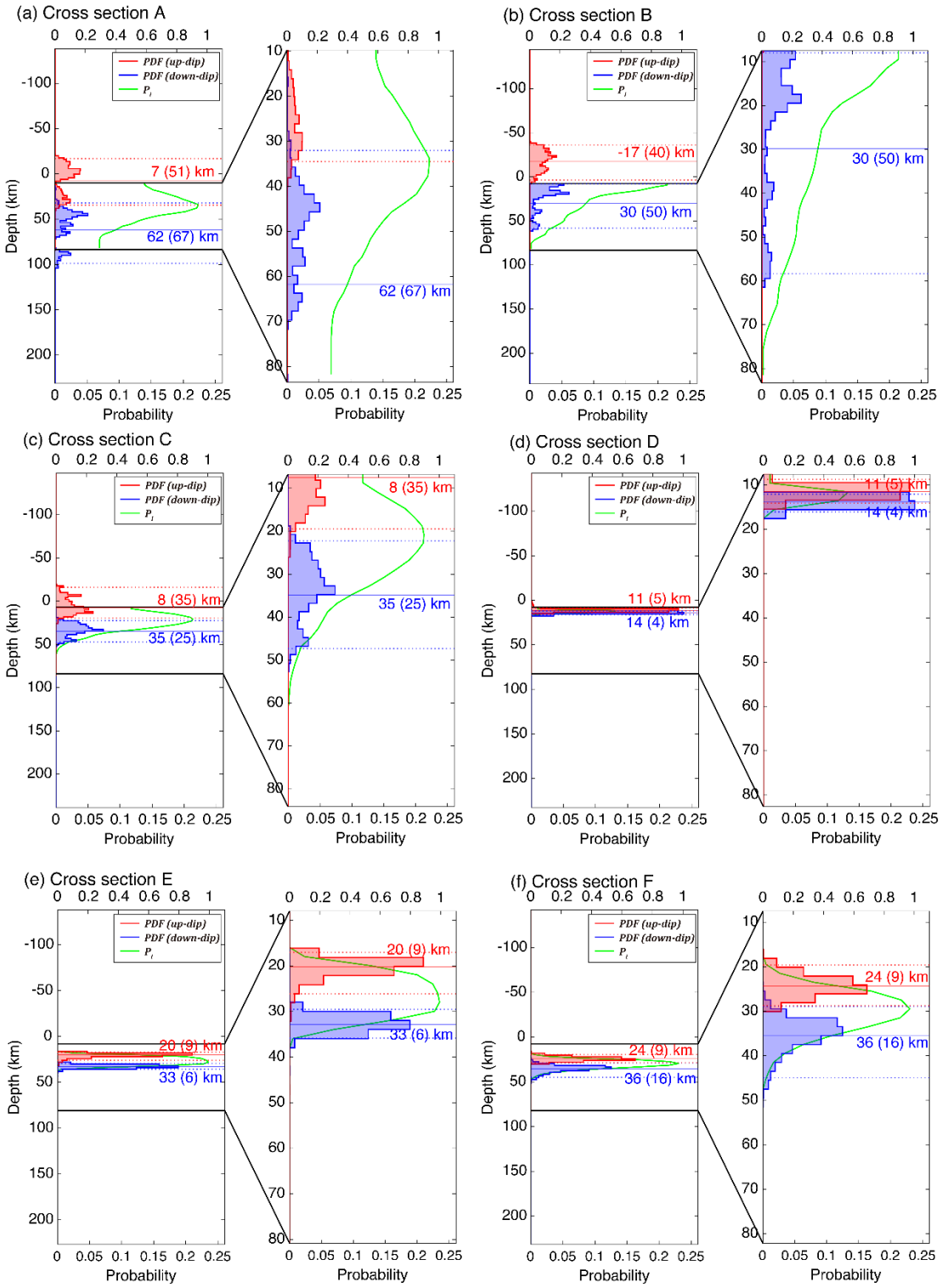

Figure 2.6. Graphs showing PDFs of the up- and down-dip depths and the locking probability P_l along lines A, B, C, D, E, and F in Figure 3.6. For each subfigure, PDFs and the locking probability are plotted for whole sampling depths in the left panels, whereas they are plotted for model area depths (i.e., top and bottom depths coincide with

the trench and 60 km depth, respectively) in the right panels. PDFs are normalized such that the sum of the value for each bin becomes 1. Horizontal red and blue solid lines indicate the mean values of the up- and down-dip depths calculated from all samples, respectively. Mean values are described on or under the lines. The 95 percentile confidence interval values are described in brackets to the right of the mean value. The scale of PDFs and locking probability is shown in the bottom and top axes for each panel, respectively.

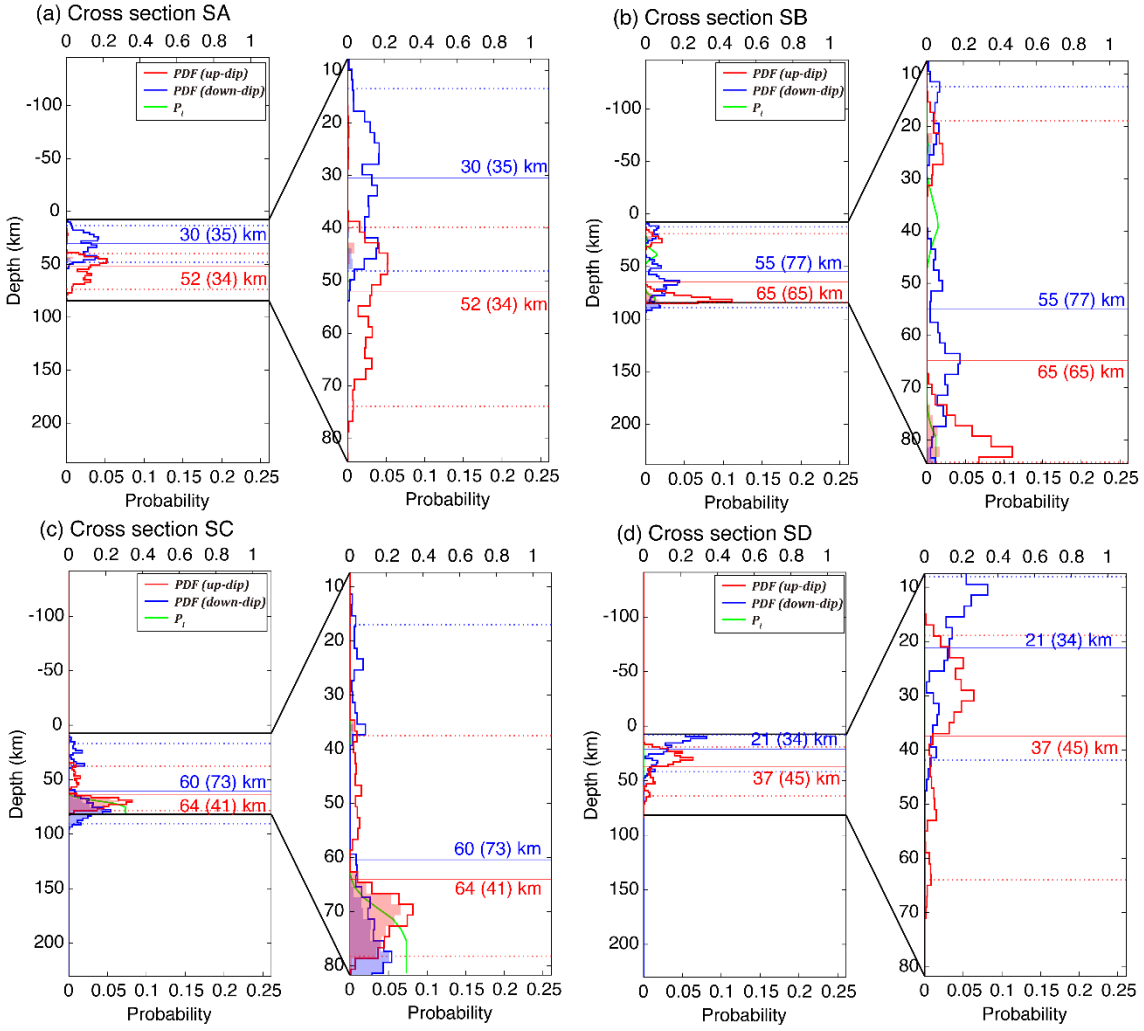

Figure 2.7. Same as Figure 2.6, but along the gray lines SA, SB, SC, and SD in Figure 2.5.

2.4. Discussion

2.4.1. Comparison with kinematic coupling distributions

I compared the estimated mechanical locking distributions with the kinematic coupling distributions estimated in previous studies to reveal the spatial relationship between the two distributions, which were obtained using conceptually distinct models. To calculate the slip deficit rate distribution based on the estimated mechanical locking distribution, I selected the subfaults whose locking probability is larger than 0.5 as comprising the mechanically locked zone (Figure 2.8a). The calculated slip deficit rate distribution is shown in Figure 2.8(b).

The maximum slip deficit rate in the mechanical locking zone is 78 mm/yr off Miyagi and Fukushima. Slip deficits due to the mechanical locking spread to the region that is sufficiently far from the mechanical locking zone, although the slip deficit rate decreases as the distance from the mechanical locking zone increases. The slip deficit rates decrease to 50% of full slip deficit rate (i.e., ~40 mm/yr) at ~35 km from the locking zone off Miyagi and ~15 km from the locking zone off Fukushima. At the region that is ~100 km north from the locking zone off Miyagi, 20% of the full slip deficit rate (i.e., ~17 mm/yr) remained. Between the locking zones off Miyagi and Fukushima, the slip deficit rate was maintained at over 20 mm/yr. This implies that slip deficits decay gradually from mechanical locking zones if the distance of multiple locking segments is small, as suggested by Herman et al. (2018).

The mechanical locking distribution off Tokachi roughly overlaps the high slip deficit rate areas estimated by previous studies (Hashimoto et al., 2012; Loveless & Meade, 2010, 2015; Suwa et al., 2006). However, the mechanically locked zones estimated in this study tended to be smaller than areas where the high slip deficit rates were estimated by previous studies. The maximum slip deficit rate is 76 mm/yr in mechanical locking zones

along the Kuril Trench. Although high slip deficit rate areas were reported to extend southwest off Tokachi to the northernmost part of Tohoku in some studies (Hashimoto et al., 2012; Loveless & Meade, 2015; Suwa et al., 2006), low or almost zero P_l values were observed in this study (Figure 2.5). I found that the slip deficit rate spreads from the mechanical locking zone off Tokachi and maintains approximately 25% of the full slip deficit rate (i.e., ~20 mm/yr) at a region that is ~95 km west from the locking zone.

At the region off Miyagi and Fukushima, this study estimated two clearly separated locking zones in these regions, unlike the one larger high-slip deficit rate area (Loveless & Meade, 2010, 2015; Suwa et al., 2006) or two vaguely separated high-slip deficit rate areas (Hashimoto et al., 2012) with very smooth gradients that were estimated in previous studies. Although Hashimoto et al. (2012) estimated the highest slip deficit rate roughly in the same region where this study estimated the mechanical locking, it was impossible to identify mechanical locking regions because the slip deficit rate is simply a kinematic value that does not indicate mechanical locking states. However, by developing and adopting a new physical model that prescribes mechanical locking states by imposing a mechanical constraint, I confirmed the regions that Hashimoto et al. (2012) estimated the highest slip deficit rate as appearing mechanically locked. The detailed positions where Hashimoto et al. (2012) estimated the highest slip deficit rate and where mechanical locking was identified by this study are slightly different. For example, the mechanical locking zone off Fukushima was estimated at the region that is ~50 km landward side of the region where Hashimoto et al. (2012) estimated the highest slip deficit rate off Fukushima. Moreover, this study estimated a mechanical locking zone whose up-dip limit extends to ~10 km in depth off Miyagi, whereas the up-dip limit of the highest slip deficit rate estimated by Hashimoto et al. (2012) is ~20 km in depth. This slight difference may be caused by using the seafloor GNSS/A in this study. Seafloor GNSS/A data may have

enhanced the resolution power in offshore areas where the mechanical locking or high slip deficit rate were estimated.

From the comparison outlined in this chapter, it was expected that the mechanical locking zones would be estimated to be included in the kinematic high-coupled zones, and the size of the mechanical locking zone would be smaller than that of the kinematic high-coupled zone when estimating mechanical locking distributions using the proposed model with interseismic geodetic observation data. Thus, even if high slip deficit rate was estimated at the wide area based on the pure kinematic model, the mechanically locked zone may only encompass a portion of the total area.

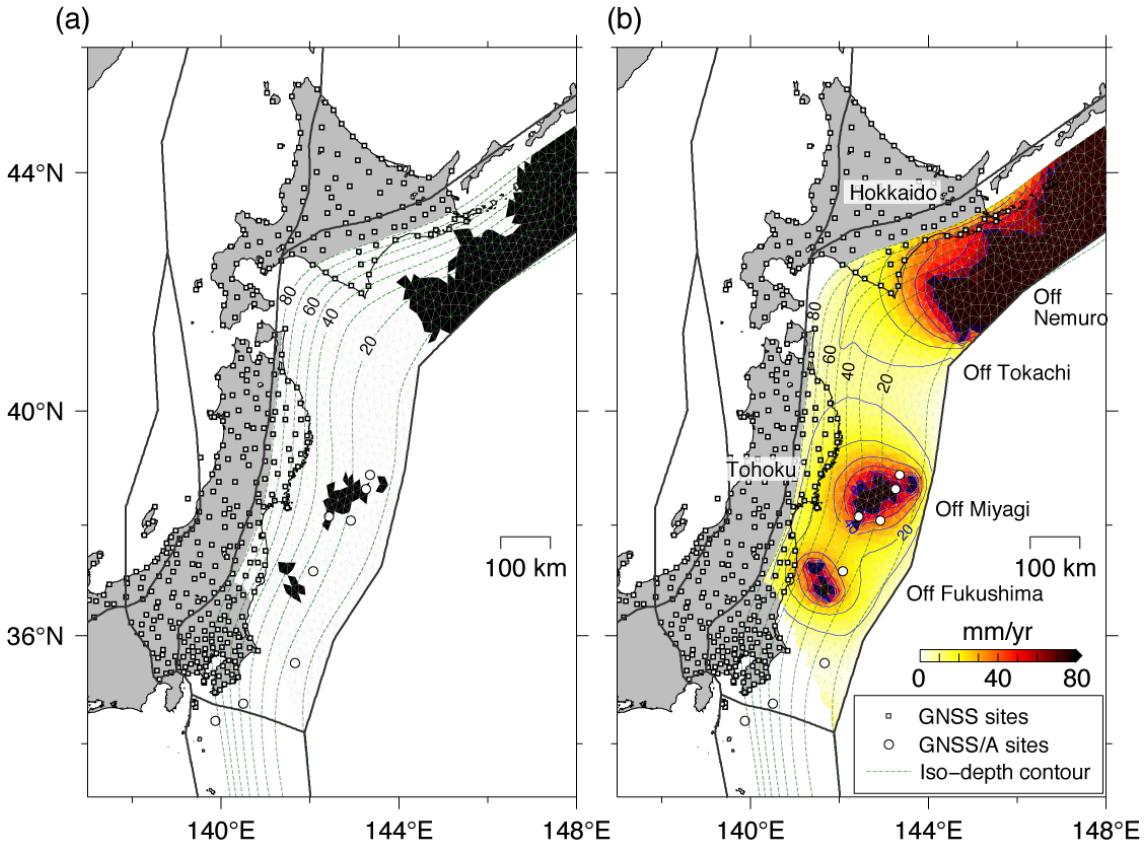

Figure 2.8. Calculated slip deficit rate distributions along the Kuril and Japan Trenches. (a) To calculate the slip deficit rate distribution, subfaults whose locking probability is larger than 0.5 (Figure 2.5) were selected to be the mechanically locked zone. The selected subfaults are denoted in black. (b) Map showing the slip deficit rate distributions derived from the locking distributions shown in (a). Blue lines indicate the slip deficit rate contours with an interval of 10 mm/yr, starting from 10 mm/yr.

2.4.2. Correspondence with interplate earthquakes

In 2011, a Mw 9.0 Tohoku Earthquake occurred off Miyagi, and its coseismic slip propagated through an extremely wide area that extended near Fukushima. The coseismic rupture began at the southern edge of the mechanical locking zone off Miyagi estimated in this study (Figure 2.9). Some previous studies estimated the coseismic slip distributions and thus released a seismic moment of 4.0×10^{22}–4.2×10^{22} Nm from the geodetic observation data (e.g., Iinuma et al., 2012; Ito et al., 2011; Yokota et al., 2011). The subfaults located off Miyagi and Fukushima and those whose locking probability was larger than 0.5 were selected as mechanical locking zones. Their areas were 5.10×10^{3} km^2 (off Miyagi segment) and 1.99×10^{3} km^2 (off Fukushima segment). These two mechanical locking segments are considered to comprise the rupture zone of the 2011 Tohoku Earthquake. Based on these two locking segments and assuming the peak coseismic slip magnitude estimated by Yokota et al. (2011) (~35 m in the segment off Miyagi and ~10 m in the segment off Fukushima) and the uniform rigidity value of 40 GPa, the possible total released seismic moment was calculated to be 7.94×10^{21} Nm. This value is only 19% of that estimated by previous studies (e.g., Iinuma et al., 2012; Ito et al., 2011; Yokota et al., 2011). Because the coseismic distributions by previous studies differ, I evaluated another scenario in which ~60 m of slip magnitude, equivalent to the maximum slip magnitude (Iinuma et al., 2012; Ito et al., 2011; Sun et al., 2017), was imposed at the rupture zone. However, the released seismic moment was calculated to be 1.30×10^{22} Nm, which is only 32% of the moment estimated by previous studies. The remaining moment would be released by the slip of areas that surround the mechanical locking zones wherein the slip deficit is accumulated during interseismic periods. This implies the possibility that the areas subjected to significant mechanical rupture during seismic events are considerably smaller than areas that release the entire seismic moment.

Rupture at the mechanical locking zone can release only 20–30% of the total moment. The remaining 70–80% of the moment would be released by the slip of the region outside of the mechanical locking zone accompanied by the rupture of mechanical locking zone.

To assess the total moment release due to total coseismic slip (i.e., rupture of the mechanical locking zone and accompanying slip outside the locking zone), simple coseismic slip simulations were conducted (Figure 2.10). In the simulation, slip was imposed only at mechanical locking zones off Miyagi and Fukushima; then, the total slip including that around the mechanical locking zone and surface responses (displacements) were calculated. The imposed slip magnitude in the locking segments were evaluated at ~35 m in the segment off Miyagi and ~10 m in the segment off Fukushima, following the estimates of Yokota et al. (2011). To calculate surface displacement, only the elastic response from the total coseismic slip was considered by assuming the constant strain states on the area outside the mechanical locking zone (i.e., the region where the slip was imposed). The simulation indicated that the coseismic slip propagated to both landward and trenchward sides (Figure 2.10(b)). However, the extremely large slip at the trench, which is sometimes called the “overshoot” and considered to be generated by dynamical rupture processes (e.g., Fukuyama & Hok, 2015; Ide et al., 2011), was not obtained because this study did not consider factors that can affect dynamical rupture processes (e.g., frictional strength or three-dimensional shape of locking zones), and coseismic slip was only calculated to satisfy the constant strain states on the plate interface outside the mechanical locking zones. The coseismic slip outside the rupture area reached regions over 100 km from the rupture area off Miyagi, whereas it reached regions 30–40 km from the rupture area off Fukushima. This occurred because the size of the rupture area off Fukushima was smaller than that observed off Miyagi, and the given slip magnitude off Fukushima was only a quarter of that observed off Miyagi. The coseismically released

moment calculated on the basis of the slip distributions was 4.68×10^{22} Nm. Although the estimated moment value is 17% larger than the moment release estimated by Yokota et al. (2011), this difference is not significant considering data and model uncertainties. Calculated displacements are clearly larger than the observed displacements (JPL and Caltech, 2011), specifically in coastal areas of Miyagi and northern Tohoku, although the average calculated displacements at the seafloor sites were roughly equivalent to the observed displacements (Figure 2.10(c)). This may have been caused by the larger slip in this simulation compared to the actual coseismic slip at the landward side of the rupture area off Miyagi. Coseismic slip distributions inverted from the geodetic, seismic, or tsunami observation data show spatial heterogeneity (e.g., Iinuma et al., 2012; Simons et al., 2011; Yokota et al., 2011), which differs from the radial-like slip distribution simulated above. Furthermore, the postseismic slips were estimated on the plate interface where the coseismic slip was relatively smaller, such as that observed at the landward side of the rupture area (e.g., Iinuma et al., 2016; Figure 2.9). The over slip calculated at the landward side of the rupture area (Figure 2.10(b)) can be partially explained by the postseismic slip.

Near the southern tip of Hokkaido, the 2003 Tokachi Earthquake occurred (Figure 2.9). The coseismic rupture began from the southwestern edge of the mechanical locking zone along the Kuril Trench estimated in this study. Based on the teleseismic wave analysis, the coseismic slip area of the earthquake, with a ~100 km width, was estimated to be north of the hypocenter (Yamanaka & Kikuchi, 2003). The seismic moment released by the earthquake was estimated to be in the range of 1.0×10^{21} – 1.7×10^{21} Nm, from the seismic observation data (Yagi, 2004; Yamanaka & Kikuchi, 2003). In addition to the 2003 Tokachi Earthquake, an Mw 8.3 earthquake occurred in 1952 in Tokachi. The earthquake rupture area was also estimated in roughly the same location as that of the 2003 Tokachi

earthquake. The study estimated an extremely large mechanical locking zone along the Kuril Trench, while the southwestern portion overlapped with the southeastern portion of the coseismic slip area of the 2003 Tokachi Earthquake. Seismic rupture from this earthquake started from the southeasternmost part of the coseismic slip zone (i.e., the western edge of the estimated mechanical locking zone along the Kuril Trench) and propagated northward to the down-dip side (Robinson & Cheung, 2010; Yagi, 2004) where the mechanical locking zone was not estimated in this study. A simple coseismic slip simulation for the 2003 Tokachi Earthquake, based on the mechanical locking distribution estimated in this study, was attempted. The mechanical locking zone where the coseismic slip area of the earthquake overlapped the rupture area. Then, a slip of ~5 m was imposed in this area (Figure 2.11(a)). As a consequence, the coseismic slip propagated concentrically around the rupture area. A slip of ~1 m reached a distance of ~55 km from the rupture area (Figure 2.11 (a)). 2.41×10^{21} Nm of moment release was calculated. The simulated moment was 50–92% larger than that estimated by previous studies (Yagi, 2004; Yamanaka & Kikuchi, 2003). This implies that the actual size of the rupture area of the 2003 Tokachi Earthquake may be much smaller than that of the rupture area assumed in the simulation. Predicted surface displacements moved in an eastward direction compared to the observed coseismic displacements (Larson & Miyazaki, 2008; Figure 2.11 (c)), and they were larger than those observed at the tip of Tokachi and smaller than those observed at the coastal area of east of Tokachi. This difference suggests that to the west (or W-NW direction) of the locking zone along the Kuril Trench, there may be hidden mechanical locking zones that could not be estimated from the geodetic observation data used in this study. Additionally, the hidden locking zones may be distributed in pieces and may be extremely small because the small coseismic slip areas with several remarkable slip peaks were estimated to extend

westward (Yagi, 2004; Yamanaka & Kikuchi, 2003), where no mechanical locking zone was estimated in this study. Developing a considerably denser geodetic observation network may enable the estimation of complex mechanical locking distribution, such as the small-scattering mechanical locking zones.

Interplate earthquakes with magnitudes of 7–8 have occurred frequently off northern Tohoku (Yamanaka & Kikuchi, 2004). However, a low or almost zero P_l value was observed, thereby leading to extremely low slip deficit rates in this area. Some previous studies as well as the present analysis that used geodetic inversion revealed a relatively low slip deficit rate in this region compared to that in other regions, such as off Tohoku and off eastern Hokkaido (Hashimoto et al., 2012; Suwa et al., 2006). One possible reason for the occurrence of interplate earthquakes with a $M > 7$ in this region, where no mechanical locking zones (or low slip deficit rate in previous studies) were estimated owing to poor resolution due to no offshore geodetic observation data, is that extremely small locking zones were scattered in this region. The 2011 Tohoku Earthquake could be explained by the two small mechanical locking zones located near Miyagi and Fukushima, as discussed above. If a single rupture at the Miyagi locking segment is assumed, the released moment magnitude could be $Mw > 8.5$ because the released moment in the off Fukushima segment might be sufficiently less than that at the off Miyagi segment. Thus, possible mechanical locking zones explaining the occurrence of M 7–8 earthquakes may be much smaller than those estimated at the Miyagi and Fukushima segments. The crustal deformations due to the small mechanical locking zones located beneath the seafloor may not be detected as clear signals with onshore geodetic observations. It is important to estimate small mechanical locking zones because the simultaneous rupturing of multiple mechanical locking zones can lead to the huge seismic moment releasing, even if each mechanical locking zone is small (Herman et al., 2018). It is possible to detect small

mechanical locking zones by developing a denser and more accurate geodetic observation network on the seafloor as well as onshore.

The mechanical locking zone estimated along the Kuril Trench extends northeastward to regions situated off Nemuro. Many large interplate earthquakes have occurred along the Kuril islands (Fukao & Furumoto, 1979). Coseismic slip models of these earthquakes were estimated by seismic waveform inversions (Yamanaka, 2005) and tsunami waveform inversions (e.g., Satake et al., 2008; Tanioka et al., 2013). One notable recent event is the M 7.8 Nemuro earthquake, which occurred in 1973 (Figure 2.9). Although this area was not evaluated in detail owing to the lack of high-resolution data, the results show large mechanical locking zones and accompanying high-slip deficit rates along the Kuril Trench extending northeastward, which may imply the occurrence potential of middle-large sized interplate earthquakes and their huge counterparts that occur by rupturing the multiple mechanical locking segments, as suggested by The Headquarters for Earthquake Research Promotion (2017).

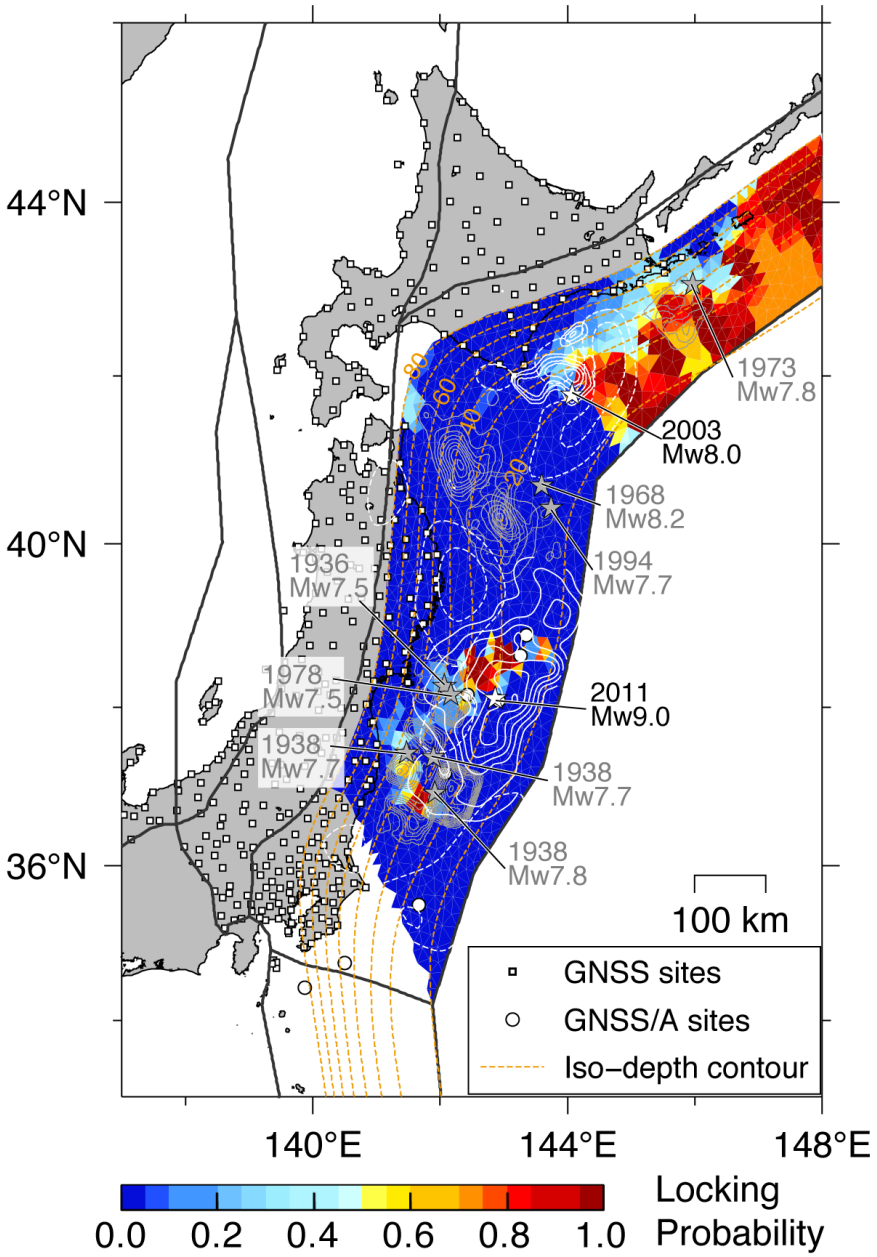

Figure 2.9. Map showing the spatial relationship between mechanical locking distributions, coseismic slips, and postseismic slips. White solid lines indicate the coseismic slip contours of the Mw 8.0 Tokachi earthquake in 2003 (Yamanaka & Kikuchi, 2003) and Mw 9.0 Tohoku earthquake in 2011 (Iinuma et al., 2012). White dashed lines indicate the postseismic slip contours of the Mw 8.0 Tokachi earthquake in 2003 (Miyazaki et al., 2004) and Mw 9.0 Tohoku earthquake in 2011 (Iinuma et al., 2016). Red stars indicate the epicenters of the two earthquakes. Gray solid lines indicate the coseismic slip contours of other interplate earthquakes occurring in northeast Japan (Murotani et al., 2003; Nagai et al., 2001; Yamanaka, 2005).

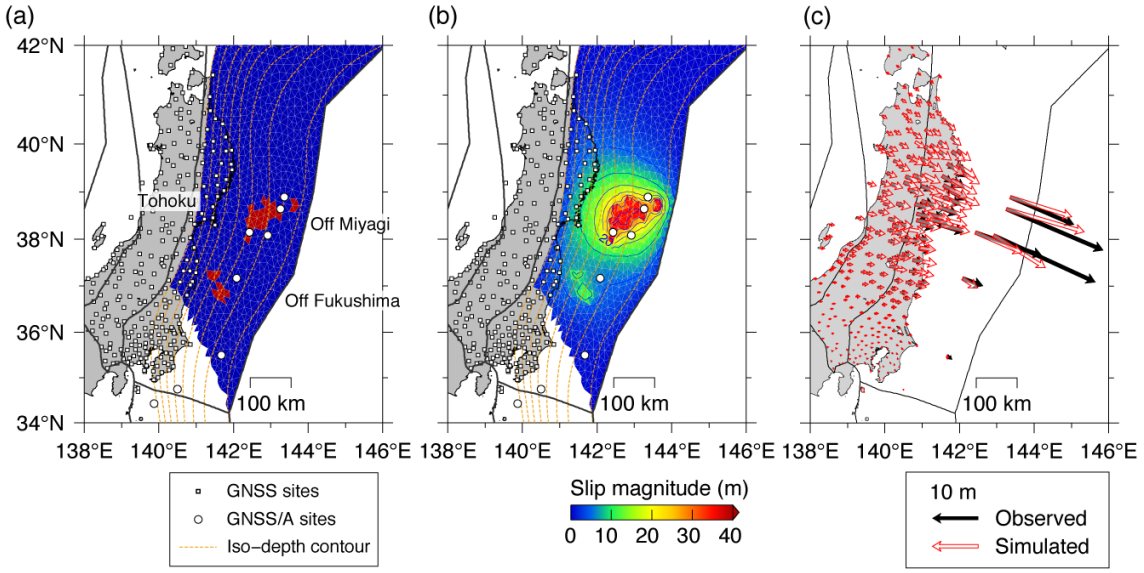

Figure 2.10. Coseismic slip simulation results of the 2011 Tohoku earthquake. (a) Map showing rupture distributions. The red areas were defined as the coseismic rupture (brittle rupture) areas, and only the coseismic slip in these areas was given. The slip magnitude provided in the simulation is 35 m in the Miyagi segment and 10 m in the Fukushima segment. Only the constant strain condition was considered on the possible slip area (blue area), and any other constraints or boundary conditions were not adopted for evaluating slip behavior in the blue area. (b) Map showing the total coseismic slip on the plate interface. Blue lines indicate slip contours with an interval of 5 m. (c) Map showing surface displacements as the response of the total slip on the plate interface at the onshore and seafloor sites used in this study. Red-enclosed white arrows indicate the calculated displacements. Black arrows indicate the observed coseismic displacements analyzed by the Advanced Rapid Imaging and Analysis team at JPL and Caltech (JPL & Caltech, 2011; ftp://sideshow.jpl.nasa.gov/pub/usrs/ARIA/) for onshore sites and the Japan Coast Guard (Yokota et al., 2018) for seafloor sites.

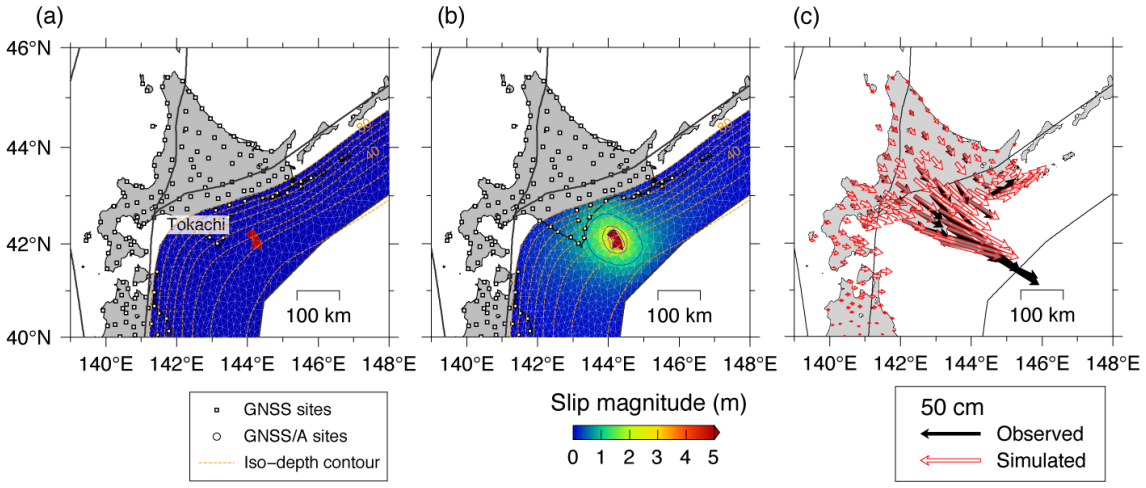

Figure 2.11. Coseismic slip simulation results of the 2003 Tokachi earthquake. (a) Map showing rupture distributions. The red areas were defined as the coseismic rupture (brittle rupture) areas, and only the coseismic slip in these areas was given. The slip magnitude provided in the simulation is 5 m in the coseismic rupture area. As same as the case of the coseismic slip simulation of the 2011 Tohoku earthquake, only the constant strain condition was considered on the possible slip area (blue area), and any other constraints or boundary conditions were not adopted for the slip behavior on the blue area. (b) Map showing the total coseismic slip on the plate interface. Blue lines indicate slip contours with an interval of 1 m. (c) Map showing the surface displacements as the response of the total slip on the plate interface at the onshore and seafloor sites used in this study. Red-enclosed white arrows indicate the calculated displacements. Black arrows indicate the observed coseismic displacements (Larson & Miyazaki, 2008).

2.4.3. Comparison with strong motion generation areas

Large earthquakes can generate seismic waves causing a strong ground motion. The radiation source of the seismic wave causing strong ground motions is called strong motion generation area (SMGA; e.g., Miyake et al., 2003). Because strong ground motion can cause significant damage, mainly to infrastructure (Kanda et al., 2004; Kawase, 1998; Nozu et al., 2012), it is important to reveal the spatial relationship between mechanical locking distributions and SMGAs for earthquake disaster prevention and mitigation efforts.

Figure 2.12 shows the SMGAs of the 2003 Tokachi Earthquake and 2011 Tohoku Earthquake. The 2003 Tokachi Earthquake was the first interplate earthquake observed by K-net and KiK-net, which are dense strong motion seismogram networks (Aoi et al., 2000; Kinoshita, 1998). The 2011 Tohoku Earthquake was the largest interplate earthquake recorded by these networks. In the Tohoku region, most SMGAs were located near the edges of the mechanical locking zones estimated in this study. Furthermore, most SMGAs tend to be concentrated at the down-dip side of the mechanical locking zones. Some SMGAs are distributed some distance away from the edges of the mechanical locking zones. However, considering the estimation errors of the mechanical locking distributions near Fukushima, most are likely also located at the edges of the mechanical locking zones. Near Tokachi, half of the SMGAs were located near the edge of the mechanical locking zone. The other half were located approximately 50–70 km west and north of the mechanical locking zone. As discussed in Chapter 2.4.2, there may be small, hidden mechanical locking zones to the west (or WNW) of the estimated mechanical locking zones along the Kuril Trench. Hence, the SMGAs located approximately 50–70 km west and north of the mechanical locking zone estimated along the Kuril Trench may be related to the hidden mechanical locking zones, although this supposition was not provable in this study.

From the comparisons presented above, it is expected that SMGA candidates for megathrust earthquakes can be predicted from mechanical locking distributions estimated from interseismic geodetic observation data using the proposed model. There may be a predictable limitation depending on the size of mechanical locking zones. As in the case of Tokachi, although the possible seismic moment released by the earthquake is sufficiently large (i.e., $M \geq 8$), SMGA candidates are not predictable if the mechanical locking zones cannot be estimated owing to the poor resolution.

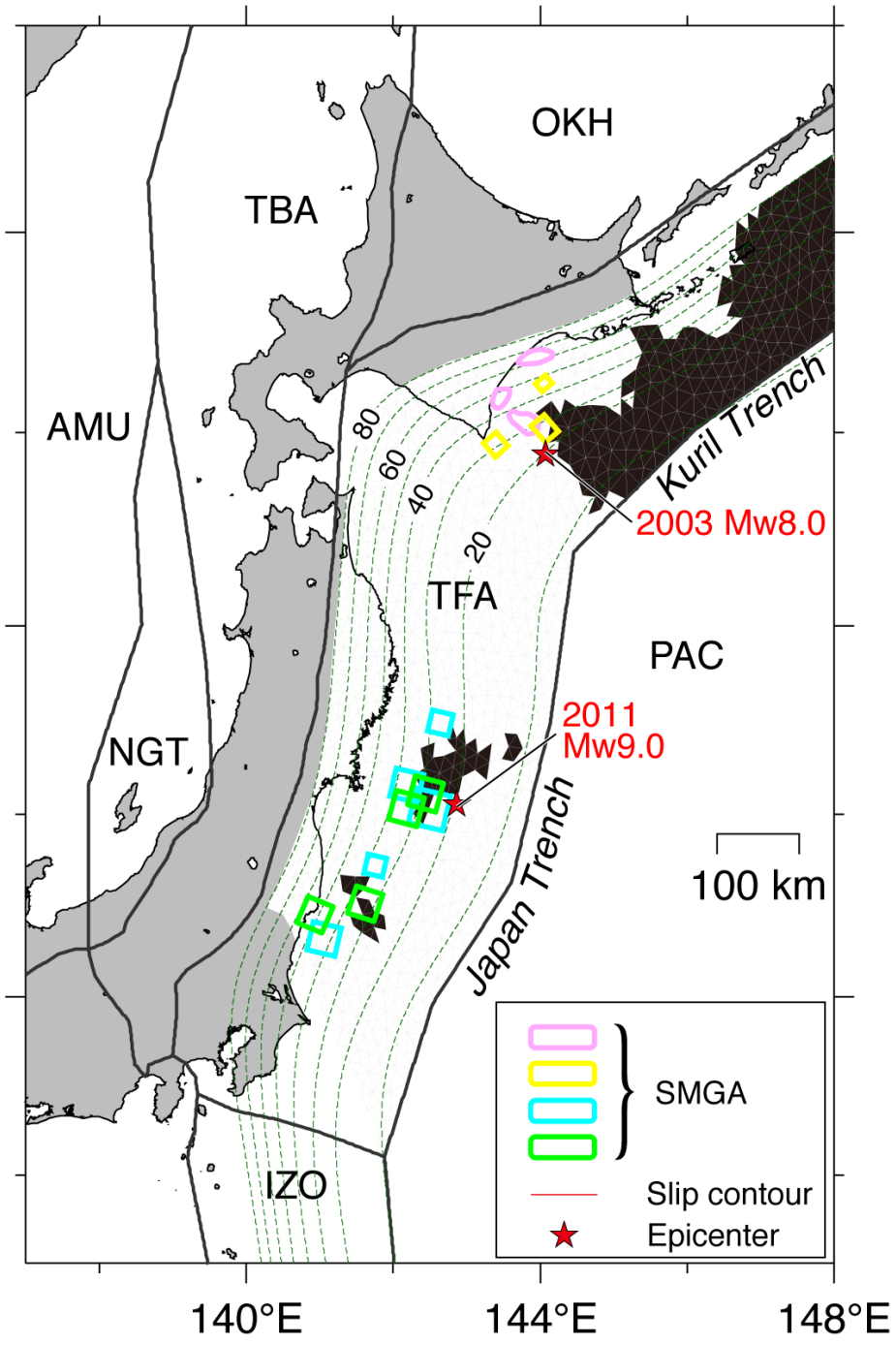

Figure 2.12. Map showing the spatial relationship between mechanical locking zones and SMGAs. Black meshes indicate the estimated mechanical locking zone shown in Figure 2.8(a). Pink and yellow closed lines indicate the SMGAs of the *Mw* 8.0 earthquake in 2003 estimated by Nozu & Irikura (2008) and Kamae & Kawabe (2004), respectively. Cyan and green closed lines indicate the SMGAs of the *Mw* 9.0 earthquake in 2011 estimated by Kurahashi & Irikura (2013) and Asano & Iwata (2012). Red stars indicate the epicenters of the two earthquakes.

2.4.4. Effects of plate interface geometries

The plate interface geometry at the Kuril and Japan trenches used in this study was taken from Iwasaki et al. (2015). Several plate geometry models of the Kuril and Japan Trench subduction zones exist (Hashimoto et al., 2004; Hayes et al., 2018; Hirose et al., 2008; Kita et al., 2010; Nakajima et al., 2009; Nakajima & Hasegawa, 2006), and plate geometry is considered a central factor affecting mechanical locking estimation. To verify this, mechanical locking distributions were estimated using two plate geometry models: "Model I" (Iwasaki et al., 2015) and "Model H" (Hirose et al., 2008; Kita et al., 2010; Nakajima et al., 2009; Nakajima & Hasegawa, 2006). The plate geometry comparison is shown in Figure 2.13(a). Although large geometries are almost equivalent between the models, there are some small-scale difference in the geometry as follows: the depths of the plate interface are deeper for Model H than that for Model I at depths shallower than 20 km; clear unevenness off southern Hokkaido was observed for Model H, whereas the iso-depth contours are smooth for Model I.

Estimated mechanical locking distributions using the two geometries are shown in Figure 2.13(b and c). The locking distributions off Tohoku and Hokkaido were fairly similar to those estimated using Model I. Although there are slight differences in the shape or location of the estimated mechanical locking along the Kuril Trench, these differences are negligible considering the resolution.

The comparison indicates that differences in plate interface geometries do not affect the estimation of mechanical locking distributions if the difference in plate interface geometry is significant, such as those between Model H and Model I. In other words, to reduce the uncertainties of estimated mechanical locking distributions owing to uncertainties of plate interface geometries, it may be required to apply well-determined plate interface geometries such as subduction zones in and around Japan. Thus, enhancing

the geodetic observation network, developing a more realistic physical model describing crustal deformation, and determining the accurate geometries of plate interfaces by robust and accurate geophysical surveys may be useful for reducing estimation uncertainty for mechanical locking distributions.

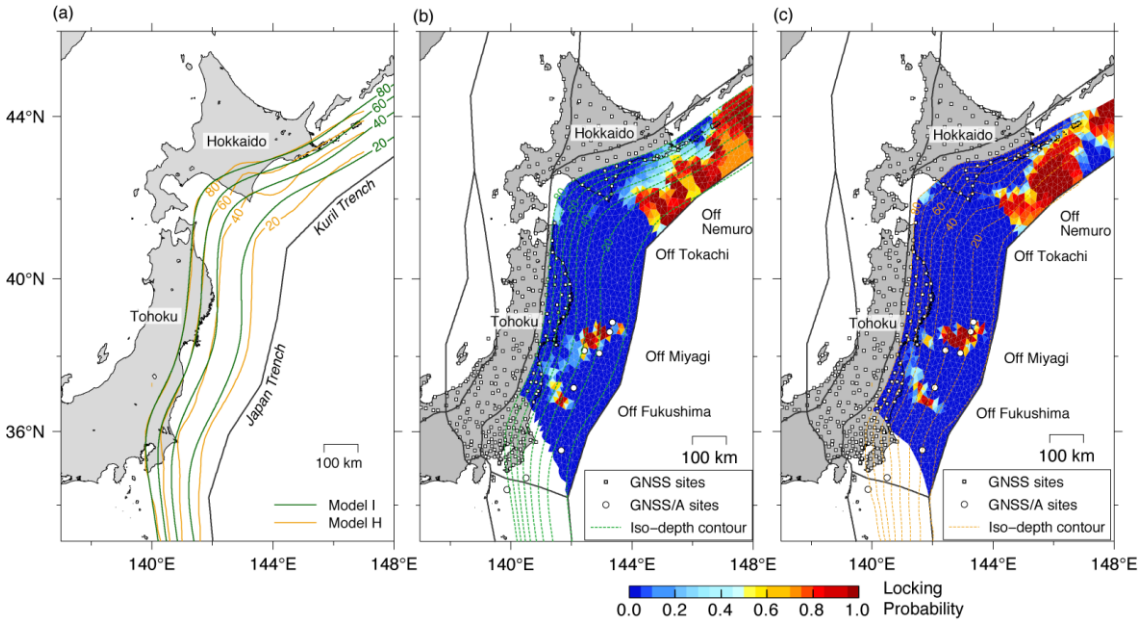

Figure 2.13. Comparison of mechanical locking distributions between two plate geometry models. (a) Map showing iso-depth contours of "Model I" (green lines; Iwasaki et al., 2015) and "Model H" (orange lines; Hirose et al., 2008; Kita et al., 2010; Nakajima et al., 2009; Nakajima & Hasegawa, 2006). The contour interval is 20 km in depth. (b) Map showing the mechanical locking distributions expressed as the locking probability estimated using Model I. (c) Same as (b) but using Model H.

2.4.5. Effects of block division models

The block division model used in this analysis contains 7 rigid blocks (Chapter 2.2.4). To test how simplifying the block division configuration affected mechanical locking distribution estimates, an additional block division model was developed (Figure 2.14). The additional block division model, “Model S,” contains 4 rigid blocks and is roughly equivalent to the PB2003 model (Bird, 2003; Figure 2.14b and d). Hereinafter, the original block division model used in the main analysis is called “Model O” for convenience.

The estimated mechanical locking distributions of Models O and S are shown in Figure 2.14(a) and (b), respectively. Two mechanically locked segments were estimated in the Miyagi and Fukushima regions in Model S. The locations and sizes of these locking segments in Model S were almost equal to that of locking segments offshore Miyagi and Fukushima estimated in Model O. One mechanically locked segment was estimated at the region off eastern Hokkaido. While the detailed location and size of the locking segment in Model S differed slightly from that of the locking segment in the region offshore eastern Hokkaido estimated in Model O, particularly at the easternmost part of off Nemuro, this disagreement is negligible if considering the low-resolution data available. Hence, Models O and S produce similar mechanical locking distributions. Regarding the residuals, differences between observed and calculated surface displacement rates in Model S were relatively larger than that estimated in Model O (Figure 2.14c and d). Particularly, there are notably larger and systematic residuals in Nemuro and Niigata in Model S, whereas almost no large and systematic residuals exist in Nemuro and Niigata in Model O. These residuals in Model S seem to vanish at the region where block boundaries were set in Model O (i.e., block boundaries between Niigata and Tohoku-backarc blocks and between Tohoku-forearc block and Okhotsk

plate). Thus, these residuals may have been caused by block configurations and imply the requirement of additional block boundaries in Model S, such as those set in Model O. The estimated mechanical locking distributions might have been biased if the rigid motion could not be distinguished from crustal deformation (i.e., if there are systematic residuals due to inappropriate block configurations). Thus, there is a possibility that the estimated mechanical locking distributions in Model S was biased owing to the lack of block boundaries, although the mechanical locking distributions estimated in Model S was similar to that estimated in Model O. As a consequence, Model O is considered to exhibit better performance than Model S.

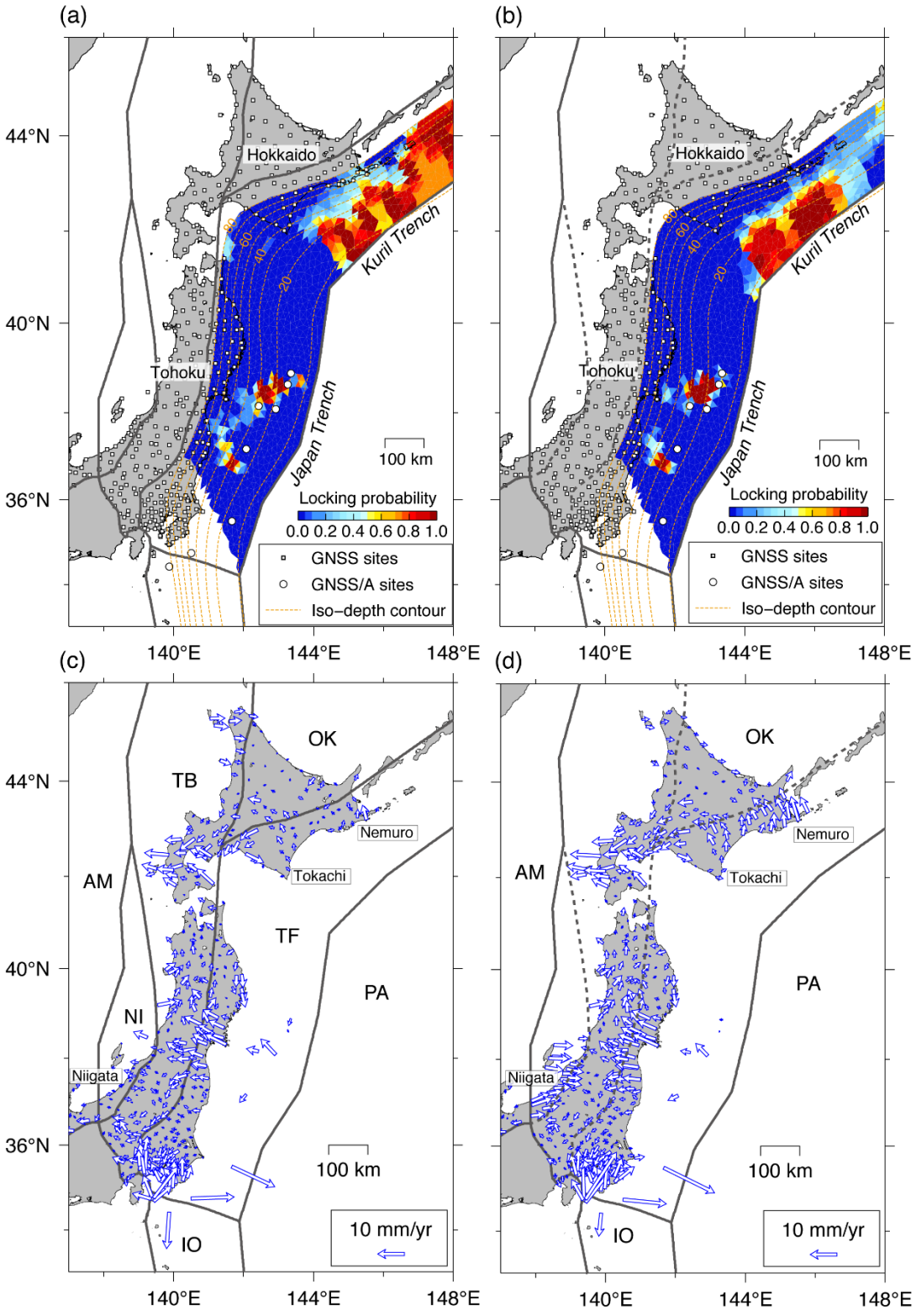

Figure 2.14. Comparison of mechanical locking distributions and residual vectors for Models O and S. (a) Map showing the mechanical locking distributions estimated in

Model O, which is the original block division model used in the main analyses and contains 7 blocks. Background color scale indicates the locking probability. Gray solid lines indicate block boundaries. (b) Same as (a) but for Model S, which is an additional block division model and contains 4 blocks. Gray dashed lines indicate the block boundaries existing in Model O but not in Model S. (c) Map showing residual vectors between observed and calculated displacement rates (observation minus calculation) for Model O. (d) Same as (c) but for Model S.

2.5. Chapter summary

The proposed model, which relates mechanical locking on the plate interface and surface crustal deformation, was discussed in this chapter. This model was applied to northeast Japan to estimate mechanical locking distributions along the Japan and Kuril Trenches based on the onshore and seafloor geodetic observation data by incorporating the REMC method.

Estimated mechanical locking distributions were compared with coseismic (postseismic) slip distributions, hypocenters, and SMGAs of the 2003 Tokachi Earthquake and 2001 Tohoku Earthquake. After comparison, the following conclusions were obtained.

- The mechanical locking zones were estimated in the region where high slip deficit rates were estimated by pure kinematic model in previous studies. Slip deficits accompanied by mechanical locking can explain the high-slip deficit rates estimated by previous studies in regions where creeping was estimated without estimated mechanical locking in this study.
- The mechanical locking zone is notably smaller than total coseismic slip areas. The coseismic slips can, therefore, occur not only in mechanical locked zones but also outside the zones accompanied by the rupture of mechanical locking zones.
- Postseismic slip may occur in the regions where the interseismic slip deficits are

induced by mechanical locking, and the seismic moment cannot be completely released by the coseismic slip.

- SMGAs tend to be located at the edges of mechanical locking zones.

Chapter 3
Interplate mechanical locking distributions along the Nankai Trough estimated by the proposed model

3.1. Introduction

In this chapter, the results of applying the proposed model reported in the previous chapter to southwest Japan for estimating mechanical locking distributions along the Nankai Trough are outlined and discussed.

Nankai Trough is the subduction zone where the Philippine Sea Plate subducts beneath the overriding plates such as Amurian and/or Okinawa plate with the convergence rate of 5–6 cm/yr (DeMets et al., 2010). Due to the plate subduction and possible interplate mechanical locking, megathrust earthquakes with > M 8 have repeatedly occurred along the Nankai Trough, and ground shaking and tsunamis following earthquakes have caused significant damages in southwest Japan (Ando, 1975; Garrett et al., 2016). The most recent significant events were the M 7.9 Tonankai Earthquake that occurred in 1944 at Kumano basin and the M 8.0 Nankai Earthquake that occurred in 1946 off Shikoku and extended to the southern Kii peninsula.

Recently, the seafloor GNSS/A observation network has been developed along the Nankai Trough by the Japan Coast Guard and Nagoya University (Tadokoro et al., 2012; Yokota et al., 2018) as well as GEONET; the crustal displacement field including onshore and seafloor can be derived from these observations. The estimation of interplate kinematic coupling distributions using combined onshore and seafloor geodetic observations have been achieved by several studies (Kimura et al., 2019; Nishimura et al., 2018; Watanabe et al., 2018; Yokota et al., 2016). Yokota et al. (2016) first estimated the

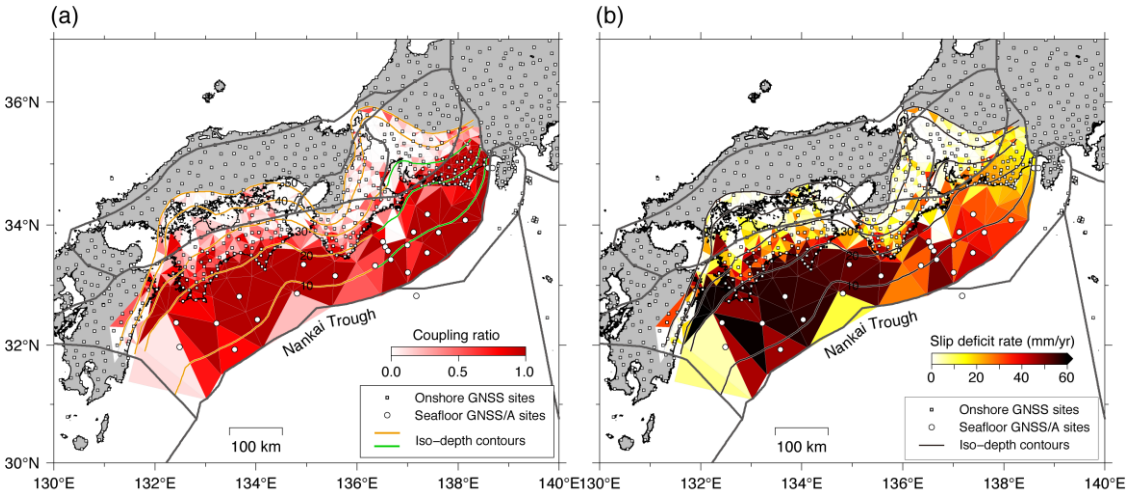

Figure 3.1. Interplate coupling estimated by Kimura et al. (2019). Squares and circles indicate the onshore GNSS and seafloor GNSS/A observation sites, respectively. (a) Map showing the coupling distributions, expressed as coupling coefficient (background color scale). Orange and green lines indicate the iso-depth contours. (b) Map showing the slip deficit rate distribution (background color scale). Black lines on the plate interface indicate the iso-depth contours.

interplate kinematic coupling distributions along the Nankai Trough using the seafloor GNSS/A and coastal GNSS observation data. They revealed the heterogeneity of the coupling distributions both along dip and strike and the strong coupling at the trough axis off Shikoku. Nishimura et al. (2018) and Watanabe et al. (2018) considered the block motion of southwest Japan to distinguish the rigid motion effect from the observed crustal deformation and estimated the kinematic coupling distributions along the Nankai and Sagami Troughs using the onshore GNSS and seafloor GNSS/A observation data. These three previous studies did not optimize the spatial heterogeneity of the uncertainties of kinematic coupling estimates and estimated the coupling coefficient with a smoothing operation. Thus, the kinematic coupling distributions near the trough axis were not reliable. To overcome this problem, Kimura et al. (2019) optimized the spatial heterogeneity of the uncertainties of kinematic coupling estimates by adjusting the

subfault sizes; adjustment was performed by minimizing the objective function that was based on the modified normalized covariance. Then, Kimura et al. (2019) estimated the kinematic coupling distribution along the Nankai Trough considering the block motion on the basis of onshore GNSS and seafloor GNSS/A observational data using the MCMC method (Figure 3.1). As a consequence, the following features were found: along-dip and along-strike heterogeneity of the interplate coupling, as suggested by Yokota et al. (2016); full coupling at the trough axis of off Shikoku and off Tokai regions, implying the possibility of giant tsunami-genesis accompanied by the coseismic slip at the shallowest portion of the plate interface during forthcoming earthquakes, such as the 2011 Tohoku Earthquake; spatial contrast in slip deficit rates between the eastern and western parts along the trough axis was observed due to the difference in convergence rates of incoming plates.

As described above, the interplate kinematic coupling or slip deficit rate distributions along the Nankai Trough have been revealed recently. However, previous studies only derived kinematic conditions on the plate interface, which are the same as in the case of northeast Japan, and the mechanical conditions could not be known from the estimated coupling distributions (Kimura et al., 2019; Nishimura et al., 2018; Watanabe et al., 2018; Yokota et al., 2016). Thus, I applied the proposed model (detailed in Chapter 2.2) to southwest Japan. The results are compared with kinematic coupling distributions estimated by Kimura et al. (2019), coseismic slip distributions, hypocenters, SMGAs of Showa Nankai Trough earthquakes (1944 Tonankai Earthquake and 1946 Nankai Earthquake), slow earthquake distributions, and subducted topographic features along the Nankai Trough.

3.2. Methods and data

3.2.1. Configuration of replica exchange Monte Carlo Sampling

I employed the proposed model and REMC method described in Chapter 2 to southwest Japan. A priori distributions are almost equal to those defined in Chapter 2.2.2. Because the model region depths are from 0 km (corresponding to the depth of trough) to 60 km, z_{W} is 60 km. The initial conditions of the Euler vectors, internal block strain rate, and coupling coefficients were determined following the method outlined in Chapter 2.2.2. The initial z_{up} and z_{down} are uniquely distributed random values ranging from 0 to 60 km that are consistent with the model region depth range. The number of iterations and number of chains are 2.06×10^{6} and 10, respectively. The temperature of the i-th chain was defined as $T_{\mathrm{i}} = 1.67^{\mathrm{i}-1}$, so that $T_{10} = 100$. the samples from the first to 10% of the total iteration were rejected as a burn-in. The calculation software and the computer were the same as in Chapter 2.2.2.

3.2.2. Crustal deformation data in southwest Japan

The displacement rates of onshore GNSS and seafloor GNSS/A observation sites in southwest Japan are described in this section. The dataset consist of displacement rates obtained from the F3 daily coordinate data at GEONET observation sites that are provided by GSI (862 sites), displacement rates obtained by campaign observations at ZENISU that is located at Zenisu Reef at southwest and ~50 km far from Kozu Island and conducted by Nagoya and Kochi Universities, previously published displacement rates obtained by campaign GNSS/A observations at seafloor sites conducted by Nagoya

University[1] and Japan Coast Guard (24 sites; Kimura et al., 2019; Yasuda et al., 2017; Yokota et al., 2016). The displacement rates of GEONET sites were obtained by following the data processing procedure described in Chapter 2.2.3, whereas those of the ZENISU site were obtained by linear regression because the campaign observations were conducted once per year; thus, the temporal resolution is too poor to detect annual and semi-annual displacements. In total, 887 sites were used in this evaluation.

The data periods are from August 2006 to December 2009 for GEONET site data, 2005 to 2010 for ZENISU site data, 2004 to 2016 for seafloor GNSS/A site data from Nagoya University (Kimura et al., 2019; Yasuda et al., 2017), and 2006 to 2015 for the seafloor GNSS/A site data of the Japan Coast Guard (Yokota et al., 2016). No major earthquakes occurred during the data period of GEONET sites. Although two intraplate earthquakes of Mj (Japan Meteorological Agency [JMA] magnitude) 7.1 and 7.4 occurred in 2004 near the trough axis southeast of the Kii peninsula, the calculated postseismic displacements of only few millimeters at the nearest seafloor site (Suito, 2017b) did not affect the REMC inversion of mechanical locking distributions, considering the observation accuracy of seafloor GNSS/A observation sites. Thus, coseismic and/or postseismic displacement were not corrected. The offset and postseismic displacement of the 2011 Tohoku Earthquake were already removed by previous studies (Yasuda et al., 2017; Yokota et al., 2016), and the seafloor GNSS/A data are assumed to exhibit a constant interseismic displacement rate.

Mean displacement rate uncertainties were 0.1 (EW), 0.1 (NS), and 0.3 mm/yr (UD) for GEONET sites, 12 (EW), 4 (NS), and 7 mm/yr (UD) for the ZENISU site, 10 (EW) and 10 mm/yr (NS) for the seafloor GNSS/A sites from Nagoya University, and 4 (EW)

[1] Seafloor GNSS/A observations performed by Nagoya and Tohoku Universities are shown with green vectors in Figure 3.2

and 4 mm/yr (NS) for the seafloor GNSS/A sites from the Japan Coast guard. Note that this study used three components (EW, NS, and UD) for GEONET and ZENISU sites but two components (EW and NS) for seafloor GNSS/A site data because the UD component of the positioning accuracy of the GNSS/A observations is significantly poor. All displacement rates were translated from the International Reference Frame (ITRF) 2005 to Amurian plate reference frame using the Euler vectors of the MORVEL plate motion model (DeMets et al., 2010; Figure 3.2; Table C.2).

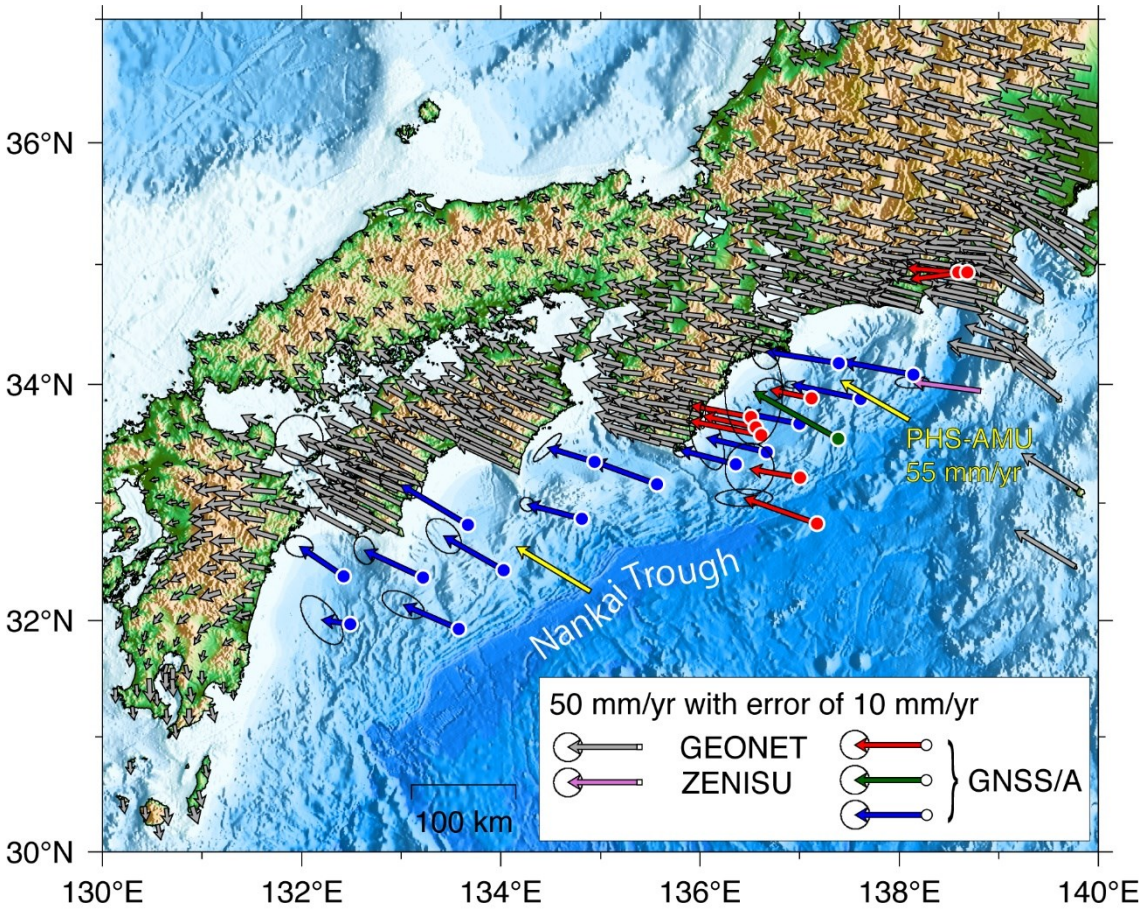

Figure 3.2. Map showing displacement rate vectors used. Gray and purple vectors represent the displacement rate vectors of GEONET and ZENISU. Red, green, and blue vectors represent the displacement rate vectors of seafloor GNSS/A site obtained by Nagoya University, Nagoya and Tohoku Universities (shared site), and the Japan Coast Guard. Yellow vectors show the Philippine Sea (PHS) plate motion relative to the Amurian (AMU) plate calculated on the basis of the MORVEL plate motion model (DeMets et al., 2010). Color scale of the map represents the elevation and bathymetry of SRTM30_PLUS (Becker et al., 2009).

3.2.3. Block boundaries

Southwest Japan spans six plates: the Philippine Sea, Pacific, Okhotsk (North America), Amurian, Okinawa, and Yangtze Plates (Bird, 2003). The Pacific Plate subducts beneath the Philippine Sea and Okhotsk Plates along the Izu–Ogasawara and Japan Trenches, respectively. Philippine Sea Plate subducts beneath the Amurian and Okinawa Plates along the Nankai Trough and Ryukyu (Nansei–Shoto) Trench, respectively. The convergence rate along the Nankai Trough is approximately 5–6 cm/yr based on the MORVEL plate model (DeMets et al., 2010). On the regional scale, the tectonic boundaries of the Amurian Plate are indicated in Figure 3.3. The Median Tectonic Line, extending from western Shikoku to Tokai, is considered to participate in strain partitioning due to the oblique subduction of Philippine Sea Plate along the Nankai Trough (Nishimura et al., 2018; Tabei et al., 2002, 2003). In the western part of the Median Tectonic Line, a right lateral (strike slip) motion of ~5 mm/yr has been estimated from dense onshore GPS observations (Tabei et al., 2002, 2003). The dip angle of the faults has been estimated to be ~30° N. The NKTZ is considered to be a wide shear zone of ~100 km in width based on GPS observations (Sagiya et al., 2000). The North Chugoku Shear Zone (NCSZ), sometimes called the San-in shear zone, is considered to young (Gutscher & Lallemand, 1999; Nishimura & Takada, 2017). Whereas no clear fault zone along the shear zone was found by trenching surveys or geophysical exploration, numerous intraplate earthquakes with a range of seismic magnitudes have been repeatedly observed along the shear zone. The Beppu–Shimabara Graben crosses central Kyushu in the ENE–ESE orientation; it is considered part of the Okinawa Trough, which is a back-arc basin formed by extension within the continental lithosphere that causes the NS extension field in central Kyushu (Tada, 1985). The Zenisu ridge, located at southeast of Nankai Trough with a strike that is roughly parallel to the Nankai Trough axis, was

considered to play an important role in subduction and sliding to the east of the Nankai Trough (Mazzotti et al., 1999, 2001), although the strain condition has not been revealed owing to the lack of available seismic and geodetic observational data.

Based on the global and regional tectonic settings described above, the crust of southwest Japan can be divided into several rigid blocks. In this study, the block division configuration was performed following Kimura et al. (2019) in which the optimum block division configuration were selected on the basis of the Akaike Information Criteria (AIC; Akaike, 1980) value. The optimum block configuration presented by Kimura et al. (2019) contains 12 blocks. In this study, I divided the Okinawa Plate, which is southwest of the Nankai block, into two independent blocks, Okinawa-North and Okinawa-South, to define the horizontal range in which the mechanical locking distributions are estimated. In total, 13 blocks were set in southwest Japan. This revision does not affect the mechanical locking estimations along the Nankai Trough because these two redefined blocks are sufficiently far from the main target region. The block boundaries in southwest Japan used in the present study are shown in Figure 3.4**3.5**.

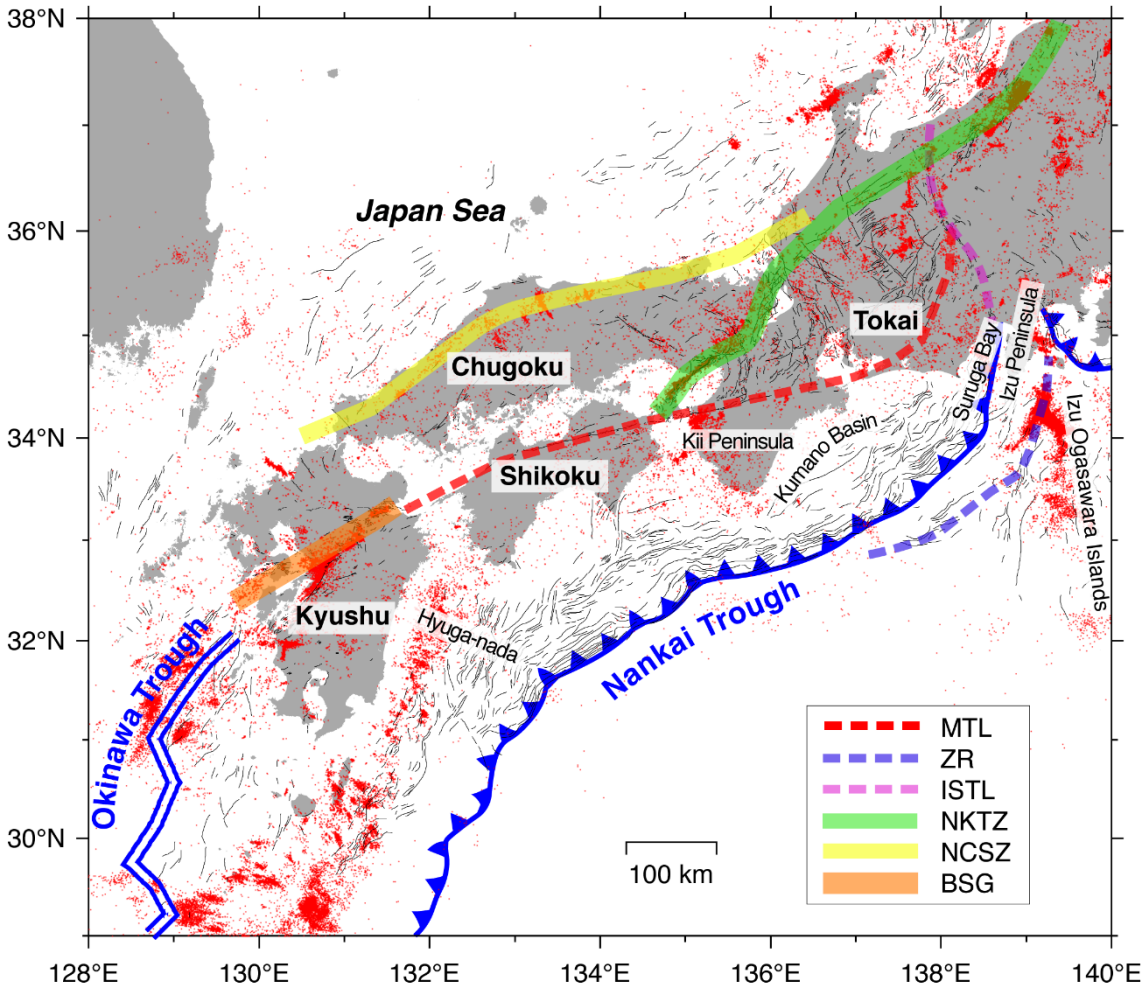

Figure 3.3. Map showing tectonic settings of southwest Japan. Black lines, red dots, and solid or dashed lines show active fault trace lines (Nakata & Imaizumi, 2002), epicenters of ordinary earthquakes, and major tectonic structures (line or zone), respectively. The detected period and magnitude range of plotted earthquakes are 1994–2016 and $Mw \geq 2$, respectively. MTL, Median Tectonic Line; ZR, Zenisu Ridge; ISTL, Itoigawa–Shizuoka Tectonic Line; NKTZ, North Chugoku Shear Zone (San-in shear zone); BSG, Beppu-Shimabara Graben.

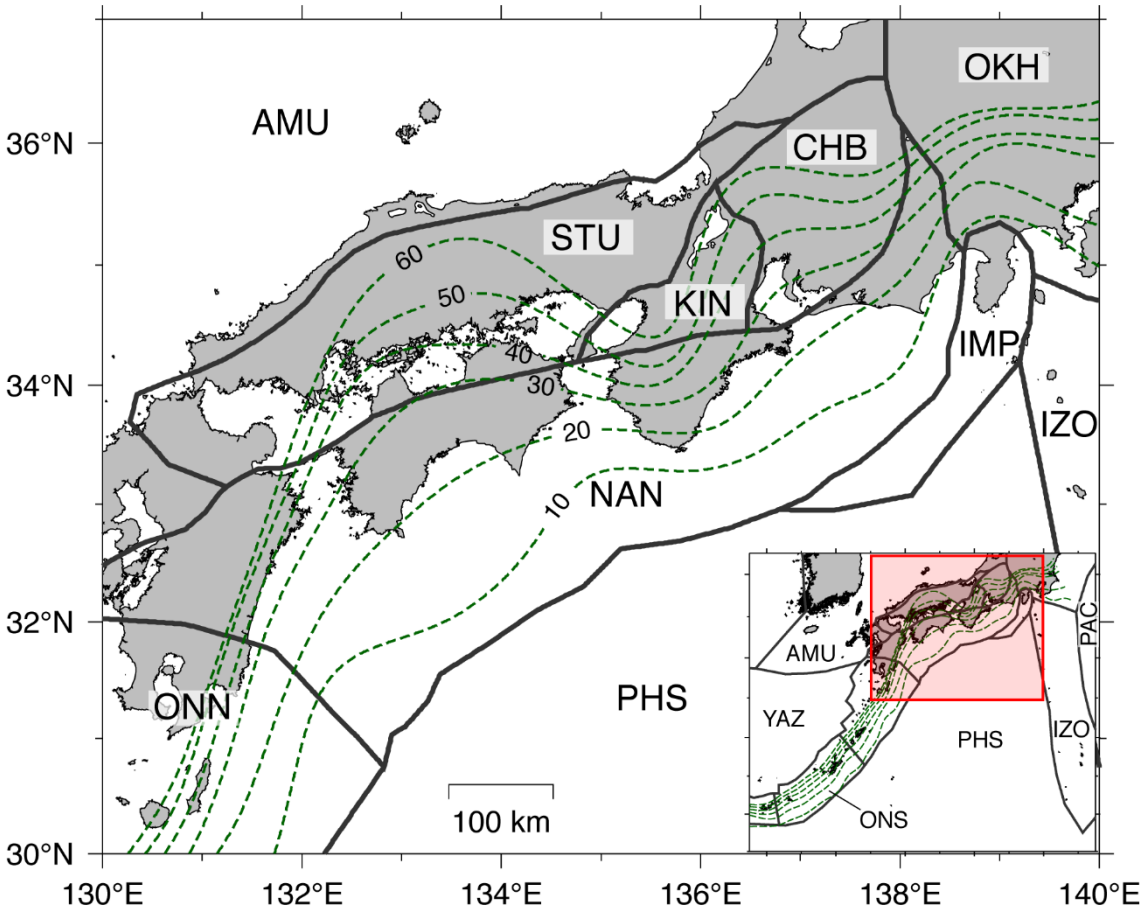

Figure 3.4. Map showing the block boundaries (black bold lines). Abbreviations indicate block names: AMU, Amurian plate; OKH, Okhotsk plate; YAZ, Yangtze plate; ONN, Okinawa-North block; ONS, Okinawa-South block; KIN, Kinki block; CHB, Chubu block; STU, Setouchi block; NAN, Nankai block; IMP, Izu Micro Plate; IZO, Izu Ogasawara block; PHS, Philippine Sea Plate; PAC, Pacific Plate. Green dashed lines indicates the iso-depth contours of subducting plate interfaces (Iwasaki et al., 2015). The small map shown at right-bottom in the map represents the entire model region. The red-hatched region in the small map was focused on in this chapter.

3.2.4. Interface geometries of block boundaries and subducting plates

A combination of subfaults was set on the subducting Philippine Sea Plate interface based on the plate geometry model compiled by Iwasaki et al. (2015). Triangular meshes were adopted for the subfault because triangles can express curved surfaces, such as subducting plate interfaces, more easily than rectangles. The length of the subfault on the plate interface is approximately 20 km in the main target region, 31–36° N and 132–139 ° E. The depth range is from the trough axis to 60 km. It is not necessary to adjust the size because the slip deficit rate on each subfault is not a model parameter; Kimura et al. (2019) adjusted the size of the subfault in the main target region by minimizing the variances of the objective function composed of Green's functions. Although I additionally generated a set of triangular subfaults on the plate interface along the Ryukyu, Sagami, Japan, and Izu–Ogasawara Trenches, their mean lengths are larger (approximately 50–90 km) compared to that of the main target region to decrease the calculation cost because these regions were not the focus of this study. The triangular subfaults are also generated on inland block boundaries. The dip angle of the subfaults is vertical at most block boundaries. Non-vertical subfaults were generated along the following inland block boundaries as an exception: ~30° north-dipping subfaults along the Median Tectonic Line (the block boundary between Nankai and Setouchi blocks) referred to Tabei et al. (2002, 2003); ~70° west-dipping subfaults along the West Sagami Bay Fracture (block boundary between Izu Micro Plate and Izu–Ogasawara block) referred to Koyama (1995); and ~25° north-dipping subfaults along the Zenisu ridge (block boundary between Philippine Sea and Izu Micro Plates) referred toLallemant et al. (1989). The mechanical locking distributions are estimated along the northern most part of Ryukyu Trench (plate interface between Philippine Sea Plate and North-Okinawa block), colliding zone of Izu peninsula (block boundary between Izu Micro and Okhotsk

plates), and Sagami Trough (plate interface between Izu–Ogasawara block and Okhotsk Plate), as well as along the Nankai Trough to avoid abrupt changes in boundary conditions at the eastern and western edges of the Nankai Trough. The coupling coefficients are estimated along the other subduction zones and block boundaries. The three-dimensional mapping of subfaults on the plate interface and block boundaries are shown in Figure 3.5(a). The z_{up} and z_{down} along the Nankai Trough were sampled along the pink lines shown in Figure 3.5(b).

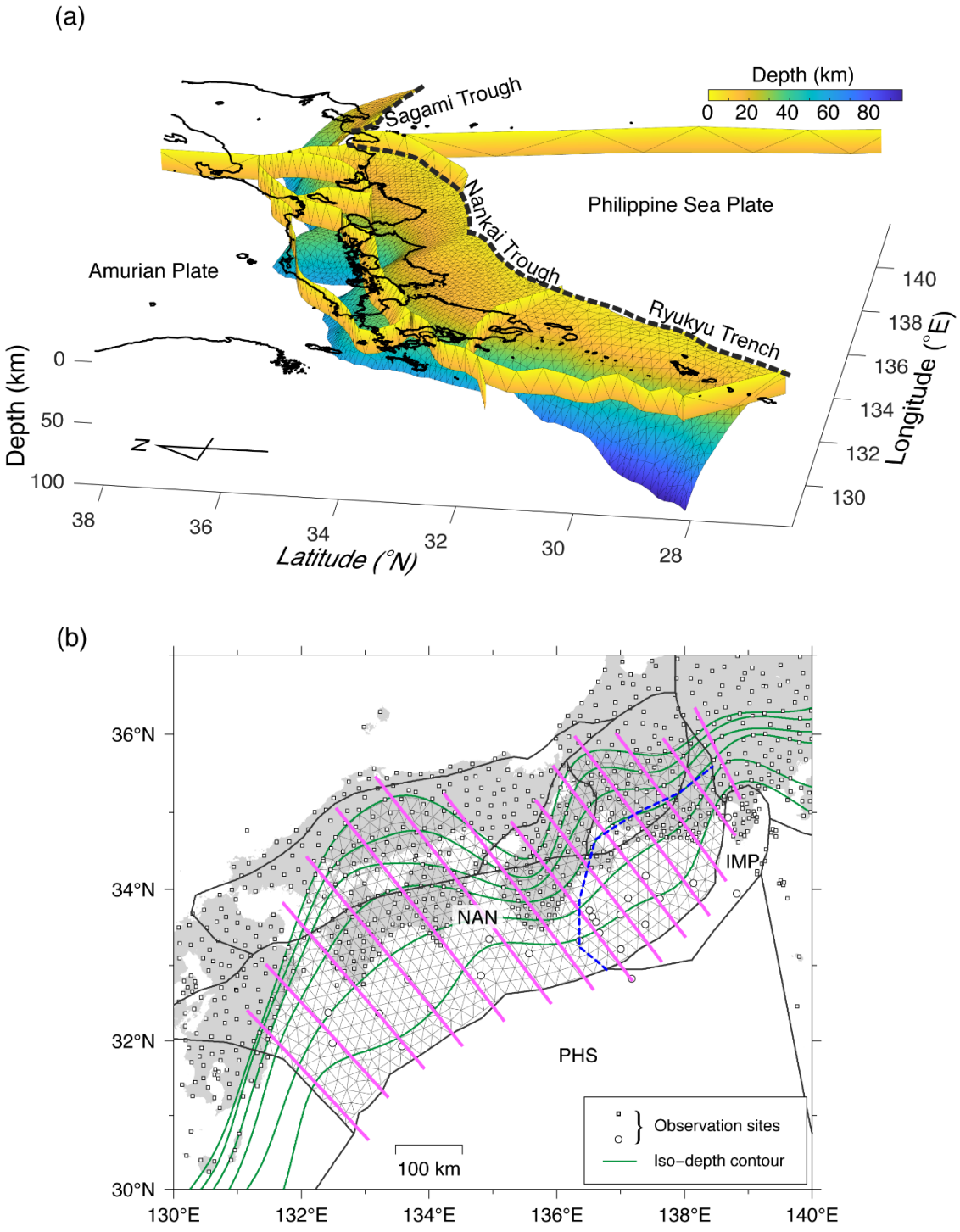

Figure 3.5. Interface geometries of block boundaries and subducting plates. (a) The three-dimensional map showing the interfaces of blocks and subducting plates. This map shows the WSW orientation. Triangular meshes on the interface are subfaults. The geometry of the subducting plate interface was taken from Iwasaki et al. (2015). The color scale

indicates the interface depths. Black solid and dashed lines represent coast lines and trough axes. (b) Map showing subfaults (gray triangles) on the plate interface along the Nankai Trough. Green lines indicate iso-depth contours of the upper surfaces of the subducting plate interfaces, with a depth interval of 10 km starting from 10 km in depth. Blue dashed line indicates the boundary of the plate interface. The lower surface of the overriding Nankai block is contacting with the upper surface of the subducting Philippine Sea Plate at the west and north of the line, whereas it is contacting with the upper surface of the subducting Izu Micro Plate at the east and south of the line.

3.3. Estimated mechanical locking distributions and slip deficit rates

The results mainly focused on the mechanical locking distributions estimated on the plate interface along the Nankai Trough. The results of the rigid block motion (Euler vectors) and block internal strain rates are summarized in the appendix section. Figure 3.6 shows the estimated mechanical locking distributions along the Nankai Trough. The color scale indicates the locking probability derived from Equation (29). Figure 3.7 shows the typical examples of PDFs of the up-and down-dip depth limits and the locking probability calculated from Equation (29) along the lines of A, B, C, D, E, and F shown in Figure 3.6. It was found that the estimated mechanical locking distributions can be divided into four segments. Hereinafter, the mechanical locking segments are called the Hyuganada, off Shikoku, off Kii, and off Tokai segments from the west to east. The plate interface of the off Shikoku, off Kii, and off Tokai segments were estimated to be mechanically locked at the trench depths, whereas the up-dip limit is ~10 km in depth at the Hyuganada segment. The down-dip limit is heterogeneous among the four locking segments: 60 km in Hyuganada, ~20 km off Shikoku, ~10 km off Kii, and 10–25 km off Tokai.

Some subfaults exhibit low P_l around the subfault with higher P_l (>0.8). The

spreading of the subfaults exhibiting low P_l around those with high P_l is assumed to be a spatial distribution of estimation uncertainties of mechanical locking depths. I quantified the uncertainties by 95 percentile confidence intervals obtained from posterior PDFs (Figure 3.7). PDFs of the down-dip depths of locking zones exhibited single peaks along five lines excluding line A in the Hyuganada segment. PDFs of the up-dip depths are shallower than the trough depths along five lines excluding line A. The 95 percentile confidence intervals of the up- and down-dip depths of the mechanical locking zone along the six lines were 27 (up-dip in A), 32 (down-dip in A), 88 (up-dip in B), 4 (down-dip in B), 32 (up-dip in C), 2 (down-dip in C), 67 (up-dip in D), 12 (down-dip in D), 90 (up-dip in E), 20 (down-dip in E), 99 (up-dip in F), and 12 km (down-dip in F). Large 95 percentile confidence intervals can be seen in up-dip limitation depths at lines B, C, D, E, and F. Moreover, the PDFs of up-dip limitation depths exhibit a flatter shape at depth ranges shallower than trench depths at these lines. The posterior PDFs at the depth ranges outside the model region depths (i.e., shallower than the trench or deeper than the bottom, ~60 km in this study) should be mathematically similar to the prior PDFs at depth ranges outside the model regions depths because the likelihood would not change when the up- or down-dip limitation depths are sampled only at depths outside the model region depths (Equation 17). That is, each depth value, which was sampled as the posterior PDF at depth ranges outside the model region depths, indicates the random value following the prior PDF and has no physical meaning. Therefore, the flattened shape PDF shape of the up-dip limitation depths at lines B, C, D, E, and F imply the sampling from the prior PDF. Moreover, large 95 percentile confidence intervals, which are exhibited in up-dip limitation depths at lines B, C, D, E, and F do not indicate the significant estimation uncertainties of up-dip limitation depths. Note that almost all posterior PDFs were obtained at depth ranges shallower than the trench at lines B, C, D, E, and F, which may

suggest mechanical locking with extremely high probability at the trench, although each depth value itself has no physical meaning. Almost all down-dip limitation depths were sampled inside the model region depths along the six lines. The 95 percentile confidence intervals of down-dip limitation depths vary within ~30 km among the six lines, indicating that the spatial heterogeneity of the 95 percentile confidence intervals of down-dip limitation depths is smaller than that in northeast Japan (Chapter 2.3). This implies that the resolution at the offshore region along the Nankai Trough is more homogeneous than that in northeast Japan. The down-dip limitation depths would be constrained by seafloor GNSS/A observation data as well as by onshore GNSS observation data. The spatial homogeneity of the onshore GNSS observation network in southwest Japan is similar to that in northeast Japan. Conversely, the spatial homogeneity of the seafloor GNSS/A observation network in southwest Japan is much higher than that in northeast Japan. The seafloor GNSS/A sites (24 sites in total) were installed from Suruga Bay to Hyuganada with average spatial intervals of 50–80 km in southwest Japan. However, there were only 8 seafloor GNSS/A observation sites from central to southern Tohoku with average spatial intervals of 60–100 km in northern Japan. No sites are installed from northern Tohoku to Hokkaido. Thus, the resolution could be homogeneously enhanced at the offshore region in southwest Japan, whereas the resolution could be enhanced only at the region where the seafloor GNSS/A network exists (i.e., central to southern Tohoku) in northeast Japan.

The slip deficit rate distributions were calculated (Figure 3.8) from Equation (10) on the basis of the mechanical locking distribution and estimated Euler vectors (Table B.1). In the calculation, I selected the subfault with a locking probability P_l larger than 0.5 as the mechanically locked subfaults. The slip deficit rate contrast can be seen between eastern and western part in the model region (~19 mm/yr in the eastern part and ~52

mm/yr in the western part), because the two individual blocks, with the Philippine Sea Plate in the western part and Izu Micro Plate in the eastern part, subduct beneath the overriding Nankai Forearc block with different convergence rates.

The slip deficit rates on the mechanical locking zone are equivalent to the plate convergence rates (relative block motion rates). Thus, the uncertainties of the slip deficit rate directly reflected by uncertainties of the relative block motion (Euler vectors). To quantitatively confirm these uncertainties, I first plotted the two-dimensional PDF of the Euler vectors of subducting Philippine Sea and Izu Micro Plates relative to the Nankai Forearc block (Figure 3.9). The differences in pole locations of the above two plates relative to the Nankai Forearc block are approximately ~10° in longitude and ~8° in latitude. Both Euler poles were estimated with uncertainties larger in longitude than in latitude. The mean angular velocities of the Euler vectors of the Philippine Sea Plate are approximately four times higher than those of the Izu Micro Plate. The uncertainty of the angular velocity of the Philippine Sea Plate is twice as large as that of the Izu Micro Plate. Figure 3.10 shows the two-dimensional PDF of the relative block motions on the mechanical locking segments in eastern and western parts of the model region. Unimodal Gaussian distribution with uncertainties of 4–5 mm/yr can be seen in PDFs of northern and eastern plate convergence rates both in eastern and western areas (Figure 3.10a, c, d, and f). Moreover, the two-dimensional PDFs exhibit concentric distributions (Figure 3.10b and e). Hence, the uncertainties are almost equal in all orientations, and there is no directivity in plate convergence rate uncertainties.

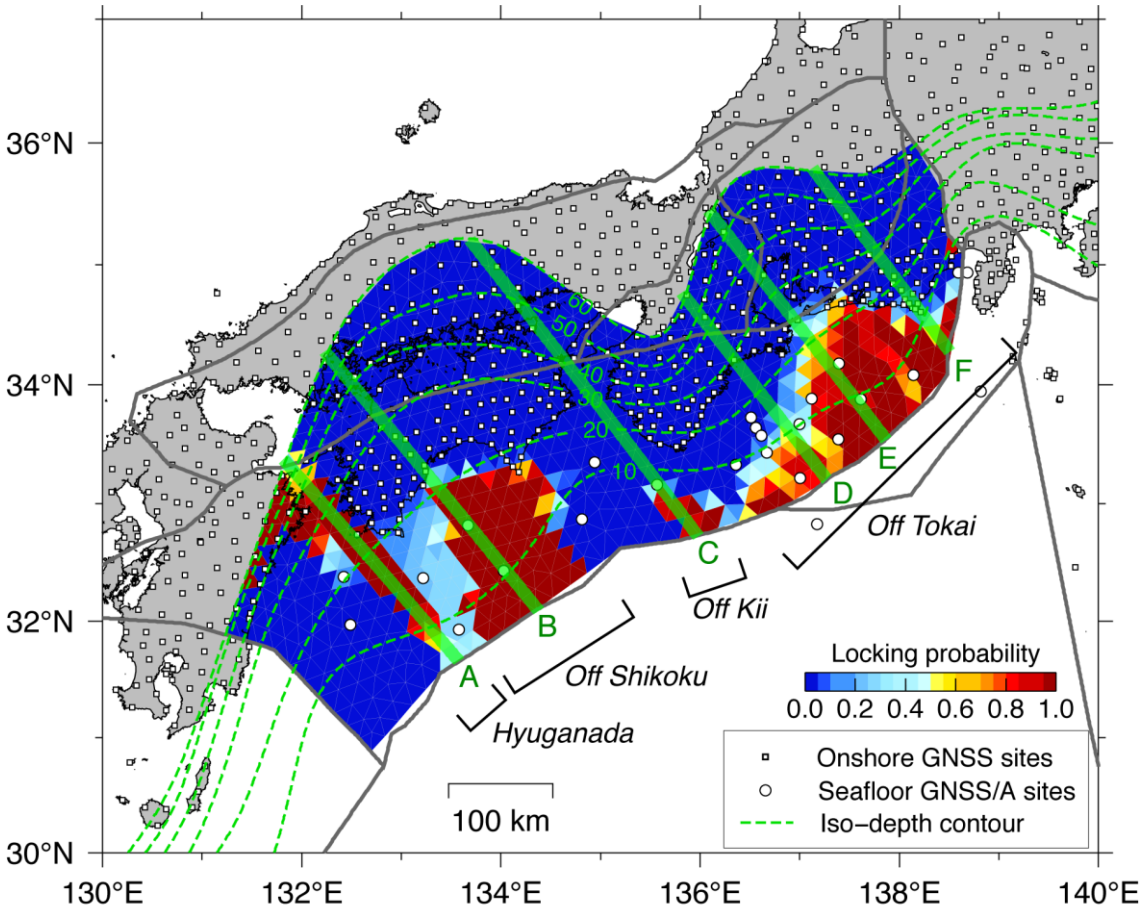

Figure 3.6. Map showing estimated mechanical locking distributions on the plate interface along the Nankai Trough. Background color scale indicates the locking probability of each subfault given by Equation (29). Green dashed lines indicate the iso-depth contours of the subducting plate interface. Names of mechanical locking segment are italicized.

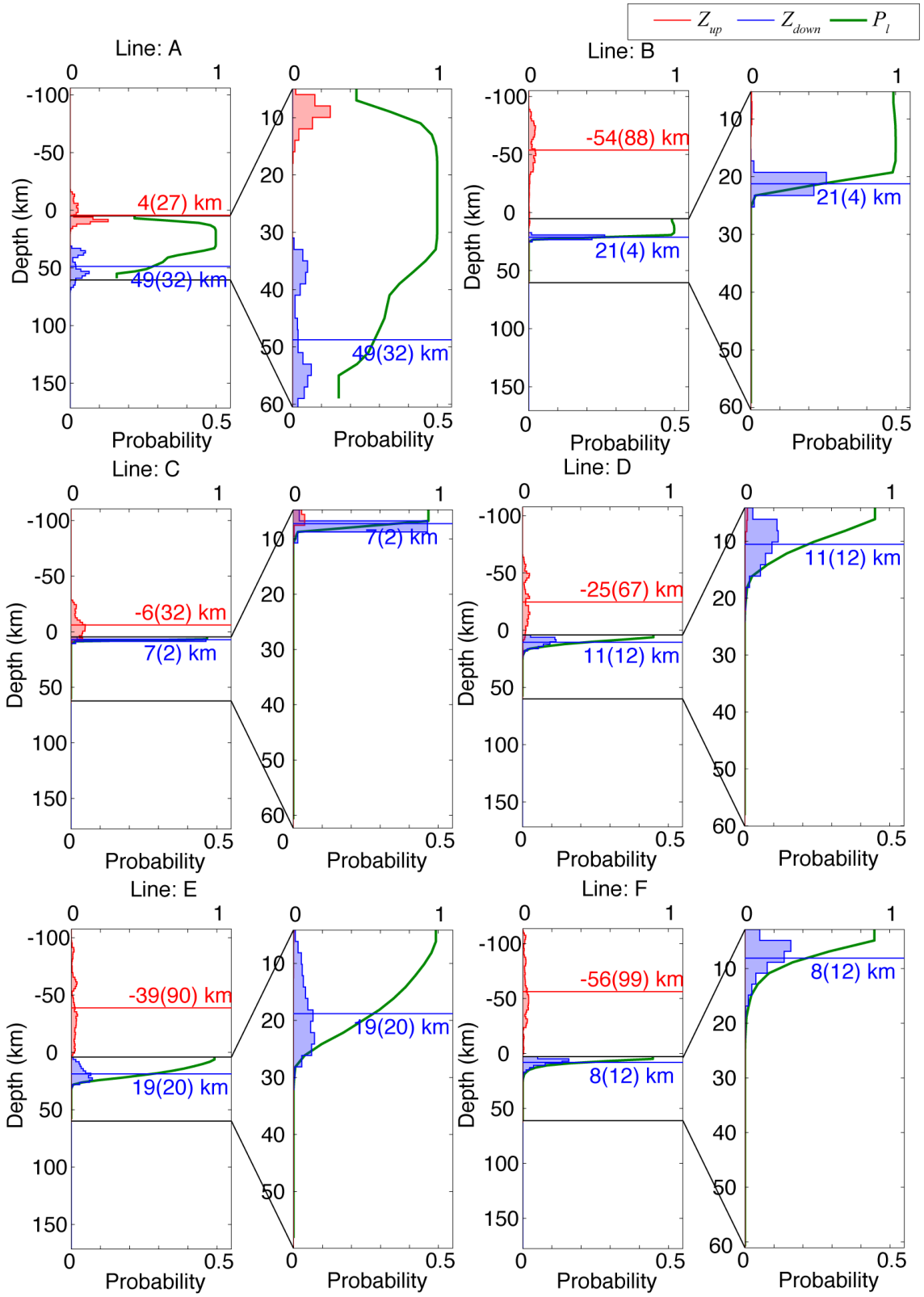

Figure 3.7. Graphs showing PDFs of the up- and down-dip depths and P_l along the line

A, B, C, D, E, and F shown with green solid lines in Figure 3.6. For each subfigure, PDFs and P_l are plotted for whole sampling depths in the left panels and for model area depths (i.e., top and bottom depths coincide with the trench and 60 km depth, respectively) in the right panels. PDFs are normalized such that the sum of the value for each bin becomes 1. Horizontal red and blue solid lines indicate the mean value of the up- and down-dip depths calculated from all the samples. Mean values are described on or under the lines. The 95 percentile confidence interval values are described in brackets to the right of the mean value. The scales of PDFs and P_l are shown in the bottom and top axes for each panel, respectively.

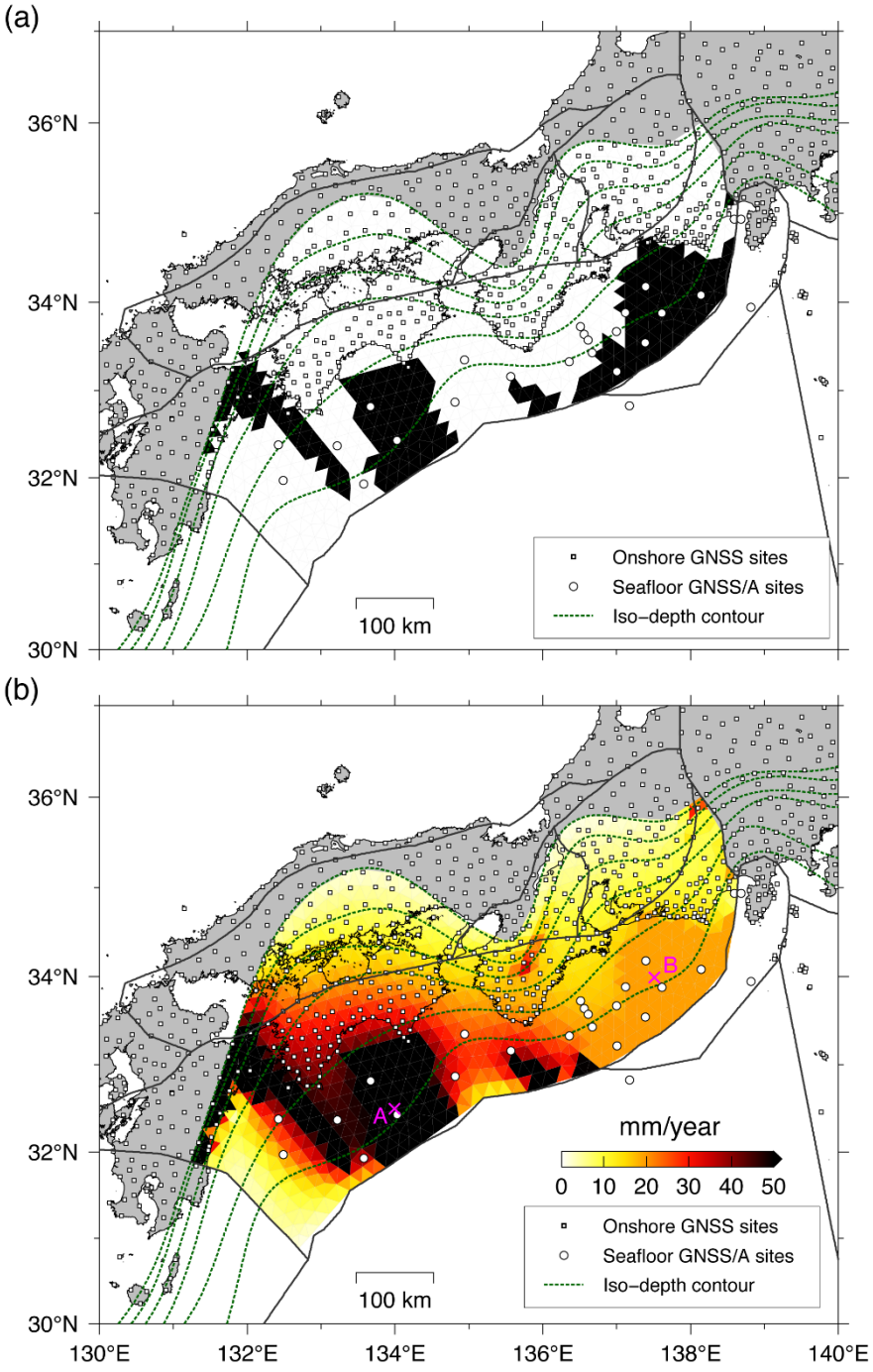

Figure 3.8. Slip deficit rate distributions along the Nankai Trough. (a) Map showing the selected subfaults (black subfault) whose locking probabilities is larger than 0.5 and that were assumed to be mechanically locked. (b) Map showing the slip deficit rate distributions calculated on the basis of the mechanical locking distributions and Equation (10). The two-dimensional PDFs of relative motion (slip deficit) rates at cross A and B are shown in Figure 3.10.

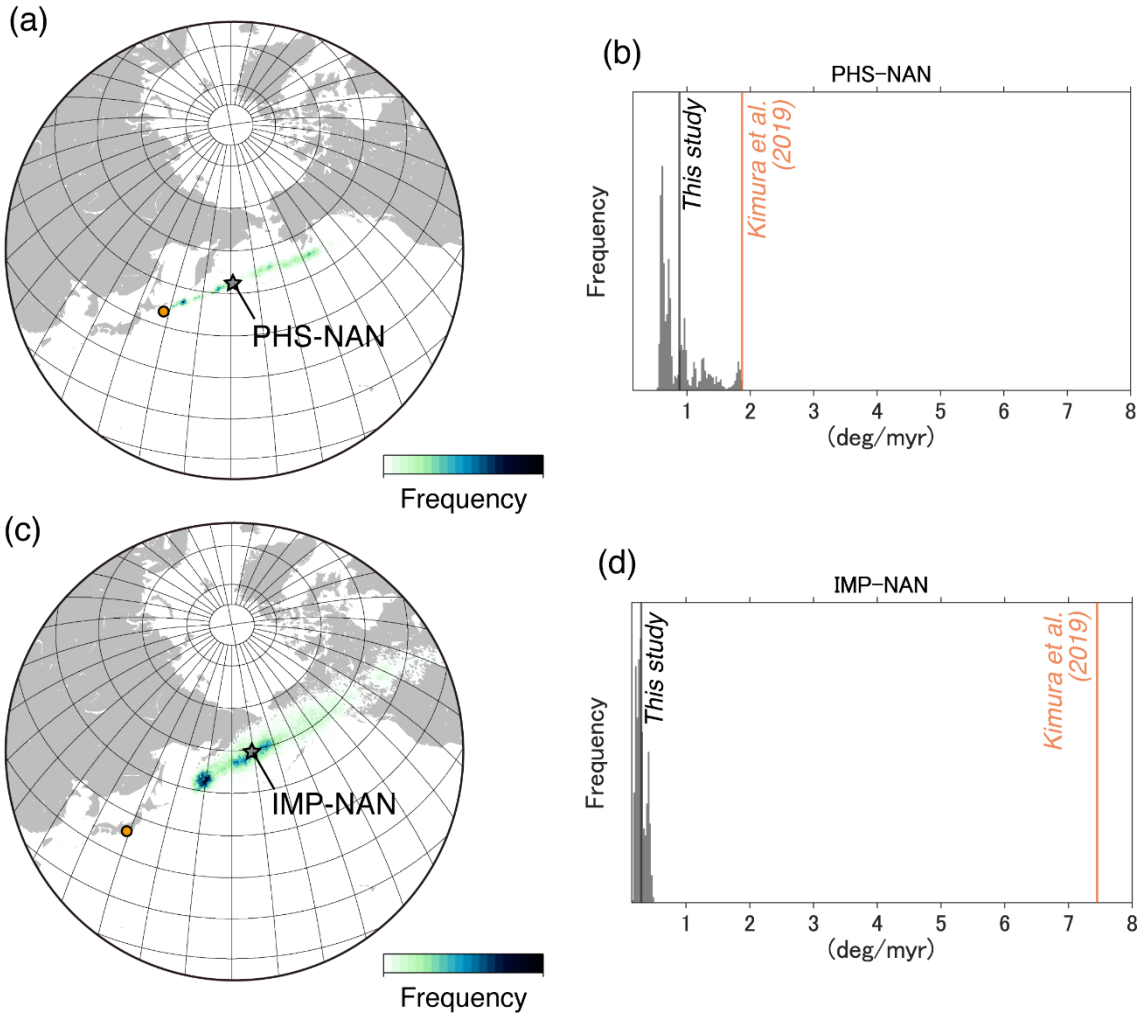

Figure 3.9. Uncertainties of Euler vectors of subducting plates relative to the Nankai Forearc block. (a) Map showing the two-dimensional PDF of the Euler vector of the subducting Philippine Sea Plate relative to Nankai Forearc block. The background color scale means the probability distribution of the Euler pole location. The gray star indicates the mean value, and the orange circle indicate the Euler pole estimated by Kimura et al. (2019). (b) Graph showing the probability distribution of the Euler pole angular velocity of the subducting Philippine Sea Plate relative to the Nankai Forearc block. The clockwise rotation corresponds to positive angular velocity. The black vertical line indicates the mean value. The orange vertical line indicates the angular velocity estimated by Kimura et al. (2019). (c) Same as (a) but the Euler vector of the subducting Izu Micro Plate relative to the Nankai Forearc block. (d) Same as (b) but the Euler vector angular velocity of the subducting Izu Micro Plate relative to the Nankai Forearc block.

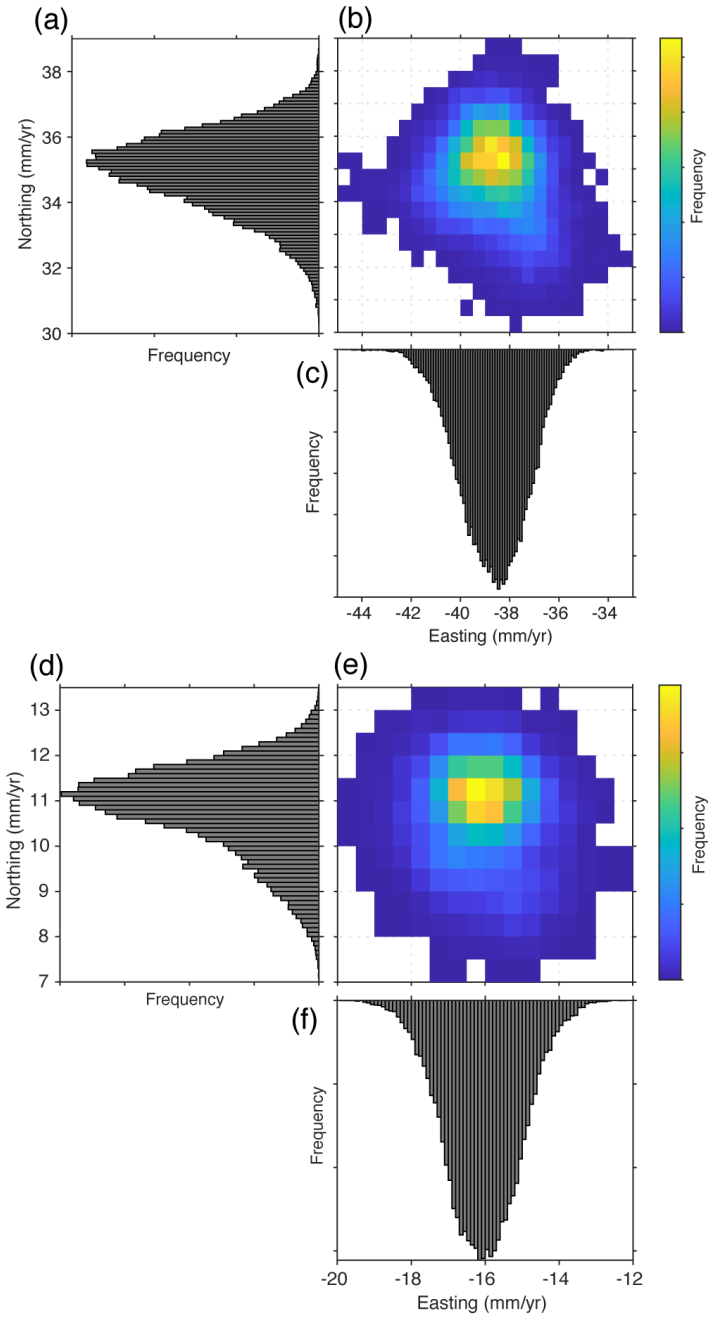

Figure 3.10. Uncertainties of relative motion rate in the western (point A in Figure 3.8b) and eastern (point B in Figure 3.8b) parts of the model region. (a), (c) Graphs showing the PDF of the northern and eastern plate convergence rates at the western part of the model region, respectively. (b) Graph showing the two-dimensional probability distribution of the northing and easting plate convergence rates at the western part of the model region. Background color indicates the normalized probability density. (d), (f) Same as (a) and (c) but for the eastern part of the model region, respectively. (e) Same as (b) but for the eastern part of the model region.

3.4. Discussion

3.4.1. Comparison with kinematic coupling distributions

In this chapter, I reveal the spatial relationship between mechanically locked and kinematic coupled regions. Although the kinematic coupling distributions along the Nankai Trough were estimated in many previous studies, the results vary owing to several factors such as the dataset, model configuration, and inversion approach. Ideally, the differences in each factor should be reduced to compare the spatial distributions of mechanical locking and kinematic coupling. Thus, I compared the result of this study with the kinematic coupling distribution estimated by Kimura et al. (2019) in which the dataset and block division configuration were the same as that in this study. While the plate interface geometry of this study is different than that used in Kimura et al. (2019), I did not discuss it in depth because the mechanical locking distribution would not change significantly owing to the slight variation in plate interface geometry, as discussed in Chapter 2.4.4.

Figure 3.11(a and b) shows the mechanical locking distributions estimated in this study and the kinematic coupling distribution (Kimura et al., 2019), respectively. Briefly, mechanically locked zones with high locking probability exhibit high coupling, such as Shikoku and Tokai. However, there are some regions that exhibit low locking probability but high kinematic coupling: offshore region between the Hyuganada and off Shikoku locking segments, offshore regions between the off Shikoku and off Kii locking segments, and the region north of the off Tokai locking segment. The regions exhibiting high locking probability in this study coincide with those exhibiting high-coupling in the study by Kimura et al. (2019), but the reverse is not always true. I selected the subfaults exhibiting locking probability larger than 0.5 as the mechanically locked zones (hatched regions in

Figure 3.11a). Figure 3.11(c) shows the slip deficit rate distributions calculated on the basis of mechanical locking distributions. Moreover, Figure 3.11(d) shows the slip deficit rate distributions estimated by Kimura et al. (2019). There are clear slip deficit rate contrasts between western and eastern parts of the model region in both slip deficit rate distributions because the two individual blocks, Philippine Sea Plate in western part and Izu Micro Plate in eastern parts subduct beneath the overriding Nankai Forearc block with different convergence rates. The slip deficit rate in this study is lower than that in Kimura et al. (2019) because the Euler vector estimates, which prescribe plate convergence rates, differ between this study and Kimura et al. (2019), as shown in Figure 3.9. High slip deficit rates can be observed at the mechanical locking regions in this study and at the regions exhibiting high kinematic coupling (Figure 3.11c and d). Additionally, some regions exhibit high slip deficit rates but low or almost zero locking probability, particularly at offshore regions between Hyuganada and Shikoku locking segments and the region north of the Tokai locking segment. As a consequence, the slip deficit rates at these regions are similar to slip deficit rates at the same regions in Kimura et al. (2019). The slip deficit rate is ~29 mm/yr and the locking probability is almost zero at the offshore region between the off Shikoku and off Kii locking segments. This value is ~60% of the slip deficit rate in the mechanical locking zone at off Shikoku segment and ~50% of the slip deficit rate estimated at the same region in Kimura et al. (2019). The residuals are similar between this study and Kimura et al. (2019) in this region excluding the coastal area of southeastern Shikoku, as shown in Figure 3.11(e and f). This indicates that the surface crustal deformation can be explained although the slip deficit rate is ~50% of that estimated by Kimura et al. (2019) at the offshore region between the off Shikoku and off Kii locking segments. If the mechanical locking is situated at this region (Figure 3.12b), residuals become larger at the seafloor GNSS/A sites and onshore GEONET sites in the

western Shikoku and southern Kii peninsula (region enclosed by the red line in Figure 3.12d). This suggests that crustal deformation in and around this region can be explained by slip deficits induced by mechanical locking in Shikoku and off Kii segments, even if the plate interface at the offshore region between the Shikoku and Kii locking segments is creeping (i.e., mechanically unlocked). It was revealed that the region between the off Shikoku and Kii locking segments is likely creeping.

Again, the plate interface exhibiting kinematic high coupling is not always mechanically locked. The high coupling (high slip deficit rate) on the plate interface that is not mechanically locked can be explained by the slip deficit induced by the mechanical locking at the adjacent regions. In the region that is not mechanically locked but where mechanical locking zones exist at the adjacent regions, it is difficult to distinguish the mechanically locked zone from the slip deficit rate distributions estimated on the basis of the pure kinematic framework, because the large slip deficit (whose velocity is lower than the slip deficit rate on the mechanical locking zone but much higher than zero) can be induced by the mechanical locking of the adjacent regions as shown in Figure 3.11(c) or suggested by Herman et al., (2018). Thus, it is useful to adopt the new physical model developed in this study to estimate the mechanical locking zone from geodetic observation data.

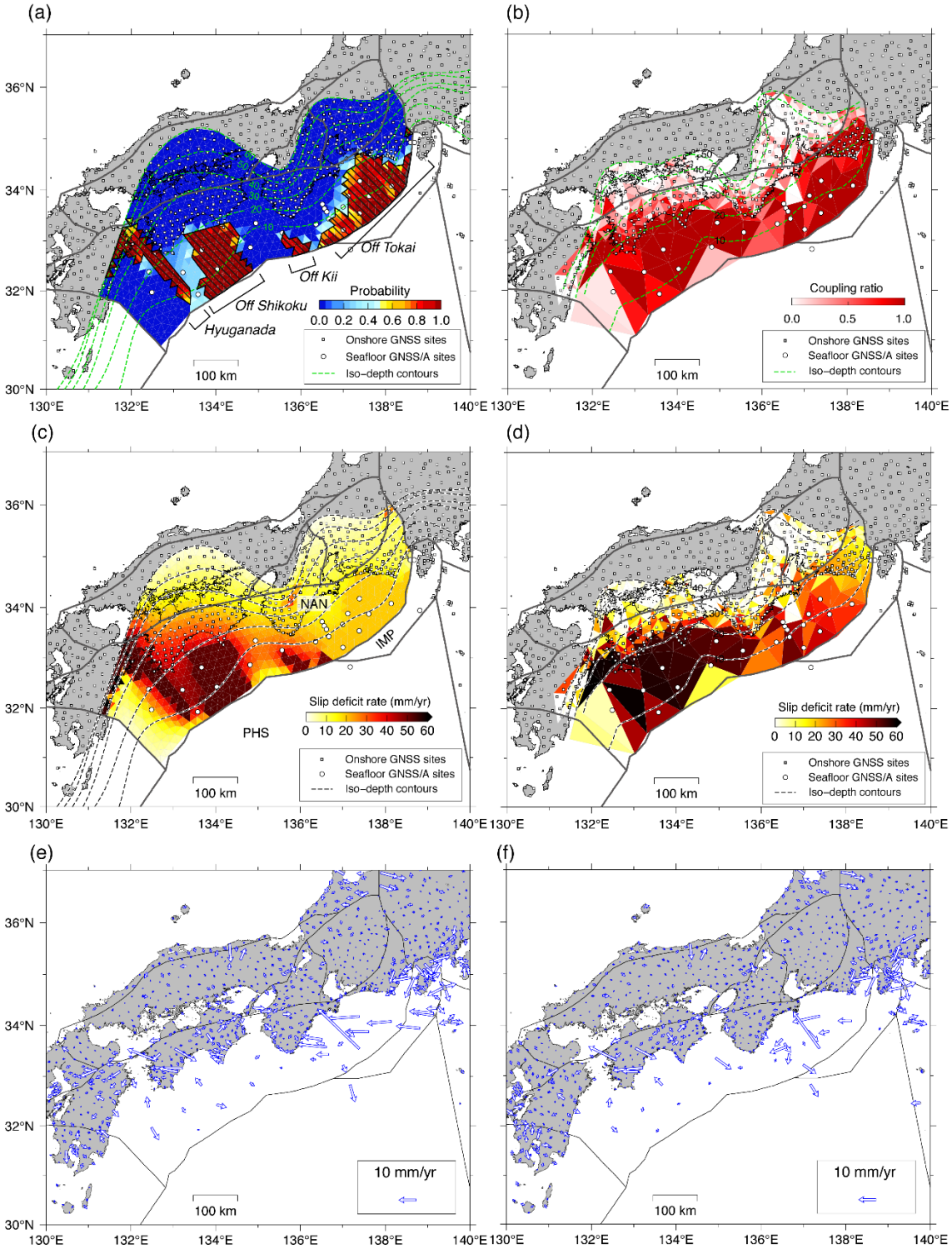

Figure 3.11. Comparison of mechanical locking distributions, kinematic coupling distributions, slip deficit rate distributions, and residuals. (a) Map showing the mechanical locking distributions along the Nankai Trough expressed as the locking probability. The hatched regions exhibit the locking probability larger than 0.5. (b) Map showing the

kinematic coupling distributions estimated by Kimura et al. (2019). The color scale means the coupling coefficient at each subfault. (c) Map showing slip deficit rate distributions on the plate interface calculated on the basis of the mechanical locking zones, hatched regions in (a). Abbreviations indicate the block name (Figure 3.4). (d) Map showing the slip deficit rate distribution on the basis of the kinematic coupling distribution (Kimura et al., 2019). (e) Map showing the residuals, observed displacement rate minus calculated displacement rate obtained in this study. (f) Same as (e) but for Kimura et al. (2019).

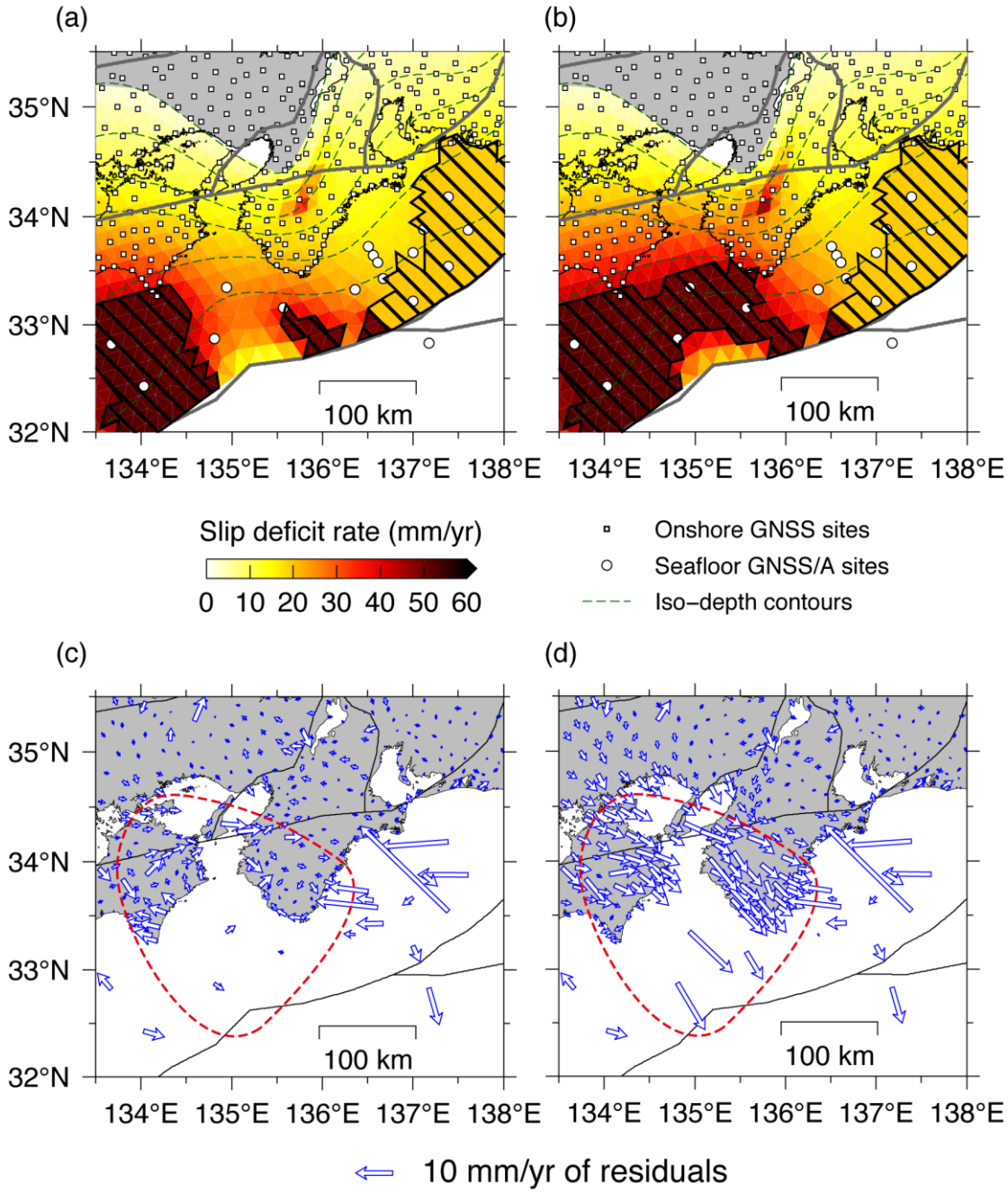

Figure 3.12. Comparison of the slip deficit rate distributions and residuals. (a) Map showing the slip deficit rate distributions at the offshore region between the Shikoku and Kii locking segments. Hatched zones represent the mechanical locking zones that are the same as those in Figure 3.11(a). (b) Same as (a) but the artificial mechanical locking zone was situated at the region exhibiting almost zero locking probability at the offshore region between the off Shikoku and off Kii locking segments. (c), (d) Residuals which were calculated on the basis of the slip deficit rate distributions shown in (a) and (b), respectively.

3.4.2. Implicated frictional states from slow earthquake distributions

Southwest Japan is a well-studied area for understanding various types of slow earthquakes (Obara, 2011) that contains low frequency tremors (LFTs, or low frequency earthquakes; LFEs), very low frequency earthquakes (VLFEs), and long (short) term slow slip events (SSEs). The signal of LFT (or LFE) and VLFE are detected by high-sensitivity or broad-band seismometers. The LFTs are weak seismic motion with a long duration time and without distinct P or S phases (Obara, 2011). The seismic wave of LFT has a predominant frequency ranging 1–10 Hz. The LFE is a pulsive-like seismic wave that sometimes occurs with LFT. The source location LFT (or LFE) is detected using a particular method, such as the envelope correlation method (Obara, 2002) because it is difficult to identify P or S wave arrivals. The VLFEs radiate weak seismic waves with a predominant frequency of 0.01–0.05 Hz that are sometimes accompanied by LFT bursts (Obara, 2011). The source location of VLFEs is difficult to determine using standard earthquake detection methods, as well as the LFT or LFE, and thus, GRiD moment tensor method (e.g., Ito et al., 2007) that is a kind of grid-search approach is used. These earthquakes have been detected at both the shallow portion (from the trench to ~10 km in depth) and the deep portion (30–45 km in depth) of the plate interface along the Nankai Trough (Obara, 2011; Obara & Ito, 2005). VLFEs at shallow portions have been detected on the splay fault in accretionary prisms (Toh et al., 2018). The SSE is detected by geodetic observational instruments such as GNSS, strain meter, and tilt meter, not detected by the seismometers because the SSE itself does not radiate seismic waves but causes crustal deformation. The duration of the SSE spans approximately few days to few months (“short-term SSE”) or few years (“long-term SSE”). SSEs have been detected mainly at depths of 30–45 km (Nishimura et al., 2013). Recently, the occurrence of shallow SSEs (~10 km in depth) have also been reported following the development of

seafloor geodetic observational instruments (Araki et al., 2017; Yokota & Ishikawa, 2020).

Figure 3.13 shows the spatial distributions of slow earthquakes detected in southwest Japan as well as the mechanical locking distributions estimated in this study. The locations of deep tremors are almost the same as those of deep VLFE. Deep SSE seems to occur not only at the depth corresponding with the deep tremor and/or VLFE occurrence zone but also at depths slightly shallower than that of tremor or VLFE, particularly in the western Shikoku and in the Tokai region. The down-dip limitation depths of the estimated mechanical locking zones are almost complementary to the occurrence zones of deep slow earthquakes. Most shallow slow earthquakes were detected at depths shallower than ~10 km. Although the deep slip earthquakes were detected continuously along the strike of the plate boundary, shallow slow earthquakes were detected with a clear gap along the trough. Comparing the mechanical locking distribution with the shallow slow earthquake occurrence zones, it was found that most shallow slow earthquakes were detected in regions exhibiting zero or low locking probabilities. The number of events detected inside the mechanical locking zone is much lower than that detected at the region exhibiting zero or low locking probabilities. The shallow slow earthquakes seem to be detected on the plate interface where the locking probability is high off southeastern Kii peninsula. However, Toh et al. (2018) analyzed the occurrence depths of shallow events detected at the segment of off southeastern Kii peninsula and suggested that the detected events in the northeastern part of the segment might occur on the splay fault in the accretionary prism, whereas that of the southeastern part of the segment might occur on the plate interface. As a consequence, regions of most shallow earthquakes off southeastern Kii peninsula do not coincide with the regions exhibiting high locking probabilities. Thus, the complementarity of spatial distributions between mechanical locking zones and the slow earthquake occurrence zones can be

observed both in shallowest part and deeper part of the plate interface. Although Kimura et al. (2019) pointed out the complementarity between the high-coupling and the deep tremor distributions, they could not discuss with respect to mechanical locking or frictional states on the plate interface based on kinematic coupling distributions.

Slip behaviors on the plate interface may be controlled by frictional states on the plate interface. The slow earthquakes are considered to exhibit a very slow slip phenomena compared to ordinary interplate earthquakes (Obara, 2009). The frictional states on the plate interface where the ordinary interplate earthquakes and the slow earthquakes are suggested to be unstable sliding (Brace & Byerlee, 1966; Dieterich, 1979) and conditionally stable (or stable) sliding (Obara, 2020; Obara & Kato, 2016). The slow earthquake and the estimated mechanical locking distributions exhibit obvious spatial complementation, implying that the estimated mechanically locked zones represent a frictionally unstable sliding interface. This implication is very important because the estimated mechanical locking distributions may correctly reflect the frictional states on the plate interface, although the new physical model used to estimate the mechanical locking distributions did not model any physical parameters exactly prescribing the frictional states on the plate interface, such as the rate- and state-dependent friction law (Dieterich, 1979). The results of the comparison of mechanical locking distributions with slow earthquake distributions indicate that the proposed model can be applied to estimate frictional properties on the plate interface. Understanding frictional property leads to the prediction of slip behaviors on the plate interface during earthquakes and thus may contribute to improved earthquake disaster mitigation.

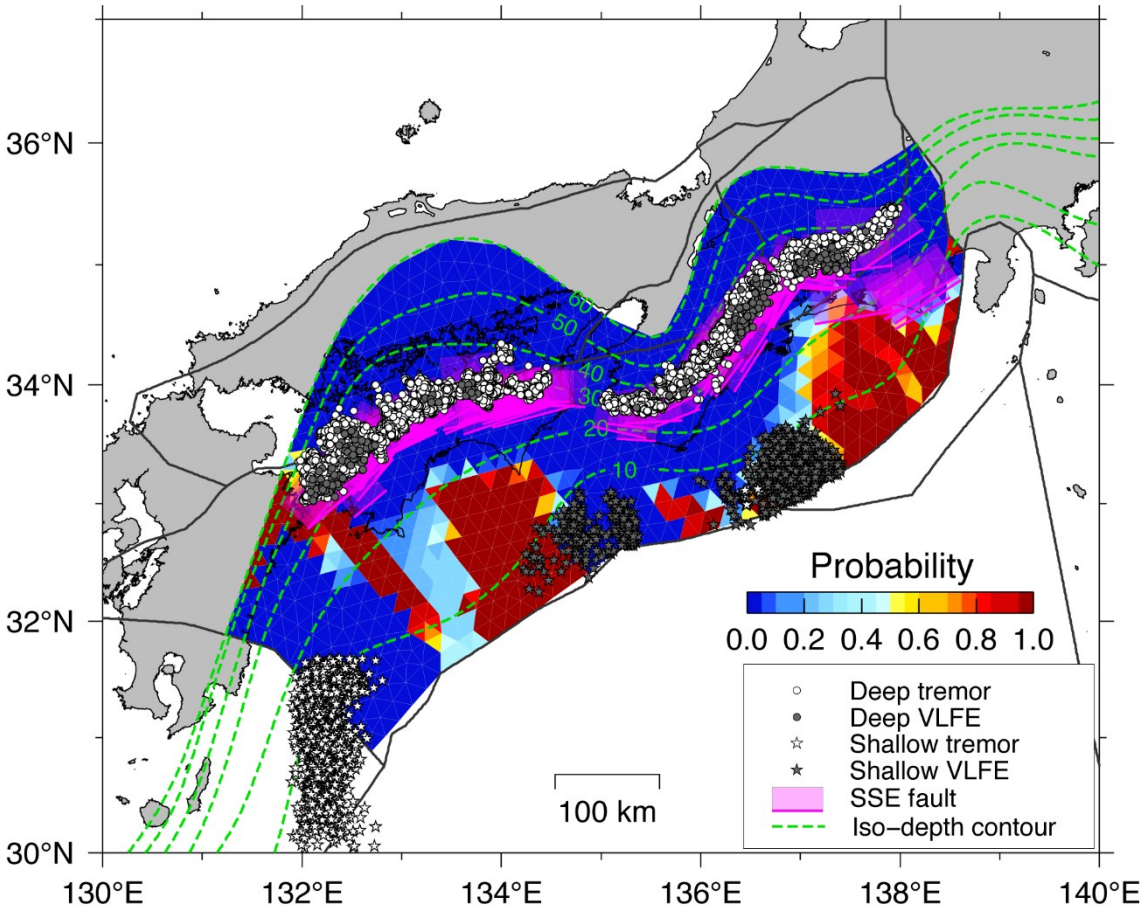

Figure 3.13. Comparison of mechanical locking distributions with slow earthquake distributions in southwest Japan. The background color indicates the locking probability. Deep tremor, deep VLFE, shallow tremor, and shallow VLFE were shown as white circles, gray circles, white stars, and gray stars, respectively. Deep SSE is shown with magenta rectangles. The following are references for each slow earthquake: Deep tremor, Obara et al. (2010); Deep VLFE, Ito et al. (2009); Deep SSE, Nishimura et al. (2013); Shallow tremor, Obana & Kodaira (2009) and Yamashita et al. (2015); Shallow VLFE, Takemura et al. (2019). Detection periods are from 2001 to 2017 for deep tremor, from 2003 to 2008 for deep VLFE, from 2004 to 2012 for deep SSE, from 2003 to 2013 for shallow tremor, from 2003 to 2018 for shallow VLFE. All data were available from Slow Earthquake Database, developed by Kano et al. (2018)

3.4.3. Correspondence with interplate earthquakes

I compared the estimated mechanical locking distributions with the coseismic slip distributions of past megathrust earthquakes. Megathrust earthquakes with $> M$ 8 have repeatedly occurred every 100–150 years along the Nankai Trough (Ando, 1975; Garrett et al., 2016). The latest events occurred in 1944 (M 7.9 Tonankai Earthquake) and 1946 (M 8.0 Nankai Earthquake). The source models (coseismic slip distributions) of the two events were estimated from geodetic, seismic, tsunami, and geological records (Baba et al., 2002; Garrett et al., 2016; Murotani et al., 2015; Sagiya & Thatcher, 1999; Tanioka & Satake, 2001; Yamanaka, 2006).

Figure 3.14 shows the coseismic slip distributions of the two described events (shown as contours). I also plotted the mechanical locking distributions estimated in this study and the kinematic coupling distributions of Kimura et al. (2019). The ruptures of these two events were initiated offshore the southern Kii peninsula. The coseismic slips might be concentrated at eastern Kumano basin and off Muroto during the 1944 and 1946 events, respectively.

From the comparisons between the mechanical locking (and kinematic coupling) distributions and coseismic slip distributions, the following three features were found. First, mechanically locked distributions roughly coincide with the region where the plate interface coseismically slipped during the 1944 and 1946 earthquakes. Second, mechanically locked zones seem to be included in coseismic slip areas, rather than covering the whole coseismic slip areas, whereas kinematic high-coupled regions roughly cover (or is larger than) the whole coseismic slip areas. Third, the coseismic distribution estimated by the geodetic inversions (Sagiya & Thatcher, 1999) is slightly different to that estimated by the seismic waveform inversions (Murotani et al., 2015; Yamanaka, 2006), and the overlapping areas between the coseismic slip distributions estimated by

seismic wave inversions (Murotani et al., 2015; Yamanaka, 2006) and mechanical locking zones are larger than the overlapping areas between the coseismic slip distributions estimated by the geodetic inversions (Sagiya & Thatcher, 1999) and mechanical locking zones. The first feature demonstrates the repeatedly occurrence of the megathrust earthquake along the Nankai Trough (Ando, 1975; Garrett et al., 2016) and the recurrence potential of earthquakes in the future as suggested by previous studies, although it is difficult to predict whether mechanically locked segments would rupture simultaneously and identify the accurate coseismic slip magnitude of forthcoming earthquakes. The second feature suggests that the coseismic slip can occur not only at the mechanically locked region but also in surrounding kinematic coupled regions. During the interseismic period, shear strains may be accumulated on the mechanically locked zones. At the surrounding regions, no shear strain is accumulated owing to the constant strain condition, whereas slip deficits accompanied with the mechanical locking can be accumulated. During the earthquakes, mechanically locked zones may exhibit brittle rupturing, and the surrounding regions may be slipping accompanied by the brittle rupture. Note that, seismic wave may be radiated not only by the brittle rupture but also by the accompanying slip of the surrounding region of the brittle rupture. The moment magnitudes estimated from the geodetic inversion and the seismic waveform inversion were similar to each other (Murotani et al., 2015; Sagiya & Thatcher, 1999). The seismic waves radiating from the brittle rupture zone may dominate the short-period components, whereas the seismic waves radiating from the accompanying slip zone (surrounding the brittle rupture area) may dominate relatively long-period components. This is supported by the result in which the radiation source estimated from the short-period band-pass filtered seismic wave was partially distributed in the radiation source estimated from the long-period band-pass filtered seismic wave (Lay et al., 2012). Whether the accompanying slip propagates to the

whole interface of the kinematic high-coupled zone may depend on the seismic moment accumulated during the interseismic period. If the accumulated seismic moment is sufficiently large, coseismic slip accompanied by the brittle rupture may propagate to the region far from the rupture zone. Otherwise, the accompanying slip propagates from the rupture zone but may stop after a short period. Although it is difficult to accurately identify the spatial distributions of slip behaviors (i.e., brittle rupture or accompanied slipping) from coseismic slip distributions, the third feature described above may support the implication obtained from the second feature. Seno (2012) pointed out that the coseismic slip distributions may vary depending on the frequency-band of coseismic data used for inversions. Because seismic waveform data predominately shows shorter period signals radiated by high velocity slips, such as brittle rupturing, compared to the geodetic data, which predominately shows longer period signals, coseismic slip distributions estimated by seismic waveform inversions may be similar to the brittle rupture area. Thus, the third feature may suggest that the mechanically locked zones may be a brittle rupture during the earthquakes, supporting the implication obtained from the second feature.

I compared the hypocenters of the Nankai Trough earthquakes that occurred in 1944 and 1946 with the estimated mechanical locking distributions. The hypocenter of the 1946 Nankai Earthquake (M 8.0) appears to be located at the mechanical locking zone off Kii peninsula segment. It is difficult to distinguish whether the hypocenter is located inside the mechanical locking zone or not because the subfault size is large relative to the locking segment size. The hypocenter of the 1944 Tonankai Earthquake (M 7.9) was located 40–50 km NW from the edge of the mechanical locking zone of in the Tokai segment. In the case of the 2011 Tohoku and 2003 Tokachi earthquakes, the hypocenters of both earthquakes appeared to be located at the edge of the mechanical locking zones (Chapter 2.4.1). Thus, the 1944 Tonankai Earthquake did not seem to follow the tendency

implicated from two earthquakes in northeast Japan. One possible explanation to explain the rupture initiation of the 1944 Tonankai Earthquake is the existence of the small hidden mechanical locking zone that could not be detected by the proposed model from geodetic observation data, as is the case in Tokachi (Chapter 2.4.2). Although the spatial density of the seafloor GNSS/A observation network in this region is relatively denser compared to that of other offshore region, some tiny mechanical locking zones might not be detected.

If seismic ruptures of megathrust earthquakes are always initiated at the edges of large mechanical locking zones, the proposed model is applicable for predicting candidates of rupture initiation points of forthcoming interplate earthquakes. However, as discussed above, ruptures of megathrust earthquakes can be initiated not only at the edge of mechanical locking zone but also outside of large mechanical locking zone (perhaps at the edge of tiny mechanical locking zones). Thus, it was revealed that the new model cannot always be used to predict candidates of the rupture initiation points of future megathrust earthquakes.

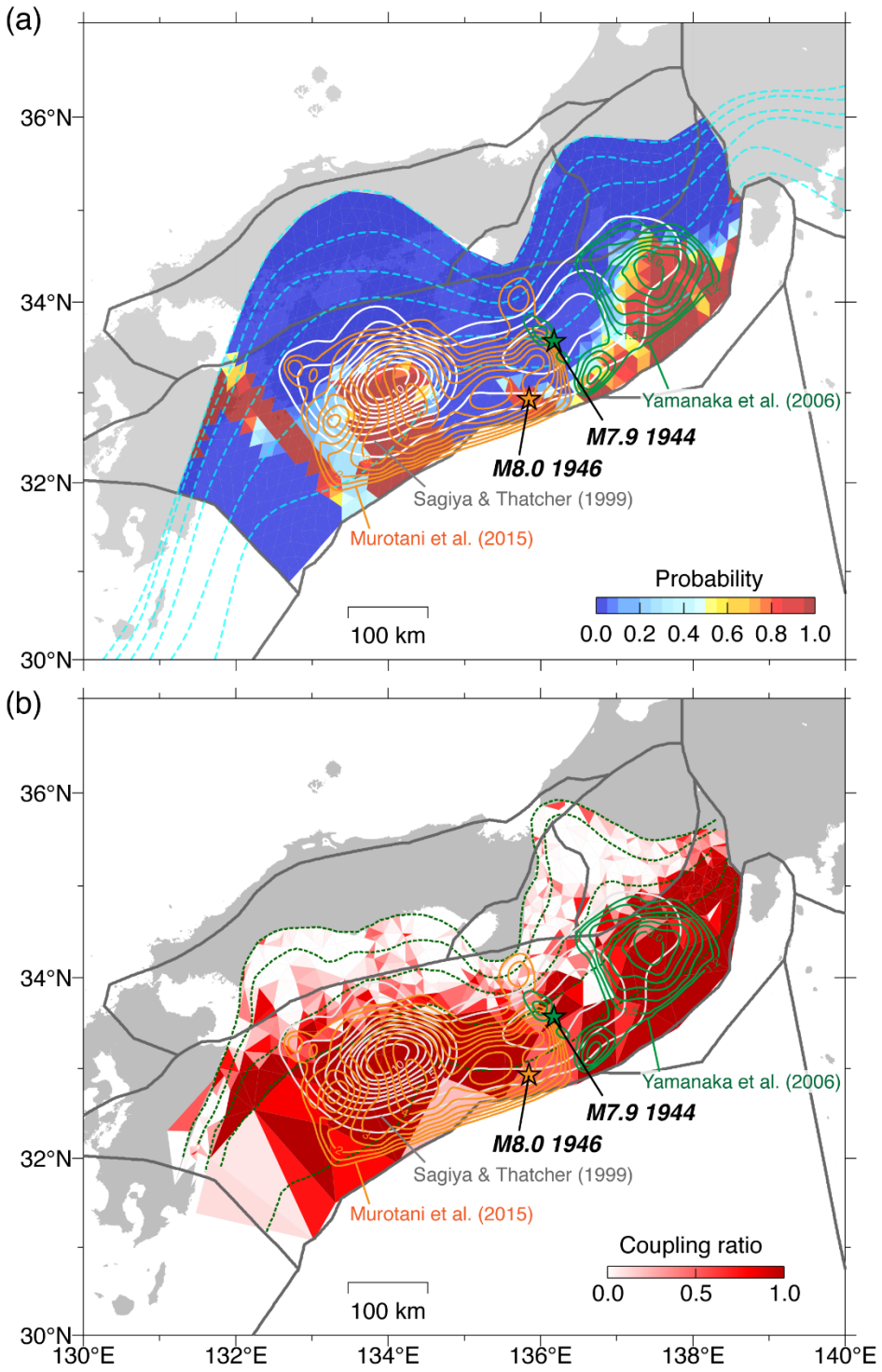

Figure 3.14. Comparison with coseismic slip area of 1944 and 1946 Nankai Trough earthquakes. Yellow stars indicate epicenters of the 1944 *M* 7.9 Tonankai and 1946 *M* 8.0 Nankai Earthquakes. These two epicenters refer to the Japan Meteorological Agency hypocenter catalogue. Coseismic slip distributions of the above two earthquakes are shown with contours. The coseismic slip distributions were estimated by seismic wave

data (Murotani et al., 2015; Yamanaka, 2006) and the geodetic observation data (Sagiya & Thatcher, 1999). (a) Map showing the coseismic slip distributions and hypocenters as well as the mechanical locking distribution. The color scale indicates the locking probability. (b) Same as (a) but as with the kinematic coupling distribution (Kimura et al., 2019). The color scale indicates the coupling coefficient.

3.4.4. Spatial relationship between mechanical locking zone and strong motion generation area

Kanda et al. (2004) estimated short-period seismic wave radiation sources from the seismic intensity inversion method based on recorded intensity data. The intensity data correlates with strong ground motion that occurred for 0.5–1 seconds and caused significant infrastructure damage (Kawase, 1998; Nozu et al., 2012). Thus, the regions of the short-period seismic wave radiation source estimated by Kanda et al. (2004) can be assumed as the SMGA. Though Kanda et al. (2004) estimated the SMGAs of four past Nankai Trough earthquakes (Hoei Earthquake in 1707, Ansei Earthquake in 1894, Showa Tonankai Earthquake in 1944, and Showa Nankai Earthquake in 1946), I focused on the latter two earthquakes because the data quality of the intensity records of the two former earthquakes is not sufficiently high.

I compared the estimated mechanical locking distributions with the SMGAs of the two earthquakes (Figure 3.15). Most SMGAs appear to be located near the edge of the mechanically locked zones excluding the northern part of the locking segment off Tokai, where the SMGA overlaps the locked zone. Similarly, SMGAs tended to be located at the edge of the mechanically locked zone in Tohoku and Tokachi in northeast Japan, as shown in Chapter 2.4.3. Thus, this spatial relationship between the SMGAs and mechanical locking zone may be a common feature for megathrust earthquakes. The physical mechanisms explaining that the SMGA is located at the edge of the mechanical locking

zone may be explained by the heterogeneity or changing of the frictional state during seismic rupture propagations. Two theories explain the short-period seismic wave radiation during the seismic rupture. The first is that rupture velocity in the coseismic slip area is heterogeneous. Miyatake et al. (2008) analytically calculated the seismic wave due to slip on the fault considering the following two cases of heterogeneities of fault parameters: heterogeneous slip magnitude with homogeneous rupture velocity and heterogeneous rupture velocity with homogeneous slip magnitude. As a consequence, Miyatake et al. (2008) concluded that the high frequency–dominant seismic wave could be effectively radiated in the rupture in which the heterogeneous rupture velocity with homogeneous slip magnitude was imposed compared to the rupture in which the heterogeneous slip magnitude with homogeneous rupture velocity was imposed. The heterogeneity of the rupture velocity considered in Miyatake et al. (2008) can be assumed to be a heterogeneity of the slip velocity because the rupture velocity is proportional to the maximum slip velocity (Ida, 1973). Thus, the high frequency-dominant seismic wave may be effectively radiated by the rupture with the heterogeneous slip velocity. The second one is the abrupt decreases in the rupture velocity (sometimes called a “stopping phase”) during rupture propagation. Bernard & Madariaga (1984) calculated displacement waveforms during the rupture with a simple crack model and suggested the discontinuity of the displacement waveform (and thus the abrupt changes of velocity and acceleration waveforms) when the rupture stopped at the edge of the crack. They concluded that abrupt changes in velocity and acceleration waveforms may cause the radiation of short period dominant waveforms. It is common that slip velocity is changing during the rupture propagation in the above two mechanisms, though these mechanisms are different to each other. According to the rate- and state-dependence frictional law (Dieterich, 1979), the slip velocity may be controlled by the frictional states on the plate

interface. Frictional states on the plate interface may vary between mechanically locked and creeping zones, as discussed in Chapter 3.4.2: mechanically locked zones coincide with frictionally locking (or unstable sliding) fields, whereas the creeping zones coincide with the conditionally stable sliding or stable sliding fields. Thus, when the rupture propagates through the edge of the mechanical locking zones, frictional states change, and the slip velocity may abruptly increase or decrease. As a consequence, the short-period seismic waveform is radiated.

As mechanical locking zone size increases, the area where SMGAs can be located may increase as well considering the implication presented above (i.e., that SMGAs may be located at the edges of mechanical locking zones). The mean size of the mechanical locking zones estimated along the Nankai Trough is larger than that estimated along the Japan Trench (Figure 3.16). Thus, the possible areas where SMGAs can be found may be larger along the Nankai Trough compared to along the Japan Trench. It is important to predict SMGAs for effective earthquake disaster mitigation. The mechanical locking distributions estimated by geodetic observation data on the basis of the new physical model developed in this study may be useful for predicting SMGA candidates of forthcoming megathrust earthquakes.

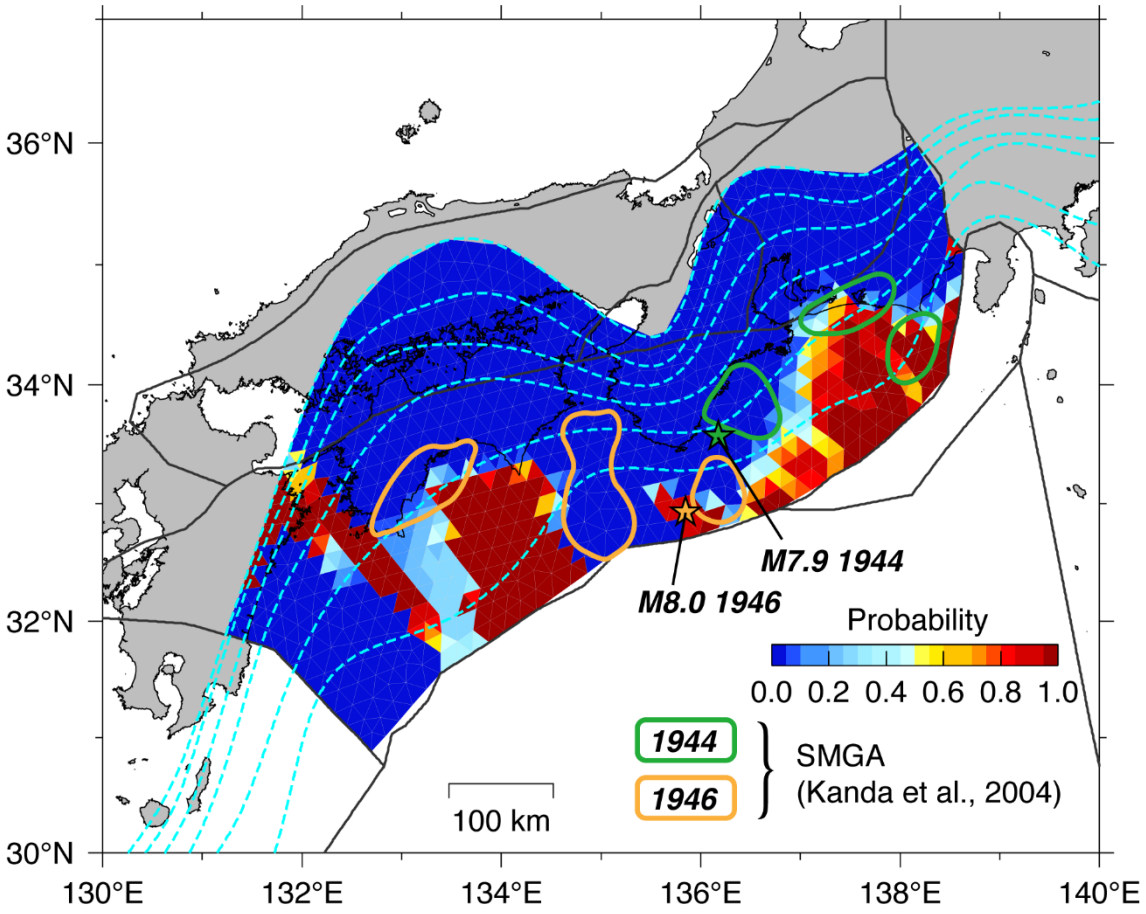

Figure 3.15. Map showing strong motion generation areas of the 1944 M 7.9 Tonankai Earthquake (cyan closed line) and 1946 M 8.0 Nankai Earthquake (yellow closed line) estimated from seismic intensity records (Kanda et al., 2004). The background color scale indicates mechanical locking distributions expressed as locking probability.

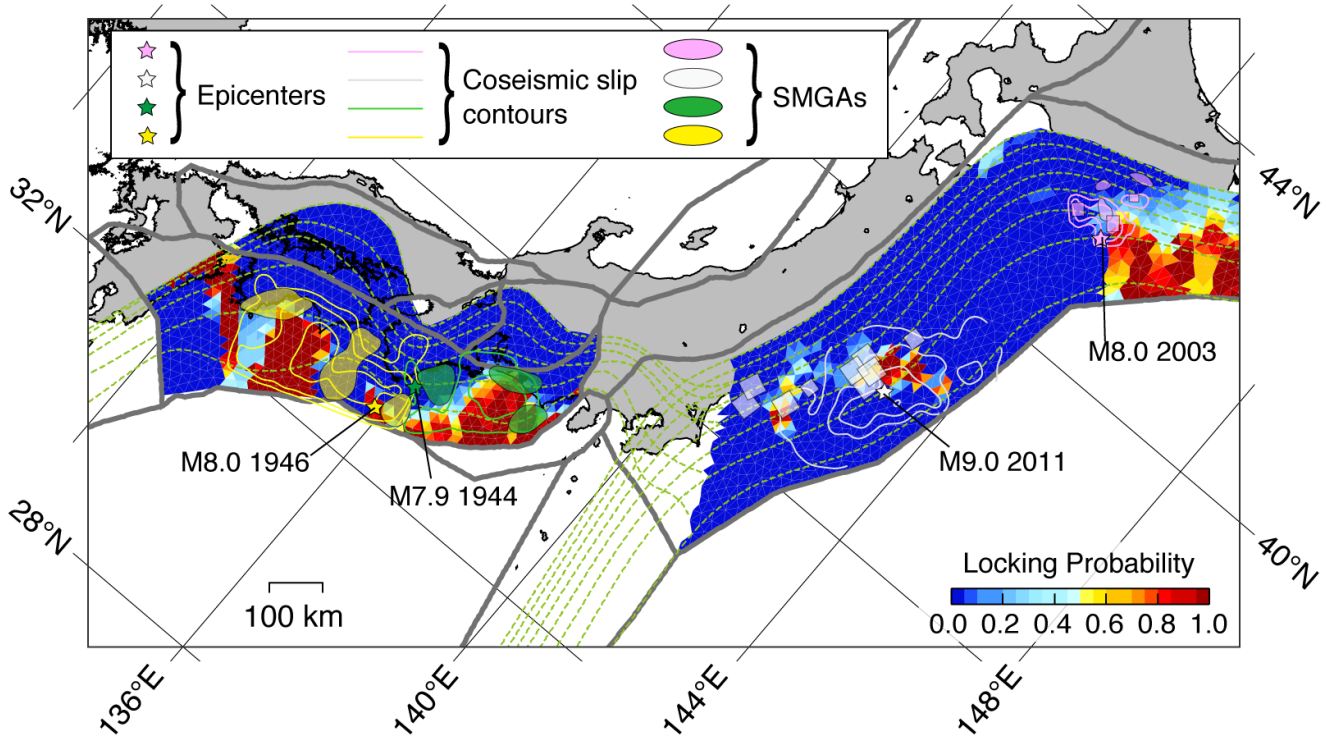

Figure 3.16. Map showing mechanical locking distributions, epicenters, coseismic slip distributions, and SMGAs along the Nankai Trough and Japan and Kuril Trench. Background color represents locking probability. Colored stars, contour lines, and enclosed area indicate epicenters, coseismic slip distributions (Murotani et al., 2015; Yamanaka, 2006; Yamanaka & Kikuchi, 2003; Yokota et al., 2011), and SMGAs (Kamae & Kawabe, 2004; Kanda et al., 2004; Kurahashi & Irikura, 2013; Nozu & Irikura, 2008), respectively, of past megathrust earthquakes. Pink, light gray, green, and yellow coloring corresponds to the 2003 Tokachi (Mw 8.0), 2011 Tohoku (Mw 9.0), 1944 Tonankai (M 7.9), and 1946 Nankai (M 8.0) earthquakes, respectively. Dashed lines indicate iso-depth contours with 10 km depth intervals. Gray lines indicate block boundaries.

3.4.5. Comparison with subducted topographic anomalies

In the previous sections, I focus on the relation between mechanical locking distributions and the frictional state on the plate interface, and it was suggested that mechanically locked zones coincide with frictionally locked (unstable sliding or stick slip) zones. In this chapter, I focus on the relation between mechanical locking distributions and topographic anomalies of the subducted plate.

Figure 3.17 shows four major topographic anomalies—Paleo Zenisu ridge (Park et al., 2004), high-density buried rock (Kaneda et al., 2006), Muroto seamount (Kodaira et al., 2002), and Kyushu–Palau ridge (Park et al., 2009)—of subducted plate interface along the Nankai Trough. As illustrated in Figure 3.17, no obvious correlation between the mechanical locking and subducted topographic anomaly distributions was observed found. Muroto seamount, high-density buried rock off Kii peninsula; the Kyushu–Palau ridge appears to be located in regions exhibiting low or near-zero locking probabilities, while the paleo Zenisu ridge overlaps the mechanically locked zone in the Tokai segment. This suggests that the subducted topographic anomalies can cause both mechanical locking and creeping (mechanically unlocked). Previous studies suggested that topographic anomalies controlling the slip propagation during the earthquake should be mechanically locking (Kodaira et al., 2002). However, this hypothesis may not explain all observed phenomena because the frictional strength on the plate interface of the subducted seamount can be decreased by pore fluid. Shallow slow earthquakes were detected in the region where the Muroto seamount subducts (Figure 3.13 and 3.17). The occurrence of shallow slow earthquakes is considered to be related to elevated pore fluid pressure on the plate interface (Araki et al., 2017). Significantly low shear wave velocity was estimated from the seismic exploration survey data at the region where the subducted

Muroto seamount was found, implying the existence of fluid on the plate interface (Tonegawa et al., 2017).

The comparison indicates that whether the plate interface is mechanically locked may be controlled by frictional states rather than by the subducted topographic features. To understand mechanical locking distributions on the plate interface, it was considered more useful to apply the proposed model developed to the geodetic observation data rather than conduct a structural survey beneath the seafloor.

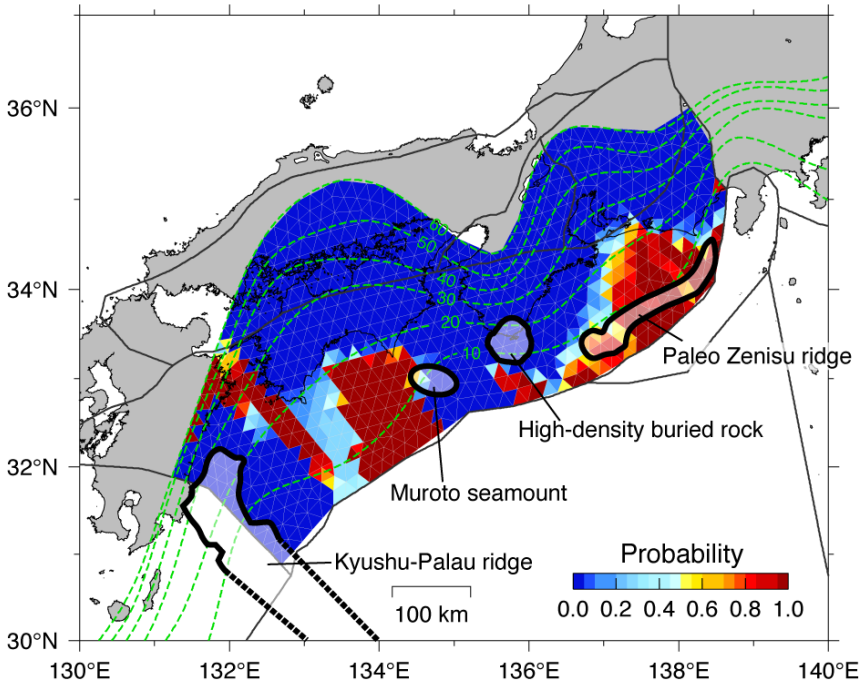

Figure 3.17. Map showing the surface tracing of major topographic anomalies on the subducted plate interface and mechanical locking distributions expressed as the locking probability along the Nankai Trough. The following are references for each topographic anomaly: Paleo Zenisu ridge, Park et al. (2004); High-density buried rock, Kaneda et al. (2006); Muroto seamount, Kodaira et al. (2002); Kyushu–Palau ridge Park et al. (2009).

3.5. Chapter summary

The proposed model discussed in the previous chapter was applied to southwest Japan to estimate mechanical locking distributions along the Nankai Trough from onshore GNSS and seafloor GNSS/A observation data.

Estimated mechanical locking distributions were compared with kinematic coupling distributions estimated by Kimura et al., (2019) in which the same dataset and block configurations were used. Moreover, estimated mechanical locking distributions were compared with slow earthquake distributions, coseismic slip distributions, hypocenters, and SMGAs of Showa Nankai Trough earthquakes in 1944 and 1946, and subducted topographic features. The following main results and implications were derived from the findings presented in this chapter.

- Four mechanical locking segments exist at Hyuganada, Shikoku, Kii peninsula, and Tokai.
- Mechanical locking zones are notably smaller than kinematic high-coupling zones. High slip deficits at regions exhibiting low locking probabilities occur due to mechanical locking in adjacent regions.
- Spatial complementation between the mechanical locking zone and slow earthquake occurrence zones was clearly observed. This suggests that estimated mechanical locking distributions indicate frictional states on the plate interface, even if physical parameters were not considered in the proposed model.
- Coseismic slip areas of Showa Nankai Trough Earthquakes are larger than mechanical locking zones but almost equal to the kinematic high-coupling areas. Moreover, estimated mechanical locking zones are similar to the coseismic slip areas estimated from the seismic waveform data rather than to those estimated from the geodetic data. This implies that mechanical locking zones correspond to brittle

rupture zones and that kinematic high-coupled but mechanically unlocked (creeping) zones correspond to the accompanying slip zones.

- SMGAs tend to be located at the edge of mechanically locked zones. Potential SMGAs are larger along the Nankai Trough than along the Japan Trench. Short-period seismic wave radiation may be caused by rupture propagations throughout the region where frictional properties significantly vary.
- There is less correlation between subducted topographic features and mechanical locking distributions. Even if remarkable topographic features exist on the plate interface, frictional states that can control mechanical locking states vary due to other physical processes, such as pore fluid pressure elevation.

Chapter 4
Conclusions

In this study, a novel physical model was developed that describes the relation between mechanical locking on the plate interface and surface crustal deformations to estimate mechanical locking distributions on the plate interface using geodetic observation data.

The mechanical locking distributions along the Japan and Kuril Trenches and along the Nankai Trough were estimated by adopting this physical model with onshore GNSS and seafloor GNSS/A observation data observed at the interseismic periods using the REMC method. Estimated mechanical locking distributions were compared with kinematic coupling and coseismic slip distributions, hypocenters, and SMGAs. Additionally, estimated mechanical locking distributions were compared with slow earthquake distributions and subducted topographic anomalies along the Nankai Trough. Figure 4.1 shows the schematic image of mechanical locking and slip behaviors on the plate interface along the Japan and Kuril Trenches and along the Nankai Trough.

It was found that mechanical locking zones were distributed as segments in both subduction zones. This suggests the trench-parallel heterogeneity of frictional properties of the plate interface because the mechanical locking zones coincide with frictional locking (unstable field) owing to notable spatial complementation between mechanical locking zones and slow earthquake occurrence zones. Although previous studies have revealed the trench-parallel heterogeneity of the slip deficit rate using geodetic inversions based on pure kinematic models, this study is the first to reveal the trench-parallel heterogeneity as a frictional heterogeneity with a geodetic approach. Because the frictional property can control the slip behaviors on the plate interface during earthquakes (or earthquake cycles), revealing the frictional distributions on the plate interface by

estimating the mechanical locking distributions using the proposed model can facilitate improved prediction of slip behaviors during earthquakes, which is essential for evaluating the occurrence potential of future megathrust earthquakes.

The mechanical locking area was included in the kinematic high-coupling area both along the Nankai Trough and along the Japan and Trench. The mechanical locking zones coincide with kinematic high-coupling regions, but the reverse is not always true. High slip deficits can be produced in creeping (mechanically unlocked) zones via mechanical locking at the adjacent regions. Particularly, the slip deficit become high in creeping zones between two mechanical locking segments. The proposed model was determined useful for detecting mechanical locking zones in such cases. However, it is difficult to detect small mechanical locking zones (such as those that are hidden and may have caused the 2003 Tokachi earthquake) using the new model. Developing a robust and accurate geodetic observation network on the seafloor as well as onshore may overcome this limitation.

SMGAs tend to be located at the edge of the mechanical locking zone both along the Nankai Trough and along the Japan Trench. Radiations of short-period dominant seismic waves at the edges of mechanical locking zones may be explained by abrupt changes in plate interface properties, such as unstable fields in mechanical locking zones and stable sliding fields in creeping zones. Potential SMGAs were suggested to be larger in the Nankai Trough compared to those along the Japan Trench because the size of the mechanical locking zone is notably larger along Nankai Trough compared to along the Japan Trench.

The locking state at the shallowest part of the plate interface differed between regions along the Nankai Trough and Japan Trench. The shallowest part of the plate interface was estimated to be mechanically locked along the Nankai Trough but mechanically unlocked

along the Japan Trench. Geological conditions, such as consolidation degrees of the sedimental layer or =localized topographic anomalies, at the toe portion of subduction zones may control the mechanical locking condition. Alternatively, the strain accumulation at the splay faults in accretionary prisms could be estimated to the mechanical locking on the plate interface, which this study did not consider. Numerous splay fault systems in accretionary prisms have been identified by geophysical surveys along the Nankai Trough (e.g., Park & Kodaira, 2012; Tsuji et al., 2014). The possibility of tsunami generation due to the slip of splay faults during the 1946 Nankai earthquake has also been reported (e.g., Cummins et al., 2001). To evaluate the tsunami potential of future megathrust earthquakes, accurate estimations of mechanical locking distributions not only along the plate interface but also along splay faults may be required. To realize this, denser and more accurate seafloor geodetic observations are necessary to improve the accuracy of derived offshore detailed crustal displacement fields, particularly in regions where splay faults are observed.

Some common features, such as segmented mechanical locking distributions, the spatial relationship between the mechanical locking distributions, coseismic slip distributions, and SMGAs, between different subduction zone types (i.e., Japan and Kuril Trench and Nankai Trough) identified using factors such as dip angle, convergence rate, and temperatures imply that the proposed model can effectively predict brittle rupture areas, coseismic slip areas, and SMGA candidates for future megathrust earthquakes. The ability to predict these factors can promote effective earthquake disaster mitigation. Particularly, predicting SMGA candidates may be useful simulating strong ground motions. There are many subduction zones where megathrust earthquakes have occurred, such as those in Kamchatka, Alaska, Chile, Indonesia, and New Zealand. The proposed method may be useful in the region where the interseismic geodetic observation data is

available for estimating mechanical locking (frictional state) distributions and thus predicting brittle rupture zones, accompanying coseismic slip zones, and SMGA candidates for future megathrust earthquakes globally. In addition, applying this model to inland block boundaries may enable researchers to estimate mechanical locking distributions at inland faults, which will contribute to the advanced evaluation of the seismic potential of inland earthquakes.

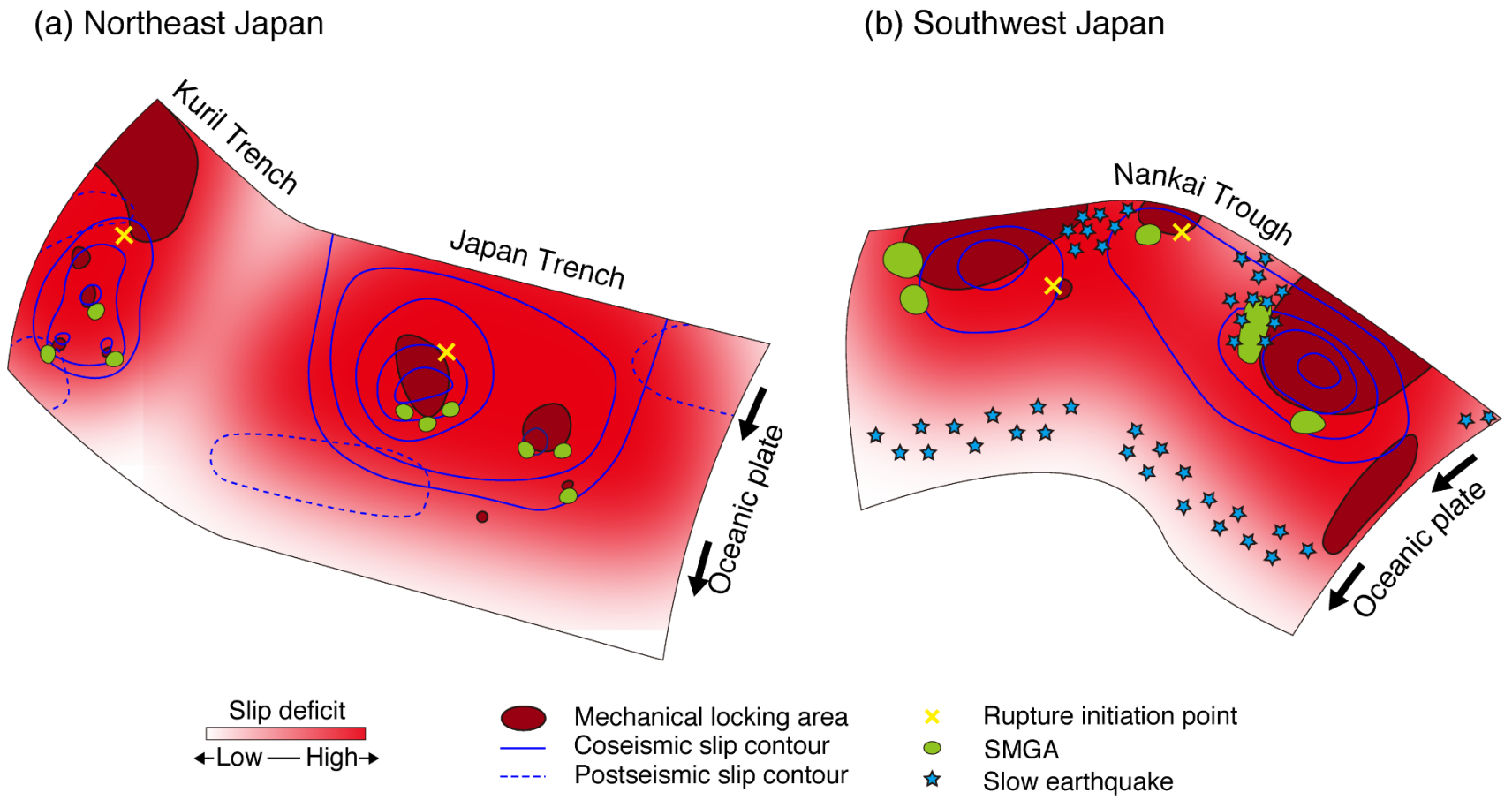

Figure 4.1. Schematic imaging of mechanical locking and slip behaviors on the plate interface along the Japan and Kuril Trenches and along the Nankai Trough.

Appendix A
Rigid motion and internal block strain results: Northeast Japan

A.1. Estimated Euler vectors and calculated rigid motions

Figure A.1(a) depicts the rigid motion component of the surface velocities at the onshore and seafloor sites calculated by Euler vector estimates (Table A.1) relative to the Eurasian Plate. Velocities plotted on the subducting Pacific Plate were based on the MORVEL plate model (DeMets et al., 2010). Almost all overriding blocks move in a west or west–northwest direction. The displacement rates were higher in the forearc side blocks (12–15 mm/yr on average), such as the Tohoku Forearc block, than in the backarc side blocks (5–10 mm/yr on average). The Pacific Plate subduction rate at the Kuril and Japan Trenches was approximately 76–78 mm/yr. This velocity was slightly lower than that of previous studies (DeMets et al., 2010; Loveless & Meade, 2010). Although the relative block motion rates were less than 5 mm/yr for most block boundaries, this study found fast relative motions in some boundaries. Between the Okhotsk and the Tohoku Forearc blocks, a 5–8 mm/yr compression (boundary–normal direction) and a 5–8 mm/yr right lateral (boundary–parallel direction) motion were estimated. Between the Tohoku Forearc and the Tohoku Backarc blocks, a 3–7 mm/yr compression was estimated. This boundary corresponds to the Ou Backbone Range, which is characterized by a reverse fault zone, and has been known as a geodetically high strain rate zone (Miura et al., 2002; Toya & Kasahara, 2005). The estimated compression consists of the high geodetic strains. Between the southern part of the Tohoku Backarc and the Niigata blocks, called the NKTZ, a 2–10 mm/yr compression and a 3–7 mm/yr right lateral motion were estimated. GNSS observations show a large velocity gradient for compressional direction near the

boundary (Figure **2.2**). This compression represents strain concentration at and/or around the boundary. Some models were presented to explain high strain rates around the boundary. Hyodo & Hirahara (2003) considered the interplate coupling on the subducting Pacific Plate interface and the localized viscoelastic layer in the elastic crust. Nishimura et al. (2012) explained this by dislocation in the crust deeper than the seismic zones and viscoelastic response considering gravity.

Table A.1. List of Euler vector estimates. All Euler vectors are relative to the Eurasian plate. Positive angular velocities indicate counterclockwise rotation. Pole location and angular velocity of the Pacific Plate area refer to the MORVEL plate model (DeMets et al., 2010). Covariances are Cartesian and have units of 10^{-8} rad^2/Myr^2.

Block	Angular velocity			Variances and covariances					
	Lat. (°E)	Lon. (°N)	ω (deg/Myr)	σ_{xx}	σ_{xy}	σ_{xz}	σ_{yy}	σ_{yz}	σ_{zz}
Amurian	-30.08	-47.32	0.56	161.91	-174.92	-163.74	189.23	177.03	165.86
Niigata	-37.80	-38.83	0.89	635.77	-559.19	-651.22	493.13	573.48	668.81
Tohoku Backarc	-57.33	-27.38	0.23	192.79	-163.88	-203.85	139.60	173.21	216.12
Okhotsk	-46.69	-35.34	0.73	641.23	-474.26	-785.76	352.54	580.64	964.42
Tohoku Forearc	-80.95	56.22	0.17	196.00	-164.25	-197.48	138.87	165.50	200.23
Izu Ogaswara	-37.42	-31.57	2.4	455.25	-360.79	-354.29	294.35	283.87	281.17
Pacific	-61.30	101.10	0.86	-	-	-	-	-	-

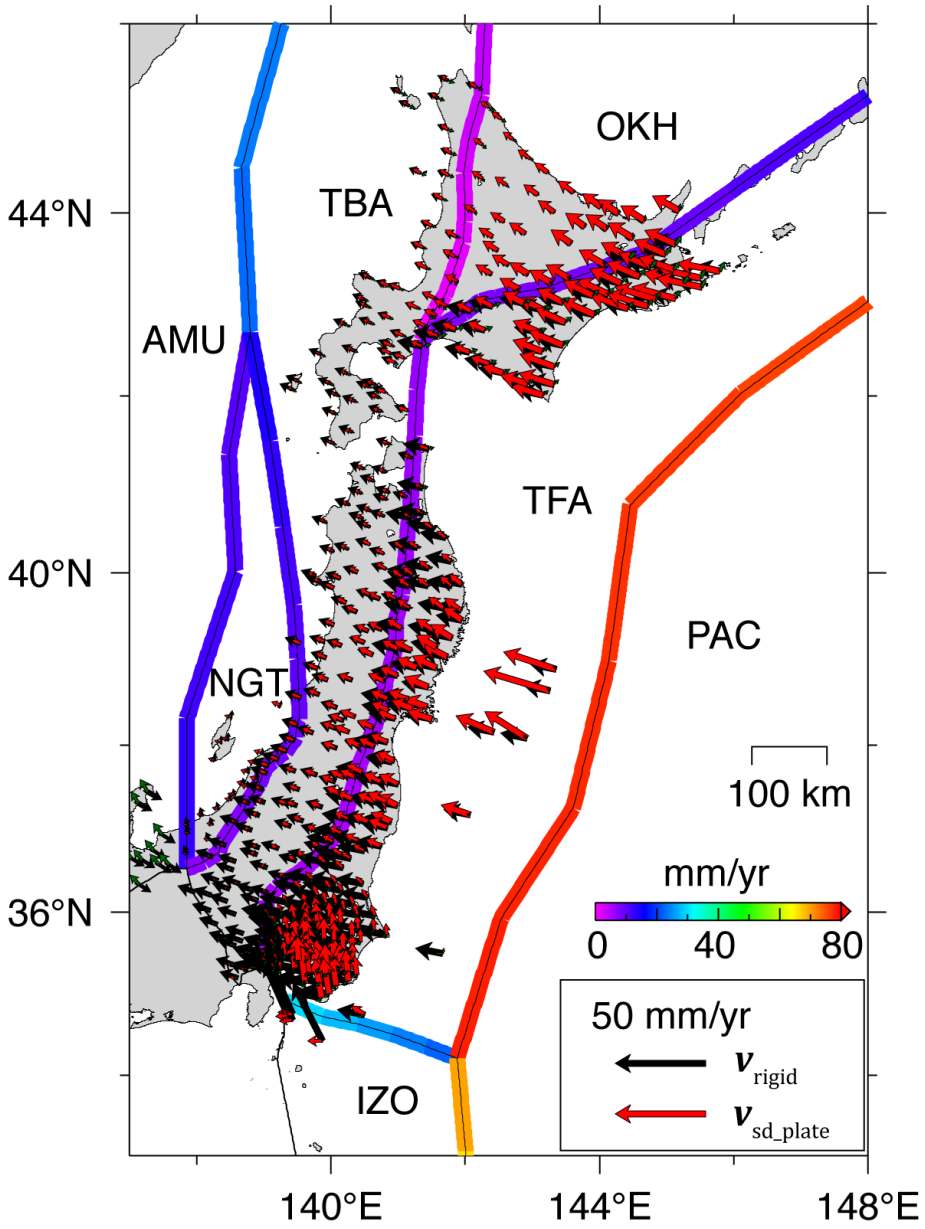

Figure A.1. Map showing calculated vectors and relative motion rates. Black and red arrows depict the rigid motion rate and elastic response from interplate slip deficits, respectively. The reference for rigid motion is the Eurasian plate. The color scale shown along the block boundary line represents the relative block motion rate.

A.2. Estimated internal block strains

In Figure A.1(b), the internal strain rate of each block is plotted with green cross vectors, the surface trace of active faults (Nakata & Imaizumi, 2002) with red lines, and the inland earthquake mechanisms with colored circles. Table S2 also lists internal block strain results. Because the study did not estimate the subducting and internal block strain rates (i.e., of the Pacific Plate and Izu–Ogasawara blocks), the figure and table for the two blocks do not show these results. The focal mechanisms plotted in the figure were observed by the F-net Broadband Seismograph Network maintained by the National Research Institute for Earth Science and Disaster Resilience (Okada et al., 2004).

The magnitude of principal strain rates seems to be larger (~20–27 nanostrain/yr) in Hokkaido, which is the southern part of the Okhotsk plate, than those in other blocks. Considering that a remarkable intraplate earthquake has not occurred in this block, the estimated strain may reflect long-term stress field formed by geological processes. Hokkaido is located in a strong deformation area owing to large-scale collisions in the Eastern Japan Sea deformation zone (Nakamura, 1983; Le Pichon et al., 1998), the convergence of the Okhotsk plate in central Hokkaido (Kato et al., 2004; Komatsubara, 2015), and the collision of the Kuril forearc sliver at the Hidaka Mountain (Kimura, 1996; Kimura & Kusunoki, 1997). The combination of these stress fields may be qualitatively expressed as the estimated strain when the uniform strain field in a block is assumed.

In the Tohoku Forearc block, 16 nanostrain/yr of compressional strain with an azimuth of 120 degree was estimated. This compressional direction is roughly perpendicular to the strike of the predominant reverse fault and consistent with the P-axis of the focal mechanism in the block, particularly in central Tohoku. The surface displacement rate calculated from the strain rate was less than 3.7 mm/yr, which was 22–25% of the mean rigid motion and elastic response from the interplate slip deficit.

In the Niigata block, the largest compressional strain was 15 nanostrain/yr with a roughly north–south orientation azimuth. The compressional strain was also estimated as another principal strain, and the magnitude was less than half of the largest one. The estimated largest compressional strain in this block was not consistent with both the P-axis of most focal mechanisms and strain fields estimated from the onshore geodetic observation data (Sagiya, 2004; Sagiya et al., 2000). This paradox may have been caused by the location of the block boundary, the treatment of the heterogeneous strain field, and the long-term geologically accumulated strain. Fortunately, because this block is sufficiently far from the forearc side of Tohoku and Hokkaido, where the surface crustal deformation would be affected by the mechanical locking on the subducting Pacific Plate interface, the mechanical locking distribution estimates on the plate interface would not be affected by the crustal deformation data and/or strain rate estimates in the Niigata block.

Table A.2. List of internal block strain estimates. Normal strain rates area measured as extensional positive. Reference points of each block are centroids of the observation site network within each block.

Block	Reference points		Principal strain rates				Uncertainties			
	Lat. (°N)	Lon. (°E)	Maximum normal strain (10^{-9}/yr)	Minimum normal strain (10^{-9}/yr)	Direction of the minimum strain (°)	Maximum shear strain (10^{-9}/yr)	Maximum normal strain (10^{-9}/yr)	Minimum normal strain (10^{-9}/yr)	Direction of the minimum strain (°)	Maximum shear strain (10^{-9}/yr)
Amurian	34.759	132.836	14.5	-17.7	193.4	16.1	3.8	2.6	6.7	2.3
Niigata	37.521	138.477	-6.3	-15.1	273.7	4.4	3.6	4.6	28.4	2.9
Tohoku Backarc	39.597	140.054	2.9	-9.7	225.4	6.3	4.1	4.1	12.6	3.0
Okhotsk	43.887	143.077	20.3	-26.9	230.4	23.6	5.5	5.8	4.9	4.3
Tohoku Forearc	38.323	141.205	8.1	-16.2	210.5	12.1	2.6	2.7	8.2	2.0

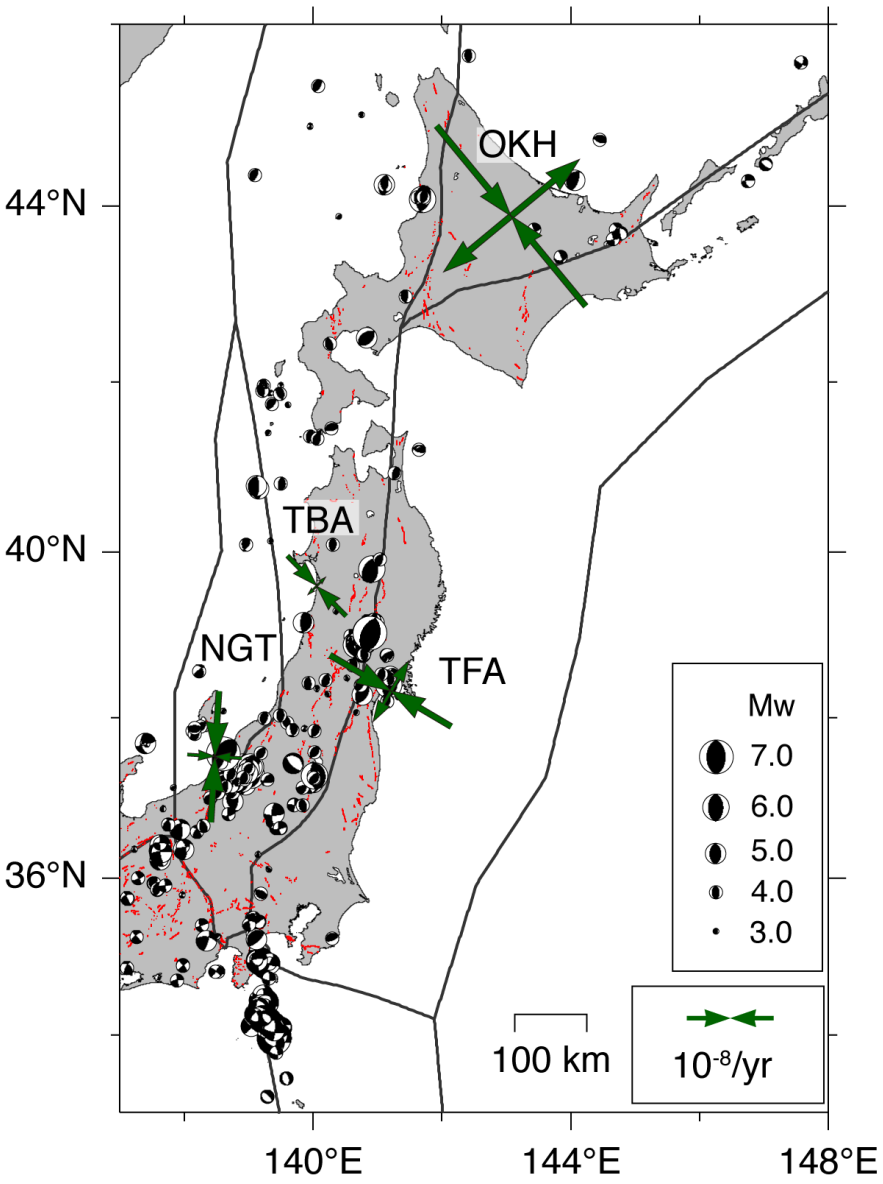

Figure A.2. Map showing principal strain rates calculated from estimated internal block strain rates. Green cross arrows indicate principal strain rates. The locations where strain crosses are plotted are reference points, which are the centroid of the observation site network within each block. Red lines are active fault tracings (Nakata & Imaizumi, 2002). The black and white circles indicate earthquake epicenters and mechanisms. Earthquakes that occurred offshore the Pacific Plate side were removed from the figure. Mechanism data were provided by the F-net broadband seismograph network maintained by the NIED (Okada et al., 2004). The data period, magnitude range, and lower depth limit are 1997–2010, 3–7.5, and 20 km, respectively.

Appendix B
Rigid motion and internal block strain results: Southwest Japan

B.1. Estimated Euler vectors and the ratio between rigid motion and displacement due to slip deficit

The estimated Euler vector and its covariance are shown in Table B.1. I calculated the rigid motion rates at the observation sites on the basis of estimated Euler vectors (Figure B.1(a)). Because the rigid motion of Amurian plate was fixed to zero in the REMC inversion, plotted rigid motion rates are relative to Amurian plate. Surface displacements rate due to slip deficits on the plate interface were also calculated and shown in the same figure. The colored line along the block boundary indicate the relative block motion rate, which was calculated as $\sqrt{v_{\mathrm{str}}^2 + v_{\mathrm{ext}}^2}$, where the v_{str} and v_{ext} represent strike slip and extension rates of the relative motion along the block boundary, respectively.

The direction of the rigid motion is WSW and WNW dominant in most blocks excluding the Okinawa-North block in which southward rigid motion was calculated from the estimated Euler vector. The rigid motion rate of the forearc side is higher than that of the backarc side, which is the same as the northeast (Chapter A.1). The average rigid motion rates in each block are shown in Figure B.1(a) are 15 (Nankai block), 10 (Okinawa-North block), 10 (Kinki block), 13 (Chubu block), 28 (Izu Micro Plate), 42 (Izu–Ogasawara block), 15 (Okhotsk plate), and 2 mm/yr (Setouchi block).

The plate (block) convergence rates along the Nankai Trough differ significantly between western and eastern sides at 50–54 mm/yr in western side (i.e., along the boundary between Philippine Sea Plate and Nankai block) and 19–20 mm/yr in eastern side (i.e., along the boundary between Izu Micro Plate and Nankai block). This

convergence rate contrast caused the slip deficit rate to contrast between western and eastern sides of the plate interface along the Nankai Trough (Chapter 3.3). Because of this, the surface displacement rate is dominated with the displacement rate due to interplate slip deficits rather than the rigid motion rate in the western Nankai block (velocity ratio between the rigid motion and the displacement due to the interplate slip deficits is approximately 0.3–0.7), whereas the rigid block motion rates are comparable to or larger than the displacement rates due to the interplate slip deficits in eastern Nankai block.

The Philippine Sea Plate subducts (or collides) beneath the Izu Micro Plate. The convergence rate at the boundary between Philippine Sea and Izu Micro Plates is 28–29 mm/yr, which is higher than the convergence rate between Izu Micro Plate and Nankai block. Along the boundary, remarkable topographic feature called the Zenisu ridge exists. Although this study did not focus on this boundary because of poor geodetic observations and unclear tectonic boundary settings around the boundary, seismic potential accompanying huge tsunami was proposed in few models (e.g., Nakata et al., 2013). Thus, it may be an urgent task to develop a seafloor geodetic observation network as well as to reveal the accurate subsurface structure by seismic exploration for the evaluation of seismic and tsunami hazard around Zenisu ridge.

Relatively rapid relative motion was found along some inland block boundaries, including that between Nankai and Setouchi blocks. This boundary corresponds to the western part of the Median Tectonic Line. The relative motion rate along the boundary was ~10 mm/yr, coinciding with the average slip rate of 5–10 mm/yr that was estimated on the basis of the regional dense GNSS observations conducted around the Median Tectonic Line in Shikoku (Tabei et al., 2002, 2003). The others are boundaries between Kinki and Setouchi blocks, Chubu and Setouchi blocks, and Chubu block and Amurian

plate. These boundaries can be connected with the block boundary that is between Niigata and Tohoku Backarc blocks (Chapter A.1), where the relatively fast relative motion rate was found in northeast Japan. As described in Chapter A.1, these boundaries correspond to the Niigata–Kobe Tectonic Zone (e.g., Sagiya et al., 2000), and some models were presented to explain high strain rates around the boundary, such as the interplate coupling on the Pacific Plate interface and the localized viscoelastic layer in the elastic crust (Hyodo & Hirahara., 2003), dislocation in the crust deeper than the seismic zones and the viscoelastic response considering gravity (Nishimura et al., 2012).

Table B.1. List of Euler vector estimates. All Euler vectors are relative to Amurian plate. Positive angular velocities are counterclockwise rotation. Pole location and angular velocity of Pacific and Yangtze plates are fixed to the value presented by MORVEL plate model (DeMets et al., 2010), and they were not estimated in this study. Covariances are Cartesian and have units of 10^{-8} rad^2/Myr^2.

Block	Angular velocity			Variances and covariances					
	Lat. (°E)	Lon. (°N)	ω (deg/Myr)	σ_{xx}	σ_{xy}	σ_{xz}	σ_{yy}	σ_{yz}	σ_{zz}
Okhotsk	-43.51	-38.47	0.99	51.63	-44.10	-53.22	38.13	45.69	55.81
Yangtze	54.20	-77.50	0.04	-	-	-	-	-	-
Okinawa North	31.94	136.76	0.92	20.65	-23.66	-18.71	28.08	22.01	17.85
Okinawa South	31.65	143.23	1.28	67.76	-74.59	-58.55	93.35	59.03	57.96
Kinki	-38.62	-44.47	1.21	243.39	-233.42	-233.24	224.19	223.82	224.15
Chubu	4.28	135.85	0.22	760.10	-694.61	-726.34	635.06	663.86	694.52
Setouchi	-38.08	-49.61	0.27	20.08	-21.20	-19.99	22.50	21.16	20.06
Nankai	-45.79	-47.18	0.53	693.45	-707.88	-667.45	722.97	681.53	643.23
Izu Micro	-52.50	-34.35	0.79	614.37	-590.64	-569.12	569.12	547.62	529.57
Izu Ogasawara	-44.03	-26.51	1.44	89.15	-62.07	-73.97	46.81	52.42	67.62
Philippine Sea	-51.33	-24.79	1.36	252.48	-287.64	-232.87	333.19	265.04	217.12
Pacific	-65.90	97.30	0.93	-	-	-	-	-	-

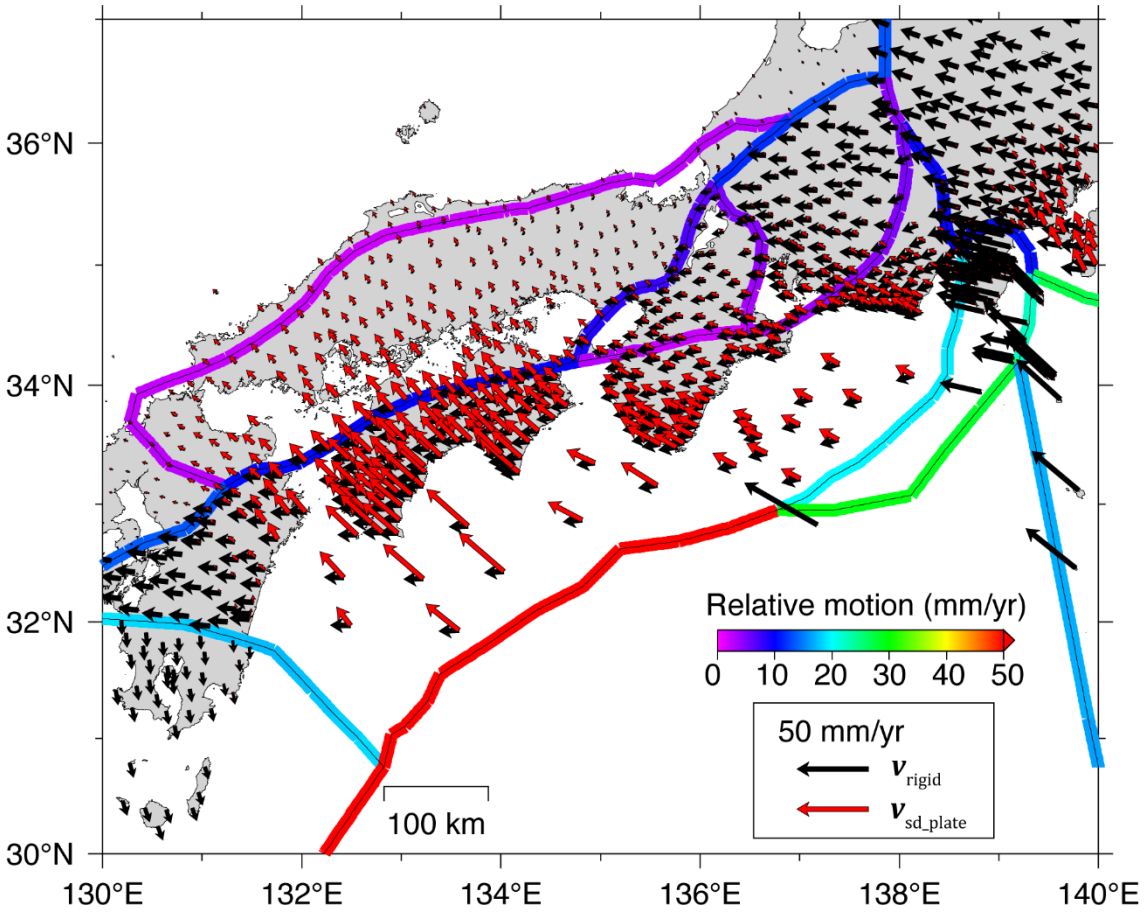

Figure B.1. Map showing the calculated displacement rates. Black and red arrows depict the rigid motion rate and elastic response from interplate slip deficits. The reference for rigid motions is the Amurian plate. The color scale shown along the block boundary line represents relative block motion rate.

B.2. Estimated internal block strains

The estimated strain rate in each block was listed in Table B.2. I calculated the principal strain rates from the estimated strain rate $\dot{e}_{xx}$, $\dot{e}_{xy}$, and $\dot{e}_{yy}$ and plotted with green cross vectors in Figure B.1(b). The surface trace of active faults (Nakata & Imaizumi, 2002) and the inland earthquake mechanisms were also respectively plotted with red lines and colored circle in the same figure. Because the strain rates of Philippine Sea, Pacific and Yangtze plates were not estimated (fixed to zero), the figure and table for the three blocks do not show these results. The focal mechanisms plotted in the figure were observed by the F-net Broadband Seismograph Network maintained by NIED (Okada et al., 2004).

Compressional strains with WNW to NNW directions were estimated in Nankai, Setouchi, Kinki, and Chubu blocks and Amurian plate, those are overriding bocks of southwest Japan. The estimated magnitude of the strain rate was estimated on the order of 10^{-9}–10^{-8}/yr. Relatively higher strain rates were estimated in Nankai (3.2×10^{-8}/yr of compression with the axis of N53° W) and Chubu (2.4×10^{-8}/yr of compression with the axis of N62° W) blocks. For overriding blocks, many intraplate earthquakes occurred in the blocks and along the inland bock boundaries (Figure B.1(b)). The mechanism of these intraplate earthquakes exhibited mainly strike slip, except for few events, which exhibited reverse fault type occurred near Ise bay and western Wakayama prefecture. However, the mechanism expected from the estimated strain rates in these blocks may be reverse fault type with the P axis of WNW–NNW direction, which conflicts with the dominant mechanisms in these blocks. Instead, the compressional strain orientation is close to the subducting direction of the Philippine Sea and Izu Micro Plates. In the new model developed in this study, only the shear stress working on the plate interface and the displacement due to the shear strain were considered. Thus, the displacement due to the

normal stress working on the plate interface may be estimated as the compressional strain with the plate subducting direction.

Table B.2. List of internal block strain estimates. The unit of strain rates is 10^{-9}/yr. Normal strain rates area measured as extensional positive. Reference points of each block area centroid of the observation site network within each block.

Block	Reference points		Principal strain rates				Uncertainties			
	Lat. (°N)	Lon. (°E)	Maximum normal strain (10^{-9}/yr)	Minimum normal strain (10^{-9}/yr)	Direction of the minimum strain (°)	Maximum shear strain (10^{-9}/yr)	Maximum normal strain (10^{-9}/yr)	Minimum normal strain (10^{-9}/yr)	Direction of the minimum strain (°)	Maximum shear strain (10^{-9}/yr)
Amurian	34.658	132.726	1.7	-8.3	206.4	5.0	2.2	1.6	29.1	1.5
Okhotsk	36.021	139.455	8.7	-12.8	291.3	10.7	2.3	1.7	53.2	1.6
Okinawa North	30.954	130.524	6.7	5.1	18.1	0.8	3.7	2.3	339.9	2.5
Okinawa South	26.557	127.867	8.7	-8.5	339.8	8.6	2.3	2.4	41.8	1.9
Kinki	34.822	135.894	0.6	-5.4	248.3	3.0	2.1	1.6	217.0	1.3
Chubu	35.452	137.238	5.2	-23.6	207.9	14.4	3.6	3.3	12.8	3.1
Setouchi	34.590	133.475	1.3	-14.9	202.8	8.1	2.1	1.7	231.8	1.2
Nankai	33.653	134.567	7.8	-32.4	216.2	20.1	3.9	4.3	3.8	3.7
Izu Micro	34.846	138.978	7.1	2.9	300.2	2.1	4.0	3.9	63.8	3.8
Izu Ogasawara	32.664	140.045	8.6	-8.8	213.0	8.7	2.2	2.1	6.3	1.8

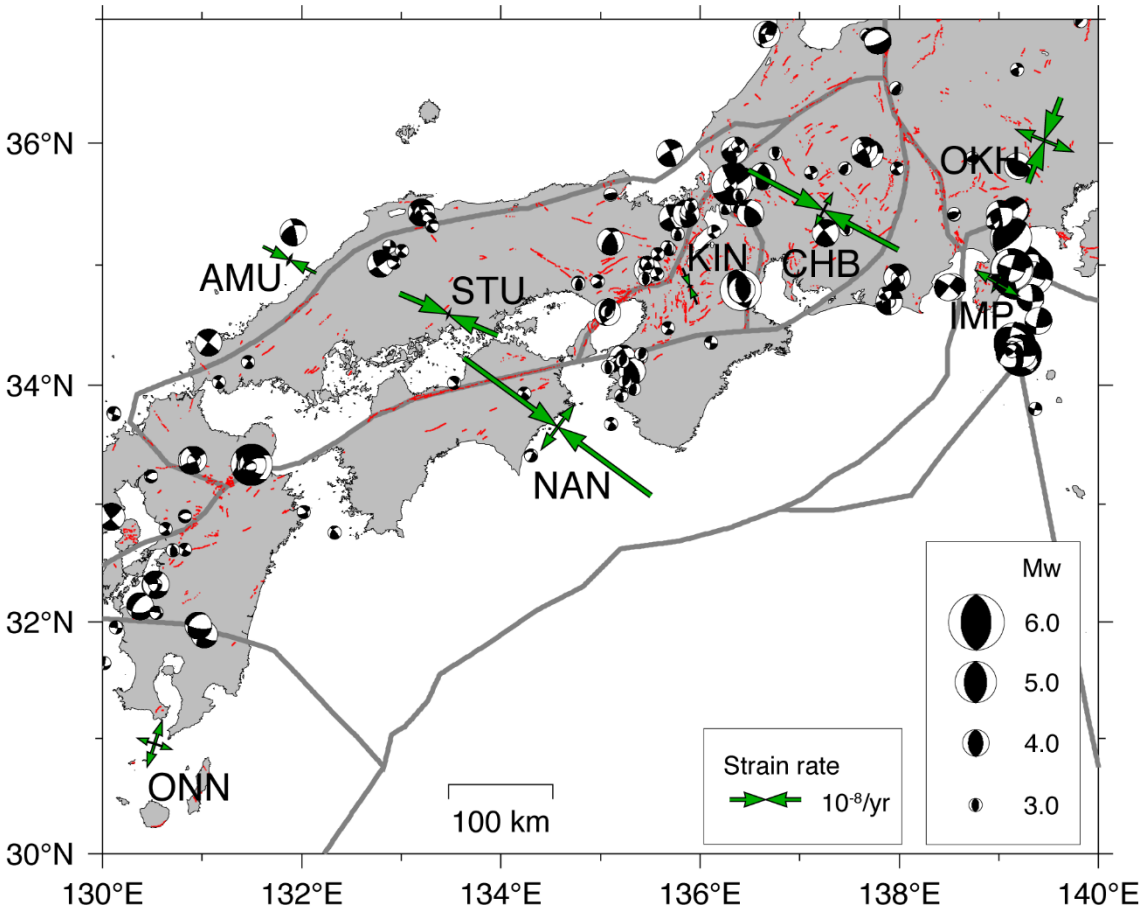

Figure B.2. Map showing the principal strain rates calculated from the estimated internal block strain rates (Table B.2). Green cross arrows are the principal internal block strain rates. The locations where the strain crosses are plotted is the reference point, which is the centroid of the observation site network within each block. Note that the actual centroid location of the observation network included in the Amurian plate is located at the point outside of the Amurian plate and near the centroid location of the Setouchi block. To avoid that one may confuse to recognize the strain rates of Setouchi block and Amurian plate, the principal strain rate cross of the Amurian plate were replotted inside of the Amurian plate. Red lines are active fault tracings (Nakata & Imaizumi, 2002). The black and white circles indicate the earthquake epicenters and mechanisms. Earthquakes that occurred offshore of the Pacific Plate side are removed from the figure. The mechanism data were provided by the F-net broadband seismograph network maintained by the NIED (Okada et al., 2004). The data period, magnitude ranging, and lower depth limit are 2006–2009 3–6, and 20 km, respectively.

Appendix C
Displacement rate data for REMC inversion

This chapter provides tables listing the displacement rate data used for REMC inversions. In each table, code (number or name), location in longitude and latitude, EW, NS, and UD components of the displacement rate, and their uncertainties are provided. The height of sites was fixed to 0 km. The UD component of the displacement rates and its uncertainties of seafloor GNSS/A sites was not estimated and thus not listed in the following tables.

C.1.Northeast Japan

Table C.1. List of displacement rates at onshore and seafloor observation sites in northeast Japan used in the analysis outlined in Chapter 2. The reference frame is the Eurasian plate, taken from the MORVEL plate motion model (DeMets et al., 2010).

Site	Site position		Displacement rate (mm/yr)			Uncertainties (mm/yr)		
	Lon. (°E)	Lat. (°N)	EW	NS	UD	EW	NS	UD
93001	139.542	36.295	-19.92	4.08	-4.76	0.07	0.06	0.10
93002	140.174	36.263	-20.43	6.17	-3.46	0.07	0.04	0.09
93003	139.811	36.204	-19.03	5.33	-12.84	0.07	0.04	0.11
93004	140.544	36.181	-21.27	6.36	-1.99	0.07	0.05	0.09
93005	139.345	36.121	-18.92	6.34	-2.20	0.07	0.04	0.10
93006	140.343	36.097	-20.59	6.70	-2.24	0.07	0.04	0.09
93007	139.637	36.087	-18.24	7.47	-6.75	0.07	0.04	0.10
93008	139.800	36.011	-18.71	7.00	-3.16	0.07	0.04	0.09
93009	140.659	35.955	-20.23	7.32	-3.20	0.08	0.05	0.09
93010	140.403	35.970	-20.16	7.63	-2.20	0.07	0.05	0.10
93011	139.464	35.926	-18.93	7.53	-0.54	0.08	0.04	0.10
93012	139.993	35.940	-19.10	7.80	-1.66	0.07	0.04	0.09
93013	139.652	35.937	-18.63	7.11	-2.97	0.07	0.04	0.10
93014	140.145	35.874	-25.07	5.36	-3.24	0.08	0.05	0.09
93015	140.407	35.803	-19.33	8.26	-4.77	0.08	0.05	0.10
93016	139.813	35.780	-18.61	9.15	-1.41	0.08	0.05	0.10
93017	139.643	35.759	-19.10	9.70	-2.22	0.08	0.05	0.09
93018	140.025	35.786	-18.37	8.29	-0.63	0.08	0.05	0.10
93019	139.488	35.710	-18.32	10.97	0.55	0.07	0.05	0.13
93020	140.315	35.717	-18.60	8.35	-8.03	0.08	0.06	0.10
93021	140.647	35.777	-19.47	8.12	-3.10	0.08	0.06	0.09
93022	140.837	35.726	-17.99	7.75	-1.46	0.09	0.05	0.09
93023	139.902	35.675	-17.95	9.55	-1.29	0.08	0.05	0.10
93024	140.448	35.642	-19.04	8.95	-7.79	0.08	0.06	0.09
93025	140.187	35.544	-16.11	11.56	-2.18	0.08	0.06	0.09
93026	139.673	35.563	-18.83	12.82	-2.86	0.08	0.05	0.09

93027	140.318	35.530	-15.89	10.67	-14.70	0.08	0.06	0.09
93028	139.468	35.521	-20.14	12.00	-1.74	0.07	0.04	0.10
93029	139.323	35.483	-21.07	11.96	-3.04	0.08	0.05	0.10
93030	140.051	35.448	-19.21	13.78	-5.90	0.09	0.06	0.10
93031	139.045	35.415	-19.05	8.91	-1.57	0.08	0.04	0.10
93032	139.654	35.436	-20.70	15.53	-3.18	0.09	0.05	0.09
93033	140.337	35.421	-20.55	12.69	-12.99	0.09	0.08	0.09
93034	139.466	35.327	-23.05	17.89	-5.63	0.08	0.05	0.10
93035	139.263	35.305	-22.53	15.84	-5.76	0.08	0.04	0.10
93036	139.826	35.312	-22.72	19.85	-4.86	0.09	0.06	0.09
93037	140.147	35.333	-18.58	17.06	-3.24	0.09	0.07	0.09
93038	138.882	35.322	-18.17	4.03	-2.15	0.08	0.04	0.11
93039	139.844	35.144	-22.98	26.07	-4.63	0.10	0.08	0.09
93040	139.624	35.132	-13.38	30.49	-5.42	0.09	0.08	0.09
93041	140.268	35.166	-18.83	19.02	-3.90	0.10	0.10	0.10
93044	140.079	35.112	-21.87	23.93	-5.23	0.10	0.07	0.10
93045	139.954	35.255	-22.46	20.98	-5.03	0.09	0.07	0.10
93047	139.864	34.954	-19.43	34.86	-5.88	0.12	0.10	0.10
93051	139.381	34.784	-24.15	41.04	2.77	0.12	0.16	0.10
93055	139.433	34.687	-15.38	38.40	-0.49	0.16	0.24	0.10
93063	139.268	35.724	-19.07	8.95	-2.32	0.07	0.04	0.11
93064	138.976	35.623	-19.06	6.54	-1.43	0.07	0.04	0.10
93065	139.157	35.610	-19.28	9.44	-1.27	0.07	0.04	0.11
93066	139.205	35.429	-18.10	14.85	-3.87	0.07	0.04	0.11
93067	139.665	35.267	-23.27	22.40	-6.55	0.09	0.06	0.10
93070	138.814	35.497	-17.07	4.73	-3.74	0.07	0.04	0.10
93071	138.563	35.362	-17.37	3.25	-3.36	0.08	0.04	0.11
93072	138.771	35.306	-18.09	2.90	-2.05	0.08	0.04	0.10
93075	138.617	35.203	-16.81	2.37	-4.98	0.08	0.05	0.10
940001	141.750	45.403	-2.05	4.70	-1.21	0.07	0.05	0.10
940002	143.224	44.434	-8.67	6.74	-0.09	0.07	0.04	0.10
940003	141.756	44.398	-5.67	4.33	-0.25	0.06	0.04	0.10
940004	144.676	43.916	-18.96	11.47	0.10	0.07	0.05	0.10
940005	144.449	43.508	-25.86	14.06	-5.75	0.07	0.05	0.10
940006	145.511	43.290	-34.20	16.07	-5.89	0.07	0.04	0.10
940007	142.482	43.590	-18.63	7.13	-2.99	0.07	0.04	0.11
940008	141.510	43.854	-8.92	4.16	0.90	0.07	0.04	0.10
940009	145.130	43.070	-35.26	15.66	-4.98	0.07	0.05	0.10
940010	144.432	42.963	-29.35	14.93	-7.95	0.07	0.05	0.10
940011	143.459	43.029	-24.83	13.30	-6.38	0.07	0.05	0.10
940012	142.402	42.981	-23.59	7.21	-0.35	0.07	0.04	0.11
940013	141.031	43.178	-10.95	3.19	-1.05	0.07	0.04	0.10
940014	141.731	42.983	-17.10	3.85	-3.59	0.07	0.04	0.10
940015	143.331	42.322	-31.17	14.51	-1.17	0.07	0.05	0.12
940016	142.365	42.357	-21.92	8.03	-2.12	0.07	0.05	0.10
940017	139.858	42.451	-17.45	3.92	1.49	0.07	0.04	0.09
940018	140.942	42.374	-15.36	7.84	-2.68	0.07	0.08	0.10
940019	143.157	42.006	-29.36	10.32	-2.83	0.07	0.04	0.10
940020	139.520	42.154	-14.02	4.52	-9.12	0.08	0.04	0.11
940021	140.107	42.008	-13.70	4.37	0.25	0.07	0.04	0.10
940022	140.748	41.826	-12.41	4.70	0.12	0.07	0.05	0.10
940023	140.041	41.466	-9.52	4.56	-0.85	0.07	0.05	0.10
940024	141.213	41.301	-14.16	5.16	-3.48	0.07	0.04	0.10
940025	140.830	40.841	-12.37	5.05	-2.26	0.13	0.08	0.19

940026	140.273	40.779	-10.42	5.70	-2.06	0.07	0.04	0.10
940027	141.789	40.133	-18.26	5.03	1.92	0.07	0.05	0.10
940028	141.940	39.572	-21.15	5.79	1.33	0.07	0.04	0.11
940030	139.776	39.968	-8.06	7.17	-0.11	0.07	0.04	0.10
940031	140.048	39.399	-12.09	8.48	-1.01	0.07	0.04	0.10
940032	139.809	38.895	-12.60	7.65	-0.62	0.07	0.04	0.10
940033	140.319	38.759	-17.59	9.37	0.18	0.07	0.05	0.12
940034	139.556	38.556	-14.24	5.90	-3.43	0.07	0.05	0.11
940035	140.366	38.331	-22.87	7.65	-1.48	0.07	0.05	0.11
940036	141.441	38.449	-34.86	10.17	-3.28	0.07	0.05	0.09
940037	140.954	38.317	-29.84	8.95	-5.22	0.07	0.04	0.10
940038	140.908	37.801	-29.94	7.97	-2.62	0.07	0.05	0.10
940039	140.325	37.362	-24.94	5.80	-7.13	0.12	0.07	0.16
940040	139.792	37.644	-18.67	5.34	-1.87	0.07	0.04	0.10
940041	140.903	37.091	-27.54	9.73	2.54	0.07	0.04	0.10
940043	139.726	36.402	-20.01	5.89	-1.39	0.07	0.04	0.09
940044	138.906	36.697	-17.69	4.71	-3.40	0.07	0.04	0.10
940045	138.865	36.259	-18.19	5.63	-1.68	0.07	0.04	0.10
940048	138.583	35.590	-20.11	6.99	-3.38	0.07	0.04	0.11
940049	139.510	38.231	-17.14	5.71	-3.04	0.07	0.04	0.11
940050	138.989	37.896	-8.63	3.74	-8.26	0.07	0.04	0.09
940051	138.574	37.398	-6.93	4.03	-2.77	0.07	0.04	0.10
940052	137.487	36.929	-2.05	2.75	-2.49	0.07	0.04	0.10
940053	136.889	37.382	1.11	2.68	-0.62	0.07	0.04	0.10
940054	136.650	36.663	0.39	1.53	-5.06	0.06	0.04	0.10
940055	136.173	36.231	1.50	2.56	-3.60	0.07	0.04	0.10
940073	133.699	35.490	5.60	5.46	-4.05	0.07	0.07	0.11
940074	133.059	35.434	14.80	-2.15	-4.14	0.14	0.06	0.12
940075	132.209	35.003	4.88	1.35	-4.36	0.07	0.04	0.10
940076	131.610	34.616	3.30	2.70	-2.33	0.07	0.04	0.10
940091	129.850	33.476	5.72	-0.81	-2.76	0.06	0.04	0.11
940092	129.860	32.700	3.75	-3.04	-0.63	0.08	0.05	0.17
942001	141.845	43.529	-12.69	4.07	0.20	0.07	0.06	0.19
942003	142.185	27.096	-53.45	25.19	-5.00	0.09	0.06	0.16
950101	142.170	45.336	-3.20	4.01	-0.97	0.07	0.04	0.10
950102	141.038	45.276	0.12	3.62	0.72	0.07	0.05	0.11
950103	142.537	45.002	-5.63	4.22	1.30	0.07	0.04	0.12
950104	141.741	44.892	-2.66	3.86	0.50	0.07	0.04	0.10
950105	142.265	44.728	-5.61	3.96	0.72	0.07	0.04	0.12
950106	141.330	44.427	-3.56	2.86	1.81	0.07	0.04	0.11
950107	142.626	44.295	-9.41	5.81	0.05	0.07	0.04	0.11
950108	144.030	44.064	-16.41	6.65	-1.14	0.07	0.05	0.10
950109	145.186	44.019	-17.79	12.84	-0.90	0.07	0.05	0.13
950110	142.152	44.007	-10.37	5.41	0.91	0.07	0.04	0.13
950111	143.334	44.006	-12.85	8.57	0.77	0.07	0.04	0.11
950112	143.927	42.895	-26.98	15.97	-5.47	0.07	0.04	0.10
950113	144.987	43.549	-26.31	13.30	-4.66	0.07	0.04	0.11
950114	143.787	43.849	-15.13	8.03	0.19	0.07	0.04	0.10
950115	145.131	43.662	-25.23	14.07	-6.13	0.07	0.04	0.11
950116	144.774	43.409	-28.48	15.00	-7.87	0.07	0.05	0.10
950117	141.431	43.405	-11.65	2.57	-1.22	0.07	0.04	0.10
950118	145.115	43.383	-30.59	15.63	-7.52	0.07	0.04	0.10
950119	145.801	43.367	-33.85	13.94	-6.74	0.07	0.05	0.10
950120	140.597	43.293	-9.31	3.15	0.93	0.09	0.05	0.15

950121	143.562	43.289	-23.24	11.16	-4.99	0.07	0.04	0.10
950122	144.325	43.233	-27.86	15.34	-8.84	0.07	0.04	0.10
950123	143.298	43.232	-22.93	11.61	-3.47	0.07	0.04	0.10
950124	144.127	43.121	-26.78	15.41	-6.16	0.07	0.04	0.10
950125	144.843	43.058	-32.75	16.33	-5.47	0.07	0.04	0.10
950126	140.499	43.057	-10.59	2.55	3.88	0.07	0.04	0.10
950127	140.544	42.985	-11.36	2.18	3.21	0.07	0.04	0.11
950128	141.290	42.971	-13.37	2.46	-1.13	0.07	0.04	0.12
950129	140.883	42.858	-12.86	1.86	0.39	0.07	0.05	0.11
950130	140.604	42.803	-15.05	-0.34	2.91	0.07	0.05	0.11
950131	140.233	42.786	-14.84	3.09	4.11	0.07	0.04	0.10
950132	141.864	42.729	-18.35	4.10	-3.83	0.07	0.05	0.11
950133	142.296	42.727	-21.58	7.35	-2.53	0.07	0.04	0.11
950134	143.103	42.699	-25.85	14.46	-1.16	0.07	0.04	0.11
950135	141.075	42.668	-16.31	-0.23	-1.99	0.07	0.05	0.12
950136	141.602	42.656	-17.15	4.02	-5.63	0.07	0.04	0.10
950138	143.461	42.552	-29.05	16.13	-1.58	0.07	0.04	0.10
950139	141.361	42.550	-16.12	4.69	-8.72	0.07	0.05	0.13
950140	140.354	42.494	-13.66	3.55	4.00	0.07	0.04	0.11
950141	142.060	42.481	-11.30	4.87	-6.23	0.07	0.04	0.10
950142	142.567	42.248	-21.63	7.43	0.11	0.07	0.04	0.10
950143	140.250	42.244	-15.60	1.59	2.17	0.07	0.07	0.11
950144	142.935	42.131	-25.57	10.11	-2.49	0.07	0.04	0.10
950145	140.004	42.131	-15.37	3.85	1.91	0.07	0.04	0.11
950146	140.569	42.099	-13.07	5.09	3.39	0.07	0.04	0.10
950147	140.806	42.043	-11.66	5.03	2.45	0.07	0.05	0.11
950148	141.141	41.834	-17.49	10.04	-5.93	0.07	0.05	0.11
950149	140.316	41.599	-10.42	4.00	1.19	0.07	0.04	0.12
950150	140.881	41.455	-13.02	5.45	-0.17	0.07	0.04	0.10
950151	140.636	41.043	-11.50	5.16	-1.27	0.07	0.04	0.11
950152	141.368	40.968	-16.01	5.77	-1.12	0.07	0.04	0.10
950153	141.198	40.625	-14.49	5.72	-2.56	0.07	0.04	0.11
950154	139.928	40.578	-12.55	6.12	-0.55	0.07	0.04	0.11
950155	140.578	40.524	-12.26	6.25	0.79	0.07	0.04	0.10
950156	141.511	40.515	-17.81	6.01	0.69	0.07	0.04	0.10
950157	141.076	40.291	-12.97	6.79	-1.33	0.07	0.04	0.11
950158	141.713	40.405	-19.14	5.48	2.21	0.07	0.04	0.11
950159	141.294	40.291	-15.60	6.54	-1.37	0.07	0.04	0.11
950160	141.462	40.049	-16.96	6.64	-3.38	0.07	0.04	0.11
950161	141.225	39.981	-17.02	7.43	-5.42	0.07	0.04	0.12
950162	141.951	39.869	-19.11	4.47	-0.13	0.07	0.04	0.11
950163	141.165	39.851	-17.99	8.54	-4.21	0.07	0.04	0.12
950164	141.804	39.849	-19.59	4.82	-0.31	0.07	0.04	0.12
950165	140.965	39.701	-17.74	8.58	-3.92	0.07	0.07	0.13
950166	141.172	39.597	-19.43	10.37	-4.39	0.07	0.04	0.11
950167	141.955	39.458	-22.39	5.90	-4.71	0.07	0.05	0.13
950168	141.055	39.363	-20.10	11.06	-3.34	0.07	0.04	0.11
950169	141.534	39.338	-23.26	9.82	-2.23	0.07	0.05	0.12
950170	141.798	39.254	-24.55	8.62	-2.44	0.07	0.05	0.12
950171	141.740	39.024	-27.78	10.13	-1.42	0.07	0.04	0.12
950172	141.573	38.903	-29.81	10.57	-2.00	0.07	0.04	0.11
950173	140.991	38.815	-25.10	11.44	-4.13	0.07	0.04	0.11
950174	140.802	38.749	-24.84	10.18	-1.14	0.07	0.04	0.12
950175	141.449	38.683	-33.00	11.31	-3.26	0.07	0.04	0.11

950176	141.148	38.539	-30.71	10.81	-5.53	0.07	0.04	0.11
950177	140.851	38.412	-27.38	8.92	-3.28	0.07	0.04	0.11
950178	140.643	38.206	-26.45	6.44	-2.28	0.07	0.04	0.13
950179	140.844	38.030	-29.25	8.78	-7.70	0.07	0.04	0.11
950180	140.443	37.990	-23.58	6.99	-0.13	0.07	0.04	0.11
950181	140.577	40.325	-12.66	8.76	1.97	0.07	0.04	0.10
950182	140.264	40.271	-12.12	7.41	2.03	0.07	0.04	0.11
950183	140.787	40.215	-12.47	7.43	-0.36	0.07	0.04	0.11
950184	140.049	40.247	-11.61	7.66	0.61	0.06	0.04	0.10
950185	140.402	40.007	-12.08	8.08	1.92	0.07	0.04	0.12
950186	140.132	39.936	-10.74	7.46	1.93	0.07	0.04	0.10
950187	140.597	39.749	-12.63	7.64	0.08	0.07	0.04	0.11
950188	140.234	39.658	-10.73	8.99	-0.93	0.07	0.04	0.10
950189	140.387	39.549	-13.77	9.02	-0.36	0.07	0.04	0.10
950190	140.560	39.327	-12.35	8.58	-4.93	0.07	0.04	0.10
950191	139.908	39.206	-9.86	7.02	-1.74	0.07	0.04	0.10
950192	140.162	39.164	-14.15	8.39	-0.34	0.07	0.05	0.15
950193	140.630	39.052	-18.62	10.98	-1.57	0.07	0.05	0.12
950194	139.548	39.186	-6.33	6.06	0.96	0.06	0.04	0.10
950195	139.957	38.760	-15.59	6.67	0.57	0.07	0.04	0.10
950196	139.832	38.594	-14.98	6.95	1.78	0.07	0.04	0.13
950197	139.742	38.146	-18.40	6.64	0.40	0.07	0.04	0.13
950198	140.094	37.964	-21.05	7.35	-0.60	0.07	0.04	0.11
950199	140.078	38.198	-20.76	9.24	0.25	0.07	0.04	0.13
950200	140.466	37.683	-26.13	5.92	-2.47	0.07	0.04	0.12
950201	140.755	37.561	-28.41	7.15	-3.07	0.07	0.04	0.13
950202	140.073	37.567	-20.82	3.87	1.31	0.07	0.04	0.11
950203	141.007	37.534	-29.80	8.80	-4.42	0.07	0.04	0.11
950204	139.529	37.473	-15.74	4.81	-1.40	0.07	0.04	0.12
950205	140.662	37.325	-26.90	6.99	-3.58	0.07	0.04	0.10
950206	139.364	37.303	-14.18	4.36	-1.98	0.07	0.04	0.12
950207	139.504	37.281	-15.79	4.83	-2.29	0.07	0.04	0.12
950208	140.994	37.285	-28.36	8.05	-3.53	0.07	0.04	0.12
950209	139.871	37.261	-19.02	3.66	-2.05	0.07	0.04	0.11
950210	140.260	37.126	-23.20	4.15	-2.53	0.07	0.04	0.11
950211	140.562	37.089	-24.95	6.87	-3.28	0.07	0.04	0.11
950212	140.413	36.862	-24.16	6.40	-3.29	0.07	0.04	0.11
950213	140.293	36.651	-22.33	6.07	-1.98	0.07	0.04	0.10
950214	140.754	36.800	-27.50	6.19	-1.05	0.07	0.04	0.11
950215	140.078	36.365	-20.79	5.99	-1.89	0.07	0.04	0.10
950216	140.476	36.344	-21.43	6.35	-1.69	0.07	0.04	0.10
950217	140.039	36.854	-22.06	5.54	-1.95	0.07	0.04	0.12
950218	139.619	36.666	-19.83	4.67	-0.55	0.07	0.04	0.11
950219	139.923	36.599	-21.42	5.55	-3.56	0.07	0.04	0.10
950220	139.225	36.770	-18.39	4.11	-0.95	0.07	0.04	0.12
950221	138.553	36.508	-18.30	4.24	-4.23	0.08	0.05	0.14
950222	139.330	36.422	-19.47	5.01	-2.54	0.07	0.04	0.10
950223	139.076	35.987	-18.77	6.43	-2.13	0.07	0.04	0.11
950224	139.796	35.896	-19.06	8.66	-2.98	0.08	0.04	0.10
950225	140.048	35.657	-17.57	8.18	-1.28	0.08	0.05	0.10
950226	140.385	35.243	-17.84	16.49	-2.42	0.10	0.12	0.11
950227	139.975	35.003	-20.74	31.28	-6.51	0.12	0.09	0.11
950228	139.631	35.664	-22.11	13.63	-4.44	0.08	0.05	0.10
950229	139.163	35.336	-20.57	14.08	-4.67	0.08	0.04	0.12

950231	139.253	38.465	-9.51	4.71	-2.99	0.07	0.04	0.11
950232	138.513	38.319	-3.46	3.55	-1.67	0.07	0.04	0.10
950233	138.472	38.063	-3.76	3.33	-0.01	0.07	0.04	0.11
950234	139.351	37.929	-15.07	6.10	-3.02	0.07	0.04	0.11
950235	138.273	37.816	-4.04	2.38	-1.95	0.07	0.04	0.12
950236	139.478	37.686	-14.74	5.42	-0.95	0.07	0.04	0.12
950237	138.781	37.668	-7.84	4.63	-4.44	0.07	0.04	0.10
950238	139.059	37.662	-12.19	5.75	-4.14	0.07	0.04	0.12
950239	138.998	37.468	-12.38	5.59	-2.36	0.07	0.04	0.12
950240	138.790	37.311	-11.60	5.85	-3.12	0.07	0.04	0.18
950241	138.334	37.231	-6.28	5.12	-2.44	0.07	0.04	0.11
950242	138.934	37.166	-14.66	5.29	-2.67	0.07	0.04	0.11
950243	138.100	37.161	-2.82	5.20	-1.37	0.07	0.04	0.11
950244	138.609	37.079	-12.11	4.47	-1.47	0.07	0.04	0.14
950245	137.874	37.045	-4.34	4.49	-3.21	0.07	0.04	0.11
950246	138.831	36.993	-15.51	5.47	-2.34	0.07	0.04	0.11
950247	138.199	36.865	-6.40	5.10	-2.33	0.07	0.04	0.12
950248	136.996	36.741	0.25	2.27	-2.43	0.07	0.04	0.11
950249	137.195	36.634	-0.76	2.92	-3.09	0.07	0.04	0.11
950250	137.440	36.579	-3.36	2.07	-3.26	0.07	0.04	0.14
950251	136.921	36.402	-2.69	3.62	-1.40	0.07	0.05	0.14
950252	136.919	37.850	2.21	2.02	-0.86	0.07	0.04	0.11
950253	137.270	37.446	0.89	1.58	-5.78	0.08	0.04	0.11
950254	136.772	37.001	1.64	1.76	-1.64	0.07	0.04	0.11
950255	136.389	36.394	0.94	1.89	-1.82	0.07	0.04	0.10
950256	136.634	36.165	-1.83	1.72	-2.60	0.07	0.04	0.14
950257	136.279	36.146	-1.07	2.41	-3.73	0.07	0.04	0.11
950263	138.316	35.856	-15.74	5.32	-3.36	0.08	0.04	0.14
950264	138.695	35.747	-17.38	4.72	-3.32	0.07	0.04	0.13
950265	138.436	36.802	-14.92	4.99	-6.35	0.07	0.04	0.14
950266	137.872	36.706	-6.55	2.55	-3.02	0.08	0.04	0.14
950267	138.247	36.665	-12.78	5.02	-5.12	0.07	0.04	0.11
950268	138.323	36.386	-14.14	4.73	-6.02	0.07	0.04	0.11
950269	138.638	36.346	-16.97	8.64	-5.54	0.07	0.05	0.12
950271	138.216	36.208	-15.42	5.86	-2.81	0.07	0.05	0.12
950272	138.461	36.131	-16.83	5.89	-2.86	0.07	0.04	0.12
950279	137.147	36.336	-5.00	2.00	-2.69	0.07	0.04	0.13
950327	135.173	35.752	1.57	2.36	-2.90	0.07	0.04	0.11
950378	134.047	35.457	3.01	2.06	-2.43	0.07	0.04	0.12
950382	133.240	36.285	6.96	2.84	-0.46	0.07	0.04	0.11
950383	132.984	36.093	6.85	0.25	-1.40	0.06	0.04	0.10
950384	132.743	35.393	9.57	0.43	-5.04	0.08	0.04	0.11
950386	132.507	35.186	6.78	0.95	-2.66	0.08	0.05	0.12
950388	131.923	34.767	2.11	-0.16	-2.74	0.07	0.04	0.11
950407	131.417	34.440	4.44	1.93	-1.17	0.06	0.04	0.11
950408	130.943	34.295	3.97	1.11	-0.90	0.06	0.04	0.11
950450	130.251	33.536	5.52	-0.59	-0.26	0.06	0.05	0.12
950453	130.565	33.206	3.35	-2.37	-1.65	0.06	0.04	0.11
950454	130.269	33.275	4.83	-0.86	-0.61	0.06	0.04	0.11
950455	130.094	33.098	4.72	-1.76	-1.45	0.06	0.04	0.11
950456	129.482	34.656	6.90	-0.40	-0.40	0.06	0.04	0.11
950457	129.312	34.268	7.37	-0.28	-1.39	0.06	0.04	0.12
950458	129.735	33.743	7.00	-0.91	-1.03	0.06	0.04	0.11
950459	129.537	33.362	7.13	-0.44	-2.45	0.06	0.04	0.11

950460	129.691	33.063	6.31	-1.80	-0.09	0.06	0.04	0.11
950461	130.271	32.871	4.06	-4.55	0.07	0.07	0.05	0.11
950462	128.843	32.669	9.34	-1.68	0.67	0.06	0.04	0.12
950463	130.155	32.637	4.64	-5.54	-1.54	0.06	0.04	0.11
950464	130.548	32.933	4.06	-3.25	-2.36	0.06	0.04	0.11
950465	130.765	32.842	1.53	-3.34	-1.66	0.06	0.04	0.11
960501	141.167	45.138	-0.38	3.01	3.18	0.08	0.06	0.17
960502	142.964	44.582	-8.15	4.97	0.70	0.07	0.05	0.11
960503	143.616	44.220	-10.61	7.50	0.90	0.07	0.04	0.10
960504	143.077	44.192	-10.12	7.02	0.92	0.07	0.05	0.17
960505	144.293	43.989	-16.74	7.80	-0.87	0.06	0.05	0.10
960506	142.578	43.908	-11.04	6.23	0.21	0.07	0.05	0.13
960507	144.115	43.828	-15.98	10.21	2.54	0.07	0.05	0.12
960508	142.410	43.739	-13.17	6.40	0.81	0.07	0.05	0.11
960509	141.874	43.741	-11.18	5.51	-2.53	0.07	0.05	0.11
960510	142.903	43.771	-14.97	7.84	-0.52	0.07	0.05	0.14
960511	143.578	43.671	-14.98	8.55	0.49	0.07	0.05	0.13
960512	145.259	43.232	-32.62	16.77	-6.44	0.07	0.05	0.11
960513	144.080	43.439	-20.87	10.38	-2.80	0.07	0.07	0.13
960514	142.395	43.336	-17.87	7.28	-0.31	0.07	0.05	0.13
960515	144.598	43.307	-28.72	15.90	-6.81	0.08	0.05	0.11
960516	141.891	43.248	-17.88	4.92	-0.68	0.06	0.04	0.11
960517	140.861	43.210	-10.33	2.82	1.85	0.07	0.04	0.11
960518	142.810	43.166	-21.62	9.34	-2.68	0.07	0.05	0.13
960519	145.520	43.195	-36.97	18.33	-5.77	0.07	0.05	0.10
960520	141.540	43.078	-13.92	2.94	-2.18	0.06	0.04	0.11
960521	143.171	42.939	-24.15	15.50	-5.15	0.06	0.04	0.11
960522	141.577	42.884	-14.95	3.45	-2.97	0.06	0.04	0.12
960523	141.407	42.773	-13.68	2.92	-3.06	0.07	0.05	0.14
960524	140.899	42.559	-14.31	4.09	-6.49	0.07	0.06	0.16
960526	140.876	42.474	-15.91	6.02	-11.86	0.08	0.07	0.21
960527	139.446	42.061	-11.42	1.96	-6.83	0.07	0.04	0.10
960528	140.667	42.123	-13.65	6.65	2.16	0.07	0.05	0.11
960529	140.715	41.977	-11.76	4.44	3.70	0.07	0.05	0.11
960530	140.071	41.803	-14.31	6.46	0.97	0.07	0.04	0.10
960531	144.719	42.983	-32.49	15.44	-5.44	0.07	0.04	0.10
960532	143.316	42.126	-31.62	13.09	-0.85	0.07	0.05	0.12
960533	141.448	41.405	-16.03	6.59	-1.83	0.07	0.04	0.10
960534	140.491	41.185	-10.27	7.12	-5.37	0.07	0.05	0.12
960535	140.822	41.146	-11.85	5.81	1.29	0.07	0.05	0.13
960536	140.872	40.913	-12.72	4.98	-2.61	0.07	0.04	0.14
960537	141.132	40.862	-14.06	7.25	-1.58	0.07	0.04	0.14
960538	140.589	40.706	-11.39	6.03	-1.54	0.07	0.05	0.12
960539	141.376	40.676	-16.19	6.22	-0.13	0.06	0.04	0.11
960540	140.479	40.624	-9.22	4.68	-11.49	0.07	0.04	0.14
960541	140.803	40.644	-11.48	6.47	0.34	0.07	0.05	0.14
960542	140.452	40.910	-10.48	5.19	0.48	0.06	0.04	0.11
960543	141.066	39.953	-13.22	9.39	-3.18	0.08	0.06	0.14
960544	140.769	39.351	-19.13	10.40	-0.54	0.07	0.05	0.17
960545	141.275	38.900	-30.01	11.36	-3.75	0.07	0.04	0.12
960546	141.575	39.143	-25.46	10.30	-2.09	0.07	0.05	0.12
960547	141.675	39.596	-19.71	6.93	1.93	0.07	0.05	0.14
960548	140.848	38.546	-26.14	9.41	-1.67	0.07	0.05	0.11
960549	141.213	38.425	-30.64	8.96	-2.05	0.17	0.16	0.16

960550	141.501	38.301	-35.91	11.37	-2.71	0.08	0.05	0.14
960551	139.849	39.891	-7.65	6.67	5.05	0.07	0.04	0.12
960552	140.045	39.826	-10.99	8.09	7.58	0.07	0.05	0.11
960553	140.733	39.703	-13.27	7.77	-1.38	0.07	0.04	0.10
960554	140.507	39.199	-15.53	10.19	-3.14	0.07	0.05	0.10
960555	139.927	39.016	-12.35	7.30	-0.11	0.07	0.04	0.11
960557	140.271	38.148	-21.09	7.87	2.06	0.07	0.05	0.12
960558	140.946	37.818	-30.01	8.24	-1.29	0.07	0.04	0.11
960559	140.206	37.616	-20.03	6.58	-1.10	0.08	0.05	0.11
960560	140.373	37.621	-24.63	5.70	-1.96	0.10	0.05	0.16
960561	140.136	37.425	-21.70	4.85	-1.41	0.07	0.04	0.11
960562	140.834	37.325	-27.32	8.13	-2.68	0.07	0.04	0.11
960563	139.586	37.097	-16.07	4.84	-1.98	0.07	0.05	0.15
960564	139.462	38.056	-16.08	6.20	-0.55	0.07	0.05	0.11
960565	138.370	38.024	-3.16	3.42	-0.50	0.07	0.05	0.12
960566	138.707	37.536	-4.84	5.01	-2.41	0.07	0.04	0.12
960567	138.516	37.349	-6.27	4.77	-1.48	0.06	0.04	0.12
960568	139.020	37.320	-12.65	5.09	-2.09	0.07	0.05	0.14
960569	138.243	37.057	-6.07	5.14	-3.44	0.07	0.05	0.14
960570	137.894	36.951	-3.70	4.52	-2.10	0.07	0.05	0.16
960571	139.074	37.752	-11.58	5.32	-4.84	0.07	0.04	0.12
960572	137.370	36.737	-1.00	2.14	-1.96	0.06	0.04	0.11
960573	137.032	36.650	0.38	3.56	-2.08	0.07	0.05	0.13
960574	137.139	37.307	1.01	1.96	-0.53	0.06	0.04	0.11
960575	136.719	37.157	1.87	2.01	-1.56	0.06	0.04	0.10
960576	136.996	37.123	0.73	1.55	-2.72	0.07	0.04	0.11
960577	136.756	36.817	1.65	2.48	-2.90	0.06	0.04	0.11
960578	136.605	36.370	0.25	2.23	-2.42	0.07	0.05	0.14
960581	140.498	36.743	-23.64	6.45	-0.93	0.07	0.04	0.10
960582	139.988	36.301	-19.91	6.46	-3.07	0.07	0.05	0.11
960583	139.931	36.115	-15.72	8.72	-17.31	0.07	0.04	0.10
960584	140.202	36.031	-19.23	6.82	-2.59	0.07	0.05	0.09
960585	140.165	36.952	-22.23	5.53	-2.46	0.07	0.04	0.11
960586	139.806	36.980	-18.81	4.97	-2.31	0.07	0.05	0.13
960587	139.854	36.776	-20.04	4.39	-2.48	0.07	0.04	0.10
960588	140.158	36.692	-21.21	5.89	-1.79	0.07	0.04	0.10
960589	139.491	36.624	-18.49	4.10	-0.04	0.09	0.06	0.14
960590	140.179	36.542	-21.60	5.81	-1.74	0.07	0.05	0.12
960591	138.591	36.616	-18.47	5.20	-3.74	0.07	0.04	0.12
960592	139.067	36.235	-18.20	6.36	-2.52	0.07	0.04	0.10
960593	138.912	36.143	-18.44	4.75	-1.93	0.07	0.04	0.10
960594	139.434	34.762	-12.14	44.56	5.16	0.14	0.20	0.13
960595	139.359	34.738	-28.54	34.95	6.95	0.12	0.17	0.12
960602	139.765	32.464	-37.50	27.04	-7.91	0.07	0.05	0.11
960603	142.163	26.635	-51.15	22.71	-4.89	0.11	0.06	0.16
960606	138.690	35.650	-16.99	5.68	-3.02	0.07	0.04	0.10
960607	139.026	35.512	-19.68	8.15	-2.88	0.07	0.04	0.12
960608	137.985	36.239	-13.63	5.38	-5.07	0.07	0.05	0.13
960610	138.499	36.285	-16.82	7.23	-4.02	0.07	0.05	0.11
960612	138.214	36.026	-15.33	5.01	-3.51	0.07	0.05	0.12
960613	138.583	35.974	-16.33	5.82	-3.01	0.07	0.05	0.13
960617	136.904	36.261	-2.76	1.29	-2.16	0.07	0.05	0.22
960627	140.086	36.104	-19.20	6.87	-2.11	0.07	0.04	0.12
960640	135.034	35.685	1.52	3.15	-4.51	0.07	0.05	0.13

960645	134.677	35.621	1.49	4.02	-3.59	0.06	0.04	0.12
960656	133.138	35.564	6.49	5.14	-2.44	0.18	0.07	0.20
960668	131.152	34.764	5.40	1.58	-3.92	0.06	0.04	0.11
960669	131.176	34.342	5.22	-0.13	-3.83	0.07	0.05	0.12
960670	131.066	34.180	3.77	1.87	-2.65	0.07	0.05	0.12
960689	129.940	33.196	5.60	-0.64	-3.15	0.07	0.05	0.13
960690	129.690	33.266	5.93	-1.36	-2.02	0.06	0.05	0.12
960691	129.126	33.256	8.97	-1.32	-2.30	0.06	0.05	0.17
960692	129.026	32.886	8.51	-1.69	-0.08	0.06	0.04	0.13
960693	130.166	32.796	5.07	-3.01	-0.82	0.06	0.04	0.12
960694	130.336	32.793	3.30	-4.21	-1.86	0.07	0.06	0.13
960695	130.217	32.712	5.07	-4.67	-1.03	0.06	0.04	0.12
960696	130.352	32.723	3.95	-4.76	-3.43	0.07	0.05	0.13
960697	130.291	32.661	4.29	-5.09	-1.25	0.06	0.04	0.12
960698	128.619	32.634	9.53	-1.84	-0.90	0.06	0.04	0.12
960699	131.063	33.122	-1.06	0.12	-3.13	0.06	0.04	0.13
960700	130.749	33.011	3.38	-2.36	-3.07	0.07	0.05	0.15
960710	130.916	33.191	2.28	-1.69	-1.54	0.07	0.05	0.13
960752	139.057	36.539	-18.12	5.23	-3.23	0.07	0.04	0.12
960753	139.269	36.004	-18.40	7.23	-2.12	0.07	0.04	0.10
960754	139.182	35.884	-17.28	9.80	-3.97	0.08	0.07	0.12
960755	139.366	35.801	-17.92	8.76	-1.13	0.07	0.04	0.10
960756	140.249	35.288	-18.83	20.65	-4.75	0.09	0.09	0.11
960757	141.204	39.110	-21.82	10.14	-3.05	0.07	0.05	0.13
960758	139.370	35.616	-18.70	11.16	-1.92	0.07	0.05	0.11
960759	139.614	35.161	-23.10	28.16	-6.95	0.08	0.07	0.11
960770	129.955	33.372	6.00	-0.54	-0.46	0.06	0.04	0.12
960771	130.445	33.346	3.75	0.26	-4.32	0.06	0.05	0.12
960772	129.990	32.946	4.89	-2.17	-0.84	0.06	0.04	0.11
970778	141.598	45.220	-1.51	4.42	-1.89	0.07	0.05	0.14
970779	142.352	45.127	-5.14	4.59	-1.26	0.07	0.05	0.16
970780	142.718	44.780	-5.76	5.09	0.58	0.08	0.05	0.16
970781	141.794	44.640	-4.30	3.76	1.07	0.07	0.05	0.14
970782	142.265	44.365	-7.82	4.11	-1.02	0.08	0.06	0.17
970783	141.665	44.149	-6.67	4.44	1.36	0.07	0.05	0.13
970784	144.506	43.723	-20.47	9.98	-2.97	0.08	0.06	0.14
970785	141.371	43.624	-8.55	3.39	-0.07	0.07	0.05	0.13
970786	142.947	43.334	-20.08	9.42	-2.79	0.08	0.05	0.23
970787	142.643	43.432	-16.65	8.02	-0.55	0.08	0.06	0.20
970788	143.902	43.102	-24.70	15.20	-7.32	0.07	0.05	0.15
970789	142.870	43.014	-21.78	12.21	-3.21	0.08	0.06	0.15
970790	142.085	42.934	-18.64	6.20	-3.55	0.07	0.05	0.15
970791	143.495	42.807	-26.30	15.21	-6.24	0.08	0.05	0.13
970792	141.081	42.421	-17.19	8.44	-5.19	0.09	0.07	0.15
970793	143.152	42.486	-27.46	12.77	-1.70	0.08	0.06	0.16
970794	140.371	41.935	-12.08	4.46	3.00	0.07	0.05	0.14
970795	141.453	39.849	-18.35	7.12	-0.73	0.07	0.05	0.14
970796	140.988	39.127	-18.80	11.23	-2.87	0.09	0.05	0.15
970797	140.646	37.984	-25.95	7.32	-2.62	0.08	0.05	0.14
970798	140.823	40.045	-12.19	7.87	-1.42	0.08	0.06	0.16
970799	140.095	38.434	-17.29	6.30	-19.43	0.08	0.06	0.48
970800	140.842	37.018	-27.23	6.94	-0.51	0.08	0.05	0.14
970801	139.402	37.037	-15.61	4.50	1.53	0.09	0.07	0.29
970802	138.945	36.778	-16.13	4.74	-4.11	0.07	0.05	0.15

970803	140.200	38.289	-19.39	7.54	-0.60	0.07	0.05	0.14
970804	139.522	35.419	-19.51	16.14	-4.20	0.07	0.07	0.12
970805	139.226	37.828	-12.23	5.52	-4.38	0.07	0.05	0.14
970806	138.880	37.777	-6.59	3.34	-6.95	0.07	0.05	0.14
970807	138.780	37.499	-6.27	3.32	-4.61	0.08	0.05	0.15
970808	137.596	36.577	-5.05	1.87	-0.37	0.16	0.10	0.34
970809	138.457	35.674	-14.38	4.43	-4.27	0.08	0.05	0.15
970810	138.920	37.590	-8.32	4.25	-11.56	0.07	0.05	0.16
970831	130.465	33.097	8.55	-0.69	-0.68	0.07	0.05	0.15
970832	129.721	32.840	6.27	-3.77	-0.87	0.07	0.05	0.15
KAMN	143.360	38.890	-45.00	12.00	-	11.00	9.00	-
KAMS	143.260	38.640	-52.00	15.00	-	18.00	14.00	-
MYGI	142.920	38.080	-45.00	25.00	-	17.00	12.00	-
MYGW	142.430	38.150	-41.00	14.00	-	6.00	13.00	-
FUKU	142.080	37.170	-35.00	6.00	-	13.00	14.00	-
CHOS	141.670	35.500	-2.00	-2.00	-	24.00	17.00	-
BOSN	140.500	34.750	-10.00	7.00	-	38.00	23.00	-
BOSS	139.870	34.430	-25.00	18.00	-	17.00	18.00	-

C.2. Southwest Japan

Table C.2. List of displacement rates at onshore and seafloor observation sites in southwest Japan used in the analysis of Chapter 3. The reference frame is Amurian plate of MORVEL plate motion model (DeMets et al., 2010).

Site	Site position		Displacement rate (mm/yr)			Uncertainties (mm/yr)		
	Lon. (°E)	Lat. (°N)	EW	NS	UD	EW	NS	UD
841	139.070	34.950	-32.95	4.66	1.01	0.06	0.05	0.17
842	138.250	34.954	-26.99	5.59	-3.51	0.06	0.05	0.18
843	134.050	35.175	-6.14	1.99	-2.38	0.06	0.05	0.16
10846	133.462	33.818	-20.30	10.79	3.69	0.06	0.06	0.18
20847	137.869	35.160	-23.53	4.37	0.68	0.05	0.04	0.18
20946	140.690	36.933	-22.62	2.56	-3.65	0.14	0.07	0.16
20947	140.386	36.476	-20.69	3.43	-2.68	0.11	0.05	0.16
20949	139.505	36.872	-21.96	4.87	-0.35	0.10	0.06	0.20
20950	139.753	36.538	-23.29	4.21	-1.85	0.08	0.04	0.16
20951	139.903	36.457	-23.10	4.18	-1.95	0.08	0.04	0.14
20952	139.061	36.837	-23.72	6.06	1.91	0.10	0.06	0.22
20953	139.234	36.608	-23.70	5.92	0.94	0.16	0.16	0.58
20954	138.848	36.591	-23.40	5.76	-0.70	0.06	0.05	0.16
20955	139.017	36.395	-23.26	5.24	-4.70	0.06	0.04	0.15
20956	139.255	36.268	-24.54	5.69	-1.25	0.06	0.04	0.15
20957	138.703	36.200	-24.58	5.74	-2.77	0.06	0.05	0.18
20958	138.926	35.930	-25.57	6.14	1.58	0.07	0.06	0.25
20959	139.968	35.144	-33.53	19.05	-2.01	0.05	0.05	0.17
20960	139.366	35.391	-30.07	12.75	-3.49	0.05	0.04	0.16
20965	140.296	36.779	-22.21	2.72	-2.30	0.10	0.05	0.15
20966	137.026	36.920	-13.05	6.86	-0.20	0.14	0.11	0.20
20967	137.551	36.864	-10.71	2.74	-1.47	0.07	0.05	0.16
20968	137.154	36.758	-11.17	4.80	-1.12	0.07	0.06	0.16
20969	136.806	36.592	-8.45	1.86	-3.40	0.05	0.05	0.21
20970	137.239	36.473	-12.27	2.40	-1.11	0.07	0.06	0.23

20973	136.541	36.537	-6.99	-0.33	-6.67	0.05	0.05	0.16
20974	136.362	36.230	-8.19	1.88	-1.95	0.05	0.05	0.19
20975	136.049	36.110	-7.67	0.86	-2.22	0.06	0.04	0.16
20976	136.658	35.901	-13.60	1.21	-1.01	0.06	0.05	0.21
20977	136.340	35.888	-10.91	1.84	-1.86	0.05	0.05	0.19
20978	135.756	35.487	-10.25	1.06	-2.58	0.06	0.05	0.19
20979	138.444	35.905	-23.98	6.61	-2.42	0.07	0.07	0.21
20980	138.950	35.754	-25.07	6.90	-1.86	0.06	0.05	0.18
20981	138.607	35.468	-26.09	6.22	-1.25	0.06	0.05	0.17
20982	138.624	36.857	-22.93	8.32	1.17	0.08	0.07	0.19
20983	138.097	36.707	-16.77	3.61	-2.45	0.06	0.05	0.17
20984	138.121	36.524	-21.01	5.54	-3.74	0.05	0.05	0.17
20985	138.366	36.261	-21.80	6.60	-4.74	0.05	0.06	0.16
20986	137.785	35.945	-20.20	3.40	-2.72	0.07	0.05	0.18
20987	138.096	35.878	-22.18	4.62	-1.82	0.06	0.05	0.19
20988	137.451	35.816	-19.72	2.30	-1.62	0.05	0.06	0.23
20989	137.620	35.661	-20.61	4.12	-1.57	0.06	0.04	0.18
20990	137.081	36.140	-16.28	3.96	-2.39	0.05	0.05	0.21
20991	136.785	35.723	-16.72	1.92	-2.00	0.06	0.05	0.18
20992	137.309	35.523	-19.93	3.62	-1.05	0.05	0.04	0.16
20993	136.545	35.480	-16.67	1.28	-0.51	0.06	0.05	0.17
20994	137.252	35.301	-20.94	5.13	2.82	0.05	0.04	0.15
20995	137.575	35.100	-23.31	5.69	4.31	0.06	0.04	0.16
20996	137.152	34.917	-24.92	5.94	5.31	0.05	0.04	0.14
20997	137.339	34.786	-25.77	6.52	4.10	0.06	0.04	0.16
20998	136.938	34.740	-25.96	5.96	3.91	0.06	0.04	0.15
20999	136.474	34.420	-23.50	2.73	1.81	0.05	0.05	0.17
21000	135.928	33.877	-26.72	5.56	2.46	0.06	0.05	0.20
21001	135.088	35.420	-8.14	1.88	-3.68	0.06	0.05	0.19
21002	135.341	35.333	-8.80	2.60	-2.03	0.05	0.04	0.17
21003	135.634	35.155	-10.95	2.00	-1.53	0.06	0.04	0.16
21004	135.220	34.326	-17.48	5.19	1.56	0.05	0.04	0.15
21005	134.483	35.528	-4.43	1.64	-2.28	0.13	0.11	0.36
21006	134.376	34.760	-7.63	3.05	-2.12	0.05	0.04	0.15
21007	136.042	34.711	-19.17	1.96	3.74	0.06	0.04	0.17
21008	136.173	34.494	-20.41	2.19	3.61	0.06	0.05	0.18
21009	136.003	34.293	-22.77	3.14	0.07	0.09	0.05	0.23
21010	135.855	34.242	-22.29	2.98	1.78	0.06	0.05	0.19
21011	135.554	33.941	-24.24	4.59	3.35	0.06	0.04	0.16
21012	135.882	33.669	-30.52	6.45	-0.16	0.06	0.05	0.17
21013	135.534	33.658	-30.66	7.88	0.67	0.06	0.05	0.19
21014	134.195	35.530	-2.91	2.36	-7.00	0.05	0.04	0.18
21015	133.495	35.507	-3.04	1.80	-1.85	0.05	0.04	0.16
21016	133.870	35.493	-3.50	1.87	-1.79	0.05	0.04	0.17
21017	134.156	35.341	-5.84	1.95	-3.30	0.06	0.06	0.20
21018	132.922	35.492	-2.48	2.24	-1.47	0.05	0.04	0.18
21019	133.192	35.311	-3.81	2.09	0.14	0.06	0.04	0.20
21020	132.903	35.310	-1.50	3.11	-3.56	0.05	0.04	0.18
21021	132.669	35.233	-3.93	2.75	-0.66	0.06	0.04	0.19
21022	132.386	35.032	-5.87	1.24	-2.16	0.05	0.04	0.16
21023	132.685	34.857	-5.66	3.55	-1.91	0.06	0.04	0.18
21024	132.109	34.778	-7.03	3.97	-0.83	0.06	0.04	0.18
21025	131.810	34.624	-5.10	3.58	-2.01	0.05	0.04	0.16
21026	133.681	35.283	-4.68	2.22	-2.45	0.06	0.05	0.18

21027	133.913	35.105	-6.07	2.26	-1.22	0.06	0.04	0.16
21028	133.800	34.738	-6.64	3.75	-0.28	0.06	0.04	0.17
21029	133.973	34.590	-7.51	4.64	-0.58	0.05	0.04	0.16
21030	132.902	35.035	-5.32	2.36	-1.07	0.06	0.05	0.17
21031	132.908	34.634	-6.51	4.88	-1.01	0.05	0.04	0.17
21032	133.341	34.612	-7.47	5.49	-1.35	0.05	0.04	0.17
21033	133.140	34.516	-7.22	6.26	3.20	0.06	0.05	0.19
21035	132.692	34.185	-10.66	8.08	1.70	0.06	0.05	0.17
21036	132.532	34.069	-11.38	8.01	3.07	0.05	0.04	0.16
21037	131.735	34.195	-7.68	4.70	0.79	0.06	0.04	0.17
21038	132.053	34.090	-9.64	6.44	1.01	0.06	0.04	0.17
21039	131.113	34.021	-6.50	3.02	0.54	0.06	0.04	0.17
21040	132.120	33.846	-12.64	7.98	2.34	0.06	0.04	0.17
21041	134.457	33.994	-19.88	7.40	2.70	0.06	0.07	0.18
21042	134.211	33.935	-22.28	11.83	0.42	0.07	0.06	0.20
21043	133.922	33.875	-25.16	12.40	2.80	0.07	0.06	0.21
21044	134.176	34.479	-8.79	5.18	-0.18	0.05	0.04	0.15
21045	133.899	34.326	-10.60	7.20	0.17	0.06	0.04	0.16
21046	133.351	33.974	-17.66	9.54	3.63	0.06	0.04	0.17
21047	133.047	33.884	-17.57	10.01	6.88	0.08	0.05	0.23
21048	132.799	33.643	-21.88	10.57	5.76	0.06	0.04	0.20
21049	132.744	33.305	-28.11	11.97	3.47	0.06	0.05	0.17
21050	132.634	33.096	-30.96	13.04	0.07	0.07	0.06	0.19
21051	133.531	33.626	-26.40	13.96	5.54	0.06	0.06	0.19
21052	133.154	33.607	-24.06	12.33	4.90	0.06	0.06	0.19
21053	134.099	33.497	-36.00	16.89	0.55	0.06	0.05	0.21
21054	133.090	33.417	-29.54	14.36	3.23	0.06	0.05	0.17
21055	134.206	33.395	-40.42	18.14	-2.02	0.07	0.04	0.20
21056	132.972	33.193	-32.33	15.68	-0.91	0.06	0.04	0.19
21057	133.105	33.082	-35.37	17.81	0.19	0.09	0.07	0.27
21058	132.831	32.961	-36.70	16.31	-2.05	0.06	0.05	0.17
21059	132.555	32.739	-34.15	18.04	-4.95	0.06	0.05	0.17
21060	130.722	33.930	-5.19	2.20	-0.65	0.06	0.04	0.17
21061	130.971	33.867	-6.37	3.36	-3.22	0.07	0.06	0.23
21062	130.297	33.683	-4.32	-0.94	-0.76	0.05	0.04	0.17
21063	130.676	33.580	-5.90	-0.28	-2.39	0.07	0.05	0.20
21064	130.995	33.565	-8.37	2.48	-0.60	0.06	0.05	0.19
21065	130.079	33.503	-2.87	-0.19	0.04	0.06	0.05	0.17
21066	130.097	33.292	-3.73	-0.86	-1.95	0.06	0.05	0.18
21067	129.863	33.073	-3.40	-0.70	0.43	0.06	0.04	0.18
21068	129.959	32.768	-3.48	-1.59	0.51	0.07	0.05	0.19
21069	130.622	33.060	-6.31	-0.52	-0.95	0.05	0.04	0.18
21070	130.873	32.996	-8.37	-0.90	-1.33	0.06	0.04	0.19
21071	130.748	32.709	-9.24	-3.32	0.07	0.06	0.04	0.18
21072	130.982	32.683	-11.13	-3.46	2.52	0.11	0.09	0.38
21073	130.827	32.396	-10.27	-4.73	1.79	0.07	0.06	0.20
21074	130.180	32.367	-3.26	-3.07	-0.95	0.06	0.05	0.18
21075	130.656	32.344	-9.07	-5.53	0.60	0.07	0.05	0.20
21076	130.986	32.292	-10.32	-4.87	1.30	0.07	0.05	0.18
21077	131.521	33.514	-13.04	5.78	2.48	0.06	0.04	0.18
21078	131.292	33.384	-11.56	3.21	0.98	0.06	0.04	0.19
21079	131.748	33.096	-24.52	2.13	1.73	0.06	0.04	0.18
21080	132.039	32.936	-22.56	7.39	-0.68	0.06	0.05	0.20
21081	131.442	32.899	-19.06	2.48	-0.94	0.06	0.05	0.19

21082	131.629	32.852	-20.24	2.90	1.92	0.06	0.05	0.20
21083	131.365	32.528	-19.79	1.58	-4.44	0.06	0.04	0.19
21084	131.583	32.316	-11.07	-2.87	-2.64	0.07	0.05	0.20
21085	131.347	32.112	-12.00	-2.15	2.03	0.07	0.05	0.20
21086	131.254	32.002	-9.94	-3.57	2.35	0.06	0.05	0.19
21087	130.977	31.878	-3.94	-6.50	0.43	0.09	0.06	0.20
21088	131.470	31.786	-7.24	-2.12	0.09	0.08	0.06	0.22
21089	130.736	31.744	-1.25	-4.02	4.70	0.06	0.05	0.20
21090	130.998	31.565	0.20	-9.27	1.38	0.06	0.05	0.20
21091	130.340	31.450	0.86	-8.92	0.23	0.06	0.05	0.19
21092	130.541	31.377	0.91	-9.42	0.49	0.08	0.05	0.20
21093	130.867	31.243	-0.17	-12.06	0.87	0.07	0.06	0.20
21094	127.994	26.386	5.87	-25.50	1.23	0.06	0.05	0.19
21095	127.760	26.313	5.54	-26.21	-0.39	0.06	0.05	0.20
21096	127.678	26.195	4.74	-26.36	-0.28	0.06	0.05	0.19
21099	137.551	36.114	-18.47	1.75	-1.84	0.07	0.09	0.17
21100	138.727	35.361	-27.39	5.92	1.53	0.09	0.07	0.18
21101	136.504	35.105	-18.20	2.55	1.36	0.09	0.05	0.21
31102	138.186	35.322	-22.36	2.82	0.49	0.08	0.07	0.27
31103	137.423	34.967	-24.24	6.12	4.37	0.05	0.04	0.15
31104	136.982	34.544	-27.59	8.07	2.39	0.06	0.04	0.15
31105	136.802	34.374	-26.39	6.07	2.76	0.06	0.04	0.16
31106	136.388	34.298	-24.60	4.19	3.25	0.06	0.05	0.19
31107	136.140	33.933	-26.86	5.89	3.20	0.06	0.05	0.18
31108	135.743	34.156	-22.29	3.34	2.21	0.06	0.05	0.20
31109	135.290	34.091	-23.21	4.97	2.76	0.05	0.04	0.17
31110	135.399	33.855	-25.74	6.16	2.49	0.05	0.05	0.18
31111	135.871	33.799	-27.17	3.62	-0.51	0.06	0.05	0.18
31112	135.406	33.647	-31.52	9.59	0.54	0.06	0.04	0.16
31113	135.834	33.520	-34.65	6.92	-5.55	0.05	0.04	0.15
31114	134.510	33.933	-23.98	8.12	0.97	0.07	0.07	0.19
31115	133.797	33.839	-20.44	5.92	2.46	0.06	0.05	0.20
31116	134.485	33.822	-25.49	10.37	1.32	0.06	0.05	0.17
31117	132.565	33.510	-22.91	10.01	5.30	0.06	0.04	0.17
31118	132.360	33.202	-26.62	12.37	3.29	0.06	0.04	0.17
31119	133.432	33.546	-28.50	14.58	2.48	0.06	0.05	0.18
31120	133.700	33.543	-30.23	15.16	4.34	0.05	0.04	0.15
31121	134.056	33.367	-40.40	18.61	-2.16	0.05	0.05	0.17
31122	134.178	33.266	-43.34	20.31	-5.40	0.06	0.04	0.16
31123	132.974	33.312	-30.78	14.86	2.69	0.07	0.05	0.17
31124	132.822	33.060	-34.42	15.29	-0.61	0.07	0.05	0.20
31125	132.982	32.869	-38.00	19.26	-2.95	0.08	0.05	0.17
31126	132.811	32.762	-37.23	19.45	-3.57	0.06	0.04	0.17
31127	137.814	35.778	-20.94	4.07	-1.16	0.08	0.05	0.17
31128	136.729	35.405	-18.61	1.74	0.85	0.06	0.05	0.15
41129	136.432	34.603	-20.26	2.64	4.92	0.07	0.05	0.17
41130	135.590	33.748	-28.30	6.54	1.99	0.06	0.05	0.19
41131	133.941	33.723	-26.01	13.94	2.58	0.07	0.06	0.20
41132	133.043	33.546	-13.76	4.94	2.71	0.11	0.08	0.21
41133	132.489	33.039	-30.66	12.24	-0.82	0.06	0.05	0.18
41134	132.923	33.391	-28.02	13.12	2.85	0.06	0.05	0.17
41135	133.700	35.490	-3.30	2.28	-1.90	0.06	0.04	0.18
41136	137.637	34.702	-28.05	7.60	0.36	0.06	0.04	0.15
41137	131.384	33.079	-18.32	0.89	-3.28	0.07	0.06	0.21

41138	137.596	36.577	-14.07	2.16	2.40	0.09	0.08	0.19
41139	136.540	34.285	-24.80	2.64	1.72	0.06	0.05	0.18
51141	132.962	33.104	-36.65	16.37	1.05	0.08	0.06	0.26
51142	132.676	32.928	-37.10	16.77	-4.35	0.08	0.06	0.24
51143	136.296	34.931	-19.51	1.78	3.49	0.07	0.06	0.23
51144	138.795	34.971	-35.52	4.22	-4.53	0.10	0.10	0.26
51146	135.426	34.085	-21.95	2.15	5.33	0.07	0.07	0.24
51147	131.835	34.044	-10.35	5.95	-0.37	0.07	0.06	0.24
61148	136.728	34.490	-25.36	5.96	3.46	0.08	0.06	0.25
61149	136.693	34.297	-27.27	5.48	2.71	0.10	0.07	0.25
61151	132.650	34.492	-8.00	5.69	-0.46	0.07	0.05	0.22
71152	133.924	33.622	-27.45	15.51	5.42	0.54	0.42	1.80
71153	134.114	33.775	-23.86	11.86	0.97	0.54	0.48	1.70
71154	135.305	33.769	-24.59	9.34	4.43	0.44	0.36	1.48
71155	135.971	33.661	-29.17	6.57	2.07	0.49	0.42	1.73
71156	136.024	33.820	-25.39	4.57	9.96	0.57	0.45	1.90
71157	132.340	34.397	-6.22	5.89	0.97	0.21	0.18	0.71
71160	137.723	34.672	-26.27	9.05	0.41	0.43	0.34	1.47
71161	137.442	34.680	-24.97	9.08	1.71	0.44	0.36	1.43
71163	139.276	36.602	-20.27	3.54	-0.75	0.47	0.40	1.65
71164	132.269	34.575	-3.23	4.17	2.10	0.52	0.44	1.70
81165	132.597	33.309	-43.23	18.45	-43.76	6.83	7.25	21.13
81166	133.219	33.155	-53.97	17.24	-59.15	6.93	5.20	22.78
81167	134.491	35.536	-5.07	0.87	-1.08	1.47	1.18	4.62
81168	129.777	32.582	-0.94	-4.00	1.35	1.21	1.11	4.28
81169	130.987	32.675	-12.81	-3.77	-9.06	1.25	1.07	4.61
81170	135.775	35.207	-7.41	-3.32	-0.81	1.22	1.15	4.08
81171	139.645	35.758	-32.93	4.14	-12.89	3.55	2.73	12.16
81172	133.106	33.082	-45.86	18.71	-13.05	2.03	1.68	6.33
92106	139.082	35.007	-31.45	7.44	1.07	0.09	0.05	0.22
92107	139.102	34.972	-30.81	8.49	-0.66	0.09	0.06	0.20
92110	140.087	36.106	-22.48	5.70	-1.90	0.07	0.04	0.12
93001	139.542	36.295	-24.03	4.95	-1.24	0.07	0.04	0.14
93002	140.174	36.263	-21.73	4.71	-0.78	0.09	0.05	0.13
93003	139.811	36.204	-22.88	5.51	-5.96	0.07	0.04	0.14
93004	140.544	36.181	-19.08	4.26	-2.01	0.11	0.05	0.13
93005	139.345	36.121	-24.16	6.37	-0.95	0.06	0.04	0.14
93006	140.343	36.097	-21.09	4.57	-1.60	0.08	0.04	0.13
93007	139.637	36.087	-23.05	6.68	-3.38	0.06	0.04	0.13
93008	139.800	36.011	-22.75	6.42	-1.06	0.05	0.04	0.13
93009	140.659	35.955	-20.15	4.68	-3.30	0.10	0.05	0.13
93010	140.403	35.970	-21.58	4.61	-0.47	0.08	0.05	0.13
93011	139.464	35.926	-24.40	7.11	-1.49	0.05	0.04	0.14
93012	139.993	35.940	-22.63	5.84	-0.53	0.06	0.04	0.13
93013	139.652	35.937	-24.67	4.31	-3.70	0.06	0.05	0.14
93014	140.145	35.874	-25.10	3.21	-1.82	0.06	0.05	0.13
93015	140.407	35.803	-22.33	3.90	-2.22	0.06	0.07	0.14
93016	139.813	35.780	-23.61	7.12	-1.78	0.05	0.04	0.15
93017	139.643	35.759	-24.47	8.16	0.35	0.05	0.04	0.14
93018	140.025	35.786	-23.35	5.80	-0.68	0.05	0.05	0.13
93019	139.488	35.710	-25.01	9.18	5.26	0.06	0.05	0.18
93020	140.315	35.717	-21.88	3.41	-6.00	0.05	0.07	0.14
93021	140.647	35.777	-22.46	3.70	-3.64	0.07	0.07	0.14
93022	140.837	35.726	-22.92	3.66	-2.97	0.07	0.06	0.14

93023	139.902	35.675	-23.45	7.44	-0.26	0.05	0.05	0.14
93024	140.448	35.642	-23.05	2.72	-5.79	0.05	0.10	0.13
93025	140.187	35.544	-22.40	6.54	-1.68	0.06	0.07	0.13
93026	139.673	35.563	-25.48	10.15	-1.28	0.05	0.05	0.14
93027	140.318	35.530	-19.89	3.15	-14.52	0.06	0.10	0.14
93028	139.468	35.521	-27.27	10.84	0.66	0.05	0.04	0.15
93029	139.323	35.483	-27.61	11.16	-0.68	0.06	0.05	0.16
93030	140.051	35.448	-25.61	9.66	-0.34	0.05	0.05	0.14
93031	139.045	35.415	-25.86	9.56	-0.37	0.06	0.05	0.17
93032	139.654	35.436	-28.59	13.09	-1.49	0.05	0.04	0.14
93033	140.337	35.421	-28.99	6.59	-5.00	0.07	0.11	0.13
93034	139.466	35.327	-31.35	15.52	-3.65	0.05	0.04	0.14
93035	139.263	35.305	-29.23	14.94	-5.36	0.07	0.04	0.16
93036	139.826	35.312	-31.20	15.69	-3.00	0.05	0.04	0.14
93037	140.147	35.333	-26.16	12.52	-0.55	0.07	0.06	0.15
93038	138.882	35.322	-26.10	5.79	0.79	0.08	0.06	0.19
93039	139.844	35.144	-33.73	21.25	-4.79	0.05	0.04	0.15
93041	140.268	35.166	-28.83	12.29	1.18	0.05	0.09	0.14
93042	139.110	35.149	-28.72	9.69	-3.11	0.09	0.06	0.21
93043	138.902	35.110	-30.64	1.60	1.88	0.05	0.05	0.16
93044	140.079	35.112	-33.39	18.01	-2.16	0.05	0.05	0.15
93045	139.954	35.255	-31.78	16.30	-2.57	0.05	0.05	0.14
93046	138.998	35.015	-30.83	3.96	-3.06	0.07	0.05	0.18
93047	139.864	34.954	-33.72	26.82	-4.74	0.06	0.05	0.15
93048	139.131	34.939	-30.00	9.77	-0.88	0.06	0.07	0.17
93049	138.925	34.916	-31.71	4.48	-4.32	0.08	0.05	0.20
93050	137.672	34.835	-24.95	5.50	0.65	0.06	0.04	0.16
93051	139.381	34.784	-36.79	27.63	2.16	0.06	0.11	0.17
93052	138.018	34.786	-28.00	6.68	-1.03	0.05	0.04	0.15
93053	138.990	34.751	-35.30	8.92	-2.08	0.07	0.06	0.18
93054	137.717	34.678	-28.45	7.78	1.02	0.10	0.07	0.27
93055	139.433	34.687	-33.49	18.35	-0.64	0.07	0.06	0.17
93056	137.414	34.672	-26.36	7.13	2.86	0.10	0.07	0.28
93057	139.258	34.372	-32.50	17.95	-1.44	0.07	0.08	0.36
93058	139.134	34.200	-43.25	8.95	7.45	0.06	0.05	0.19
93059	139.504	34.121	-32.27	28.77	7.38	0.07	0.06	0.18
93060	139.547	34.059	-29.87	26.26	6.22	0.09	0.06	0.22
93061	139.014	34.922	-33.70	5.91	-2.11	0.08	0.05	0.17
93062	139.124	34.878	-32.60	7.39	1.66	0.10	0.13	0.23
93063	139.268	35.724	-25.26	9.38	1.20	0.05	0.04	0.16
93064	138.976	35.623	-25.17	7.87	-0.53	0.06	0.05	0.18
93065	139.157	35.610	-26.03	9.10	1.01	0.05	0.05	0.16
93066	139.205	35.429	-26.10	13.13	-0.03	0.06	0.05	0.17
93067	139.665	35.267	-32.23	18.57	-4.01	0.06	0.04	0.15
93068	139.049	35.246	-26.92	9.01	1.37	0.08	0.07	0.22
93069	138.445	35.444	-25.55	6.07	-0.94	0.07	0.06	0.21
93070	138.814	35.497	-25.96	8.24	-2.09	0.06	0.05	0.17
93071	138.563	35.362	-28.38	4.87	-0.56	0.07	0.05	0.19
93072	138.771	35.306	-27.29	4.13	1.48	0.07	0.05	0.18
93073	138.446	35.289	-26.81	4.06	-2.86	0.08	0.06	0.20
93074	138.254	35.201	-27.50	5.59	-0.04	0.06	0.05	0.18
93075	138.617	35.203	-29.56	1.80	-3.61	0.06	0.06	0.17
93076	138.722	35.174	-30.07	0.77	-0.36	0.06	0.06	0.16
93077	138.525	35.067	-29.48	4.38	-3.19	0.06	0.07	0.16

93078	138.369	35.103	-26.04	5.20	-4.60	0.06	0.06	0.17
93079	138.135	35.104	-23.06	2.83	-2.42	0.07	0.05	0.18
93081	138.378	34.991	-27.51	5.26	-7.84	0.05	0.06	0.17
93084	137.695	35.079	-23.60	5.01	3.27	0.06	0.05	0.16
93085	138.786	34.776	-36.04	6.60	-3.95	0.07	0.04	0.15
93086	138.838	34.610	-38.05	8.84	-1.30	0.06	0.05	0.14
93088	138.075	34.940	-26.02	5.81	-3.99	0.06	0.05	0.17
93089	137.932	34.844	-27.79	5.52	-1.24	0.05	0.04	0.15
93090	137.818	34.941	-25.54	5.57	-1.45	0.06	0.05	0.17
93091	138.137	34.758	-28.35	6.92	-5.94	0.05	0.04	0.14
93092	138.226	34.738	-30.23	7.43	-5.61	0.05	0.04	0.15
93093	138.054	34.715	-29.37	6.98	-4.17	0.06	0.04	0.16
93094	138.129	34.643	-33.62	6.12	-6.43	0.05	0.04	0.14
93095	137.937	34.670	-30.08	7.23	-2.61	0.05	0.04	0.14
93096	137.911	34.755	-28.19	6.88	-2.04	0.06	0.04	0.15
93097	137.792	34.793	-27.95	6.79	-0.12	0.05	0.04	0.14
93098	137.823	34.672	-29.78	7.47	-1.29	0.05	0.04	0.15
93099	137.575	34.938	-25.21	5.94	3.93	0.06	0.04	0.16
93101	138.216	34.605	-33.56	12.80	-11.84	0.05	0.19	0.27
93102	137.434	34.865	-25.56	4.61	3.09	0.06	0.05	0.17
93103	137.554	34.809	-25.68	7.22	2.34	0.07	0.04	0.16
93104	137.515	34.718	-27.05	7.79	3.52	0.06	0.04	0.16
940042	140.612	36.540	-19.25	0.05	1.95	0.13	0.08	0.16
940043	139.726	36.402	-23.46	3.99	-3.15	0.07	0.04	0.14
940044	138.906	36.697	-23.71	6.05	-1.00	0.07	0.06	0.18
940045	138.865	36.259	-24.44	5.93	-1.81	0.06	0.04	0.15
940046	137.851	36.500	-16.68	2.43	-5.20	0.07	0.05	0.20
940047	137.944	35.924	-20.96	3.66	-3.57	0.08	0.05	0.20
940048	138.583	35.590	-25.96	7.44	-0.74	0.06	0.05	0.18
940052	137.487	36.929	-11.40	3.80	-0.53	0.07	0.05	0.16
940054	136.650	36.663	-8.18	-0.20	-5.25	0.06	0.05	0.15
940055	136.173	36.231	-6.28	0.95	-2.72	0.05	0.04	0.15
940056	136.106	35.603	-11.79	2.21	-1.19	0.06	0.05	0.19
940057	135.233	35.550	-7.90	2.25	-2.82	0.05	0.05	0.18
940058	137.348	36.136	-18.02	2.56	-2.38	0.06	0.05	0.21
940059	137.248	35.800	-19.79	1.63	-1.81	0.06	0.04	0.17
940060	136.900	35.526	-18.94	2.25	-0.15	0.05	0.04	0.15
940061	137.468	35.397	-19.48	4.07	1.49	0.05	0.04	0.15
940062	136.158	35.095	-16.78	1.49	1.68	0.06	0.04	0.18
940063	137.041	35.128	-21.99	4.66	3.16	0.05	0.04	0.15
940064	136.502	34.759	-21.01	2.91	3.48	0.06	0.05	0.18
940065	136.851	34.465	-24.58	7.25	6.15	0.06	0.05	0.25
940066	136.198	34.061	-25.88	5.19	2.19	0.07	0.05	0.19
940067	135.501	34.838	-13.74	2.01	0.83	0.06	0.05	0.18
940068	135.851	34.392	-20.41	2.79	2.88	0.06	0.04	0.16
940069	135.221	34.158	-20.34	5.25	3.35	0.05	0.05	0.15
940070	135.764	33.483	-37.06	9.46	-4.47	0.06	0.04	0.16
940071	134.550	34.785	-7.54	3.39	-2.48	0.05	0.04	0.15
940072	134.331	35.586	-3.84	-6.91	-5.60	0.06	0.04	0.17
940074	133.059	35.434	-2.86	2.15	-1.08	0.05	0.04	0.17
940075	132.209	35.003	-4.09	3.30	-1.04	0.05	0.04	0.17
940076	131.610	34.616	-4.72	3.75	-1.41	0.06	0.05	0.17
940077	133.528	34.549	-7.69	5.55	0.29	0.06	0.04	0.17
940078	132.575	34.340	-8.26	7.22	0.09	0.05	0.04	0.15

940079	130.914	33.997	-5.56	2.01	-0.82	0.06	0.04	0.17
940080	134.024	34.286	-11.13	7.25	1.91	0.05	0.04	0.16
940081	134.626	33.927	-23.05	9.28	2.10	0.06	0.05	0.16
940082	134.122	33.316	-42.08	19.46	-4.64	0.05	0.04	0.17
940083	133.578	33.529	-30.16	14.71	4.55	0.05	0.05	0.16
940084	133.242	33.273	-35.16	17.15	2.04	0.06	0.05	0.17
940085	132.966	32.756	-38.36	20.85	-3.93	0.06	0.05	0.17
940086	132.281	33.469	-21.59	8.27	3.37	0.06	0.04	0.16
940087	130.477	33.731	-5.62	1.20	-0.06	0.05	0.04	0.16
940088	131.691	33.462	-16.69	5.58	2.96	0.06	0.04	0.17
940089	130.968	33.331	-9.09	1.64	-1.22	0.06	0.05	0.18
940090	131.876	32.925	-23.17	5.83	3.04	0.06	0.05	0.18
940091	129.850	33.476	-2.34	0.11	0.17	0.06	0.04	0.17
940092	129.860	32.700	-11.19	0.14	-5.08	0.43	0.30	1.01
940093	130.646	32.546	-8.25	-4.44	-0.43	0.06	0.04	0.18
940094	131.632	32.445	-17.55	3.04	1.76	0.06	0.05	0.18
940095	131.470	32.022	-11.39	0.10	-2.17	0.06	0.05	0.19
940096	130.190	32.013	-3.64	-6.64	-0.17	0.05	0.04	0.17
940097	130.466	31.504	0.87	-16.42	-2.05	0.06	0.05	0.18
940098	130.299	31.265	1.32	-9.21	0.09	0.06	0.05	0.17
940099	131.088	31.259	2.79	-10.33	9.44	0.11	0.10	0.37
940100	127.769	26.145	10.42	-14.64	-2.17	0.06	0.12	0.19
942004	130.879	31.425	1.78	-11.04	0.72	0.09	0.06	0.30
950212	140.413	36.862	-22.42	2.61	-3.14	0.12	0.06	0.15
950213	140.293	36.651	-21.65	2.85	-2.80	0.11	0.08	0.15
950214	140.754	36.800	-21.05	1.74	-1.93	0.14	0.08	0.15
950215	140.078	36.365	-22.03	4.27	-2.00	0.09	0.04	0.14
950216	140.476	36.344	-19.26	3.51	-1.88	0.12	0.05	0.14
950217	140.039	36.854	-23.46	3.50	-1.42	0.09	0.06	0.15
950218	139.619	36.666	-23.76	4.21	-1.64	0.09	0.05	0.16
950219	139.923	36.599	-23.06	4.15	-0.91	0.09	0.05	0.15
950220	139.225	36.770	-23.74	4.89	1.06	0.08	0.07	0.18
950221	138.553	36.508	-24.05	5.00	-5.83	0.09	0.07	0.16
950222	139.330	36.422	-23.94	5.00	-2.47	0.07	0.04	0.16
950223	139.076	35.987	-24.67	6.80	-1.31	0.05	0.04	0.15
950224	139.796	35.896	-23.12	6.54	-1.05	0.05	0.04	0.15
950225	140.048	35.657	-23.05	5.90	-1.77	0.05	0.05	0.15
950226	140.385	35.243	-23.60	7.13	2.17	0.09	0.16	0.15
950227	139.975	35.003	-33.65	24.15	-4.09	0.05	0.04	0.14
950228	139.631	35.664	-26.29	9.05	-0.56	0.05	0.04	0.16
950229	139.163	35.336	-27.28	12.99	-2.47	0.08	0.06	0.18
950230	139.142	35.269	-26.15	13.24	-2.41	0.10	0.05	0.18
950246	138.831	36.993	-23.45	8.15	-1.91	0.10	0.08	0.16
950247	138.199	36.865	-14.65	5.22	-2.81	0.08	0.05	0.20
950248	136.996	36.741	-9.58	3.73	-0.99	0.06	0.05	0.15
950249	137.195	36.634	-10.43	3.98	-0.85	0.06	0.05	0.16
950250	137.440	36.579	-12.66	2.92	0.11	0.06	0.05	0.18
950251	136.921	36.402	-10.35	3.08	-1.47	0.06	0.06	0.19
950255	136.389	36.394	-6.75	0.85	-2.44	0.05	0.04	0.16
950256	136.634	36.165	-9.55	1.00	-1.42	0.06	0.05	0.19
950257	136.279	36.146	-7.83	1.85	-2.67	0.05	0.04	0.16
950258	136.505	35.985	-11.60	1.75	-3.04	0.05	0.05	0.18
950259	135.990	35.945	-7.53	1.11	-4.09	0.05	0.05	0.15
950260	136.197	35.793	-10.97	1.72	-2.17	0.06	0.05	0.17

950261	135.908	35.534	-8.81	0.04	-6.52	0.10	0.08	0.27
950262	135.609	35.463	-9.26	2.08	-1.73	0.05	0.05	0.16
950263	138.316	35.856	-23.27	6.04	-1.56	0.07	0.05	0.18
950264	138.695	35.747	-24.12	6.48	-1.80	0.05	0.04	0.16
950265	138.436	36.802	-22.38	5.18	-2.38	0.07	0.06	0.24
950266	137.872	36.706	-14.25	3.09	-2.38	0.11	0.05	0.28
950267	138.247	36.665	-20.38	5.40	-5.31	0.05	0.04	0.15
950268	138.323	36.386	-22.09	5.27	-4.55	0.06	0.06	0.15
950269	138.638	36.346	-25.24	5.49	-5.24	0.06	0.05	0.16
950270	137.903	36.322	-18.04	3.33	-4.82	0.06	0.05	0.20
950271	138.216	36.208	-22.30	5.57	-3.07	0.07	0.05	0.17
950272	138.461	36.131	-23.77	6.18	-3.06	0.07	0.05	0.19
950273	137.983	36.121	-20.95	3.85	-3.96	0.06	0.04	0.18
950274	137.696	35.784	-20.32	3.64	-3.56	0.06	0.05	0.18
950275	138.038	35.556	-22.27	5.06	-1.75	0.06	0.05	0.18
950276	137.815	35.521	-21.58	4.78	0.16	0.06	0.05	0.17
950277	137.925	35.317	-22.14	4.97	-0.19	0.06	0.05	0.16
950278	137.588	35.247	-22.39	5.40	2.32	0.05	0.04	0.15
950279	137.147	36.336	-13.93	2.75	-1.85	0.06	0.06	0.19
950280	136.953	36.033	-16.04	1.63	-2.69	0.06	0.05	0.17
950281	137.535	35.973	-18.52	2.99	-1.23	0.06	0.05	0.16
950282	136.863	35.867	-15.63	1.52	-2.68	0.06	0.04	0.16
950283	136.975	35.758	-19.61	3.62	-2.28	0.06	0.05	0.17
950284	137.425	35.657	-20.26	3.64	-1.69	0.05	0.04	0.16
950285	136.489	35.636	-12.68	1.79	-2.81	0.06	0.06	0.18
950286	136.611	35.633	-15.91	1.63	-1.43	0.06	0.05	0.17
950287	137.174	35.612	-19.26	2.78	-0.81	0.05	0.04	0.14
950288	136.687	35.488	-17.30	0.99	-0.09	0.05	0.04	0.16
950289	137.125	35.479	-19.57	2.72	0.03	0.05	0.04	0.15
950291	136.550	35.372	-17.03	1.72	-0.46	0.06	0.04	0.16
950292	137.110	35.367	-20.10	4.02	1.46	0.05	0.04	0.15
950293	137.406	35.262	-21.51	5.16	2.62	0.05	0.04	0.15
950294	136.593	35.228	-19.53	1.18	-0.64	0.07	0.05	0.19
950295	137.980	35.032	-24.60	4.48	-0.10	0.06	0.05	0.19
950296	138.516	34.986	-30.81	4.46	-3.14	0.06	0.07	0.16
950297	138.922	34.866	-32.65	5.95	-2.63	0.11	0.07	0.22
950298	136.930	35.335	-19.88	3.23	1.57	0.05	0.04	0.15
950299	136.829	35.190	-20.37	3.46	1.44	0.05	0.04	0.14
950300	137.254	35.139	-23.07	5.08	2.77	0.05	0.04	0.15
950301	137.313	35.039	-23.15	5.55	2.82	0.05	0.04	0.14
950302	137.060	34.995	-23.60	5.23	5.85	0.05	0.04	0.15
950303	137.300	34.920	-24.48	6.05	4.82	0.05	0.04	0.15
950304	136.868	34.823	-23.33	5.97	4.10	0.05	0.04	0.14
950305	137.119	34.795	-24.69	5.76	5.85	0.05	0.04	0.15
950306	137.278	34.649	-26.61	6.54	2.99	0.06	0.04	0.15
950307	137.068	34.609	-26.44	6.93	3.02	0.05	0.04	0.15
950309	136.637	34.914	-21.21	3.02	3.55	0.06	0.04	0.17
950310	136.183	34.743	-18.26	2.04	3.52	0.05	0.04	0.16
950311	136.551	34.547	-23.27	3.70	3.97	0.06	0.04	0.17
950312	136.334	34.433	-22.76	3.19	2.68	0.06	0.06	0.18
950314	136.821	34.253	-27.95	6.61	1.11	0.06	0.04	0.15
950315	136.086	33.875	-27.18	5.64	1.96	0.06	0.05	0.18
950316	136.011	33.741	-28.70	6.38	0.72	0.06	0.05	0.18
950317	136.198	35.557	-12.65	1.09	-1.77	0.06	0.04	0.17

950318	136.054	35.466	-12.59	0.97	-1.76	0.07	0.05	0.19
950319	135.913	35.351	-11.80	1.45	-1.76	0.06	0.05	0.17
950320	136.063	35.319	-13.22	2.01	0.78	0.08	0.07	0.23
950321	136.236	35.269	-15.71	2.24	-0.26	0.05	0.04	0.15
950322	135.871	35.137	-13.96	1.65	-1.42	0.06	0.05	0.16
950323	136.145	34.986	-17.77	2.06	1.33	0.06	0.04	0.15
950324	135.906	34.940	-16.19	1.83	1.46	0.06	0.04	0.17
950326	136.055	34.869	-17.77	3.11	1.15	0.06	0.05	0.17
950327	135.173	35.752	-6.13	1.86	-3.00	0.05	0.04	0.15
950328	134.932	35.556	-6.75	1.71	-3.28	0.06	0.05	0.17
950329	135.164	35.292	-9.01	2.92	-1.44	0.05	0.04	0.16
950330	135.774	35.210	-10.04	0.63	3.34	0.14	0.12	0.42
950331	135.367	35.164	-9.94	3.06	-1.55	0.05	0.04	0.15
950332	135.565	35.078	-11.67	2.81	-1.70	0.05	0.04	0.15
950333	135.665	34.989	-13.47	2.58	-1.60	0.06	0.04	0.16
950334	135.864	34.747	-18.87	2.74	-0.77	0.06	0.04	0.17
950335	135.685	34.778	-17.21	1.84	2.10	0.06	0.05	0.16
950336	135.518	34.678	-16.21	3.17	-1.55	0.06	0.04	0.16
950337	135.481	34.527	-16.88	3.62	2.93	0.05	0.04	0.14
950338	135.627	34.479	-18.63	3.48	2.39	0.06	0.04	0.16
950339	135.587	34.425	-17.93	3.48	1.96	0.05	0.05	0.15
950340	135.364	34.406	-16.74	4.94	2.63	0.05	0.04	0.15
950341	134.582	35.437	-5.24	2.16	-3.22	0.06	0.05	0.18
950342	134.819	35.315	-7.26	2.24	-4.97	0.06	0.05	0.16
950343	135.182	35.105	-8.94	2.83	-1.33	0.05	0.05	0.16
950344	134.586	35.094	-7.86	2.75	-1.28	0.06	0.04	0.17
950345	134.973	35.091	-9.30	3.06	-2.28	0.05	0.04	0.15
950346	134.404	34.998	-7.17	2.61	-1.94	0.05	0.04	0.15
950347	134.767	34.985	-8.44	2.93	-2.18	0.05	0.04	0.15
950348	135.326	34.977	-10.44	3.65	0.39	0.05	0.05	0.15
950349	135.176	34.945	-10.60	4.80	-1.69	0.05	0.04	0.15
950350	134.545	34.897	-7.95	2.19	-2.34	0.05	0.04	0.15
950351	135.216	34.812	-11.63	3.28	-1.02	0.05	0.05	0.15
950352	134.997	34.805	-10.26	3.65	-1.07	0.05	0.04	0.15
950353	135.342	34.791	-13.00	3.14	-0.10	0.06	0.05	0.15
950354	134.829	34.787	-8.80	2.18	-1.81	0.05	0.04	0.15
950355	135.380	34.724	-14.98	1.93	0.46	0.06	0.05	0.16
950356	135.172	34.687	-13.60	3.37	-0.72	0.06	0.04	0.15
950357	134.520	34.670	-8.80	4.35	-1.24	0.06	0.04	0.15
950358	134.966	34.670	-10.36	3.74	-0.44	0.05	0.04	0.15
950359	135.024	34.577	-12.51	2.49	-1.54	0.06	0.04	0.15
950360	134.861	34.493	-10.71	4.55	-0.94	0.09	0.07	0.28
950361	134.882	34.350	-13.14	6.17	-2.13	0.06	0.05	0.17
950362	134.735	34.334	-13.20	5.96	-2.91	0.05	0.04	0.15
950363	134.737	34.224	-15.18	6.76	0.62	0.06	0.04	0.15
950364	136.050	34.567	-19.92	2.05	1.57	0.06	0.05	0.16
950365	135.731	34.539	-20.40	2.94	2.38	0.06	0.04	0.16
950366	135.704	34.388	-18.08	3.45	-0.25	0.07	0.05	0.18
950367	135.964	34.038	-23.97	4.51	2.51	0.09	0.05	0.21
950368	135.358	34.256	-19.00	5.80	6.21	0.05	0.04	0.16
950369	135.066	34.271	-14.34	6.68	-0.83	0.06	0.05	0.15
950370	135.590	34.222	-17.23	3.43	2.47	0.05	0.04	0.16
950371	135.385	33.962	-24.99	6.12	1.84	0.06	0.05	0.16
950372	135.180	33.914	-24.13	8.70	5.14	0.06	0.06	0.24

950373	135.782	33.815	-29.93	4.44	-4.62	0.07	0.06	0.35
950374	135.508	33.785	-26.97	7.76	1.46	0.06	0.04	0.16
950375	135.396	33.744	-28.09	7.59	1.31	0.05	0.04	0.16
950376	135.921	33.584	-32.93	7.75	-2.83	0.05	0.04	0.15
950377	135.599	33.506	-35.91	10.35	-2.69	0.06	0.04	0.16
950378	134.047	35.457	-5.78	0.98	2.19	0.06	0.05	0.20
950379	133.439	35.346	-5.72	2.12	-2.53	0.06	0.05	0.18
950380	134.237	35.266	-6.44	2.19	-2.54	0.06	0.05	0.17
950381	133.309	35.165	-8.64	3.29	-3.81	0.07	0.05	0.17
950382	133.240	36.285	-0.43	2.95	-1.40	0.06	0.05	0.17
950383	132.984	36.093	-1.59	1.50	-1.07	0.06	0.05	0.17
950384	132.743	35.393	-2.63	2.71	-4.34	0.05	0.04	0.17
950385	132.995	35.196	-5.00	3.65	-2.03	0.05	0.04	0.18
950386	132.507	35.186	-3.10	2.77	-2.21	0.05	0.04	0.15
950387	132.721	35.020	-3.94	1.51	-2.84	0.06	0.04	0.16
950388	131.923	34.767	-5.62	2.42	-2.26	0.05	0.04	0.16
950389	133.792	35.264	-5.32	1.91	-1.85	0.07	0.06	0.18
950390	134.320	35.100	-6.64	6.53	-3.05	0.05	0.05	0.15
950391	134.235	35.021	-6.54	2.74	-1.95	0.05	0.04	0.15
950392	133.735	35.003	-5.82	2.85	-1.48	0.06	0.04	0.16
950393	133.961	34.983	-6.52	2.72	-2.27	0.05	0.04	0.16
950394	133.598	34.810	-6.26	4.46	0.20	0.06	0.05	0.16
950395	133.929	34.791	-7.41	2.26	-2.71	0.06	0.04	0.16
950396	134.166	34.658	-6.93	2.90	-2.59	0.05	0.04	0.15
950397	133.797	34.439	-9.35	6.44	0.91	0.06	0.04	0.15
950398	133.120	34.943	-5.64	4.07	-1.92	0.07	0.06	0.20
950399	132.277	34.727	-5.38	4.06	-1.74	0.06	0.04	0.17
950400	132.540	34.679	-7.24	3.58	-1.85	0.06	0.05	0.16
950401	133.108	34.672	-6.68	4.63	-0.92	0.05	0.04	0.16
950402	132.824	34.571	-7.20	5.77	-1.84	0.06	0.05	0.17
950403	132.463	34.539	-7.40	5.03	-3.01	0.05	0.04	0.16
950404	132.269	34.575	-4.93	4.77	-1.51	0.18	0.15	0.49
950405	133.010	34.379	-9.04	7.08	1.13	0.05	0.04	0.16
950406	132.345	34.370	-6.69	6.82	-6.51	0.32	0.30	0.93
950407	131.417	34.440	-4.96	3.66	-1.22	0.06	0.04	0.18
950408	130.943	34.295	-4.81	2.72	-1.11	0.06	0.04	0.17
950409	131.563	34.284	-5.99	5.33	-2.07	0.07	0.05	0.19
950410	131.953	34.259	-7.84	5.49	0.65	0.06	0.05	0.17
950411	131.346	34.189	-6.26	3.62	-0.38	0.06	0.05	0.18
950412	131.531	34.057	-7.95	4.43	-0.29	0.06	0.04	0.17
950413	131.286	33.978	-7.96	3.30	-0.73	0.06	0.04	0.16
950414	132.104	33.975	-11.66	6.96	1.76	0.06	0.05	0.16
950415	134.352	34.097	-17.29	8.33	0.86	0.06	0.05	0.16
950416	134.560	34.060	-19.05	8.11	2.38	0.06	0.04	0.16
950417	134.049	34.052	-17.54	9.89	4.97	0.07	0.05	0.20
950418	134.230	34.038	-18.51	9.42	2.38	0.06	0.05	0.17
950419	133.681	33.937	-19.87	11.34	4.06	0.06	0.05	0.17
950420	134.389	33.879	-23.86	9.79	1.56	0.07	0.07	0.19
950421	134.058	33.878	-19.65	14.54	0.95	0.08	0.06	0.16
950422	134.668	33.830	-26.05	10.24	1.33	0.06	0.05	0.16
950423	134.533	33.725	-28.12	11.31	-0.73	0.06	0.05	0.17
950424	134.372	33.618	-32.43	14.30	0.63	0.06	0.05	0.17
950425	134.314	34.472	-8.82	4.94	-0.89	0.07	0.05	0.17
950426	134.242	34.255	-12.37	7.09	0.72	0.05	0.04	0.15

950427	133.715	34.217	-12.63	8.12	1.60	0.05	0.04	0.16
950428	133.648	34.068	-16.36	9.42	3.68	0.06	0.05	0.16
950429	133.926	34.164	-14.14	8.73	2.38	0.06	0.05	0.15
950430	132.990	34.078	-13.02	8.45	2.96	0.06	0.04	0.16
950431	133.538	33.939	-18.53	6.80	2.71	0.06	0.05	0.17
950432	133.201	33.921	-18.03	9.91	3.03	0.06	0.04	0.17
950433	132.912	33.796	-19.38	10.67	4.13	0.06	0.05	0.20
950434	132.684	33.723	-19.85	9.80	5.88	0.06	0.05	0.17
950435	132.938	33.569	-24.44	11.72	5.88	0.06	0.05	0.15
950436	132.693	33.447	-29.88	7.25	0.35	0.06	0.07	0.16
950437	132.562	32.964	-32.00	14.30	-4.63	0.06	0.05	0.17
950438	133.656	33.767	-23.43	12.60	4.23	0.06	0.05	0.17
950439	133.805	33.654	-27.26	14.63	2.57	0.06	0.05	0.18
950440	134.107	33.604	-31.37	15.71	0.51	0.06	0.06	0.17
950441	134.281	33.528	-35.85	15.52	-2.02	0.06	0.05	0.17
950442	133.904	33.506	-33.78	15.85	0.66	0.05	0.04	0.16
950443	133.281	33.468	-30.98	14.80	2.71	0.06	0.05	0.17
950444	134.007	33.428	-37.99	17.97	-3.05	0.05	0.04	0.16
950445	133.403	33.408	-32.98	16.18	2.60	0.06	0.05	0.15
950447	132.793	33.172	-31.34	14.18	-0.75	0.07	0.05	0.19
950448	132.999	32.991	-36.79	17.75	0.26	0.06	0.04	0.16
950449	132.704	32.841	-36.31	17.71	-5.41	0.06	0.04	0.17
950450	130.251	33.536	-3.48	-0.28	-0.88	0.06	0.06	0.19
950451	130.522	33.500	-7.94	1.97	-2.74	0.06	0.05	0.18
950452	130.829	33.465	-7.41	1.52	-0.40	0.06	0.05	0.18
950453	130.565	33.206	-6.35	-1.39	-1.88	0.05	0.04	0.17
950454	130.269	33.275	-3.98	-0.46	-0.86	0.06	0.04	0.16
950455	130.094	33.098	-3.55	-0.88	-1.31	0.06	0.05	0.17
950456	129.482	34.656	-1.41	0.92	0.31	0.06	0.04	0.16
950457	129.312	34.268	-0.96	1.08	0.02	0.06	0.05	0.17
950458	129.735	33.743	-1.77	0.63	0.41	0.06	0.04	0.17
950459	129.537	33.362	-1.75	0.37	0.14	0.06	0.04	0.16
950460	129.691	33.063	-2.50	-0.44	0.20	0.06	0.04	0.16
950461	130.271	32.871	-5.49	-2.77	-0.73	0.06	0.05	0.17
950462	128.843	32.669	-0.12	-0.94	0.31	0.06	0.05	0.18
950463	130.155	32.637	-5.10	-4.15	0.05	0.06	0.04	0.17
950464	130.548	32.933	-6.42	-0.92	-0.17	0.06	0.04	0.17
950465	130.765	32.842	-8.22	-1.72	-0.82	0.06	0.04	0.16
950466	131.099	32.741	-14.02	-1.62	-1.16	0.06	0.05	0.17
950467	129.987	32.326	-4.19	-5.65	-0.01	0.06	0.04	0.16
950468	130.507	32.299	-7.22	-5.44	-0.77	0.06	0.05	0.17
950469	130.803	32.239	-8.35	-5.09	0.95	0.07	0.05	0.18
950470	131.564	33.671	-11.58	5.92	0.86	0.11	0.09	0.19
950471	131.169	33.496	-10.06	3.41	-0.31	0.06	0.05	0.18
950472	131.347	33.254	-14.69	1.43	-1.01	0.08	0.06	0.19
950473	131.798	33.239	-21.62	5.13	4.22	0.06	0.05	0.18
950474	131.286	33.009	-17.49	-1.91	-1.38	0.06	0.06	0.19
950475	131.588	32.987	-20.58	2.81	0.95	0.06	0.05	0.17
950476	131.757	32.704	-21.36	5.97	0.41	0.06	0.06	0.18
950477	131.328	32.685	-17.20	-0.63	-0.99	0.06	0.06	0.18
950478	131.149	32.457	-12.94	-2.16	-1.03	0.07	0.06	0.21
950479	131.185	32.246	-14.66	-4.56	0.02	0.08	0.05	0.18
950480	131.516	32.170	-14.36	0.53	1.60	0.07	0.05	0.18
950481	131.079	31.965	-8.44	-5.61	0.75	0.07	0.05	0.21

950482	131.022	31.740	-2.06	-7.80	-0.90	0.06	0.05	0.19
950483	131.369	31.677	-3.25	-4.87	0.17	0.07	0.06	0.22
950484	131.217	31.469	-0.01	-8.06	0.74	0.06	0.05	0.19
950485	130.598	32.058	-6.03	-7.09	-0.35	0.06	0.05	0.17
950486	130.760	31.856	-2.64	-6.33	3.78	0.07	0.05	0.19
950487	129.795	31.769	0.54	-7.80	0.04	0.06	0.05	0.17
950488	130.278	31.717	-0.44	-8.80	4.56	0.06	0.05	0.20
950489	130.836	31.617	2.30	-10.18	2.10	0.07	0.05	0.20
950490	130.640	31.235	0.76	-10.47	-3.62	0.06	0.05	0.19
950491	130.723	31.106	1.40	-10.04	1.32	0.06	0.05	0.18
950492	130.964	30.531	2.90	-11.44	0.87	0.06	0.05	0.19
950493	130.638	30.382	1.56	-11.60	1.47	0.08	0.07	0.26
950494	129.489	28.399	-0.31	-17.09	0.57	0.08	0.07	0.20
950495	128.432	27.032	4.23	-24.59	1.85	0.06	0.06	0.17
950496	127.898	26.695	2.96	-25.97	-0.72	0.07	0.06	0.19
95105	139.171	35.041	-30.39	13.61	-2.50	0.07	0.05	0.18
95113	139.797	33.120	-39.32	24.64	1.89	0.09	0.08	0.23
960570	137.894	36.951	-11.21	3.48	-1.75	0.07	0.05	0.18
960572	137.370	36.737	-11.07	3.94	-1.65	0.07	0.05	0.15
960573	137.032	36.650	-9.64	3.70	-1.43	0.06	0.05	0.16
960577	136.756	36.817	-8.02	0.06	-4.22	0.06	0.05	0.16
960578	136.605	36.370	-8.03	0.99	-2.41	0.05	0.05	0.17
960579	136.185	35.969	-9.85	1.35	-1.88	0.05	0.04	0.16
960580	136.056	35.837	-9.88	1.23	-3.36	0.05	0.04	0.16
960581	140.498	36.743	-21.45	2.55	-2.50	0.13	0.06	0.15
960582	139.988	36.301	-22.30	4.67	-1.05	0.08	0.05	0.14
960583	139.931	36.115	-20.94	6.84	-11.11	0.06	0.04	0.13
960584	140.202	36.031	-21.79	5.10	-0.92	0.07	0.04	0.12
960585	140.165	36.952	-23.31	2.02	-1.79	0.11	0.06	0.18
960586	139.806	36.980	-22.13	3.17	-1.05	0.09	0.06	0.17
960587	139.854	36.776	-23.36	3.26	-2.20	0.09	0.05	0.16
960588	140.158	36.692	-22.59	3.55	-3.05	0.10	0.05	0.14
960589	139.491	36.624	-23.83	4.69	-1.94	0.08	0.06	0.17
960590	140.179	36.542	-21.70	3.50	-2.81	0.10	0.05	0.15
960591	138.591	36.616	-24.54	6.17	-3.08	0.09	0.06	0.20
960592	139.067	36.235	-24.03	5.11	-2.99	0.06	0.04	0.16
960593	138.912	36.143	-24.97	5.00	-1.81	0.06	0.04	0.15
960594	139.434	34.762	-28.75	26.73	3.08	0.10	0.07	0.22
960595	139.359	34.738	-43.23	20.92	4.16	0.12	0.05	0.21
960596	139.271	34.520	-36.57	15.92	0.91	0.07	0.05	0.17
960597	139.211	34.333	-38.64	13.21	-1.12	0.06	0.05	0.18
960598	139.138	34.240	-45.08	9.41	8.72	0.06	0.05	0.18
960599	139.562	34.094	-29.10	24.81	-1.22	0.13	0.07	0.29
960600	139.479	34.076	-40.52	24.61	11.79	0.07	0.05	0.22
960601	139.613	33.884	-35.68	27.55	-0.54	0.10	0.06	0.20
960602	139.765	32.464	-42.16	25.28	-6.02	0.12	0.10	0.20
960606	138.690	35.650	-24.74	7.00	-2.07	0.05	0.04	0.16
960607	139.026	35.512	-26.47	9.64	-0.81	0.05	0.05	0.16
960608	137.985	36.239	-20.79	4.54	-4.53	0.06	0.04	0.19
960609	137.872	36.228	-19.25	3.37	-3.59	0.07	0.05	0.19
960610	138.499	36.285	-23.70	6.47	-2.67	0.06	0.06	0.15
960611	137.683	36.085	-18.91	3.24	-2.03	0.08	0.06	0.21
960612	138.214	36.026	-22.72	5.01	-2.77	0.05	0.04	0.17
960613	138.583	35.974	-24.12	6.02	-2.69	0.07	0.05	0.18

960614	137.598	35.880	-18.09	2.91	-1.45	0.09	0.06	0.21
960615	137.984	35.726	-21.92	4.68	-1.25	0.08	0.05	0.21
960616	137.676	35.344	-21.57	5.09	2.33	0.05	0.05	0.15
960617	136.904	36.261	-11.84	2.15	-1.93	0.07	0.06	0.21
960618	137.363	36.286	-16.14	2.10	-2.84	0.05	0.05	0.19
960619	137.201	35.912	-19.52	2.14	-2.71	0.06	0.04	0.16
960620	138.777	34.855	-34.21	5.50	-3.21	0.07	0.05	0.17
960621	138.928	35.204	-29.52	2.38	1.34	0.07	0.05	0.18
960622	138.098	34.680	-30.28	7.52	-5.76	0.06	0.04	0.15
960623	138.183	34.678	-31.28	7.68	-6.14	0.05	0.04	0.15
960624	138.047	34.666	-30.17	7.91	-4.88	0.05	0.04	0.15
960625	138.159	34.635	-32.50	8.66	-6.69	0.06	0.04	0.15
960626	138.907	35.047	-30.94	2.32	-1.90	0.06	0.05	0.17
960627	140.086	36.104	-22.11	5.51	-3.36	0.07	0.04	0.12
960628	138.939	34.699	-37.55	8.98	-2.95	0.07	0.05	0.16
960629	137.074	35.239	-21.98	4.25	-0.71	0.05	0.04	0.15
960630	136.966	35.168	-21.60	4.18	3.05	0.05	0.04	0.15
960631	136.863	34.984	-23.04	3.88	3.15	0.05	0.04	0.15
960632	136.832	34.904	-22.89	4.05	4.43	0.05	0.04	0.14
960633	136.694	35.051	-21.05	2.88	3.08	0.06	0.04	0.16
960634	136.393	34.855	-19.85	2.37	1.72	0.06	0.05	0.19
960635	136.330	34.649	-20.85	2.06	4.51	0.09	0.05	0.21
960636	136.628	34.431	-24.62	4.67	2.91	0.06	0.05	0.17
960637	136.343	34.208	-25.01	4.76	1.27	0.06	0.05	0.18
960638	136.265	35.420	-14.51	1.12	-0.90	0.05	0.04	0.16
960639	136.041	35.086	-16.91	2.53	1.38	0.06	0.04	0.16
960640	135.034	35.685	-5.87	2.33	-2.67	0.05	0.04	0.15
960641	135.416	35.482	-8.58	1.91	-3.37	0.05	0.05	0.16
960642	135.550	35.276	-10.88	2.72	-2.28	0.05	0.05	0.16
960643	135.773	35.053	-13.74	1.53	-0.96	0.05	0.04	0.17
960644	135.772	34.953	-15.23	2.36	5.46	0.05	0.04	0.16
960645	134.677	35.621	-5.58	2.83	-3.41	0.06	0.04	0.18
960646	134.729	35.461	-6.76	2.19	-2.22	0.07	0.05	0.18
960647	135.022	35.238	-8.74	2.51	-2.89	0.06	0.05	0.17
960648	134.771	35.163	-7.67	1.96	-3.34	0.06	0.05	0.17
960649	134.945	34.936	-9.40	3.53	-2.02	0.05	0.04	0.16
960650	135.528	34.312	-18.38	4.53	3.59	0.05	0.05	0.16
960652	135.168	34.025	-19.78	0.91	-2.31	0.06	0.06	0.20
960653	135.496	33.554	-33.78	9.98	-1.57	0.05	0.04	0.16
960654	133.340	35.436	-2.68	2.62	-1.61	0.05	0.04	0.16
960655	134.325	35.361	-5.81	2.56	-3.03	0.06	0.05	0.17
960656	133.138	35.564	-4.57	4.69	-3.31	0.06	0.05	0.18
960657	132.457	34.893	-5.15	2.96	-1.55	0.06	0.06	0.17
960658	132.014	34.571	-5.19	4.03	-1.66	0.06	0.05	0.18
960659	131.864	34.440	-6.40	4.21	-0.07	0.07	0.05	0.18
960660	133.564	35.170	-4.63	2.46	-2.65	0.06	0.05	0.18
960662	133.396	34.993	-5.82	2.82	-1.30	0.06	0.04	0.17
960663	132.852	34.812	-4.79	3.34	-2.33	0.05	0.04	0.16
960664	133.338	34.778	-6.64	3.95	-1.82	0.05	0.04	0.15
960665	132.195	34.370	-7.86	5.72	-0.10	0.06	0.04	0.17
960666	132.456	34.261	-9.32	6.68	0.66	0.06	0.04	0.16
960667	132.884	34.210	-10.40	7.79	1.91	0.05	0.04	0.16
960668	131.152	34.764	-3.28	2.61	-1.41	0.06	0.04	0.16
960669	131.176	34.342	-6.58	2.33	2.40	0.07	0.05	0.20

960670	131.066	34.180	-5.44	3.18	-0.39	0.07	0.05	0.18
960672	132.358	33.910	-12.87	8.08	3.13	0.06	0.05	0.17
960673	134.605	34.172	-16.21	6.75	-0.32	0.05	0.04	0.15
960674	133.875	34.040	-16.32	11.86	1.94	0.06	0.04	0.17
960675	134.301	33.790	-26.21	11.60	2.26	0.06	0.05	0.18
960676	133.999	34.445	-8.15	5.88	-2.64	0.06	0.04	0.16
960677	133.781	34.383	-9.04	7.08	-0.58	0.05	0.04	0.15
960678	133.189	34.252	-10.29	7.23	1.80	0.08	0.08	0.17
960679	132.782	33.959	-14.06	9.25	4.72	0.06	0.04	0.16
960680	132.487	33.612	-20.27	9.75	3.83	0.07	0.09	0.20
960681	132.544	33.178	-27.75	10.93	-4.70	0.06	0.05	0.17
960683	133.228	33.327	-33.83	17.08	2.03	0.06	0.05	0.16
960684	133.129	33.215	-34.17	17.43	0.86	0.06	0.04	0.16
960685	130.750	33.746	-6.33	2.56	-3.31	0.06	0.05	0.18
960686	131.017	33.697	-8.08	2.80	-1.76	0.06	0.04	0.18
960687	130.824	33.640	-7.19	2.05	0.84	0.06	0.04	0.19
960688	130.701	33.327	-6.53	0.14	-1.84	0.06	0.07	0.18
960689	129.940	33.196	-3.10	0.42	0.27	0.06	0.04	0.18
960690	129.690	33.266	-2.51	-0.25	-0.98	0.06	0.05	0.17
960691	129.126	33.256	0.42	0.31	-0.31	0.06	0.04	0.16
960692	129.026	32.886	-0.66	-0.98	0.68	0.06	0.05	0.17
960693	130.166	32.796	-4.12	-2.27	-0.35	0.06	0.04	0.17
960694	130.336	32.793	-6.62	-2.74	-1.41	0.08	0.08	0.22
960695	130.217	32.712	-4.88	-2.67	-1.31	0.06	0.04	0.18
960696	130.352	32.723	-6.23	-2.66	-1.93	0.08	0.06	0.20
960697	130.291	32.661	-6.20	-3.05	-0.51	0.06	0.05	0.17
960698	128.619	32.634	0.36	-1.42	1.11	0.06	0.05	0.17
960699	131.063	33.122	-11.21	1.41	-4.37	0.06	0.05	0.20
960700	130.749	33.011	-7.64	-0.85	-1.34	0.06	0.04	0.17
960701	130.996	32.871	-9.15	-0.95	-4.92	0.07	0.05	0.19
960702	130.795	32.577	-9.90	-4.18	-0.11	0.06	0.05	0.17
960703	131.093	32.951	-14.83	-3.45	-2.53	0.07	0.06	0.22
960704	131.132	32.845	-16.05	-1.47	-3.27	0.07	0.06	0.21
960705	131.357	33.537	-11.25	4.80	0.31	0.06	0.04	0.17
960706	131.588	33.350	-17.34	4.36	2.62	0.07	0.05	0.20
960707	131.121	33.270	-10.80	2.06	-0.41	0.06	0.05	0.21
960709	131.579	33.228	-20.28	2.80	-0.06	0.06	0.05	0.20
960710	130.916	33.191	-8.37	0.53	-1.02	0.06	0.05	0.18
960711	131.531	32.557	-17.59	1.67	0.75	0.07	0.05	0.17
960712	131.334	32.384	-14.33	-0.87	0.26	0.07	0.05	0.19
960713	131.486	32.069	-10.93	-2.59	-2.75	0.06	0.05	0.18
960714	130.866	32.048	-8.02	-6.13	0.84	0.07	0.05	0.19
960715	131.306	31.842	-6.81	-4.07	-0.14	0.06	0.05	0.19
960716	131.306	31.399	0.63	-6.37	-1.27	0.07	0.05	0.20
960717	130.180	32.197	-7.18	-3.07	-2.27	0.06	0.05	0.17
960718	130.440	31.909	-2.12	-7.47	-0.54	0.06	0.05	0.17
960719	130.652	31.624	-3.22	-10.12	6.68	0.07	0.06	0.19
960720	130.709	31.592	0.03	-12.51	-1.29	0.10	0.07	0.22
960721	130.637	31.552	-0.06	-12.25	3.46	0.06	0.06	0.19
960722	130.699	31.496	0.92	-12.23	2.82	0.06	0.05	0.18
960723	130.275	30.785	0.80	-9.06	-0.47	0.07	0.05	0.19
960724	131.029	30.753	2.00	-9.35	2.10	0.06	0.05	0.18
960725	130.198	30.461	1.64	-9.88	-0.60	0.08	0.07	0.20
960726	130.903	30.399	4.03	-12.17	-0.11	0.06	0.05	0.19

960727	130.424	30.396	0.95	-10.21	0.50	0.09	0.09	0.27
960728	130.555	30.236	2.17	-10.37	0.51	0.09	0.08	0.26
960729	129.706	29.615	0.96	-12.39	-0.32	0.09	0.08	0.21
960730	129.694	28.487	2.22	-14.65	0.89	0.11	0.05	0.19
960731	130.029	28.371	3.75	-17.41	6.87	0.08	0.12	0.20
960732	129.922	28.294	1.02	-15.18	4.39	0.07	0.06	0.18
960733	129.320	28.138	0.85	-16.97	0.50	0.07	0.06	0.20
960734	128.894	27.817	2.97	-19.08	1.18	0.07	0.08	0.20
960735	128.651	27.401	4.57	-22.83	3.22	0.06	0.06	0.20
960736	127.945	26.944	4.02	-24.94	0.51	0.06	0.05	0.17
960737	128.248	26.859	4.44	-25.04	0.26	0.07	0.05	0.19
960738	128.144	26.708	5.41	-24.80	0.72	0.07	0.07	0.20
960739	127.232	26.583	5.62	-28.31	0.52	0.07	0.09	0.18
960740	127.972	26.483	5.74	-23.09	-0.89	0.07	0.07	0.20
960741	127.833	26.447	5.50	-25.86	0.30	0.06	0.05	0.19
960742	127.144	26.373	5.15	-28.28	0.59	0.06	0.05	0.18
960744	127.345	26.179	5.33	-27.72	-0.52	0.06	0.05	0.18
960745	127.826	26.169	5.92	-26.54	1.87	0.06	0.05	0.18
960752	139.057	36.539	-23.33	5.97	-4.20	0.06	0.05	0.17
960753	139.269	36.004	-25.45	7.18	-4.54	0.06	0.04	0.15
960754	139.182	35.884	-23.41	7.76	-1.33	0.05	0.04	0.17
960755	139.366	35.801	-24.70	8.42	0.24	0.05	0.04	0.15
960756	140.249	35.288	-28.75	16.43	-4.06	0.09	0.08	0.15
960758	139.370	35.616	-25.70	9.85	-0.15	0.05	0.05	0.16
960759	139.614	35.161	-33.25	22.47	-4.63	0.05	0.04	0.15
960760	135.790	34.882	-16.40	0.70	1.06	0.05	0.04	0.16
960761	135.619	34.621	-17.17	2.67	2.75	0.06	0.06	0.17
960762	134.660	34.864	-8.13	3.05	-1.98	0.05	0.04	0.15
960763	135.706	34.698	-17.49	1.77	2.85	0.08	0.05	0.23
960764	135.820	34.574	-18.77	2.42	2.23	0.06	0.04	0.17
960765	134.176	34.810	-7.01	3.50	-1.81	0.05	0.04	0.15
960766	133.757	34.579	-7.61	5.28	-0.48	0.05	0.04	0.15
960767	133.288	34.450	-8.76	6.42	0.10	0.06	0.04	0.16
960768	132.820	34.335	-7.61	5.06	0.48	0.06	0.04	0.16
960769	132.219	34.191	-10.32	5.48	-0.57	0.06	0.04	0.15
960770	129.955	33.372	-2.70	0.09	0.46	0.06	0.04	0.17
960771	130.445	33.346	-5.03	0.04	-2.16	0.10	0.11	0.21
960772	129.990	32.946	-4.24	-1.79	-0.35	0.06	0.05	0.17
960773	130.430	32.582	-7.35	-3.87	-0.97	0.06	0.04	0.17
960774	130.085	32.525	-5.14	-4.73	-0.13	0.06	0.05	0.16
960775	130.324	32.426	-6.65	-3.74	-1.78	0.06	0.05	0.18
960776	130.469	31.675	-2.00	-7.67	1.23	0.06	0.05	0.20
960777	130.136	31.416	-0.24	-9.52	-0.73	0.07	0.05	0.18
970802	138.945	36.778	-23.54	7.12	-3.34	0.09	0.07	0.20
970804	139.522	35.419	-30.48	12.86	-2.15	0.05	0.06	0.14
970809	138.457	35.674	-22.90	6.83	-2.31	0.07	0.06	0.21
970811	137.529	35.575	-20.64	4.47	1.54	0.05	0.04	0.16
970812	136.470	35.360	-16.19	2.04	-2.11	0.06	0.05	0.19
970813	138.974	35.114	-29.99	3.11	0.13	0.06	0.05	0.19
970814	138.876	34.719	-36.29	7.33	-2.89	0.06	0.04	0.16
970815	138.610	35.117	-30.74	2.91	-3.59	0.06	0.06	0.16
970817	138.210	35.067	-27.71	-1.88	-5.14	0.06	0.06	0.17
970818	138.082	35.045	-24.33	3.71	0.61	0.06	0.05	0.19
970819	137.947	34.902	-26.30	5.97	1.01	0.06	0.04	0.18

970820	138.177	34.849	-27.46	6.35	-4.36	0.06	0.05	0.17
970821	137.681	34.752	-28.09	7.59	0.45	0.05	0.04	0.15
970822	136.789	35.301	-19.62	2.37	1.04	0.05	0.04	0.15
970823	134.588	35.283	-3.79	8.94	-6.00	0.06	0.05	0.17
970824	136.097	34.180	-23.76	3.82	1.55	0.07	0.05	0.20
970825	135.735	33.969	-24.18	4.58	2.91	0.06	0.05	0.19
970826	135.709	33.637	-31.57	7.02	-1.30	0.07	0.05	0.17
970827	134.393	34.218	-13.87	7.15	0.58	0.06	0.05	0.16
970828	132.046	33.368	-22.87	8.76	3.40	0.06	0.04	0.16
970829	132.475	33.384	-24.12	10.23	4.03	0.06	0.05	0.16
970830	133.363	33.704	-23.25	12.14	4.01	0.06	0.05	0.18
970831	130.465	33.097	-5.37	-0.51	-0.82	0.05	0.04	0.17
970832	129.721	32.840	-2.44	-2.37	-0.36	0.06	0.04	0.17
970833	131.207	33.128	-18.27	-2.65	-5.49	0.07	0.06	0.20
970834	130.361	32.098	-5.06	-6.81	-0.34	0.06	0.05	0.17
970835	130.239	31.906	-1.25	-7.31	-0.22	0.06	0.05	0.17
970836	130.408	31.796	-1.76	-7.90	0.29	0.06	0.05	0.17
970837	130.600	31.824	-2.78	-6.11	1.52	0.07	0.05	0.19
990838	138.763	34.690	-36.92	7.49	-3.52	0.07	0.05	0.16
990840	138.331	34.836	-30.42	6.71	-5.38	0.08	0.04	0.16
950497	131.228	25.831	-66.41	37.50	0.07	0.06	0.05	0.18
960746	131.291	25.954	-66.98	36.99	0.67	0.06	0.05	0.18
52007	142.195	27.068	-52.08	20.50	1.39	0.17	0.09	0.35
942003	142.185	27.096	-53.17	21.65	0.31	0.11	0.08	0.23
960603	142.163	26.635	-56.31	24.58	-1.34	0.12	0.07	0.25
21098	153.979	24.290	-96.87	36.49	1.19	0.10	0.08	0.36
51140	136.081	20.426	-74.68	30.53	-3.18	0.29	0.17	1.66
ZENISU	138.818	33.944	-47.76	6.25	-2.76	11.91	4.19	7.25
TOK1	138.140	34.080	-49.00	9.00	-	2.00	1.00	-
TOK2	137.610	33.880	-48.00	10.00	-	2.00	1.00	-
TOK3	137.390	34.180	-51.00	8.00	-	4.00	5.00	-
KUM1	137.000	33.670	-36.00	7.00	-	1.00	2.00	-
KUM2	136.670	33.430	-42.00	10.00	-	5.00	9.00	-
KUM3	136.360	33.330	-39.00	10.00	-	2.00	2.00	-
SIOW	135.570	33.160	-44.00	16.00	-	2.00	2.00	-
MRT1	134.940	33.350	-33.00	10.00	-	4.00	4.00	-
MRT2	134.810	32.870	-38.00	10.00	-	2.00	2.00	-
TOS1	133.670	32.820	-47.00	28.00	-	6.00	4.00	-
TOS2	134.030	32.430	-42.00	24.00	-	5.00	5.00	-
ASZ1	133.220	32.370	-41.00	19.00	-	3.00	4.00	-
ASZ2	133.580	31.930	-39.00	17.00	-	6.00	4.00	-
HYG1	132.420	32.380	-31.00	21.00	-	4.00	3.00	-
HYG2	132.490	31.970	-20.00	3.00	-	6.00	7.00	-
KMN	136.508	33.726	-42.00	8.00	-	1.00	4.00	-
KMC	136.558	33.642	-37.00	8.00	-	2.00	9.00	-
KMS	136.612	33.577	-50.00	10.00	-	2.00	2.00	-
KME	137.117	33.885	-29.00	6.00	-	10.00	8.00	-
TCA	137.001	33.219	-35.00	6.00	-	17.00	18.00	-
TOA	137.174	32.829	-51.00	18.00	-	20.00	6.00	-
TCB	137.386	33.544	-59.00	33.00	-	20.00	37.00	-
SNW	138.591	34.934	-36.00	3.00	-	9.00	6.00	-
SNE	138.682	34.935	-40.00	-5.00	-	8.00	2.00	-

References

Akaike, H. (1980). Likelihood and the Bayes procedure. *Trabajos de Estadistica Y de Investigacion Operativa*, *31*(1), 143–166. https://doi.org/10.1007/BF02888350

Almeida, R., Lindsey, E. O., Bradley, K., Hubbard, J., Mallick, R., & Hill, E. M. (2018). Can the Updip Limit of Frictional Locking on Megathrusts Be Detected Geodetically? Quantifying the Effect of Stress Shadows on Near-Trench Coupling. *Geophysical Research Letters*, *45*(10), 4754–4763. https://doi.org/10.1029/2018GL077785

Ando, M. (1975). Source mechanisms and tectonic significance of historical earthquakes along the nankai trough, Japan. *Tectonophysics*, *27*(2), 119–140. https://doi.org/10.1016/0040-1951(75)90102-X

Aoi, S., Obara, K., Hori, S., Kasahara, K., & Okada, Y. (2000). New strong-motion observation network: KiK-net. *EOS. Trans. Am. Geophys. Union*, *81*, 329.

Araki, E., Saffer, D. M., Kopf, A. J., Wallace, L. M., Kimura, T., Machida, Y., et al. (2017). Recurring and triggered slow-slip events near the trench at the Nankai Trough subduction megathrust. *Science*, *356*(6343), 1157–1160. https://doi.org/10.1126/science.aan3120

Asano, K., & Iwata, T. (2012). Source model for strong ground motion generation in the frequency range 0.1–10 Hz during the 2011 Tohoku earthquake. *Earth, Planets and Space*, *64*(12), 1111–1123. https://doi.org/10.5047/eps.2012.05.003

Baba, T., Tanioka, Y., Cummins, P. R., & Uhira, K. (2002). The slip distribution of the 1946 Nankai earthquake estimated from tsunami inversion using a new plate model. *Physics of the Earth and Planetary Interiors*, *132*(1–3), 59–73. https://doi.org/10.1016/S0031-9201(02)00044-4

Becker, J. J., Sandwell, D. T., Smith, W. H. F., Braud, J., Binder, B., Depner, J., et al. (2009). Global Bathymetry and Elevation Data at 30 Arc Seconds Resolution: SRTM30_PLUS. *Marine Geodesy*, *32*(4), 355–371. https://doi.org/10.1080/01490410903297766

Bernard, P., & Madariaga, R. (1984). a New Asymptotic Method for the Modeling of Near-Field Accelerograms. *Bulletin of the Seismological Society of America*, *74*(2), 539–557.

Bird, P. (2003). An updated digital model of plate boundaries. *Geochemistry, Geophysics, Geosystems*, *4*(3). https://doi.org/10.1029/2001GC000252

Brace, W. F., & Byerlee, J. D. (1966). Stick-Slip as a Mechanism for Earthquakes. *Science*, *153*(3739), 990–992. https://doi.org/10.1126/science.153.3739.990

Bürgmann, R. (2005). Interseismic coupling and asperity distribution along the Kamchatka subduction zone. *Journal of Geophysical Research*, *110*(B7), B07405. https://doi.org/10.1029/2005JB003648

Carvajal-Soto, L. A., Ito, T., Protti, M., & Kimura, H. (2020). Earthquake potential in Costa Rica using three scenarios for the central Costa Rica deformed belt as western boundary of the Panama microplate. *Journal of South American Earth Sciences*, *97*(July 2019), 102375. https://doi.org/10.1016/j.jsames.2019.102375

Cummins, P. R., Hori, T., & Kaneda, Y. (2001). Splay fault and megathrust earthquake slip in the Nankai Trough. *Earth, Planets and Space*, *53*(4), 243–248. https://doi.org/10.1186/BF03352381

DeMets, C., Gordon, R. G., & Argus, D. F. (2010). Geologically current plate motions.

Geophysical Journal International, *181*(1), 1–80. https://doi.org/10.1111/j.1365-246X.2009.04491.x
Dieterich, J. H. (1979). Modeling of rock friction: 1. Experimental results and constitutive equations. *Journal of Geophysical Research*, *84*(B5), 2161. https://doi.org/10.1029/JB084iB05p02161
Earl, D. J., & Deem, M. W. (2005). Parallel tempering: Theory, applications, and new perspectives. *Physical Chemistry Chemical Physics*, *7*(23), 3910. https://doi.org/10.1039/b509983h
Fukao, Y., & Furumoto, M. (1979). Stress drops, wave spectra and recurrence intervals of great earthquakes – implications of the Etorofu earthquake of 1958 November 6. *Geophysical Journal International*, *57*(1), 23–40. https://doi.org/10.1111/j.1365-246X.1979.tb03769.x
Garrett, E., Fujiwara, O., Garrett, P., Heyvaert, V. M. A., Shishikura, M., Yokoyama, Y., et al. (2016). A systematic review of geological evidence for Holocene earthquakes and tsunamis along the Nankai-Suruga Trough, Japan. *Earth-Science Reviews*, *159*, 337–357. https://doi.org/10.1016/j.earscirev.2016.06.011
Gutscher, & Lallemand. (1999). Birth of a major strike-slip fault in SW Japan. *Terra Nova*, *11*(5), 203–209. https://doi.org/10.1046/j.1365-3121.1999.00247.x
Habeck, M., Nilges, M., & Rieping, W. (2005). Replica-Exchange Monte Carlo Scheme for Bayesian Data Analysis. *Physical Review Letters*, *94*(1), 018105. https://doi.org/10.1103/PhysRevLett.94.018105
Hanifa, N. R., Sagiya, T., Kimata, F., Efendi, J., Abidin, H. Z., & Meilano, I. (2014). Interplate coupling model off the southwestern coast of Java, Indonesia, based on continuous GPS data in 2008–2010. *Earth and Planetary Science Letters*, *401*, 159–171. https://doi.org/10.1016/j.epsl.2014.06.010
Hashimoto, C., Fukui, K., & Matsu'ura, M. (2004). 3-D Modelling of Plate Interfaces and Numerical Simulation of Long-term Crustal Deformation in and around Japan. *Pure and Applied Geophysics*, *161*(9–10), 2053–2068. https://doi.org/10.1007/s00024-004-2548-8
Hashimoto, C., Noda, A., Sagiya, T., & Matsu'ura, M. (2009). Interplate seismogenic zones along the Kuril–Japan trench inferred from GPS data inversion. *Nature Geoscience*, *2*(2), 141–144. https://doi.org/10.1038/ngeo421
Hashimoto, C., Noda, A., & Matsu'ura, M. (2012). The Mw 9.0 northeast Japan earthquake: total rupture of a basement asperity. *Geophysical Journal International*, *189*(1), 1–5. https://doi.org/10.1111/j.1365-246X.2011.05368.x
Hastings, W. K. (1970). Monte Carlo Sampling Methods Using Markov Chains and Their Applications. *Biometrika*, *57*(1), 97. https://doi.org/10.2307/2334940
Hayes, G. P., Moore, G. L., Portner, D. E., Hearne, M., Flamme, H., Furtney, M., & Smoczyk, G. M. (2018). Slab2, a comprehensive subduction zone geometry model. *Science*, *362*(6410), 58–61. https://doi.org/10.1126/science.aat4723
Herman, M. W., & Govers, R. (2020). Locating Fully Locked Asperities Along the South America Subduction Megathrust: A New Physical Interseismic Inversion Approach in a Bayesian Framework. *Geochemistry, Geophysics, Geosystems*, *21*(8), e2020GC009063. https://doi.org/10.1029/2020GC009063
Herman, M. W., Furlong, K. P., & Govers, R. (2018). The Accumulation of Slip Deficit in Subduction Zones in the Absence of Mechanical Coupling: Implications for the Behavior of Megathrust Earthquakes. *Journal of Geophysical Research: Solid*

Earth, *123*(9), 8260–8278. https://doi.org/10.1029/2018JB016336
Hirose, F., Nakajima, J., & Hasegawa, A. (2008). Three-dimensional seismic velocity structure and configuration of the Philippine Sea slab in southwestern Japan estimated by double-difference tomography. *Journal of Geophysical Research: Solid Earth*, *113*(B9). https://doi.org/10.1029/2007JB005274
Hyodo, M., & Hirahara, K. (2003). A viscoelastic model of interseismic strain concentration in Niigata-Kobe Tectonic Zone of central Japan. *Earth, Planets and Space*, *55*(11), 667–675. https://doi.org/10.1186/BF03352473
Ida, Y. (1973). The maximum acceleration of seismic ground motion. *Bulletin of the Seismological Society of America*, *63*(3), 959–968.
Iinuma, T., Hino, R., Kido, M., Inazu, D., Osada, Y., Ito, Y., et al. (2012). Coseismic slip distribution of the 2011 off the Pacific Coast of Tohoku Earthquake (M9.0) refined by means of seafloor geodetic data. *Journal of Geophysical Research: Solid Earth*, *117*(B7), n/a-n/a. https://doi.org/10.1029/2012JB009186
Iinuma, T., Hino, R., Uchida, N., Nakamura, W., Kido, M., Osada, Y., & Miura, S. (2016). Seafloor observations indicate spatial separation of coseismic and postseismic slips in the 2011 Tohoku earthquake. *Nature Communications*, *7*(1), 13506. https://doi.org/10.1038/ncomms13506
Ioki, K., & Tanioka, Y. (2016). Rupture Process of the 1969 and 1975 Kurile Earthquakes Estimated from Tsunami Waveform Analyses. *Pure and Applied Geophysics*, *173*(12), 4179–4187. https://doi.org/10.1007/s00024-016-1402-0
Ito, T., Ozawa, K., Watanabe, T., & Sagiya, T. (2011). Slip distribution of the 2011 off the Pacific coast of Tohoku Earthquake inferred from geodetic data. *Earth, Planets and Space*, *63*(7), 21. https://doi.org/10.5047/eps.2011.06.023
Ito, Y., Obara, K., Shiomi, K., Sekine, S., & Hirose, H. (2007). Slow Earthquakes Coincident with Episodic Tremors and Slow Slip Events. *Science*, *315*(5811), 503–506. https://doi.org/10.1126/science.1134454
Ito, Y., Obara, K., Matsuzawa, T., & Maeda, T. (2009). Very low frequency earthquakes related to small asperities on the plate boundary interface at the locked to aseismic transition. *Journal of Geophysical Research: Solid Earth*, *114*(B11), 1–16. https://doi.org/10.1029/2008JB006036
Itoh, Y., Nishimura, T., Ariyoshi, K., & Matsumoto, H. (2019). Interplate Slip Following the 2003 Tokachi-oki Earthquake From Ocean Bottom Pressure Gauge and Land GNSS Data. *Journal of Geophysical Research: Solid Earth*, 2018JB016328. https://doi.org/10.1029/2018JB016328
Iwasaki, T., Sato, H., Ishiyama, T., Shinohara, M., & Hashima, A. (2015). Fundamental structure model of island arcs and subducted plates in and around Japan. In *2015 Fall Meeting* (Vol. 2015, pp. T31B-2878). San Francisco: American Geophysical Union.
Johnson, K. M., & Fukuda, J. (2010). New methods for estimating the spatial distribution of locked asperities and stress-driven interseismic creep on faults with application to the San Francisco Bay Area, California. *Journal of Geophysical Research*, *115*(B12), B12408. https://doi.org/10.1029/2010JB007703
Kaidzu, M., Nishimura, T., Murakami, M., Ozawa, S., Sagiya, T., Yarai, H., & Imakiire, T. (2000). Crustal deformation associated with crustal activities in the northern Izu-islands area during the summer, 2000. *Earth, Planets and Space*, *52*(8), ix–xviii. https://doi.org/10.1186/BF03351658

Kamae, K., & Kawabe, H. (2004). Source model composed of asperities for the 2003 Tokachi-oki, Japan, earthquake (M JMA = 8.0) estimated by the empirical Green's function method. *Earth, Planets and Space*, *56*(3), 323–327. https://doi.org/10.1186/BF03353059

Kanda, K., Takemura, M., & Usami, T. (2004). Short-period Seismic Wave Radiation Zones of a Megathrust Fault along the Nankai Trough Deduced from Inversion Analysis of Seismic Intensity Data. *Zisin (Journal of the Seismological Society of Japan. 2nd Ser.)*, *57*(2), 153–170. https://doi.org/10.4294/zisin1948.57.2_153

Kaneda, Y., Park, J.-O., Obana, K., Kinoshita, M., Hori, T., Kodaira, S., et al. (2006). Crustal Structure and Urgent Aftershock Observation of the 2004 Off Kii-Peninsula Earthquake. *Zisin (Journal of the Seismological Society of Japan. 2nd Ser.)*, *59*(2), 187–197. https://doi.org/10.4294/zisin.59.187

Kano, M., Aso, N., Matsuzawa, T., Ide, S., Annoura, S., Arai, R., et al. (2018). Development of a Slow Earthquake Database. *Seismological Research Letters*, *89*(4), 1566–1575. https://doi.org/10.1785/0220180021

Kato, N., Sato, H., Orito, M., Hirakawa, K., Ikeda, Y., & Ito, T. (2004). Has the plate boundary shifted from central Hokkaido to the eastern part of the Sea of Japan? *Tectonophysics*, *388*(1), 75–84. https://doi.org/https://doi.org/10.1016/j.tecto.2004.04.030

Kawase, H. (1998). Metamorphosis of near-field strong motions by underground structures and their destructiveness to man-made structures-Learned from the damage belt formation during the Hyogo-ken Nanbu earthquake of 1995. In *Proc. 10th Japan Earthquake Engineering Symp., 1998* (pp. 29–34). Yokohama, Japan.

Kido, M., Fujimoto, H., Hino, R., Ohta, Y., Osada, Y., Iinuma, T., et al. (2015). Progress in the Project for Development of GPS/Acoustic Technique Over the Last 4 Years. In *International Association of Geodesy Symposia* (pp. 3–10). https://doi.org/10.1007/1345_2015_127

Kimura, G. (1986). Oblique subduction and collision: Forearc tectonics of the Kuril arc. *Geology*, *14*(5), 404. https://doi.org/10.1130/0091-7613(1986)14<404:OSACFT>2.0.CO;2

Kimura, G. (1996). Collision orogeny at arc-arc junctions in the Japanese Islands. *Island Arc*, *5*(3), 262–275. https://doi.org/10.1111/j.1440-1738.1996.tb00031.x

Kimura, G., & Kusunoki, K. (1997). Geological and Tectonic Background of the Hidaka Belt, The Hidaka Orogeny and tectonics of arc-arc junction. *The Memoirs of the Geological Society of Japan*, *47*, 295–305. Retrieved from https://ci.nii.ac.jp/naid/110003025971/

Kimura, H., Ito, T., Tadokoro, K., & Sasajima, R. (2019). Estimation of Interplate Mechanical Coupling Distribution along the Chishima and Japan Trench in Northeast Japan based on Onshore and Seafloor Geodetic Observations. In *AGU Fall Meeting Abstracts* (pp. G43B-0749). American Geophysical Union.

Kimura, H., Tadokoro, K., & Ito, T. (2019). Interplate Coupling Distribution Along the Nankai Trough in Southwest Japan Estimated From the Block Motion Model Based on Onshore GNSS and Seafloor GNSS/A Observations. *Journal of Geophysical Research: Solid Earth*, *124*(6), 6140–6164. https://doi.org/10.1029/2018JB016159

Kinoshita, S. (1998). Kyoshin Net (K-NET). *Seismological Research Letters*, *69*(4), 309–332. https://doi.org/10.1785/gssrl.69.4.309

Kita, S., Okada, T., Hasegawa, A., Nakajima, J., & Matsuzawa, T. (2010). Anomalous deepening of a seismic belt in the upper-plane of the double seismic zone in the Pacific slab beneath the Hokkaido corner: Possible evidence for thermal shielding caused by subducted forearc crust materials. *Earth and Planetary Science Letters*, *290*(3), 415–426. https://doi.org/https://doi.org/10.1016/j.epsl.2009.12.038

Klein, E., Vigny, C., Fleitout, L., Grandin, R., Jolivet, R., Rivera, E., & Métois, M. (2017). A comprehensive analysis of the Illapel 2015 Mw8.3 earthquake from GPS and InSAR data. *Earth and Planetary Science Letters*, *469*, 123–134. https://doi.org/10.1016/j.epsl.2017.04.010

Kodaira, S., Kurashimo, E., Park, J.-O., Takahashi, N., Nakanishi, A., Miura, S., et al. (2002). Structural factors controlling the rupture process of a megathrust earthquake at the Nankai trough seismogenic zone. *Geophysical Journal International*, *149*(3), 815–835. https://doi.org/10.1046/j.1365-246X.2002.01691.x

Komatsubara, T. (2015). Plate tectonics around the Japan arc system inferred from slip rate of active faults. *Active Fault Research*, *2015*(43), 17–34. https://doi.org/10.11462/afr.2015.43_17

Koper, K. D., Hutko, A. R., Lay, T., & Sufri, O. (2012). Imaging short-period seismic radiation from the 27 February 2010 Chile (M W 8.8) earthquake by back-projection of P , PP , and PKIKP waves. *Journal of Geophysical Research: Solid Earth*, *117*(B2), n/a-n/a. https://doi.org/10.1029/2011JB008576

Koyama, M. (1995). Reevaluation of the West Sagami Bay Fracture and Seismotectonics in and around the Northwestern Sagami Bay, Japan. *Journal of Geography (Chigaku Zasshi)*, *104*(1), 45–68. https://doi.org/10.5026/jgeography.104.45

Kurahashi, S., & Irikura, K. (2013). Short-Period Source Model of the 2011 Mw 9.0 Off the Pacific Coast of Tohoku Earthquake. *Bulletin of the Seismological Society of America*, *103*(2B), 1373–1393. https://doi.org/10.1785/0120120157

Lallemant, S., Chamot-Rooke, N., Le Pichon, X., & Rangin, C. (1989). Zenisu Ridge: a deep intraoceanic thrust related to subduction, off southwest Japan. *Tectonophysics*, *160*(1–4), 151–174. https://doi.org/10.1016/0040-1951(89)90389-2

Larson, K. M., & Miyazaki, S. (2008). Resolving static offsets from high-rate GPS data: the 2003 Tokachi-oki earthquake. *Earth, Planets and Space*, *60*(8), 801–808. https://doi.org/10.1186/BF03352831

Lay, T., Kanamori, H., Ammon, C. J., Koper, K. D., Hutko, A. R., Ye, L., et al. (2012). Depth-varying rupture properties of subduction zone megathrust faults. *Journal of Geophysical Research: Solid Earth*, *117*(B4), n/a-n/a. https://doi.org/10.1029/2011JB009133

Liu, Z., Owen, S., Dong, D., Lundgren, P., Webb, F., Hetland, E., & Simons, M. (2010). Estimation of interplate coupling in the Nankai trough, Japan using GPS data from 1996 to 2006. *Geophysical Journal International*, *181*(3), 1313–1328. https://doi.org/10.1111/j.1365-246X.2010.04600.x

Loveless, J. P., & Meade, B. J. (2010). Geodetic imaging of plate motions, slip rates, and partitioning of deformation in Japan. *Journal of Geophysical Research*, *115*(B2), B02410. https://doi.org/10.1029/2008JB006248

Loveless, J. P., & Meade, B. J. (2015). Kinematic Barrier Constraints on the Magnitudes of Additional Great Earthquakes Off the East Coast of Japan.

Seismological Research Letters, *86*(1), 202–209. https://doi.org/10.1785/0220140083

Mazzotti, S., Henry, P., LePichon, X., & Sagiya, T. (1999). Strain partitioning in the zone of transition from Nankai subduction to Izu–Bonin collision (Central Japan): implications for an extensional tear within the subducting slab. *Earth and Planetary Science Letters*, *172*(1–2), 1–10. https://doi.org/10.1016/S0012-821X(99)00189-2

Mazzotti, S., Henry, P., & Le Pichon, X. (2001). Transient and permanent deformation of central Japan estimated by GPS 2. Strain partitioning and arc-arc collision. *Earth and Planetary Science Letters*, *184*(2), 455–469. https://doi.org/10.1016/S0012-821X(00)00336-8

Meade, B. J. (2007). Algorithms for the calculation of exact displacements, strains, and stresses for triangular dislocation elements in a uniform elastic half space. *Computers & Geosciences*, *33*(8), 1064–1075. https://doi.org/10.1016/j.cageo.2006.12.003

Menke, W. (2012). Chapter 8 - Linear Inverse Problems and Non-Gaussian Statistics. In W. Menke (Ed.), *Geophysical Data Analysis: Discrete Inverse Theory (Third Edition)* (Third Edit, pp. 149–161). Boston: Academic Press. https://doi.org/https://doi.org/10.1016/B978-0-12-397160-9.00008-4

Métois, M., Vigny, C., & Socquet, A. (2016). Interseismic Coupling, Megathrust Earthquakes and Seismic Swarms Along the Chilean Subduction Zone (38°–18°S). *Pure and Applied Geophysics*, *173*(5), 1431–1449. https://doi.org/10.1007/s00024-016-1280-5

Metropolis, N., Rosenbluth, A. W., Rosenbluth, M. N., Teller, A. H., & Teller, E. (1953). Equation of state calculations by fast computing machines. *The Journal of Chemical Physics*, *21*(6), 1087–1092. https://doi.org/10.1063/1.1699114

Miura, S., Sato, T., Tachibana, K., Satake, Y., & Hasegawa, A. (2002). Strain accumulation in and around Ou Backbone Range, northeastern Japan as observed by a dense GPS network. *Earth, Planets and Space*, *54*(11), 1071–1076. https://doi.org/10.1186/BF03353304

Miyake, H., Iwata, T., & Irikura, K. (2003). Source Characterization for Broadband Ground-Motion Simulation: Kinematic Heterogeneous Source Model and Strong Motion Generation Area. *Bulletin of the Seismological Society of America*, *93*(6), 2531–2545. https://doi.org/10.1785/0120020183

Miyatake, T., Miyake, H., Kimura, T., & Sumitani, K. (2008). A Study on the Radiation Mechanism of Short Period Seismic Wave. *Zisin (Journal of the Seismological Society of Japan. 2nd Ser.)*, *61*(2), 91–97. https://doi.org/10.4294/zisin.61.91

Miyazaki, S., & Larson, K. M. (2008). Coseismic and early postseismic slip for the 2003 Tokachi-oki earthquake sequence inferred from GPS data. *Geophysical Research Letters*, *35*(4), L04302. https://doi.org/10.1029/2007GL032309

Miyazaki, S., Segall, P., Fukuda, J., & Kato, T. (2004). Space time distribution of afterslip following the 2003 Tokachi-oki earthquake: Implications for variations in fault zone frictional properties. *Geophysical Research Letters*, *31*(6). https://doi.org/10.1029/2003GL019410

Moreno, M., Rosenau, M., & Oncken, O. (2010). 2010 Maule earthquake slip correlates with pre-seismic locking of Andean subduction zone. *Nature*, *467*(7312), 198–202. https://doi.org/10.1038/nature09349

Murotani, S., Kikuchi, M., & Yamanaka, Y. (2003). Rupture processesof large Fukushima-oki earthquakesin 1938. In *Japan Geoscience Union Meeting*. Chiba, Japan.

Murotani, S., Shimazaki, K., & Koketsu, K. (2015). Rupture process of the 1946 Nankai earthquake estimated using seismic waveforms and geodetic data. *Journal of Geophysical Research: Solid Earth*, *120*(8), 5677–5692. https://doi.org/10.1002/2014JB011676

Nagai, R., Kikuchi, M., & Yamanaka, Y. (2001). Comparative Study on the Source Processes of Recurrent Large Earthquakes in Sanriku-oki Region: the 1968 Tokachi-oki Earthquake and the 1994 Sanriku-oki Earthquake. *Zisin (Journal of the Seismological Society of Japan. 2nd Ser.)*, *54*(2), 267–280. https://doi.org/10.4294/zisin1948.54.2_267

Nakagawa, H., Toyofuku, T., Kotani, K., Miyahara, B., Iwashita, C., & Kawamoto, S. (2009). Development and validation of geonet new analysis strategy (version 4). *Times of Geospatial Information Authority of Japan*.

Nakajima, J., & Hasegawa, A. (2006). Anomalous low-velocity zone and linear alignment of seismicity along it in the subducted Pacific slab beneath Kanto, Japan: Reactivation of subducted fracture zone? *Geophysical Research Letters*, *33*(16), L16309. https://doi.org/10.1029/2006GL026773

Nakajima, J., Hirose, F., & Hasegawa, A. (2009). Seismotectonics beneath the Tokyo metropolitan area, Japan: Effect of slab-slab contact and overlap on seismicity. *Journal of Geophysical Research: Solid Earth*, *114*(B8). https://doi.org/10.1029/2008JB006101

Nakamura, K. (1983). Possible Nascent Trench along the Eastern Japan Sea as the Convergent Boundary between Eurasian and North American Plates. *Bulletin of the Earthquake Research Institute, University of Tokyo*, *58*(3), 711–722.

Nakata, T., & Imaizumi, T. (2002). *Digital active fault map of Japan*. Tokyo, Japan: Univ. of Tokyo Press. Retrieved from https://ci.nii.ac.jp/ncid/BA57141039

Nakata, T., Tokuyama, E., Suzuki, Y., Muroi, S., WAtanabe, M., Suzuki, Y., et al. (2013). Active fault traces of Zenisu fault, south of Nankai trough and historical earhtquakes. *Proceedings of the General Meeting of the Association of Japanese Geographers*, *2013s*, 240. https://doi.org/10.14866/ajg.2013s.0_240

Nishimura, T., & Takada, Y. (2017). San-in shear zone in southwest Japan, revealed by GNSS observations. *Earth, Planets and Space*, *69*(1). https://doi.org/10.1186/s40623-017-0673-8

Nishimura, T., Suito, H., Kobayashi, T., & Tobita, M. (2012). Crustal Deformation in and around the Echigo Plain Clarified by Geodetic Observation across the Niigata-Kobe Tectonic Zone. *Zisin (Journal of the Seismological Society of Japan. 2nd Ser.)*, *64*(4), 211–222. https://doi.org/10.4294/zisin.64.211

Nishimura, T., Matsuzawa, T., & Obara, K. (2013). Detection of short-term slow slip events along the Nankai Trough, southwest Japan, using GNSS data. *Journal of Geophysical Research: Solid Earth*, *118*(6), 3112–3125. https://doi.org/10.1002/jgrb.50222

Nishimura, T., Yokota, Y., Tadokoro, K., & Ochi, T. (2018). Strain partitioning and interplate coupling along the northern margin of the Philippine Sea plate, estimated from Global Navigation Satellite System and Global Positioning System-Acoustic data. *Geosphere*, *14*(2), 535–551. https://doi.org/10.1130/GES01529.1

Noda, A., Saito, T., & Fukuyama, E. (2018). Slip-Deficit Rate Distribution Along the Nankai Trough, Southwest Japan, With Elastic Lithosphere and Viscoelastic Asthenosphere. *Journal of Geophysical Research: Solid Earth*, *123*(9), 8125–8142. https://doi.org/10.1029/2018JB015515

Nozu, A., & Irikura, K. (2008). Strong-Motion Generation Areas of a Great Subduction-Zone Earthquake: Waveform Inversion with Empirical Green's Functions for the 2003 Tokachi-oki Earthquake. *Bulletin of the Seismological Society of America*, *98*(1), 180–197. https://doi.org/10.1785/0120060183

Nozu, A., Yamada, M., Nagao, T., & Irikura, K. (2012). Generation of Strong Motion Pulses during Huge Subduction Earthquakes and Scaling of Their Generation Areas. *Journal of Japan Association for Earthquake Engineering*, *12*(4), 4_209-4_228. https://doi.org/10.5610/jaee.12.4_209

Obana, K., & Kodaira, S. (2009). Low-frequency tremors associated with reverse faults in a shallow accretionary prism. *Earth and Planetary Science Letters*, *287*(1–2), 168–174. https://doi.org/10.1016/j.epsl.2009.08.005

Obara, K. (2002). Nonvolcanic Deep Tremor Associated with Subduction in Southwest Japan. *Science*, *296*(5573), 1679–1681. https://doi.org/10.1126/science.1070378

Obara, K. (2009). Inhomogeneous distribution of deep slow earthquake activity along the strike of the subducting Philippine Sea Plate. *Gondwana Research*, *16*(3–4), 512–526. https://doi.org/10.1016/j.gr.2009.04.011

Obara, K. (2011). Characteristics and interactions between non-volcanic tremor and related slow earthquakes in the Nankai subduction zone, southwest Japan. *Journal of Geodynamics*, *52*(3–4), 229–248. https://doi.org/10.1016/j.jog.2011.04.002

Obara, K. (2020). Characteristic activities of slow earthquakes in Japan. *Proceedings of the Japan Academy, Series B*, *96*(7), 297–315. https://doi.org/10.2183/pjab.96.022

Obara, K., & Ito, Y. (2005). Very low frequency earthquakes excited by the 2004 off Kii peninsula earthquakes: A dynamic deformation process in the large accretionary prism. *Earth, Planets and Space*, *57*(4), 321–326. https://doi.org/10.1186/BF03352570

Obara, K., & Kato, A. (2016). Connecting slow earthquakes to huge earthquakes. *Science*, *353*(6296), 253–257. https://doi.org/10.1126/science.aaf1512

Obara, K., Tanaka, S., Maeda, T., & Matsuzawa, T. (2010). Depth-dependent activity of non-volcanic tremor in southwest Japan. *Geophysical Research Letters*, *37*(13), n/a-n/a. https://doi.org/10.1029/2010GL043679

Ohzono, M., Takahashi, H., & Ichiyanagi, M. (2015). An intraplate slow earthquake observed by a dense GPS network in Hokkaido, northernmost Japan. *Geophysical Journal International*, *200*(1), 144–148. https://doi.org/10.1093/gji/ggu380

Okada, Y., Kasahara, K., Hori, S., Obara, K., Sekiguchi, S., Fujiwara, H., & Yamamoto, A. (2004). Recent progress of seismic observation networks in Japan —Hi-net, F-net, K-NET and KiK-net—. *Earth, Planets and Space*, *56*(8), xv–xxviii. https://doi.org/10.1186/BF03353076

Ortega, F. H. C. (2013). Aseismic Deformation in Subduction Megathrusts : Central Andes and North-East Japan, *2013*, 1–198.

Park, J.-O., & Kodaira, S. (2012). Seismic reflection and bathymetric evidences for the Nankai earthquake rupture across a stable segment-boundary. *Earth, Planets and Space*, *64*(3), 299–303. https://doi.org/10.5047/eps.2011.10.006

Park, J.-O., Moore, G. F., Tsuru, T., Kodaira, S., & Kaneda, Y. (2004). A subducted

oceanic ridge influencing the Nankai megathrust earthquake rupture. *Earth and Planetary Science Letters*, *217*(1–2), 77–84. https://doi.org/10.1016/S0012-821X(03)00553-3

Park, J.-O., Hori, T., & Kaneda, Y. (2009). Seismotectonic implications of the Kyushu-Palau ridge subducting beneath the westernmost Nankai forearc. *Earth, Planets and Space*, *61*(8), 1013–1018. https://doi.org/10.1186/BF03352951

Le Pichon, X., Mazzotti, S., Henry, P., & Hashimoto, M. (1998). Deformation of the Japanese Islands and seismic coupling: an interpretation based on GSI permanent GPS observations. *Geophysical Journal International*, *134*(2), 501–514. https://doi.org/10.1046/j.1365-246x.1998.00595.x

Robinson, D. P., & Cheung, L. T. (2010). Source process of the Mw 8.3, 2003 Tokachi-Oki, Japan earthquake and its aftershocks. *Geophysical Journal International*, *181*(1), 334–342. https://doi.org/10.1111/j.1365-246X.2010.04513.x

Sagiya, T. (2004). A decade of GEONET: 1994–2003 —The continuous GPS observation in Japan and its impact on earthquake studies—. *Earth, Planets and Space*, *56*(8), xxix–xli. https://doi.org/10.1186/BF03353077

Sagiya, T., & Thatcher, W. (1999). Coseismic slip resolution along a plate boundary megathrust: The Nankai Trough, southwest Japan. *Journal of Geophysical Research: Solid Earth*, *104*(B1), 1111–1129. https://doi.org/10.1029/98JB02644

Sagiya, T., Miyazaki, S., & Tada, T. (2000). Continuous GPS Array and Present-day Crustal Deformation of Japan. In *Pure and Applied Geophysics* (Vol. 157, pp. 2303–2322). Basel. https://doi.org/10.1007/978-3-0348-7695-7_26

Satake, K. (2015). Geological and historical evidence of irregular recurrent earthquakes in Japan. *Philosophical Transactions of the Royal Society A: Mathematical, Physical and Engineering Sciences*, *373*(2053), 20140375. https://doi.org/10.1098/rsta.2014.0375

Satake, K., Nanayama, F., & Yamaki, S. (2008). Fault models of unusual tsunami in the 17th century along the Kuril trench. *Earth, Planets and Space*, *60*(9), 925–935. https://doi.org/10.1186/BF03352848

Sato, M., Fujita, M., Matsumoto, Y., Ishikawa, T., Saito, H., Mochizuki, M., & Asada, A. (2013). Interplate coupling off northeastern Japan before the 2011 Tohoku-oki earthquake, inferred from seafloor geodetic data. *Journal of Geophysical Research: Solid Earth*, *118*(7), 3860–3869. https://doi.org/10.1002/jgrb.50275

Savage, J. C. (1983). A dislocation model of strain accumulation and release at a subduction zone. *Journal of Geophysical Research: Solid Earth*, *88*(B6), 4984–4996. https://doi.org/10.1029/JB088iB06p04984

Seno, T. (2012). Great Earthquakes along the Nankai Trough. *Zisin (Journal of the Seismological Society of Japan. 2nd Ser.)*, *64*(2), 97–116. https://doi.org/10.4294/zisin.64.97

Simons, M., Minson, S. E., Sladen, A., Ortega, F., Jiang, J., Owen, S. E., et al. (2011). The 2011 Magnitude 9.0 Tohoku-Oki Earthquake: Mosaicking the Megathrust from Seconds to Centuries. *Science*, *332*(6036), 1421–1425. https://doi.org/10.1126/science.1206731

Suito, H. (2017a). Detectability of Interplate Fault Slip around Japan, Based on GEONET Daily Solution F3. *Journal of the Geodetic Society of Japan*, *62*(3), 109–120. https://doi.org/10.11366/sokuchi.62.109

Suito, H. (2017b). Viscoelastic Relaxation Caused by the 2004 off the Kii Peninsula

Earthquake. *Zisin (Journal of the Seismological Society of Japan. 2nd Ser.)*, *70*, 135–145. https://doi.org/10.4294/zisin.2016-11

Sun, T., Wang, K., Fujiwara, T., Kodaira, S., & He, J. (2017). Large fault slip peaking at trench in the 2011 Tohoku-oki earthquake. *Nature Communications*, *8*(1), 14044. https://doi.org/10.1038/ncomms14044

Suwa, Y., Miura, S., Hasegawa, A., Sato, T., & Tachibana, K. (2006). Interplate coupling beneath NE Japan inferred from three-dimensional displacement field. *Journal of Geophysical Research*, *111*(B4), B04402. https://doi.org/10.1029/2004JB003203

Swendsen, R. H., & Wang, J.-S. (1986). Replica Monte Carlo Simulation of Spin-Glasses. *Physical Review Letters*, *57*(21), 2607–2609. https://doi.org/10.1103/PhysRevLett.57.2607

Tabei, T., Hashimoto, M., Miyazaki, S., Hirahara, K., Kimata, F., Matsushima, T., et al. (2002). Subsurface structure and faulting of the Median Tectonic Line, southwest Japan inferred from GPS velocity field. *Earth, Planets and Space*, *54*(11), 1065–1070. https://doi.org/10.1186/BF03353303

Tabei, T., Hashimoto, M., Miyazaki, S., & Ohta, Y. (2003). Present-day deformation across the southwest Japan arc: Oblique subduction of the Philippine Sea plate and lateral slip of the Nankai forearc. *Earth, Planets and Space*, *55*(10), 643–647. https://doi.org/10.1186/BF03352471

Tada, T. (1985). Spreading of the Okinawa Trough and Its Relation to the Crustal Deformation in the Kyushu (2). *Zisin (Journal of the Seismological Society of Japan. 2nd Ser.)*, *38*(1), 1–12. https://doi.org/10.4294/zisin1948.38.1_1

Tadokoro, K., Ikuta, R., Watanabe, T., Ando, M., Okuda, T., Nagai, S., et al. (2012). Interseismic seafloor crustal deformation immediately above the source region of anticipated megathrust earthquake along the Nankai Trough, Japan. *Geophysical Research Letters*, *39*(10), n/a-n/a. https://doi.org/10.1029/2012GL051696

Takemura, S., Noda, A., Kubota, T., Asano, Y., Matsuzawa, T., & Shiomi, K. (2019). Migrations and Clusters of Shallow Very Low Frequency Earthquakes in the Regions Surrounding Shear Stress Accumulation Peaks Along the Nankai Trough. *Geophysical Research Letters*, *46*(21), 11830–11840. https://doi.org/10.1029/2019GL084666

Tanioka, Y., & Satake, K. (2001). Detailed coseismic slip distribution of the 1944 Tonankai Earthquake estimated from tsunami waveforms. *Geophysical Research Letters*, *28*(6), 1075–1078. https://doi.org/10.1029/2000GL012284

Tanioka, Y., Ruff, L., & Satake, K. (1996). The Sanriku-Oki, Japan, Earthquake of December 28, 1994 (M w 7.7): Rupture of a different asperity from a previous earthquake. *Geophysical Research Letters*, *23*(12), 1465–1468. https://doi.org/10.1029/96GL01132

Tanioka, Y., Satake, K., & Hirata, K. (2013). Recurrence of Recent Large Earthquakes Along the Southernmost Kurile-Kamchatka Subduction Zone. In *Volcanism and Subduction: The Kamchatka Region* (pp. 145–152). American Geophysical Union (AGU). https://doi.org/10.1029/172GM13

The Advanced Rapid Imaging and Analysis, Preliminary GPS early postseismic displacement data (version 0.3) for march 11, 2011 M9 Japanese earthquake. (2011). Retrieved from ftp://sideshow.jpl.nasa.gov/pub/usrs/ARIA/

The Headquarters for Earthquake Research Promotion, Long-term evaluation of

seismic activity along the Kuril Trench: Third edition. (2017). Retrieved from http://www.jishin.go.jp

Toh, A., Obana, K., & Araki, E. (2018). Distribution of very low frequency earthquakes in the Nankai accretionary prism influenced by a subducting-ridge. *Earth and Planetary Science Letters*, *482*(March 2011), 342–356. https://doi.org/10.1016/j.epsl.2017.10.062

Tonegawa, T., Araki, E., Kimura, T., Nakamura, T., Nakano, M., & Suzuki, K. (2017). Sporadic low-velocity volumes spatially correlate with shallow very low frequency earthquake clusters. *Nature Communications*, *8*(1), 2048. https://doi.org/10.1038/s41467-017-02276-8

Toya, Y., & Kasahara, M. (2005). Robust and exploratory analysis of active mesoscale tectonic zones in Japan utilizing the nationwide GPS array. *Tectonophysics*, *400*(1–4), 27–53. https://doi.org/10.1016/j.tecto.2005.02.003

Tsuji, T., Ashi, J., & Ikeda, Y. (2014). Strike-slip motion of a mega-splay fault system in the Nankai oblique subduction zone. *Earth, Planets and Space*, *66*(1), 120. https://doi.org/10.1186/1880-5981-66-120

Villegas-Lanza, J. C., Chlieh, M., Cavalié, O., Tavera, H., Baby, P., Chire-Chira, J., & Nocquet, J. -M. (2016). Active tectonics of Peru: Heterogeneous interseismic coupling along the Nazca megathrust, rigid motion of the Peruvian Sliver, and Subandean shortening accommodation. *Journal of Geophysical Research: Solid Earth*, *121*(10), 7371–7394. https://doi.org/10.1002/2016JB013080

Wallace, L. M. (2004). Subduction zone coupling and tectonic block rotations in the North Island, New Zealand. *Journal of Geophysical Research*, *109*(B12), B12406. https://doi.org/10.1029/2004JB003241

Wang, K., & Dixon, T. (2004). Coupling semantics and science in earthquake research. *Eos*, *85*(17), 180. https://doi.org/10.1029/2001JB001227.References

Watanabe, S., Bock, Y., Melgar, D., & Tadokoro, K. (2018). Tsunami Scenarios Based on Interseismic Models Along the Nankai Trough, Japan, From Seafloor and Onshore Geodesy. *Journal of Geophysical Research: Solid Earth*, *123*(3), 2448–2461. https://doi.org/10.1002/2017JB014799

Wessel, P., Smith, W. H. F., Scharroo, R., Luis, J., & Wobbe, F. (2013). Generic Mapping Tools: Improved Version Released. *Eos, Transactions American Geophysical Union*, *94*(45), 409–410. https://doi.org/10.1002/2013EO450001

Yagi, Y. (2004). Source rupture process of the 2003 Tokachi-oki earthquake determined by joint inversion of teleseismic body wave and strong ground motion data. *Earth, Planets and Space*, *56*(3), 311–316. https://doi.org/10.1186/BF03353057

Yagi, Y., & Fukahata, Y. (2011). Rupture process of the 2011 Tohoku-oki earthquake and absolute elastic strain release. *Geophysical Research Letters*, *38*(19), n/a-n/a. https://doi.org/10.1029/2011GL048701

Yamanaka, Y. (2005). Asperity Map along the subduction zone in Hokkaido region. In *Seismological Society of Japan* (pp. S052-004). Sapporo, Japan.

Yamanaka, Y. (2006). Reconsideration-1944 Tonankai Earthquake-. *Programme and Abstracts, the Seismological Society of Japan, 2006*, *12*. Retrieved from https://ci.nii.ac.jp/naid/10030364007/

Yamanaka, Y., & Kikuchi, M. (2003). Source process of the recurrent Tokachi-oki earthquake on September 26, 2003, inferred from teleseismic body waves. *Earth, Planets and Space*, *55*(12), e21–e24. https://doi.org/10.1186/BF03352479

Yamanaka, Y., & Kikuchi, M. (2004). Asperity map along the subduction zone in northeastern Japan inferred from regional seismic data. *Journal of Geophysical Research: Solid Earth*, *109*(B7). https://doi.org/10.1029/2003JB002683

Yamashita, Y., Yakiwara, H., Asano, Y., Shimizu, H., Uchida, K., Hirano, S., et al. (2015). Migrating tremor off southern Kyushu as evidence for slow slip of a shallow subduction interface. *Science*, *348*(6235), 676–679. https://doi.org/10.1126/science.aaa4242

Yasuda, K., Tadokoro, K., Taniguchi, S., Kimura, H., & Matsuhiro, K. (2017). Interplate locking condition derived from seafloor geodetic observation in the shallowest subduction segment at the Central Nankai Trough, Japan. *Geophysical Research Letters*, *44*(8), 3572–3579. https://doi.org/10.1002/2017GL072918

Yokota, Y., & Ishikawa, T. (2020). Shallow slow slip events along the Nankai Trough detected by GNSS-A. *Science Advances*, *6*(3), eaay5786. https://doi.org/10.1126/sciadv.aay5786

Yokota, Y., Koketsu, K., Fujii, Y., Satake, K., Sakai, S., Shinohara, M., & Kanazawa, T. (2011). Joint inversion of strong motion, teleseismic, geodetic, and tsunami datasets for the rupture process of the 2011 Tohoku earthquake. *Geophysical Research Letters*, *38*(24), 1–5. https://doi.org/10.1029/2011GL050098

Yokota, Y., Ishikawa, T., Watanabe, S., Tashiro, T., & Asada, A. (2016). Seafloor geodetic constraints on interplate coupling of the Nankai Trough megathrust zone. *Nature*, *534*(7607), 374–377. https://doi.org/10.1038/nature17632

Yokota, Y., Ishikawa, T., & Watanabe, S. (2018). Seafloor crustal deformation data along the subduction zones around Japan obtained by GNSS-A observations. *Scientific Data*, *5*(1), 180182. https://doi.org/10.1038/sdata.2018.182